2014

Experimental Studies of Interacting Electronic States in NaCs

Carl Faust
Lehigh University

Experimental Studies of Interacting Electronic States in NaCs

by
Carl E. Faust

A Dissertation
Presented to the Graduate and Research Committee
of Lehigh University
in Candidacy for the Degree of
Doctor of Philosophy
in
Physics

Lehigh University
August 31, 2014

Approved and recommended for acceptance as a dissertation in partial fulfillment of the requirements for the degree of Doctor of Philosophy.

Carl E. Faust
Experimental Studies of Interacting Electronic States in NaCs

_____
Date

_____
John P. Huennekens, Dissertation Chair

_____
Accepted Date

Committee Members:

_____
A. Peet Hickman

_____
Michael Stavola

_____
Ivan Biaggio

_____
James Roberts

Acknowledgements

There are many people that I would like to thank for their support throughout my time at Lehigh. First and foremost, I would like to thank my wife, Bree, for her constant love and support. She has kept me grounded and focused through the most stressful times at Lehigh. Whether she was listening to countless iterations of practice talks, delivering dinner for late nights of lab work, or simply providing uplifting words, Bree is source of love and encouragement that got me through my graduate career. It is my hope that the work I have done at Lehigh will serve as a reflection of the unconditional love and support I received from Bree (and, of course, our little Stewie). I would like to thank my parents, Pamela and Carl Faust, my sister Jessica Faust, and Bree's father, Valdo Meneses. The support of my family has been and will always continue to be a constant source of motivation and strength.

I would like to express my sincerest thanks to my advisor, Prof. John Huennekens. He has been an amazing teacher and mentor who has given me a shining example of what it means to be an effective scientist and educator. Prof. Huennekens is not only an incredibly knowledgeable researcher but is also very patient and takes the time to work through problems with his students which facilitates a deeper understanding of experimentation. His passion for atomic and molecular physics makes research enjoyable and rewarding. Prof. Huennekens is a great teacher and excellent role model and I am deeply thankful for the opportunity to have had him as an advisor.

I would also like to thank my dissertation committee: Prof. Huennekens, Prof. Hickman, Prof. Stavola, Prof. Biaggio, and Prof. Roberts. Their advice and guidance throughout my time here, especially in constructing this dissertation, has

been invaluable. I would like to thank Prof. DeLeo for his support during my time at Lehigh. Prof. DeLeo has shown me tremendous support towards my aspirations to become an effective educator. He has shown me the importance of truly being excited education. I am also thankful to him for encouraging me to step outside of my comfort zone and be confident in my teaching abilities. I would also like to thank those that I have has the pleasure of collaborating with throughout my time at Lehigh. I would like to thank Prof. Marjatta Lyyra and Ergin Ahmed at Temple University, and Amanda Ross and Patrick Crozet from the University of Lyon, France.

Finally, I would like to thank all the fellow graduate students who have made my time at Lehigh enjoyable. Specifically, I would like to thank Seth Ashman and Chris Wolfe who trained me in the ways of the AMO lab. Other previous AMO grad students: Ruthie Malenda (for Googling), Dave Kashinski, and Brett McGeehan. I would like to thank Josh Jones for being an amazing partner in the lab. With his help we were able to tackle many of the toughest problems that so often came up in the lab and win the game. I would also like to thank the AMO students to follow: Kara Richter and Teri Price. Many thanks to the grad students in my year: Brian Knorr for enhancing productivity and lots of Cantalobber construction, Massooma Pirbhai for laughs, encouragement and chocolate, and Ling Cai for some of the most entertaining conversations I've had.

To all the people listed here and to everyone that I'm sure I have missed, I thank you more than I can possibly express.

Contents

List of Figures

List of Tables

Abstract

This dissertation describes methods and results of spectroscopic studies of the NaCs molecule. NaCs is of particular interest in many labs where experimental studies of ultra-cold molecules are being conducted. Data obtained in the present work will also be useful as benchmarks for various theoretical calculations. Our goals in studying this molecule were to map out high lying electronic states and to understand how these states interact with one another.

Sodium and cesium metal were heated in a heat-pipe oven to form a vapor of NaCs molecules. These molecules were excited using narrow band, continuous wave (cw), tunable lasers. We employed the optical-optical double resonance (OODR) technique to obtain Doppler-free spectra of transitions to rotational and vibrational levels of high lying electronic states. One state of particular interest was the $12(0^+)$ electronic state. Rovibrational level energies corresponding to this state were measured and used to generate a potential energy curve using computer programs to implement both the Rydberg-Klein-Rees (RKR) method [1] and the inverted perturbation approach (IPA) [2].

By observing fluorescence from the $12(0^+)$ state resolved as a function of wavelength, we determined that this state interacts with the nearby $11(0^+)$ electronic state, which was previously mapped out by Ashman *et al.* [3]. A two-stage coupling model was devised to describe the resolved fluorescence originating from these two interacting states. The electronic states interact via spin-orbit coupling, while the individual rovibrational levels interact via a second mechanism, likely nonadiabatic coupling. This two-stage coupling between the levels of these states causes quantum interference between fluorescence pathways associated with different components of

the wavefunctions describing these levels. This interference results in more complicated resolved fluorescence spectra. The model was used to fit parameters describing these interactions so that the resolved fluorescence spectra could be reproduced.

The NaCs $4^3\Pi_{0^+}$ electronic state was also studied in this work. Energies of many rovibrational levels belonging to the $4^3\Pi_{0^+}$ electronic state were measured. This state is interesting because it likely has a potential energy curve with a double minimum, which results in a different type of quantum interference, directly observed in resolved spectra. The state also very likely has interactions with the $11(0^+)$ and $12(0^+)$ states. Energies of many rovibrational levels lying above the energy of the barrier between the two minima were measured, and it appears that we also observed a few levels lying below the barrier. Since the laser wavelengths necessary to excite the lowest vibrational levels were not available, an experimental potential curve could not be produced. Therefore, rovibrational level energies and spectroscopic constants are tabulated.

Chapter 1

Introduction

Spectroscopic studies of diatomic molecules, specifically alkali diatomics, have provided a great deal of information about many interesting and fundamental ideas surrounding molecular quantum mechanics. Information gathered from the study of these molecules can be useful for many different areas of research. Currently a great deal of work is being done with diatomic alkali molecules in attempts to devise efficient processes of producing ultracold ground state molecules. Photoassociated ultracold atoms are brought to some of the lowest rovibrational levels of the lowest triplet or singlet states of LiCs [4], RbCs [5], Cs_2 [6], and NaCs [7] through various single and multistep schemes. The schemes for doing this often require accurate spectroscopic data, such as rovibrational level structure, electronic state interactions, and transition dipole moment functions.

Our group has chosen to work primarily with heteronuclear alkali molecules. Unlike homonuclear diatomics, heteronuclear molecules have permanent electric dipole moments, which are of interest due to possible applications for quantum computing. It has been suggested that electric fields could be used to trap and orient the polar molecules to form a type of qubit [8]. Of all the heteronuclear diatomic molecules, NaCs has the second largest permanent dipole moment (Table 1.1). Spectroscopic information on NaCs is therefore particularly valuable since it would be a very useful molecule for such an application.

The permanent electric dipole moment of NaCs is not its only attractive quality.

Molecule	Expt. Dipole Moment (Debye)
LiNa	0.47
LiK	3.45
LiRb	4.05
LiCs	6.30
NaK	2.73
NaRb	3.10
NaCs	4.75
KRb	0.20
KCs	2.58
RbCs	2.39

Table 1.1: Permanent dipole moments of heteronuclear alkali molecules in the $1(X)^1\Sigma^+$ state [9].

Atomic Symbol	Splitting (cm^{-1})
Li	0.335
Na	17.196
K	57.71
Rb	273.595
Cs	554.393
Fr	1686.589

Table 1.2: Spin-orbit splitting of alkali atoms in the first excited state ($E[\mathrm{P}_{J=\frac{3}{2}}] - E[\mathrm{P}_{J=\frac{1}{2}}]$) [10].

NaCs is also interesting due to the large spin-orbit interaction in this molecule. The spin-orbit interaction is a result of the magnetic interaction of the magnetic moment produced by an electron's spin with the magnetic field produced by its orbital angular momentum about the nucleus. This interaction is particularly strong when the molecule contains a heavy atom such as Cs (see Table 1.2). The large spin-orbit effect causes stronger interactions between electronic states and more global perturbations of level energies. A molecule with a large spin-orbit interaction such as NaCs is expected to follow Hund's coupling case (c), instead of the more commonly observed cases (a) or (b) [11] (Hund's cases are described in detail in Sec. 2.2). When the angular momentum vectors couple according to case (c), the energy level structure and resolved fluorescence spectra can be very different and sometimes more complicated than those observed in molecules with relatively smaller spin-orbit interactions.

Theory also benefits from spectroscopic data obtained from the present work. Theoretical calculations of potentials [12], transition dipole moment functions [13], and collision cross sections [14] are becoming sufficiently accurate to be useful for preliminary predictions of experimental data. This comparison is a good test for

computer codes and methods used for these calculations.

Several previous studies, both experimental and theoretical, provide critical foundations for the experiments presented in this dissertation. Docenko *et al.* [15] determined rovibrational energies of the $1(X)^1\Sigma^+$ and $1(a)^3\Sigma^+$ states of NaCs, and used this information to map potential curves and determine Dunham coefficients. Zaharova *et al.* [16] performed spectroscopic measurements and deperturbation analysis on the mixed $1(b)^3\Pi_{0^+} \sim 2(A)^1\Sigma^+$ states. More recently, work in our lab by Ashman *et al.* [3] determined Dunham coefficients for the NaCs $5^3\Pi_{0^+}$ state and mapped the potential energy curve using the inverted perturbation approach (IPA). This study also involved a detailed analysis of resolved bound-free fluorescence spectra in order to accurately determine the $5^3\Pi_{0^+} \rightarrow 1(a)^3\Sigma^+$ transition dipole moment function and the repulsive wall of the $1(a)^3\Sigma^+$ state. In this disseration, I will refer to the $5^3\Pi_{0^+}$ state as the $11(0^+)$ state using the Hund's case (c) notation described in Sec. 2.2. Theoretical potential energy curves, which include spin-orbit effects, were calculated by Korek *et al.* [12] and are shown in Figure 1.1. Theoretical transition dipole moment functions were calculated by Aymar and Dulieu [17]. Both of these studies were very useful in calculations of rovibrational level energies and simulations of bound-free spectra. Finally, work done by Brett McGeehan [18] at Lehigh to improve the flexibility and utility of the BCONT program was very useful for the analysis described in Chapter 6.

Chapter 2 contains background on fundamental molecular physics including the Born-Oppenheimer approximation and Hund's cases. A description of the experimental setup and equipment used to perform these experiments is found in Chapter 3. Experimental techniques, including optical-optical double resonance (OODR) excitation and resolved fluorescence detection, are described in Chapter 4. Chapter 5 describes our studies of the $12(0^+)$ electronic state of NaCs and explains the process of determining an experimental potential energy curve. Chapter 6 discusses the model we use to describe the resolved bound-free fluorescence from the $12(0^+)$ state and how simulations of bound-bound and bound-free spectra with this model can provide information about two-stage coupling between the $11(0^+)$ and $12(0^+)$ states of NaCs. Spectroscopic studies of the NaCs $4^3\Pi_{0^+}$ state can be found in Chapter

7. Finally, Chapter 8 presents the conclusions reached in this work and includes ideas for future work. Appendices A, B, and C include tables of rovibrational level energies for the NaCs $1(b)^3\Pi_{0^+}$ $\sim 2(A)^1\Sigma^+$, $12(0^+)$, and $4^3\Pi_{0^+}$ states, respectively, obtained in this work. Appendix D lists diode array detector wavelength response efficiencies (described in Sec. 3.4.3) as a function of array pixel for use in future work.

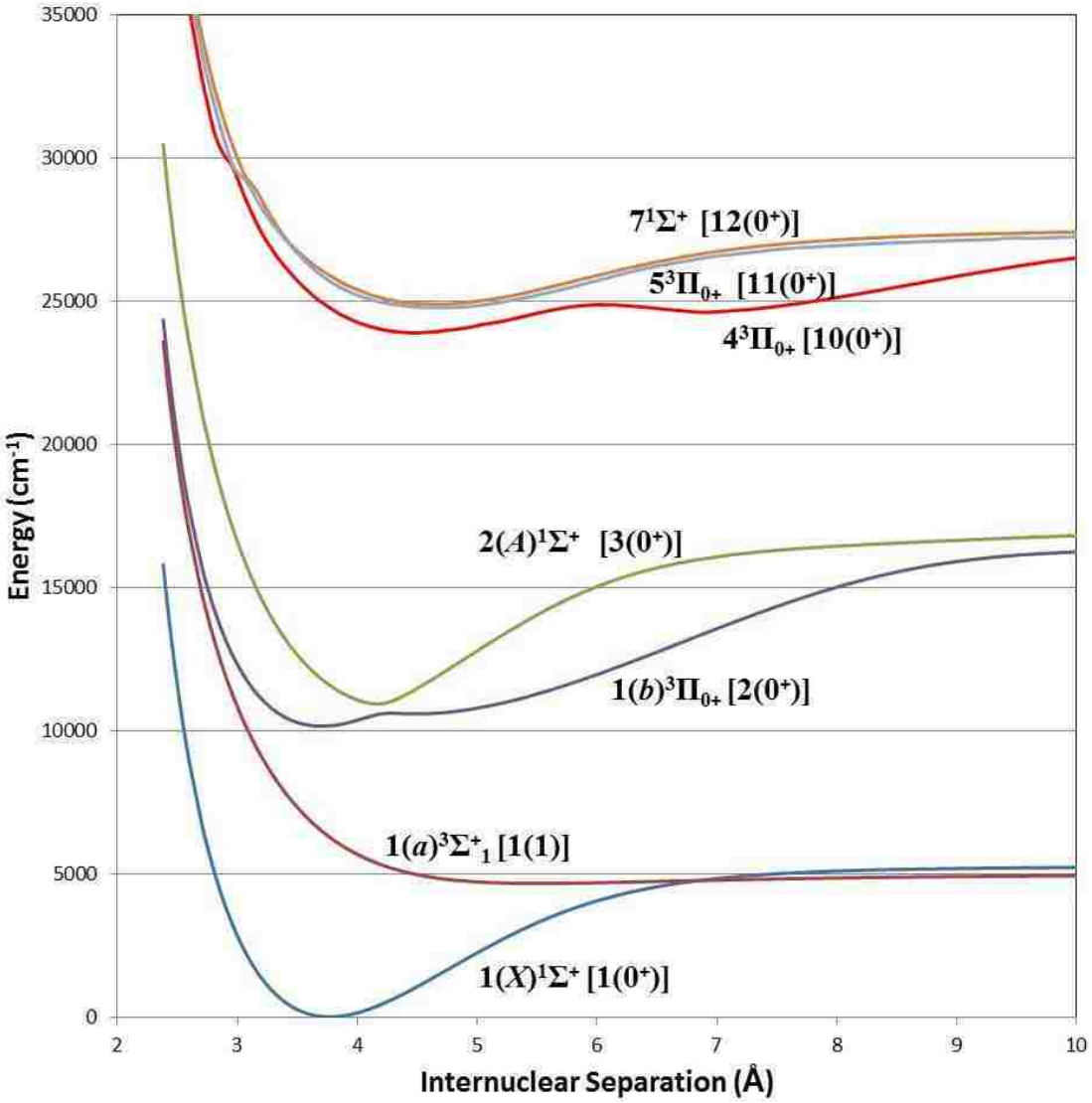

Figure 1.1: Theoretically calculated NaCs potential energy curves [12] for electronic states relevant to the present work. Labels reflect Hund's case (a) [Hund's case (c) notation].

Chapter 2

Molecular Physics

2.1 Born-Oppenheimer Approximation

The time-independent Schrödinger equation,

$$\hat{H}\Psi(\vec{q},\vec{R}) = E\Psi(\vec{q},\vec{R}), \tag{2.1}$$

can be solved to obtain the energy eigenvalues, E, and wavefunctions, Ψ associated with the states of the molecule. The total wavefunction, Ψ, depends on all the electronic corrdinates abbreviated $\vec{q}$, where $\vec{q} = \{\vec{r}_1, ..., \vec{r}_N\}$, and the nuclear coordinates, $\vec{R}$. The Hamiltonian, $\hat{H}$, for the system contains terms that describe the kinetic and potential energies of the nuclei and electrons.
We have the electronic kinetic energy

$$\hat{T}_{\text{elec}} = \frac{-\hbar^2}{2m_{\text{e}}}\sum_{i=1}^{N}\nabla^2_{\vec{q}}, \tag{2.2}$$

where m_{e} is the mass of the electron, and the nuclear kinetic energy

$$\hat{T}_{\text{nucl}} = \frac{-\hbar^2}{2\mu}\nabla^2_{\vec{R}}, \tag{2.3}$$

where $\mu = \frac{M_{\text{A}}M_{\text{B}}}{M_{\text{A}}+M_{\text{B}}}$ is the reduced mass of nuclei A and B and derivatives are taken in the center of mass frame. Addditionally, there is there electron-electron Coulomb

repulsion potential energy

$$V_{\text{ee}} = \sum_{i=1}^{N} \sum_{j>i}^{N} \frac{e^2}{4\pi\epsilon_0 r_{ij}}, \tag{2.4}$$

where $r_{ij} = |\vec{r}_i - \vec{r}_j|$ is the separation of electrons i and j, the electron-nuclei Coulomb attraction potential energy

$$V_{\text{eN}} = -\sum_{i=1}^{N} \sum_{\alpha=1}^{2} \frac{Z_\alpha e^2}{4\pi\epsilon_0 r_{i\alpha}}, \tag{2.5}$$

where $r_{i\alpha} = |\vec{r}_i - \vec{r}_\alpha|$ is the separation of electron i and nuclear α, and finally the nuclear Coulomb repulsion energy

$$V_{\text{NN}} = \frac{Z_1 Z_2 e^2}{4\pi\epsilon_0 R}. \tag{2.6}$$

where $R = \left|\vec{R}_A - \vec{R}_B\right|$ is the internuclear separation.

To simplify the process of solving the total Schrödinger equation, we first solve the Schrödinger equation for the electronic eigenstates by fixing the internuclear separation. The resulting energies, E_n, and wavefunctions, Φ_n, depend on R parametrically:

$$[\hat{T}_{\text{elec}} + V_{\text{ee}}(\vec{q}) + V_{\text{eN}}(\vec{q};\vec{R}) + V_{\text{NN}}(\vec{R})]\Phi_n(\vec{q};\vec{R}) = E_n(R)\Phi_n(\vec{q};\vec{R}). \tag{2.7}$$

Assuming that the electronic wavefunctions can be calculated, we will then in principle have a complete set of orthonormal functions, $\Phi_n(\vec{q};\vec{R})$ for each R. This complete set of basis functions is used to express the solution to the total Schrödinger equation:

$$\Psi(\vec{q},\vec{R}) = \sum_n \psi_n(\vec{R})\Phi_n(\vec{q};\vec{R}). \tag{2.8}$$

Since the total wavefunction must certainly depend on R, the expansion coefficients must also depend on R. In the Born-Oppenheimer approximation, these $\psi_n(\vec{R})$ will turn out to be the nuclear wavefunctions and are determined by substituting this expansion back into the total molecular Schrödinger equation. After substituting

Eq. (2.8) into Eq. (2.1), we multiply on the left by $\Phi_m^*(\vec{q};\vec{R})$ and integrate over all the electronic coordinates. Since the electronic wavefunctions form a complete orthonormal set, the equation simplifies to

$$\left[\int \Phi_m^*(\vec{q};\vec{R})\left(\frac{-\hbar^2}{2\mu}\right)\nabla_{\vec{R}}^2\left(\sum_n \psi_n(\vec{R})\Phi_n(\vec{q};\vec{R})\right)d^3\vec{q}\right] + [E_m(R) - E]\psi_m(\vec{R}) = 0. \tag{2.9}$$

The analysis of the Coulomb interactions has been exact up to this point. However, the problem is now to deal with the nuclear kinetic energy term in this equation. The Born-Oppenheimer approximation consists of assuming that the electronic wavefunctions vary sufficiently slowly with internuclear separation such that the kinetic energy term in the previous equation can be written as:

$$\begin{aligned}
&\nabla_{\vec{R}}^2\left(\psi_n(\vec{R})\Phi_n(\vec{q};\vec{R})\right) \\
&\quad = \psi_n(\vec{R})\nabla_{\vec{R}}^2\Phi_n(\vec{q};\vec{R}) + 2\nabla_{\vec{R}}\psi_n(\vec{R})\cdot\nabla_{\vec{R}}\Phi_n(\vec{q};\vec{R}) + \Phi_n(\vec{q};\vec{R})\nabla_{\vec{R}}^2\psi_n(\vec{R}) \\
&\quad \approx \Phi_n(\vec{q};\vec{R})\nabla_{\vec{R}}^2\psi_n(\vec{R}).
\end{aligned} \tag{2.10}$$

This approximation can break down when electronic wavefunctions change suddenly with internuclear separation, for example, near particular regions of electronic potentials $[E_m(R)]$ that exhibit avoided crossings with other potentials.

If the approximation of Eq. (2.10) is satisfactory then Eq. (2.9) reduces to:

$$\left[\frac{-\hbar^2}{2\mu}\nabla_{\vec{R}}^2 + E_m(R) - E\right]\psi_m(\vec{R}) = 0. \tag{2.11}$$

The electronic energy as a function of internuclear separation $[E_m(R)]$ acts as an effective potential energy function which gives rise to the nuclear wavefunctions. The nuclear wavefunctions have a separate radial (vibration) and angular (rotation) dependence since $\nabla_{\vec{R}}^2$ can be broken up into radial and angular parts. Vibrational and rotation quantum numbers, v and J respectively, should now be included as labels on $\psi_{m,v}^J(\vec{R})$ to identify particular solutions to Eq. (2.11). Note that the

nuclear wavefunctions associated with each electronic state (including continuum levels) form a complete set for that particular electronic state.

The nuclear kinetic energy term, Eq. (2.3), can be further broken up as:

$$\hat{T}_{\text{nucl}}(R,\theta,\phi) = \hat{T}_{\text{radial}}(R) + \hat{H}_{\text{rot}} = \hat{T}_{\text{radial}}(R) + \frac{\hbar^2[J(J+1)-\Omega^2]}{2\mu R^2}, \tag{2.12}$$

where the nuclear coordinates, $\vec{R}$, are now explicitly written as R, θ, ϕ, which are the radial, polar angle, and azimuthal angle coordinates respectively. In Eq. (2.12), the second term describes the rotation of the nuclei about their center of mass. This term is written assuming a Hund's case (c) coupling case (see Sec. 2.2.4). The rotational quantum number is J, and Ω is the projection of the total electronic angular momentum onto the internuclear axis. Substituting this into Eq. (2.11), gives an equation which depends only on R. The centrifugal potential adds energy to the potential with the added amount scaling as $\frac{1}{R^2}$. Typically, potentials determined either experimentally or theoretically are "rotationless" meaning $J = 0$ in Eq. (2.12). However, once a rotationless potential has been determined, it is easy to find the corresponding potential for any particular J values.

2.2 Hund's Cases

Using the Born-Oppenheimer approximation to find solutions to the molecular Schrödinger equation implies that the nuclear and electronic motion can be separated in a simple way. In reality, we would like to find a way to describe the effects that the electronic and nuclear motions have on one another. Specifically, the different ways in which the angular momenta of the molecule couple together can be described using Hund's coupling cases [11]. The various angular momenta associated with the molecule are electron orbital ($\vec{L}$), electron spin ($\vec{S}$), nuclear orbital or rotation ($\vec{R}$, not to be confused with the internuclear separation coordinate, which is also labeled by $\vec{R}$), and nuclear spin ($\vec{I}$). In this work, we will ignore the effects of nuclear spin. There are five main Hund's cases called (a), (b), (c), (d), and (e).

The differences between these Hund's cases depend on the relative strengths of the various interactions between the angular momenta of the molecule. Cases (d) and (e) are used to describe coupling schemes where rotational coupling is dominant, which is not the case in NaCs. Therefore descriptions in the following sections will only be given for cases (a), (b), and (c). Vector coupling diagrams for these three cases are shown in Figure 2.1. Note that all Hund's cases are limiting cases and states of real molecules are likely best described by some intermediate case.

2.2.1 Hund's Case (a)

In the case (a) limit, the electronic orbital angular momentum couples electrostatically to the internuclear axis. As the electronic orbital angular momentum vector, $\vec{L}$, precesses, only its component along the internuclear axis, $\Lambda \equiv |M_L|$, is well defined. Similarly, $\Sigma \equiv |M_S|$ is the well defined component of electron spin, $\vec{S}$, along the internuclear axis. The total electronic angular momentum along the internuclear axis is then $\vec{\Omega} = \vec{\Lambda} + \vec{\Sigma}$. Finally, $\vec{\Omega}$ couples with the nuclear rotation angular momentum vector, $\vec{R}$, which is perpendicular to the internuclear axis, to form the total angular momentum vector, $\vec{J}$ [$\vec{J} = \vec{\Omega} + \vec{R}$]. In this coupling limit, J, Λ, Σ and, hence, Ω are all good quantum numbers. Electronic state labels have the form $n^{2S+1}\Lambda_\Omega$. The quantum number Λ is designated by capital Greek letters such as, Σ for $\Lambda = 0$, Π for $\Lambda = 1$, Δ for $\Lambda = 2$, etc. In this coupling limit, electrostatic interactions are most important.

2.2.2 Hund's Case (b)

In the case (b) limit, the electronic angular momentum couples electrostatically to the internuclear axis, as in case (a). The electronic spin, $\vec{S}$, however, does not couple to the internuclear axis. Instead, $\vec{\Lambda}$ and the nuclear rotation angular momentum, $\vec{R}$, precess around each other to form $\vec{N}$ [$\vec{N} = \vec{\Lambda} + \vec{R}$]. The electronic spin then couples to this intermediate angular momentum vector. $\vec{S}$ and $\vec{N}$ precess around each other to form the total angular momentum, $\vec{J}$ [$\vec{J} = \vec{N} + \vec{S}$]. In this Hund's coupling limit, electrostatic interactions are still strong, however, spin-orbit interactions are

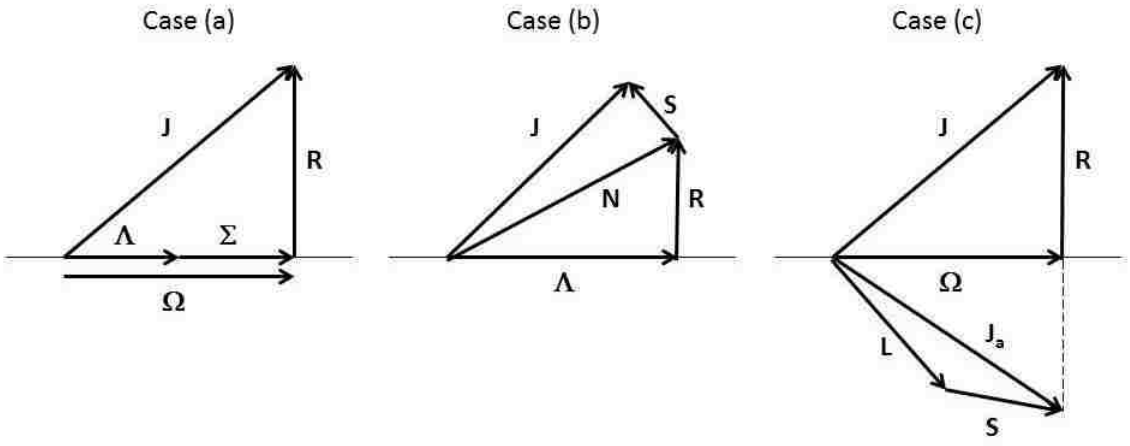

Figure 2.1: Vector coupling models for Hund's cases (a), (b), and (c). The thin horizontal line represents the internuclear axis.

relatively weaker, which results in the spin interacting more strongly with the nuclear rotation. Electronic states with $\Lambda = 0$ are pure case (b) states since, in this situation, the spin vector does not couple to the internuclear axis. A transition can also occur between case (a) and case (b) within a single electronic state when the rotation of the molecule becomes sufficiently rapid that the electron spin can no longer precess about $\vec{\Lambda}$. As a result of this transition, known as spin uncoupling, case (b) is appropriate when describing states with large J. Because case (b) implies weak spin-orbit interactions, it is typically not well suited to describe electronic states of NaCs.

2.2.3 Hund's Case (c)

In the case (c) limit, spin-orbit coupling between $\vec{L}$ and $\vec{S}$ is stronger than the electrostatic coupling of either of them to the internuclear axis. Because of the strong spin-orbit interaction, $\vec{L}$ and $\vec{S}$ precess around each other to form an intermediate angular momentum vector, $\vec{J}_a$ [$\vec{J}_a = \vec{L} + \vec{S}$]. This vector then precesses about the internuclear axis and its component along that axis is $\vec{\Omega}$. As in case (a), $\vec{\Omega}$ then couples to the nuclear rotation angular momentum vector, $\vec{R}$, to form the total

angular momentum $\vec{J}$ [$\vec{J} = \vec{\Omega} + \vec{R}$]. The quantum numbers Λ and Σ are no longer valid quantum numbers and the electronic states are described only by Ω.

2.2.4 Rotational Hamiltonian

From the vector coupling models, we can see how to express the rotational energies in terms of good quantum numbers. Following [19], the rotational part of the nuclear kinetic energy term of Hamiltonian shown in Eq. (2.12) is:

$$\boldsymbol{H}_{\text{rot}} = \frac{\boldsymbol{R}^2}{2\mu R^2}, \tag{2.13}$$

with $\boldsymbol{R}$ being the rotational angular momentum operator. In general, the total angular momentum vector, $\vec{J}$, is the vector sum of electronic orbital angular momentum, $\vec{L}$, electronic spin, $\vec{S}$, and nuclear rotation, $\vec{R}$. However depending on which Hund's case best describes the molecule, the $\boldsymbol{R}$ operator must be expressed using appropriate quantum numbers valid for that particular Hund's case.

In Hund's case (a), we can write an expression for $\boldsymbol{R}$ in terms of other angular momentum operators since the angular momentum vectors can be related with

$$\vec{R} = \vec{J} - \vec{L} - \vec{S}. \tag{2.14}$$

Using Eq. (2.14), and the fact that the rotational angular momentum never has a z-component because nuclear motion must always take place in a plane containing the internuclear axis, Eq. (2.13) can be rewritten as

$$\boldsymbol{H}_{\text{rot}} = \frac{1}{2\mu R^2}(\boldsymbol{R}_x^2 + \boldsymbol{R}_y^2) = \frac{1}{2\mu R^2}[(\boldsymbol{J}_x - \boldsymbol{L}_x - \boldsymbol{S}_x)^2 + (\boldsymbol{J}_y - \boldsymbol{L}_y - \boldsymbol{S}_y)^2]. \tag{2.15}$$

Finally, linear combinations of x and y components of the angular momentum operators can be expressed in terms of raising and lowering operators:

$$\boldsymbol{J}^{\pm} = \boldsymbol{J}_x \pm i\boldsymbol{J}_y,\ \boldsymbol{L}^{\pm} = \boldsymbol{L}_x \pm i\boldsymbol{L}_y,\ \boldsymbol{S}^{\pm} = \boldsymbol{S}_x \pm i\boldsymbol{S}_y. \tag{2.16}$$

This gives the final expression for the rotational Hamiltonian in case (a):

$$\boldsymbol{H}_{\rm rot} = \frac{1}{2\mu R^2}[(\boldsymbol{J}^2 - \boldsymbol{J}_z^2) + (\boldsymbol{L}^2 - \boldsymbol{L}_z^2) + (\boldsymbol{S}^2 - \boldsymbol{S}_z^2) + (\boldsymbol{L}^+\boldsymbol{S}^- + \boldsymbol{L}^-\boldsymbol{S}^+) - (\boldsymbol{J}^+\boldsymbol{L}^- + \boldsymbol{J}^-\boldsymbol{L}^+) - (\boldsymbol{J}^+\boldsymbol{S}^- + \boldsymbol{J}^-\boldsymbol{S}^+)]. \quad (2.17)$$

The last three terms in this expression are off-diagonal terms in the Hamiltonian matrix that can cause interactions between electronic states. The first three terms, however, are diagonal and give the rotational energies:

$$E_{\rm rot} = \frac{\hbar^2}{2\mu R^2}[J(J+1) - \Omega^2 + S(S+1) - \Sigma^2 + L(L+1) - \Lambda^2]. \quad (2.18)$$

In general L is not a good quantum number so the $\frac{\hbar^2}{2\mu R^2}[L(L+1) - \Lambda^2]$ term is incorporated into the electronic energy of a particular state. Although Σ is a good quantum number, the $S(S+1) - \Sigma^2$ term is also typically included in the electronic energy. Therefore, the rotational energies in Hund's case (a) are usually written as

$$E_{\rm rot} = \frac{\hbar^2}{2\mu R^2}[J(J+1) - \Omega^2]. \quad (2.19)$$

In Hund's case (b), $\vec{N} = \vec{L} + \vec{R}$ so Eq. (2.13) is written as

$$\boldsymbol{H}_{\rm rot} = \frac{1}{2\mu R^2}(\boldsymbol{N} - \boldsymbol{L})^2 = \frac{1}{2\mu R^2}[\boldsymbol{N}^2 - \boldsymbol{N}_z^2 + \boldsymbol{L}^2 - \boldsymbol{L}_z^2 - (\boldsymbol{N}^+\boldsymbol{L}^- + \boldsymbol{N}^-\boldsymbol{L}^+)], \quad (2.20)$$

with $\boldsymbol{N}^\pm = \boldsymbol{N}_x \pm i\boldsymbol{N}_y$. The last term in parentheses results in off-diagonal matrix elements responsible for coupling of states with $\Delta\Lambda = \pm 1$. The other terms yield diagonal matrix elements giving the rotational energies in Hund's case (b). As in Hund's case (a), the $\boldsymbol{L}^2 - \boldsymbol{L}_z^2$ terms are typically incorporated into the electronic energy. Since $\vec{R}$ is perpendicular to the internuclear axis, the component of $\vec{N}$ along the internuclear axis, $\vec{N}_z$, is $\vec{\Lambda}$. Therefore the rotational energies in terms of Hund's case (b) quantum numbers are

$$E_{\rm rot} = \frac{\hbar^2}{2\mu R^2}[N(N+1) - \Lambda^2]. \quad (2.21)$$

Finally, in Hund's case (c), $\vec{J} = \vec{J}_a + \vec{R}$ so Eq. (2.13) is written as

$$\boldsymbol{H}_{\rm rot} = \frac{1}{2\mu R^2}(\boldsymbol{J} - \boldsymbol{J}_a)^2 = \frac{1}{2\mu R^2}[\boldsymbol{J}^2 - \boldsymbol{J}_z^2 + \boldsymbol{J}_a^2 - \boldsymbol{J}_{az}^2 - (\boldsymbol{J}^+\boldsymbol{J}_a^- + \boldsymbol{J}^-\boldsymbol{J}_a^+)], \quad (2.22)$$

with $\boldsymbol{J}_a^{\pm} = \boldsymbol{J}_{ax} \pm i\boldsymbol{J}_{ay}$. The last term in parentheses yields off-diagonal matrix elements responsible for coupling of states with $\Delta\Omega = \pm 1$. The first terms are diagonal matrix elements giving the rotational energies in Hund's case (c). Similar to the $\boldsymbol{L}^2 - \boldsymbol{L}_z^2$ terms in Hund's cases (a) and (b), the $\boldsymbol{J}_a^2 - \boldsymbol{J}_{az}^2$ terms are typically incorporated into the electronic energy, since J_a is not a good quantum number. Finally, the rotational energies in terms of Hund's case (c) quantum numbers are

$$E_{\rm rot} = \frac{\hbar^2}{2\mu R^2}[J(J+1) - \Omega^2]. \quad (2.23)$$

We retain the Ω^2 term in the rotational energy since its inclusion in $E_{\rm rot}$ can be useful in identifying the character of the electronic state, as is described in more detail in Sec. 5.1.

2.3 Nuclear Motion

Separating the molecular wavefunction as described in Sec. 2.1 is a useful approximation since it allows the total energy of the molecule to be broken up into parts associated with the various motions of the molecule. When separating the wavefunction in this way the total energy is

$$E = E_{\rm e} + E_{\rm v} + E_{\rm r}, \quad (2.24)$$

where $E_{\rm e}$, $E_{\rm v}$, and $E_{\rm r}$ are the electronic, vibrational, and rotational energies, respectively. The electronic part has been described above. As a first approximation, the vibration of the molecule can be described as a harmonic oscillator and the rotation as a rigid rotor. Higher order terms are then added to these simple descriptions such that the energy levels of typical electronic potentials can be described in a straightforward and general way.

2.3.1 Vibration

A reasonable starting point for describing the vibrational motion of the nuclei is the harmonic oscillator approximation. Using a Taylor series expansion, any potential with a minimum can be approximated, to lowest order, as a harmonic oscillator. For diatomic electronic potentials, this approximation is often reasonably good near the bottom of the well. A particular molecular potential, $V(R)$, can be expanded as

$$V(R) = V(R_{\rm eq}) + \left(\frac{dV}{dR}\right)_{R=R_{\rm eq}} (R - R_{\rm eq}) + \frac{1}{2}\left(\frac{d^2V}{dR^2}\right)_{R=R_{\rm eq}} (R - R_{\rm eq})^2 + \cdots , \quad (2.25)$$

where $R_{\rm eq}$ is the equilibrium internuclear separation. Since $R_{\rm eq}$ is the minimum, the derivative in the second term is zero and the first term is a constant that can be incorporated into the electronic energy. So, neglecting higher order terms, the potential can be considered to be a harmonic oscillator with the second derivative of the potential at the minimum equal to an effective spring constant, k. The energy solutions for such a potential are well known,

$$E_{\rm HO} = \hbar\omega\left(v + \frac{1}{2}\right), \quad (2.26)$$

with $\omega = \sqrt{\frac{k}{\mu}}$; i.e. the energy levels are equally spaced. Typical electronic states, however, do not follow harmonic oscillator level spacings at higher values of v. As shown in Figure 2.2, the inner wall is usually more steep and the outer wall is less steep than the harmonic oscillator potential at higher energies. These features require the addition of higher order terms to account for the anharmonicity of the potential. The energy can be expanded in a power series [11] in $(v + \frac{1}{2})$ as

$$E_v = \omega_e\left(v + \frac{1}{2}\right) - \omega_e x_e\left(v + \frac{1}{2}\right)^2 + \omega_e y_e\left(v + \frac{1}{2}\right)^3 + \cdots \quad (2.27)$$

where ω_e, $\omega_e x_e$, and $\omega_e y_e$ are constants with units of energy. Note the negative sign in the second term. This term is negative for physical potentials since the curves typically open up faster than the harmonic oscillator potential at higher energies

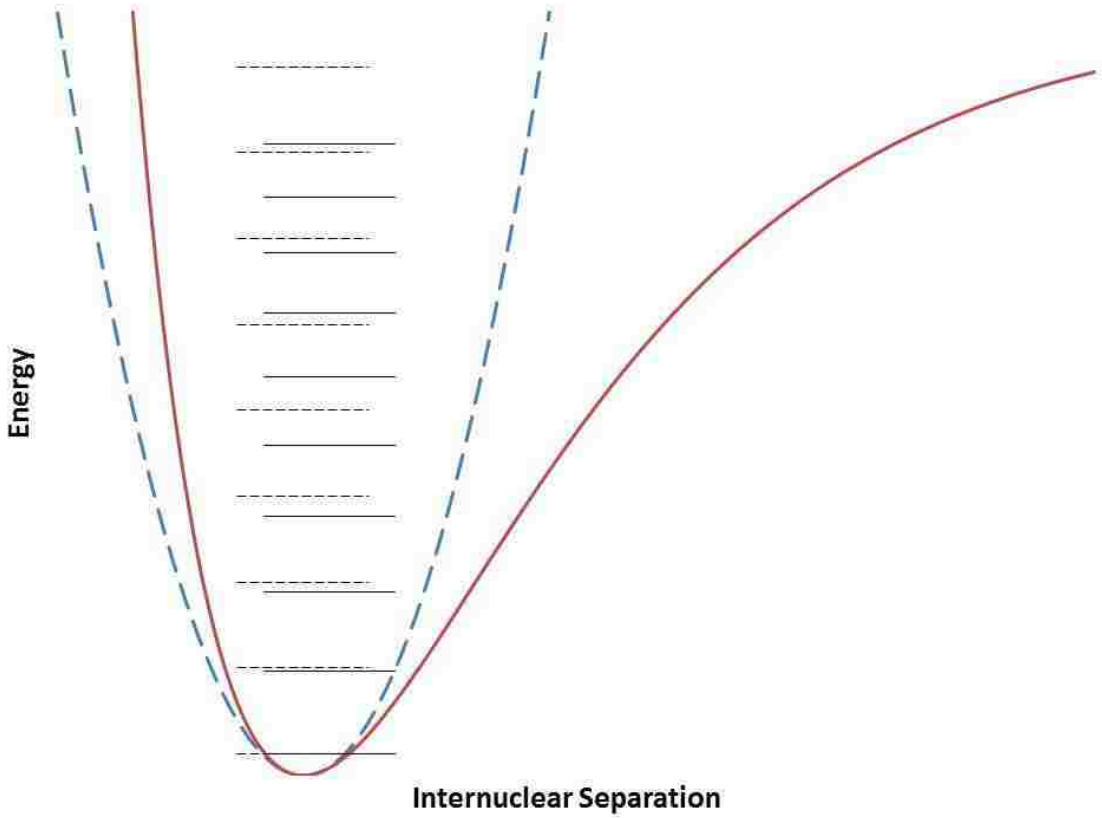

Figure 2.2: Comparison of a harmonic oscillator potential and energy levels (dashed) and a typical Morse electronic state potential and energy levels (solid). The harmonic oscillator energies are regularly spaced while the energies of the anharmonic Morse potential get closer together as they approach the dissociation limit.

causing the levels to become more and more closely spaced as they approach the dissociation limit.

2.3.2 Rotation

The part of the nuclear kinetic energy term in Eq. (2.12) that depends only on nuclear angular coordinates, θ and ϕ, describes how the nuclei rotate about their center of mass. The rotational energies of the molecule can be described using the rigid rotor approximation which gives

$$E_{\text{rot}} = \frac{\hbar^2}{2\mu R_{\text{eq}}^2} J(J+1) = B_e J(J+1). \tag{2.28}$$

Here, μR_{eq}^2 is the moment of inertia of the molecule and R_{eq} is the equilibrium internuclear separation. As the name implies, the rigid rotor approximation assumes that the separation between the nuclei is constant. However, as J gets bigger the molecule rotates faster which results in an increase in the average internuclear separation. A larger internuclear separation means a larger moment of inertia and hence a smaller rotational energy. If a power series [11] in $J(J+1)$ is used to describe the rotational energy, then the second term in

$$E_r = B_e J(J+1) - D_e[J(J+1)]^2 + \cdots \tag{2.29}$$

accounts for this stretching, where D_e is called the centrifugal distortion constant. This term is negative because the stretching will always descrease the rotational energy.

2.3.3 Dunham Expansion

We would like to be able to describe the rovibrational level energies in a more general way so it is often not sufficient to rely on a model based on uncoupled vibration and rotation. For example, as the vibrational energies get larger, the average internuclear separation tends to increase as shown in Fig. 2.3. This means a correction should be added to the rigid rotor expression to include the effects of the vibrating rotor:

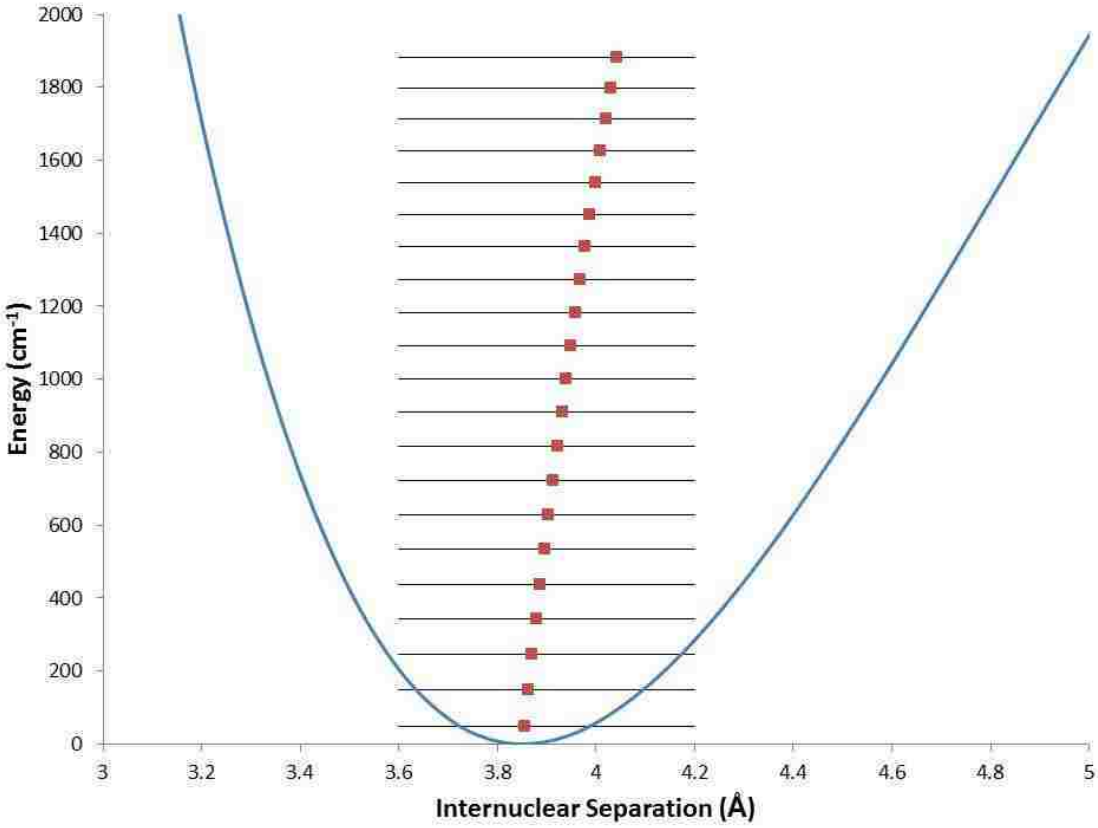

Figure 2.3: Energy level diagram illustrating the vibrating rotor for the first 20 vibrational levels. Points represent the values of R_{eq} for each vibrational level. Since the values of R_{eq} tend to increase with larger v, the moment of inertia of the molecule increases with v resulting in a lower rotational energy for larger v.

$$E = B_e J(J+1) - \alpha_e \left(v + \frac{1}{2}\right)[J(J+1)] + \cdots \tag{2.30}$$

Here the second term is negative since the moment of inertia is generally larger for larger v, lowering the rotational energy. A similar expansion can be made to describe how the centrifugal distortion terms depend on vibration. In principle, one could add higher and higher order terms to describe the energy level structure of a particular electronic state, gaining as much accuracy as desired. To write these expansions in a more compact form, the Dunham expansion is used [20]. This double power series [11] is written as

$$E(v, J) = \sum_{i,k} Y_{i,k} \left(v + \frac{1}{2}\right)^i [J(J+1) - \Omega^2]^k, \tag{2.31}$$

where the $Y_{i,k}$ are called Dunham coefficients. Here we have replaced $[J(J+1)]$ by $[J(J+1) - \Omega^2]$ as per the discussion in Sec. 2.2.4. Computer programs such as DParFit written by Robert Le Roy [21] can determine these coefficients from a set of experimental level energies for a particular electronic state. This expansion is well suited for typical Morse-like potentials but becomes less useful when describing states that are highly perturbed; i.e., more and more higher order corrections are needed to accurately reproduce level energies. The Dunham expansion also becomes invalid for describing levels close to the dissociation limit. Reference [22] states that the Dunham expansion is only valid when describing a Morse-like potential within the range $0 \leq R \leq 2R_{\text{eq}}$.

2.4 Transition Intensities

By detecting fluorescence emitted when a molecule in an excited electronic state decays to a lower state and examining its intensity as a function of wavelength we obtain information about the energy levels and wavefunctions (and by extension the potentials) of the electronic states involved, and about the transition dipole moment function coupling the upper and lower states. Emission from a single ro-vibrational

level can result in two very different types of spectra. Bound-bound emission produces fluorescence to discrete bound levels of another lower bound electronic state. Bound-free emission produces broad continuous fluorescence to lower free, or repulsive, electronic states. To describe this fluorescence the Classical Franck-Condon Approximation (CFCA) [23] is often used as a crude first estimation of bound-bound or bound-free fluorescence intensity patterns. Computer programs such as BCONT [24] and LEVEL [25] written and distributed by Robert Le Roy use fully quantum mechanical treatments of the states involved to determine the transition intensities.

2.4.1 Classical Franck-Condon Approximation

In a transition, the emission of a photon occurs essentially instantaneously. This means that the molecule does not have time to change position or velocity during a transition. The idea of an instantaneous transition is the central idea of the Classical Franck-Condon Approximation. Assuming that the nuclei do not move during an electronic transition means that the internuclear separation, R, is constant during a transition, and the transition can be represented by a vertical arrow connecting the initial and final states. Classically, the momentum of the nuclei also cannot change, since according to $\vec{F} = \frac{d\vec{p}}{dt}$, a change of momentum by a finite amount in an infinitesimally short time would require an infinite force. This means that both the velocity and kinetic energy are approximately conserved in an electronic transition. These ideas can be used to qualitatively describe which transitions between electronic states will be the strongest.

A classical harmonic oscillator spends a large fraction of its time near the end points of its oscillation range, where its velocity and kinetic energy are small. The quantum mechanical motion of the nuclei is similar in that the square of the vibrational wavefunction is largest near distances corresponding to classical turning points of the potential curve. The square of the upper state nuclear radial wavefunction gives the probability that the molecule is separated by a particular value of R. Therefore, a transition is most probable when turning points from each of the two levels involved are located at the same (or close to the same) value of R. Figure

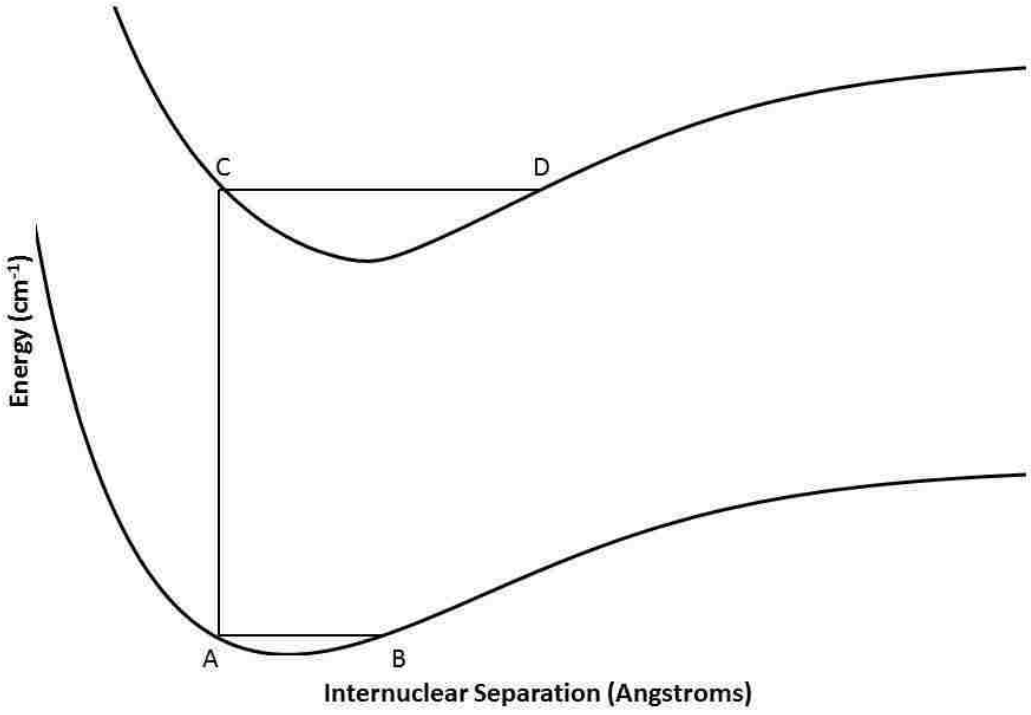

Figure 2.4: Vertical transition showing the most probable transition between two bound levels. A transition between levels AB and CD is highly likely because the inner turning points are located at the same R value and according to the CFCA the internuclear separation, R, is constant.

2.4 illustrates a situation where a transition between levels AB and CD is highly likely because the inner turning points are located at the same R value. Although the nuclei will still be at the same separation after the transition, they will vibrate about a different equilibrium separation since the potentials are not parallel. Figure 2.5 shows a resolved bound-bound fluorescence spectrum. Each doublet represents a pair of transitions down to a particular vibration level of the lower state (a different lower state v for each doublet). Using the CFCA, we expect to see doublets with stronger intensity where there is a large degree of overlap of the turning points between the two electronic states. However, as can be seen in Fig. 2.5, other maxima are also observed, which can be explained qualitatively in terms of the Mullikan difference potential (see next paragraph). But the actual bound-bound intensities should be calculated using a full quantum mechanical description as discussed in Sec. 2.4.2.

The CFCA also provides a qualitative explanation of the shape of bound-free spectra. Using the approximation that both internuclear separation and kinetic energy are conserved when a molecule in an upper bound level makes a radiative transition down to a repulsive (free) electronic state or to the dissociative continuum of a bound state, one can determine a function for the wavelength of the emitted photons, $\lambda(R)$. This function, along with the square of the upper state vibrational wavefunction, can give a qualitative representation of a bound-free spectrum intensity pattern. The function $\lambda(R)$ represents the wavelength corresponding to the energy difference of the upper and lower electronic potential curves at each separation R. The kinetic energy of the upper state is added to the lower state potential to form what is called the Mullikan difference potential (see Fig. 2.6). The difference between the upper state energy level and the Mullikan difference potential is equal to the difference of the two potentials at each R. If the Mullikin difference potential is monotonic, the spectrum will simply be a reflection of the square of the upper state wavefunction like the spectra shown in Figure 2.7. If $\lambda(R)$ is not monotonic, there are quantum interference effects due to the fact that more than one value of R contributes to fluorescence at the same wavelength. A good example of this is the $4^3\Pi_{0^+} \rightarrow 1(a)^3\Sigma^+$ electronic transition of NaCs, which is described further in

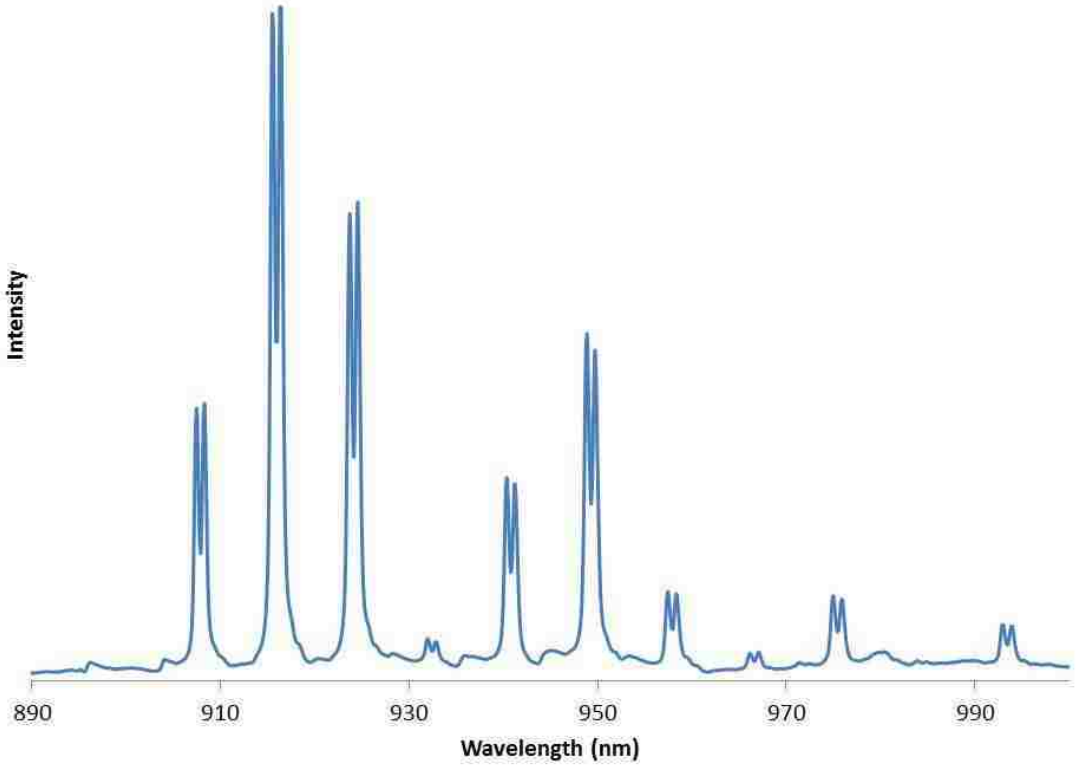

Figure 2.5: Bound-bound resolved fluorescence spectrum.

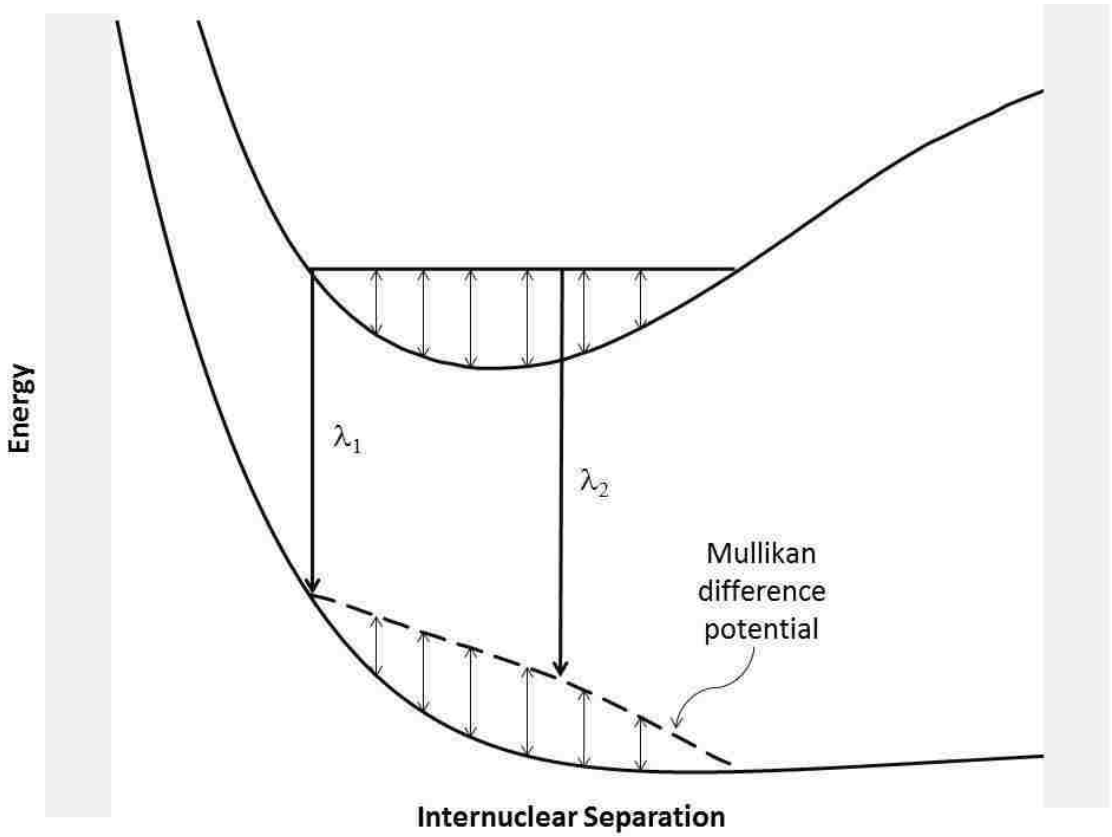

Figure 2.6: Typical monotonic Mullikan difference potential for transitions from a bound upper state to a free lower state. The total energy of the molecule in the upper state is given by the horizontal line, hence the difference between this and the upper potential is the kinetic energy (shown with double headed arrows). Since, under the CFCA, kinetic energy is conserved in a transition, this is added to the lower state potential to determine the Mullikan difference potential (dashed curve). The difference between the upper state energy and the Mullikan difference potential give wavelengths that we expect to observe in the bound-free fluorescence.

Chapter 7.

The CFCA does a reasonable job of qualitatively describing the features of bound-bound and bound-free spectra. However, since the CFCA is only an approximation there are several ways in which it is not adequate. The idea that a unique function, $\lambda(R)$, can be used to describe the wavelengths involved in the transition is not accurate. $\lambda(R)$ implies that only one (or more, in the case of a non-monotonic difference potential) value of R contributes to a particular wavelength. In reality, the quantum mechanical wavefunction tells us that the nuclei are not separated by one particular value of R, but rather exist in a state corresponding to a simultaneous superposition of R values with the probability of finding a particular R value being proportional to the square of the nuclear radial wavefunction at that R. The CFCA also does not take into account how the intensities of the transitions are affected by the electronic part of the wavefunctions. This latter effect is described by the transition dipole moment function. To obtain more detailed information, the transitions must be described using a fully quantum mechanical approach.

2.4.2 Quantum Mechanical Description of Fluorescence Intensities

To calculate the expected intensity distribution of the observed fluorescence from an upper bound level to a lower bound (or free) electronic state, one needs to use the total wavefunctions for both the upper and lower states. Following Herzberg's [11] description of emission intensities, one can obtain the intensity of a bound-bound transition from an upper level (α, v) to a particular lower level (α', v') is

$$I_{\alpha v \alpha' v'} = \frac{64\pi^4 N_{\alpha v} c}{3\lambda^4_{\alpha v \alpha' v'}} \left| \int \Psi_{\alpha v} \boldsymbol{M} \Psi_{\alpha' v'} d\tau \right|^2 , \tag{2.32}$$

where $N_{\alpha v}$ is the number of molecules in the upper level (α, v), Ψ is the total wavefunction of a particular state, $\boldsymbol{M}$ is the electric dipole operator, and $d\tau = d\vec{q}d\vec{R}$ represents intergration over all electronic and nuclear coordinates. Vibrational quantum numbers are designated with v and v' while α and α' represent all other quantum

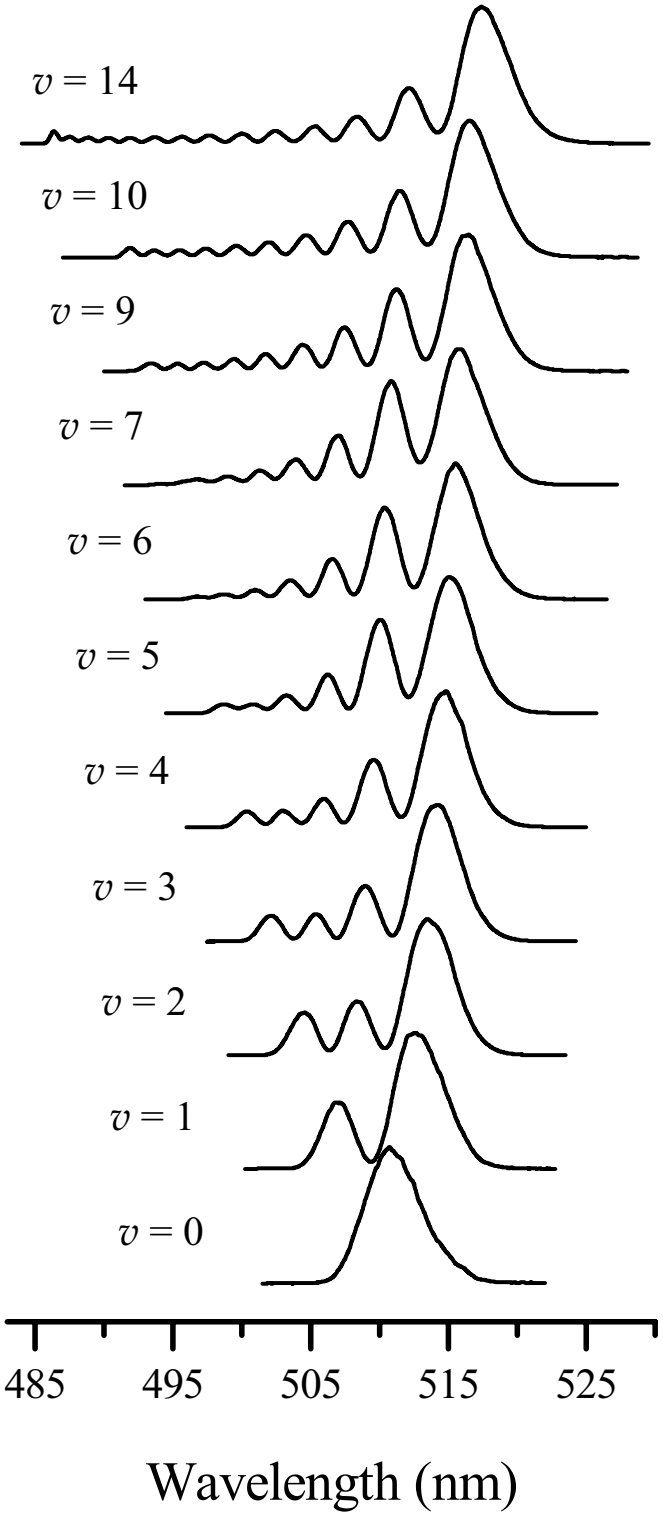

Figure 2.7: NaCs $11(0^+) \rightarrow 1(a)^3\Sigma^+$ bound-free spectra for low lying vibrational levels of the $11(0^+)$ state.

numbers needed to describe the states. The electric dipole moment operator is a vector operator given by

$$\boldsymbol{M} = Z_1 e\vec{R_1} + Z_2 e\vec{R_2} - \sum_{i=1}^{N} e\vec{r_i}. \tag{2.33}$$

Here e is the electron charge, $Z_1 e$ and $Z_2 e$ are the charges of nucleus 1 and nucleus 2, respectively, $\vec{R_1}$ and $\vec{R_2}$ are the vectors describing the positions of nucleus 1 and nucleus 2 relative to the center of mass, respectively, and $\vec{r_i}$ is the location of the ith electron relative to the molecular center of mass. The matrix element of first two terms in Eq. (2.33) is zero when the two levels involved in the transition belong to different electronic states since this term does not depend on the electronic coordinates and the electronic wavefunctions are orthonormal. In the present work, we are only concerned with the second term since all transitions considered here are between different electronic states. Remembering that we can factor the total wavefunction into nuclear and electronic parts as in Eq. (2.8), we can substitute the second term in Eq. (2.33) into the integral in the intensity expression, Eq. (2.32), to give

$$I_{\alpha v \alpha' v'} = \frac{64\pi^4 N_{\alpha v} c}{3\lambda^4_{\alpha v \alpha' v'}} \frac{S_{J,J'}}{2J+1} \left| \sum_{i=1}^{N} \int \Phi_\alpha \chi_{\alpha v} (-e\vec{r_i}) \Phi_{\alpha'} \chi_{\alpha' v'} R^2 dR d\vec{q} \right|^2, \tag{2.34}$$

where $S_{J,J'}$ is the Hönl-London factor [11] resulting from the angular part of the integral over the nuclear coordinates and $\chi_{\alpha v}$ is the nuclear radial wavefunction which is normalized with respect to $R^2 dR$. Defining the vibrational wavefunction, $\xi = \frac{\chi}{R}$, where ξ is normalized with respect to dR, we can rewrite Eq. (2.34) as

$$I_{\alpha v \alpha' v'} = \frac{64\pi^4 N_{\alpha v} c}{3\lambda^4_{\alpha v \alpha' v'}} \frac{S_{J,J'}}{2J+1} \left| \sum_{i=1}^{N} \int \Phi_\alpha \xi_{\alpha v} (-e\vec{r_i}) \Phi_{\alpha'} \xi_{\alpha' v'} dR d\vec{q} \right|^2. \tag{2.35}$$

The electronic part of the integral in Eq. (2.35) is typically rewritten as:

$$\mu_{\alpha\alpha'}(R) = \sum_{i=1}^{N} \int \Phi_\alpha (-e\vec{r_i}) \Phi_{\alpha'} d\vec{q}, \tag{2.36}$$

and this quantity is usually called the electronic transition dipole moment function. Finally we end up with the emission intensity in terms of the vibrational wavefunctions of each of the levels involved in the transition:

$$I_{\alpha v \alpha' v'} = \frac{64\pi^4 N_{\alpha v} c}{3\lambda^4_{\alpha v \alpha' v'}} \frac{S_{J,J'}}{2J+1} \left| \int \xi_{\alpha v} \mu_{\alpha\alpha'}(R) \xi_{\alpha' v'} dR \right|^2 . \tag{2.37}$$

Programs such as LEVEL [25] can be used to calculate emission intensities by first solving the radial Schrödinger equation to find the vibrational wavefunctions. Integrals in Eq. (2.37) are then evaluated with these calculated wavefunctions and user-specified transition dipole moment functions. LEVEL also calculates Franck-Condon factors, which are the squares of vibrational overlap integrals involving the product of the two wavefunctions i.e.

$$\text{FCF} = \left| \int \xi_{\alpha v}(R) \xi_{\alpha' v'}(R) dR \right|^2 . \tag{2.38}$$

These Franck-Condon factors are useful as an estimate of relative transition intensities; however, they rely on the approximation that the transition dipole moment varies sufficiently slowly with R that it can be removed from the integral.

Emission intensity for a bound-free transition is similar. However, a few modifications need to be made since the final state in the transition is part of a continuum. Since the lower state is no longer a discrete level it cannot be labeled by a vibrational quantum number, v. Instead it is characterized by its energy, E, and its rotational quantum number, J'. Because of this programs such as BCONT [24] calculate the intensity of transitions from the bound upper level to a band of lower levels that lie in the range E' to $E' + dE'$:

$$dI_{\alpha v} = \frac{64\pi^4 N_{\alpha v} c}{3\lambda^4} \left| \int \Psi_{\alpha v} \boldsymbol{M} \Psi_{\alpha' E'} d\tau \right|^2 dE'. \tag{2.39}$$

To obtain an expression that can more easily be compared to experimental spectra, we would like an expression for the intensity produced over a small range of wavelengths $d\lambda$ rather than over a small range of energies dE'. Converting an energy interval to a wavelength interval introduces two more factors of λ since

$$\frac{dE'}{d\lambda} = \frac{d}{d\lambda}\left(\frac{hc}{\lambda}\right) = -\frac{hc}{\lambda^2}. \tag{2.40}$$

Using this substitution, we obtain an expression for the intensity per unit wavelength interval for transitions to lower states corresponding to transition wavelengths between λ and $\lambda + d\lambda$:

$$\frac{dI_{\alpha v}}{d\lambda}d\lambda = \frac{64\pi^4 N_{\alpha v} hc^2}{3\lambda^6}\frac{S_{J,J'}}{2J+1}\left|\int \xi_{\alpha v}\mu_{\alpha\alpha'}(R)\xi_{\alpha' E}dR\right|^2 d\lambda, \tag{2.41}$$

where $\xi_{\alpha' E'}$ is the free state nuclear radial wavefunction. These free state radial wavefunctions no longer has discrete v' quantum numbers associated with it but rather energies, which can be continuous.

2.4.3 Selection Rules

The intensity of a transition between any two bound levels of a molecule is proportional to the integral in Eq. (2.35) times the Hönl-London factor, $S_{J,J'}$ [11]. This integral involves the electronic wavefunctions and vibrational wavefunctions of both levels and the dipole moment operator. If the result of this integral is zero or if the Hönl-London factor is zero, the transition is said to be "dipole forbidden" [11]. For the integral and Hönl-London factors to both be non-zero, the quantum numbers of the initial and final state must differ only by certain values. These differences are summarized by selection rules. The following are selection rules for transitions between electronic states of heteronuclear diatomic molecules [26]:

$$\Delta\Lambda = 0, \pm 1, \tag{2.42}$$

$$\Delta S = 0, \tag{2.43}$$

$$\Delta\Omega = 0, \pm 1. \tag{2.44}$$

For NaCs, where spin-orbit coupling is strong and Hund's case (c) notation is more appropriate, the selection rule on Λ is not strictly followed since Λ is not a good

quantum number. Similarly, when spin-orbit coupling is strong, S is not a good quantum number, and the selection rule Eq. (2.43) can be violated. Since each alkali atom has only one electron outside closed shells, the alkali diatomic molecules can only have electronic states with total electron spins of zero (singlet) or one (triplet). Even for lighter alkali molecules, where spin-orbit coupling is relatively weak, the interaction can still be sufficient to mix nearly degenerate rovibrational levels of a singlet state and a triplet state of the same J. Thus such levels have both singlet and triplet character. These mixed rovibrational levels, especially in the $1(b)^3\Pi_{0^+} \sim 2(A)^1\Sigma^+$ manifold, are called "window levels" since they allow access to upper triplet states from the singlet ground electronic state. In NaK, these interactions are sufficiently small that only a minority of close lying singlet and triplet rovibrational levels are mixed. However, in NaCs, the spin-orbit interaction is so strong that it causes a global perturbation where every rovibrational level of both electronic states has significant singlet and significant triplet character.

The selection rules on the nuclear quantum numbers are the following:

$$\Delta v = \text{anything} \tag{2.45}$$

$$\Delta J = 0, \pm 1 \text{ unless } \Omega = 0 \rightarrow \Omega = 0, \text{ then } \Delta J = \pm 1. \tag{2.46}$$

There is no selection rule on the vibrational quantum since wavefunctions of vibrational levels belonging to two different electronic states are not orthogonal. The probability of vibrational transitions is therefore governed by Eq. (2.37). In the selection rule on J, ΔJ is defined as $J_{\text{upper}} - J_{\text{lower}}$, and $\Delta J = -1, 0, +1$ transitions are labeled P, Q, R transitions, respectively. The selection rule on J results from the Hönl-London factor.

Chapter 3

Experimental Apparatus

This chapter describes the experimental apparatus used for this study, which is shown schematically in Fig. 3.1. Descriptions of the heat pipe oven used to generate the molecular vapor, the laser systems, and detection systems, specifically the charge coupled device (CCD) array detector, are included.

3.1 The Heat Pipe Oven

The experiment is centered around a six arm heat pipe oven as shown in Figure 3.1. The heat pipe oven was first introduced by Vidal and Cooper in 1969 [27]. The particular heat pipe oven used in this work was constructed by Seth Ashman and Joe Zelinski in 2006. A more detailed description of the construction and components is given in Seth Ashman's PhD. dissertation [28]. The heat pipe oven is made of 1.5" diameter stainless steel arms, which are each about 12" long and that were welded together to form a set of perpendicular axes. Two of the four horizontal sidearms are used for the propagation of the laser beams. The other two perpendicular horizontal arms are used for fluorescence detection, white light alignment, and white light absorption spectra. The fifth (vertical) arm is used to load the alkali metal. The downward pointing vertical arm is much shorter (about 2") and is used to contain the liquid sodium and cesium. Conflat flanges at the ends of the four horizontal and upward vertical arms are used to secure BK7 windows

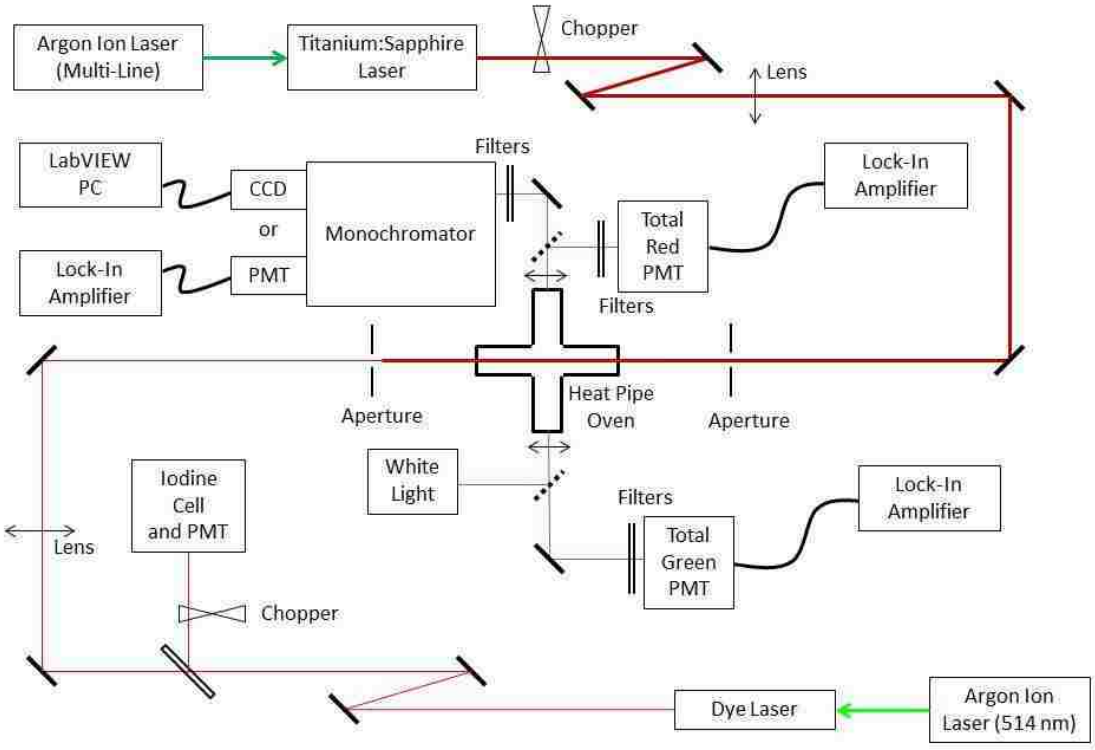

Figure 3.1: Schematic diagram of the apparatus used in all experiments described in this work. Note: the CCD diode array and PMT are not attached to the monochromator at the same time.

with o-rings to make a vacuum seal. Clamshell heaters are attached to each arm of the heat pipe and wrapped in pieces of ceramic insulating blanket. Inlets drilled near the ends of the four horizontal and upward vertical arms are connected to the vacuum and gas-handling system so that we could steadily flow a buffer gas through the heat pipe oven. Chilled water flows through copper tubing that is wrapped around the ends of each arm near the window. The cooling water and argon buffer gas prevent the alkali metals from coming in contact with the windows.

Solid sodium and liquid cesium were carefully loaded into the center of the heat pipe. The voltage of the clamshell heaters is controlled by variacs in order to produce temperatures of 290 to 310 °C inside the heat pipe oven. Heating the alkali metals produces atomic Na and Cs vapor and molecular species Na_2, Cs_2, and NaCs. As the temperature increases, the alkali vapor migrates out from the central region of the heat pipe until it meets the region of cooler argon buffer gas. A rolled sheet of fine wire mesh lines the inside of each arm and acts as a wick to bring the condensed metal back to the central hot region. The temperature is monitored using chromel-alumel thermocouples attached to each arm of the heat pipe. Pressure is monitored using a capacitance manometer located a few feet away from the oven in the vacuum and gas-handling system. In our experiments, argon was chosen as the buffer gas. Valves regulating the flow of buffer gas from the tank and pumping from the vacuum system were adjusted such that the pressure in the oven was approximately 3 to 5 Torr.

3.2 Laser Systems

For most experiments two lasers were used in a pump-probe scheme. The pump laser is a Coherent 899 Titanium:Sapphire (Ti:Saph) continuous wave (cw) ring laser which is pumped by all visible lines of a Coherent Innova 200 argon ion laser. 10 W of pump power usually produces approximately 100 to 500 mW of Ti:Saph power. We currently have access to two sets of optics for the Ti:Saph laser, mid-wave and short-wave. For all the experiments done here, we have used the mid-wave optics

which allows a wavelength tuning range from approximately 780 nm to 900 nm. The probe laser is a Coherent 699 cw ring dye laser. LDS 722 dye is used and the dye laser is pumped with the 514 nm line of a Coherent Innova Sabre argon ion laser. Approximately 7.9 W of pump power usually produces approximately 100 to 400 mW of dye laser power with a wavelength tuning range of about 720 to 775 nm.

The Coherent operator's manual [29] gives details about the features of the Ti:Saph laser along with detailed alignment procedures. Figure 3.2 shows a schematic of the Ti:Saph laser cavity. With the exception of the lasing medium, the features and components of the both the Ti:Saph and dye laser are very similar. One important feature of the lasers is the narrow single mode linewidth. The birefringent filter and the two etalons contained in the intracavity assembly act as frequency filters in order to reduce the number of lasing cavity modes to one. The frequency of this mode is stabilized in two ways. First, all the laser optics and components are mounted on an Invar bar, which has a very small coefficient of thermal expansion. This provides thermal stabilization of the cavity length of less than one micron per degree centigrade. Further frequency stabilization is achieved using an electronic servo loop and temperature stabilized reference cavity. The laser control box uses signals from the reference cavity to determine an error signal when the frequency drifts. This signal is used by the control box to make small changes in the cavity length by moving the tweeter assembly (which is a small cavity mirror mounted on a piezoelectric bar) or the Brewster plate. Frequency filters and stabilization result in single mode lasing with linewidths as low as 500 kHz.

The lasers are scanned by rotating the Brewster plate. The rotation allows for small continuous changes in the optical cavity length, which allows for a continuous scan range of up to 30 GHz. The frequency remains stable during a scan because it is locked to a fringe of the temperature stabilized reference cavity containing an identical Brewster plate whose rotation is synchronized with the laser cavity Brewster plate. Both lasers make use of built-in wavemeters and are controlled by the Coherent Autoscan program. The wavemeter allows for accurate determination of wavelength and continuous scanning by stitching together many continuous 10 GHz segments. The beams from the two lasers are counter propagated through the heat

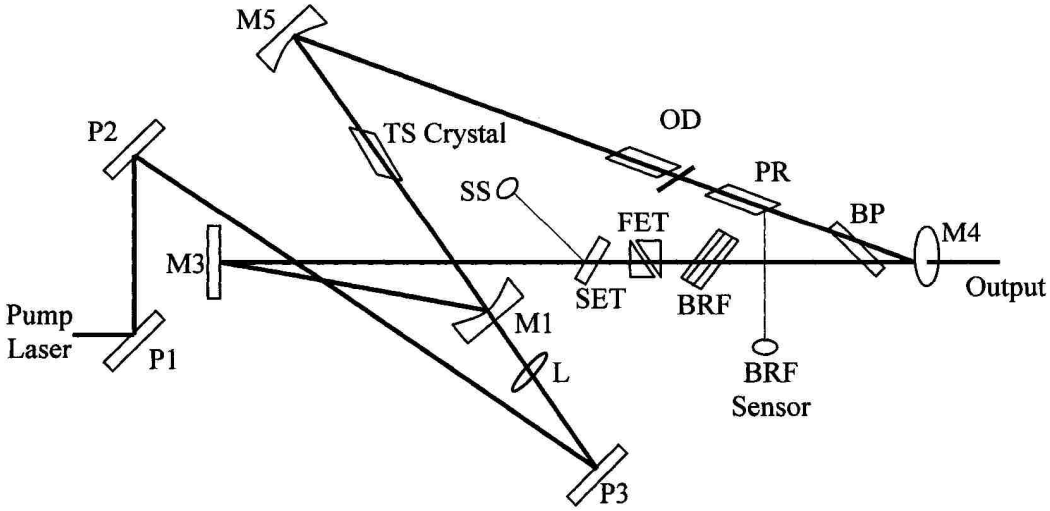

Figure 3.2: Schematic diagram of the Coherent 899-21 single mode cw Titanium Sapphire laser cavity. Mirrors labeled with P are pump laser mirrors, mirrors label with M form the laser cavity ring, L is the pump laser focusing lens, TS is the Titanium Sapphire crystal, BP is the Brewster plate, OD is the optical diode, PR is the pickoff rhomb, BRF is the birefringent filter, FET is the thick (fat) etalon, SET is the thin (skinny) etalon, and SS is the SET sensor. Schematic reprinted from [28].

pipe and focused such that their spot sizes are approximately 1 mm at the center of the heat pipe.

Since accurate frequency measurements are critical to this work, both lasers need to be well calibrated. The transitions excited by the Ti:Saph laser were calibrated by comparison of wavemeter readout to one of two known sources: uranium transitions or previously calibrated NaCs $2(A)^1\Sigma^+ \leftarrow 1(X)^1\Sigma^+$ transitions. To obtain a calibration from the uranium hollow cathode lamp, a small part of the beam is split off and sent into the lamp. The optogalvanic signal (change in lamp current associated with laser frequency resonance with a uranium transition) from the lamp is monitered while scanning the laser across a known transition from a uranium atlas [30]. The Ti:Saph wavemeter readout of a particular uranium line is compared to the known frequency in the atlas to determine the wavemeter error. Once the error is known, unique red fluorescence signals due to exciting $2(A)^1\Sigma^+ \leftarrow 1(X)^1\Sigma^+$ transitions can be used for subsequent calibrations. Dye laser transitions are calibrated using fluorescence from an iodine cell. Again, a small part of the beam is split off and sent into the iodine cell where a photomultipler tube, which has been filtered to eliminate Ti:Saph laser scatter, detects the fluorescence as a function of dye laser frequency. These transitions can be compared to those tabulated in an iodine atlas [31]. The dye laser is used as the probe in these studies and thus must be scanned much more often than the Ti:Saph, hence, it is much more critical to know the calibration error as the dye laser is scanned. One known problem of our dye laser is that the error accumulates for longer scans (more than 1 cm^{-1}). Errors obtained by comparing measured iodine frequencies with known frequencies are fit linearly to correct the frequency scale of these longer spectra.

3.3 Detection

When one of the lasers is resonant with a transition, fluorescence emitted in a direction perpendicular to the laser propagation direction. For the pump step, fluorescence is focused and collected onto the photocathode of a freestanding photomultiplier tube (PMT) ("Total Red PMT" in Fig. 3.1, side-on Hamamatsu R928). Figure 3.3 shows an example of the total red fluorescence signal as a function of pump laser frequency. For the probe step, fluorescence is focused and collected onto a second freestanding PMT ("Total Green PMT" in Fig. 3.1, side-on Hamamatsu R928) that is filtered to pass green light with short pass (SP) filters [SP575 (Reynard Corporation R00920-00), SP650 (Reynard Corporation R00940-00), SP675 (Reynard Corporation R00942-00), SP700 (Reynard Corporation R00944-00), and SP800 (Melles Griot 03SW618)]. Figure 3.4 shows an example of the total green fluorescence signal as a function of probe laser frequency. In order to discriminate molecular fluorescence from background light sources, lock-in detection was used, which was done by passing the laser beam through a rotating circular mechanical "chopper" wheel with has 30 equally spaced slots. This modulates the laser beam, and as a result, also modulates the induced fluorescence. The frequency of this modulation is controlled by a Stanford Research Systems Model SR540 Chopper Controller. The modulation reference frequency signal was sent to a Stanford Research Systems Model SR850 DSP Lock-In Amplifier. The current from the anode of the PMT was also sent to the lock-in amplifier, which only amplifies signals that are modulated at the chopper frequency. This ensures that the signal observed was only due to fluorescence created by transitions induced by the laser. Chopping the pump beam and looking for variations in signal while scanning the probe laser and using lock-in detection ensures that the recorded signals depend on photons from both the pump and probe lasers, while preventing detection of fluorescence due to the absorption of two photons from a single laser.

There are two cases in which information about the fluorescence as a function of wavelength is needed. First, with the pump laser fixed on a transition (probe laser blocked), the resolved fluorescence provides information on the quantum number

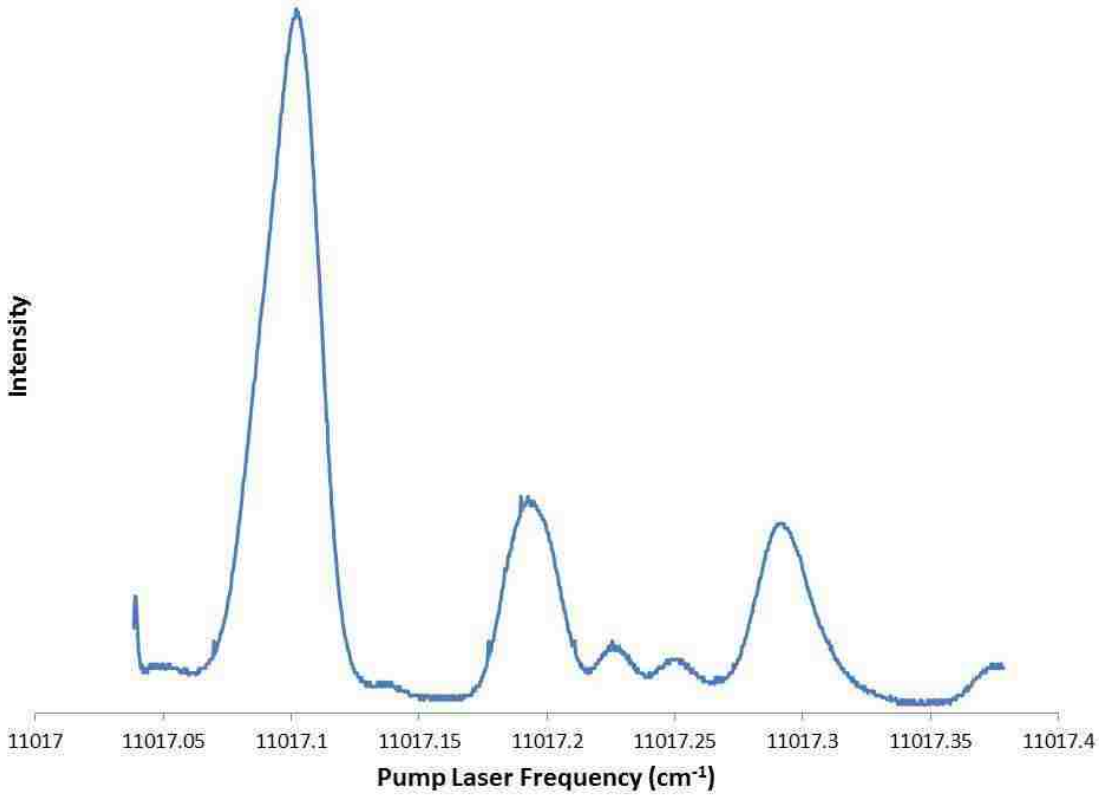

Figure 3.3: Typical pump laser excitation scan.

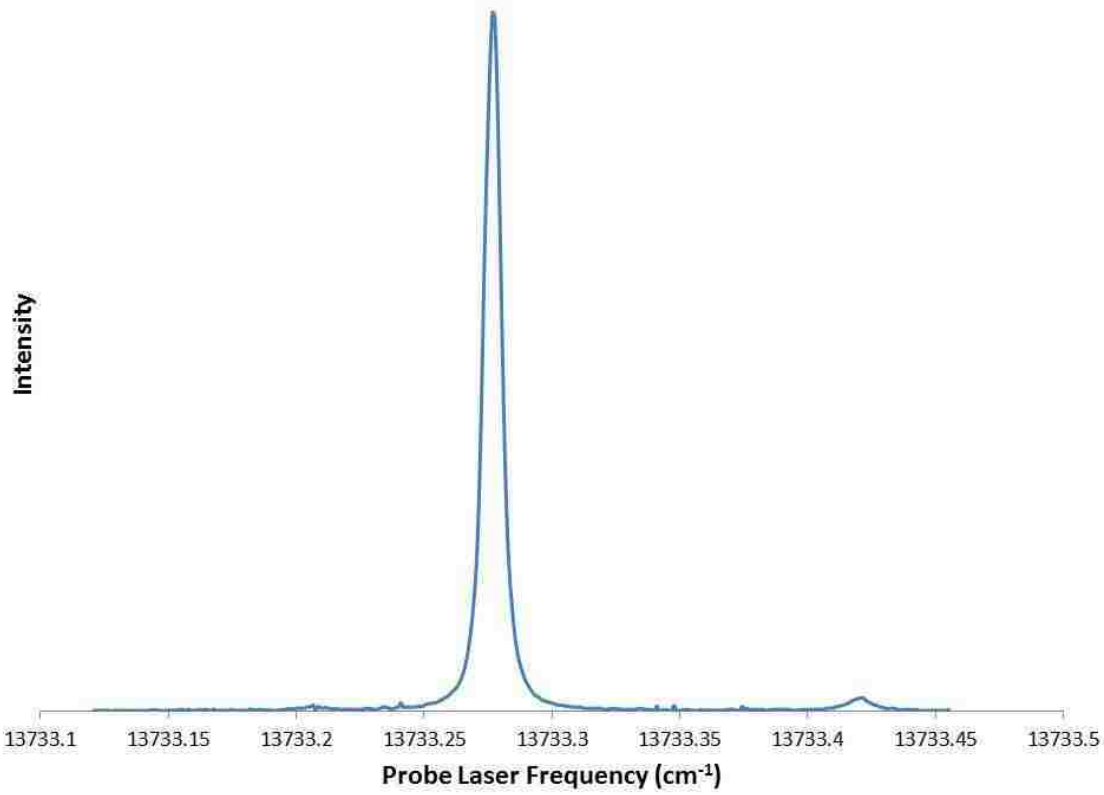

Figure 3.4: Typical probe laser excitation scan.

assignment for that particular transition. Second, with both pump and probe lasers fixed on a double resonance transition, the resolved fluorescence can be used to identify the upper electronic state excited by the transition. Details about the analysis of these processes are given in Chapter 4. Experimentally, the fluorescence is focused onto the entrance slit of a monochromator (Spex270M, labeled "Monochromator" in Fig. 3.1) using a lens and mirrors in a periscope arrangement. The periscope arrangement of the mirrors is important so that the image of the horizontal strip of fluorescence produced by the lasers is rotated to be aligned with the vertical opening of the entrance slit (maximizing transmission). The fluorescence passes through the entrance slit is collimated with the first internal mirror of the monochromator, and then a diffraction grating separates the fluorescence by wavelength. The diffraction grating used in this experiment has 600 grooves per millimeter and is blazed for 1 μm. The blaze of a grating means that the grating is most efficient at reflecting light in a particular direction or angle corresponding to a particular wavelength in first order, in this case, 1 μm. Because of the blaze of the grating, the monochromator was often used in second order with proper filtering, since second order 500 nm light is reflected in the same direction as first order 1 μm light as given by the grating equation:

$$a \sin \theta = m\lambda. \tag{3.1}$$

Here a is the grating groove spacing, θ is the angle of the diffracted light with respect to the grating normal, and m is the diffraction order for wavelength λ. The diffracted light then hits the second monochromator mirror which refocuses it onto the detector. We have two options available to us for detection at the output of the monochromator. One is to use the exit slit with PMT mounted behind it. In this setup, the lock-in amplifier is used to ensure that we only detect signal due to laser-induced fluorescence. The lock-in signal is recorded using a LabVIEW program as the grating of the monochromator is rotated. The advantage of using the PMT is that calibration of the wavelength scale is relatively simple, if the starting and ending points are known along with any grating offset. With this setup, the narrow

wavelength band that passes through the exit slit changes in a continuous way to map the spectrum as a function of wavelength. The second detection option is to use the charge-coupled device (CCD) diode array detector mounted in the exit slit plane. The exit slits are not used with the CCD so that a large range of wavelengths is focused onto the pixels of the array detector. The use of the CCD diode array detector has different advantages and challenges; it is described in more detail in the next section.

3.4 CCD diode array detector

The use of the charge-coupled device (CCD) diode array detector has greatly increased the efficiency with which resolved fluorescence spectra can be obtained in our lab. One major disadvantage to scanning the monochromator grating and recording the output with a PMT is that it requires the total signal to be constant in time throughout the duration of the scan. If the frequency of one or both of the lasers drifts off the line or if the power of either laser fluctuates during the scan, then the scan must be corrected or abandoned altogether. However since the CCD array observes all wavelengths at the same time, a laser frequency drift or change in laser power will only cause the observed spectra to change by an overall scaling factor. The CCD also has a strong advantage in that the time required to obtain a reasonable size signal is significantly less than the time it would take to record the same spectrum by scanning the grating for the same size signal.

The monochromator is operated electronically using a HandScan remote controller. The HandScan controls parameters such as slit widths, grating position, scan starting and ending points and scan speed. The only important parameters when using the CCD are the entrance slit width and the grating position. A LabVIEW program controls the exposure time of the detector and saves the data. The program also controls an option that switches between continuous acquisition or a feature called “snap”. When the program runs in continuous acquisition mode, the

CCD continually takes exposures and the data are displayed and saved automatically after each. In the "snap" acquisition mode, the CCD waits to take a single exposure until the user selects the "snap" button. It will display and save only this exposure. For very small exposure times (usually anything less than a second), it is preferable to use the "snap" feature to save only a single data set at a given time so that the data file does not automatically fill up with huge lists of numbers. For data with longer exposure times or poor signal to noise, continuous acquisition is preferable so that multiple exposure data sets can be easily averaged. The last and possibly most important feature of the LabVIEW program is the ability to acquire and subtract a background. A particular exposure can be set as a background and then subtracted from subsequent exposures. This removes the background from the subsequent exposures, both on the display and in the stored data files. Background subtraction is critical for the CCD since, unlike the PMT signal, lock-in detection cannot be used. It is most important to subtract a background when using long exposure times to look at small signals. Although most lights in the lab are off, background from computer displays and lasers can be an issue. Most prominently, the 514 nm argon ion line from the argon laser used to pump the dye laser is a major background light source. This line would show up in all triplet bound-free spectra obtained using the CCD if not for background subtraction.

3.4.1 Alignment

Before the CCD could be used it needed to be properly attached and aligned on the monochromator. First, the exit slit and PMT assembly were removed from the monochromator. A special adaptor designed for the SPEX270M has one end with a large circular opening which attaches to the exit port of the monochromator and another cylindrical end which can be attached to the CCD detector head. This special adaptor allows free translation and rotation of the detector head with respect to the exit port. The detector head is attached to a signal processor which is connected to a PC so that the signal can be displayed and recorded using LabVIEW software. To align and calibrate the system, a small mercury lamp was placed such

that it illuminated the entrance slit of the monochromator. The grating was rotated to the position at which the controller reads 435 nm. This produced an image of the mercury line approximately near the center pixel of the array. The entrance slit was set to the smallest open setting of 6.25 microns so that the image of the mercury line on the exit plane was as narrow as possible. The detector was then translated and rotated in its adaptor mount to fulfill two criteria: the rotation of the array must be such that the wavelength range associated with an individual pixel is as small as possible, and the detector array must be translated such that it lies in the focal plane of the last monochromator mirror. The LabVIEW program was set to have a relatively short exposure time (about half a second) and to continuously display sequential exposures so the display could be used for real time feedback of the alignment of the detector. The detector was first rotated such that the mercury line was as narrow as possible. The goal was to make the detector array perpendicular to the image of the entrance slit. If this is not the case, then several pixels may be illuminated by the same range of wavelengths, resulting in broader lines. Once the rotation was properly adjusted, the detector head was translated toward or away from the last monochromator mirror until it was in the focal plane. Again, this was confirmed by observing the mercury line on the display and translating the detector such that the line is as narrow as possible. As with the rotation, if the detector is too close or too far from the mirror, the light will not be focused, and this will result in broader lines. Typically this process was iterated a few times to be sure that the optimal position was found. Once the alignment process was done, screws on the monochromator end of the adaptor were tightened so that the detector stayed in this position.

3.4.2 Wavelength Calibration

Once the detector was aligned properly, data could be collected and recorded in a computer file. However the format of the data file gives intensity as a function of pixel number. To obtain meaningful spectra, the wavelength scale must be calibrated. Calibrating the wavelength scale for spectra obtained with the CCD array is

not as straightforward as calibrating the wavelength scale for spectra obtained with an exit slit and PMT. When using an exit slit and PMT detector, the wavelength displayed on the HandScan controller corresponds to the nominal wavelength that the grating transmits in the direction of the exit slit. Therefore moving the grating position to a new wavelength reading sends that new nominal wavelength to the exit slit. It is relatively simple to calibrate the wavelength scale to correct for any offset in the grating position by scanning over a few standard known mercury lines. In general, we find the offset is approximately constant with wavelength and we can obtain an average offset that is used to correct the wavelength axis. This is not the case when using the CCD array. When using the array, each pixel is effectively a separate exit slit, each right next to one another. Having these pixels spread out over the array allows us to see the entire spectrum at one time, but it also means that the grating is sending a large range of wavelengths to the array for a single grating position.

To understand how the wavelength range is distributed, we can examine the grating equation for incident light at an angle [32],

$$a(\sin\theta_m - \sin\theta_i) = m\lambda. \tag{3.2}$$

Here a is the grating groove spacing, θ_i and θ_m are the angles the incident and diffracted light make with the grating normal, respectively, and m is the diffraction order for wavelength λ. We would like to obtain an expression for the dispersion of the light across the pixel array, $\frac{\Delta\lambda}{\Delta\text{pixel}}$. To do this, it is easiest to break this quantity up into several parts:

$$\frac{\Delta\lambda}{\Delta\text{pixel}} = \frac{\Delta\lambda}{\Delta\theta_m}\frac{\Delta\theta_m}{\Delta y}\frac{\Delta y}{\Delta\text{pixel}}. \tag{3.3}$$

In this equation, y refers to the distance along the array. We are only concerned with the angles associated with the diffracted light, θ_m, since for any CCD measurement the grating is held in place, so θ_i is constant. The three ratios on the right side of (3.3) can each be evaluated separately to determine the wavelength dependence of the pixel dispersion. The third term is simply a measure of the pixel width

which can be easily determined from the number of pixels, N, and the length of the array, l; i.e., $\frac{\Delta y}{\Delta \text{pixel}} = \frac{l}{N}$. The second term can be evaluated geometrically. The optical length, L, between the grating and the array is approximately 50 cm while the array width is 2.5 cm. So the small angle approximation is certainly valid, and yields $\frac{\Delta \theta_m}{\Delta y} = \frac{1}{L}$. Finally, the first term can be obtained by taking the derivative of the grating equation. Remembering that θ_i is constant, we find:

$$\frac{\Delta \lambda}{\Delta \theta_m} = \frac{a \cos \theta_m}{m} = \frac{\lambda \cos \theta_m}{(\sin \theta_m - \sin \theta_i)}. \tag{3.4}$$

This is the term which gives the wavelength dependence of the dispersion. Unfortunately, values for this angular dispersion cannot be analytically calculated as a function of wavelength because θ_m obviously depends on wavelength via the grating equation. However, values can be obtained relatively easily using numerical methods. Finally all together the pixel dispersion is given by:

$$\frac{\Delta \lambda}{\Delta \text{pixel}} = \frac{l \lambda \cos \theta_m}{NL(\sin \theta_m - \sin \theta_i)}. \tag{3.5}$$

To experimentally determine the wavelength dispersion versus pixel, a mercury lamp was used. The grating was tuned to a location at which more than one calibrated mercury line could clearly be observed in the spectra. This was done for several sets of lines in both first and second order. The pixel number corresponding to each peak was identified, and the pixel dispersion was calculated using the known mercury line wavelength (in air). Figure 3.5 shows a plot of the theoretically calculated dispersion as a function of wavelength [from equation (3.5)] along with the experimentally determined dispersion. Both sets of results have the same basic shape and can be easily fit with a quadratic. The offset between the theoretical and experimental points is likely due to errors in measuring the array width and monochromator focal length. Additionally, the second geometrical factor may not be exactly $\frac{1}{L}$. Since the reflection from the second curved monochromator mirror may decrease the dispersion slightly. The fit obtained from the experimental data was used to correct the wavelength scale on any CCD spectrum shown in this dissertation.

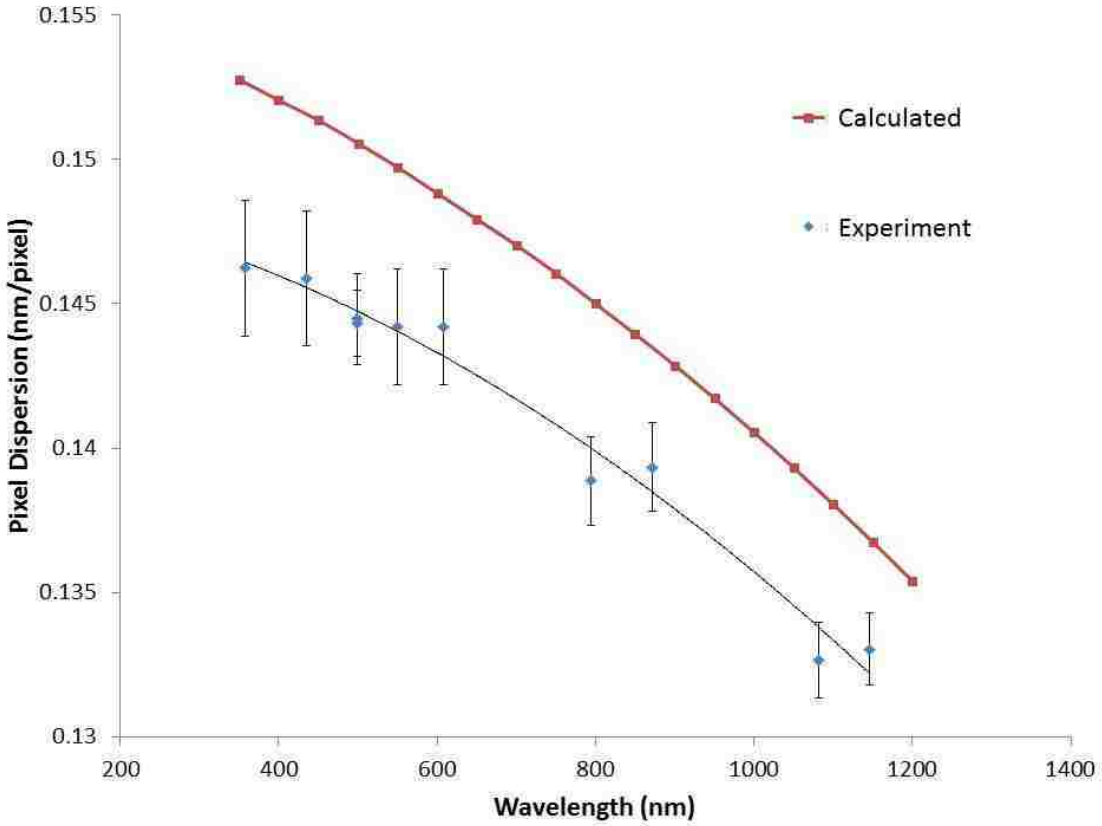

Figure 3.5: Plot showing calculated and experimental pixel dispersion versus wavelength. Dispersions shown here are for first order. Second order dispersions are half of those shown here.

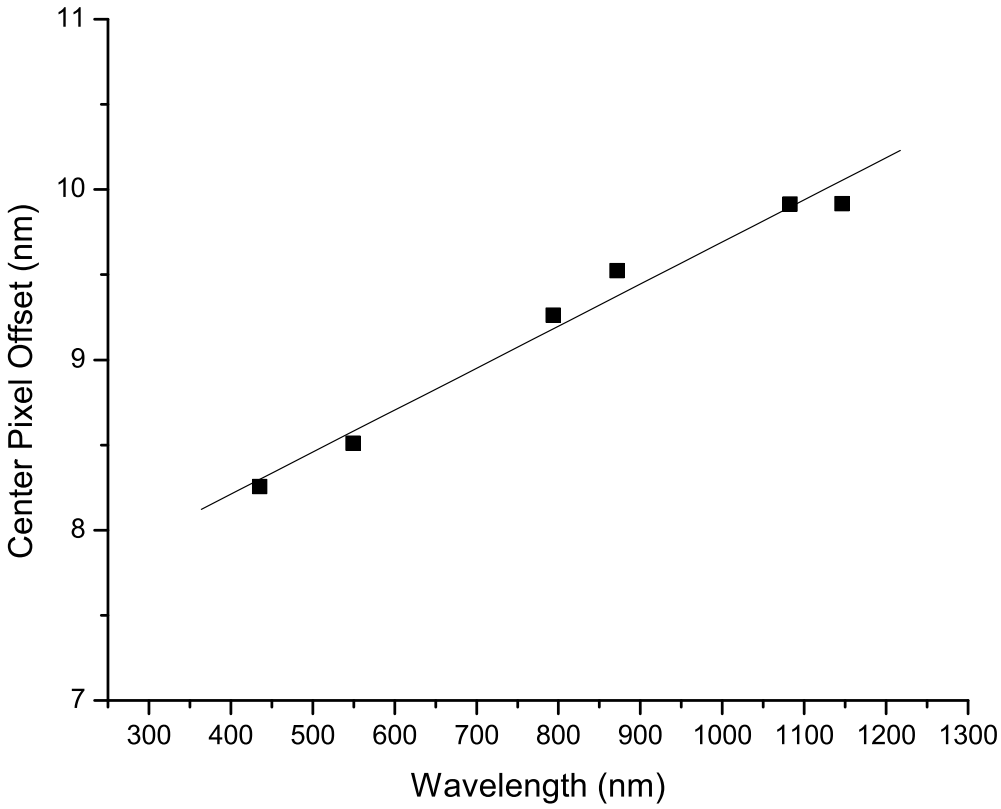

Figure 3.6: Wavelength offset of the center pixel of diode array versus wavelength. Offsets shown here are for first order. Second order offsets are half of these.

The known pixel dispersion gives the overall width of the wavelength scale for a resolved spectrum. To put the entire spectrum on an absolute scale, the center pixel offset must be determined. Again the mercury lamp was employed. Several spectra were taken of calibrated mercury lines in both first and second order. The nominal grating position wavelength, according to the HandScan, was taken to be the wavelength of the center pixel (pixel number 522). The measured position of the peaks on the spectra were compared to the calibrated line positions to obtain the wavelength offset for the center pixel. As shown in figure 3.6, this offset has a slight wavelength dependence but is well described by a linear fit. The wavelength dependence to the offset could be due to the fact that the center pixel may not be exactly aligned with the original exit slit position, coupled with the wavelength dependent pixel dispersion. Using the center pixel offset obtained from this fit, along with the dispersion, a calibrated wavelength scale can be calculated for any spectrum obtained with the CCD array using only the grating position wavelength read by the HandScan.

3.4.3 Efficiency versus Wavelength Calibration

The primary use of the CCD array is to obtain quick bound-free spectra for the purpose of identifying the electronic state excited by a particular set of pump-probe transitions. For this purpose, relative intensity calibration is not very crucial. However, in some cases, intensities as a function of wavelength needed to be corrected, because the detection system is not equally sensitive to all wavelengths. This correction is particularly important when spectra are to be compared to theoretical simulations produced by the program BCONT, which is discussed in Sec. 6.3. Therefore, we needed to determine the efficiency of the detection system as a function of wavelength. The detection system includes lenses, mirrors, interference filters, the monochromator grating and mirrors, and the CCD detector. Even though each of these elements has its own relative efficiency for transmitting/detecting light of different wavelengths, we require the overall relative efficiency for the entire system. This means that if new filters are used or the grating is changed, a new efficiency

curve must be determined. The CCD detector is also slightly more complicated in that there are two separate sources of wavelength dependence in the response function. Each individual pixel has its own particular efficiency as a function of wavelength, but this efficiency might be slightly different for each of the pixels along the array. To circumvent this issue, bound-free spectra that required calibrated relative intensities were only taken at specific grating positions to ensure that the same efficiency curve was applicable to each spectrum. To be sure that the grating could be sent to the same place multiple times, a very narrow mercury line was recorded multiple times after resetting the grating position. Each time the grating was moved and sent back to this standard position, the location of the peak of the mercury line did not change by more than one pixel.

To determine the efficiency, a GTE Sylvania model 6.6A/T4Q/1CL-200W quartz-iodine tungsten filament lamp was used as a light source with a calibrated standard relative intensity. This lamp is a secondary intensity standard with known relative intensity versus wavelength (see Figure 3.7 [33]) when operated with a current of 6.5 A. The light was focused at the center of the heat pipe oven and then refocused on to the entrance slit of the monochromator with interference filters in place. The intensity detected by the CCD was monitored using LabVIEW. The exposure time was adjusted so that the entire spectrum was on scale. Since the lamp is so bright, very small exposure times, typically a few milliseconds, were used.

The measured intensity as a function of wavelength can be compared to the calibrated emission curve to determine the detection system efficiency, as shown in Fig. 3.8. For the CCD array, it is convenient to express the efficiency as a function of pixel number for each specific grating position. When a spectrum is recorded with a particular grating position, it can be corrected by simply dividing by those efficiencies pixel by pixel. Appendix D contains tables and plots of the efficiencies as a function of pixel number for several grating positions.

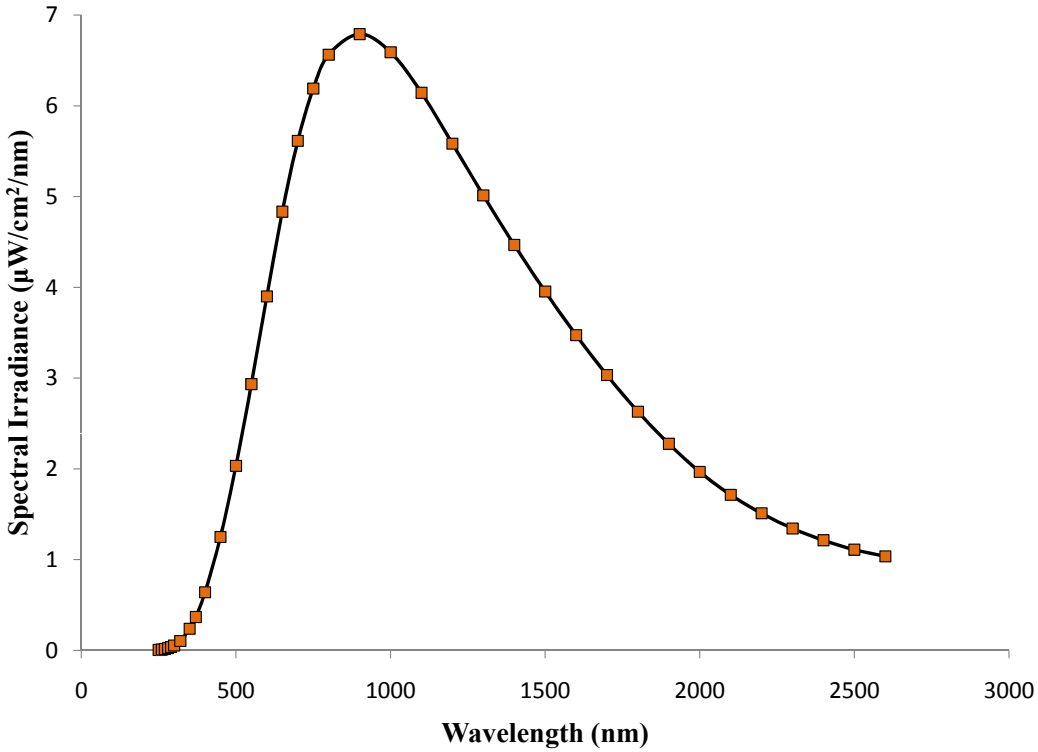

Figure 3.7: Standard intensity emission curve for GTE Sylvania model 6.6A/T4Q/1CL-200W quartz-iodine tungsten filament lamp operated at 6.5 A [33].

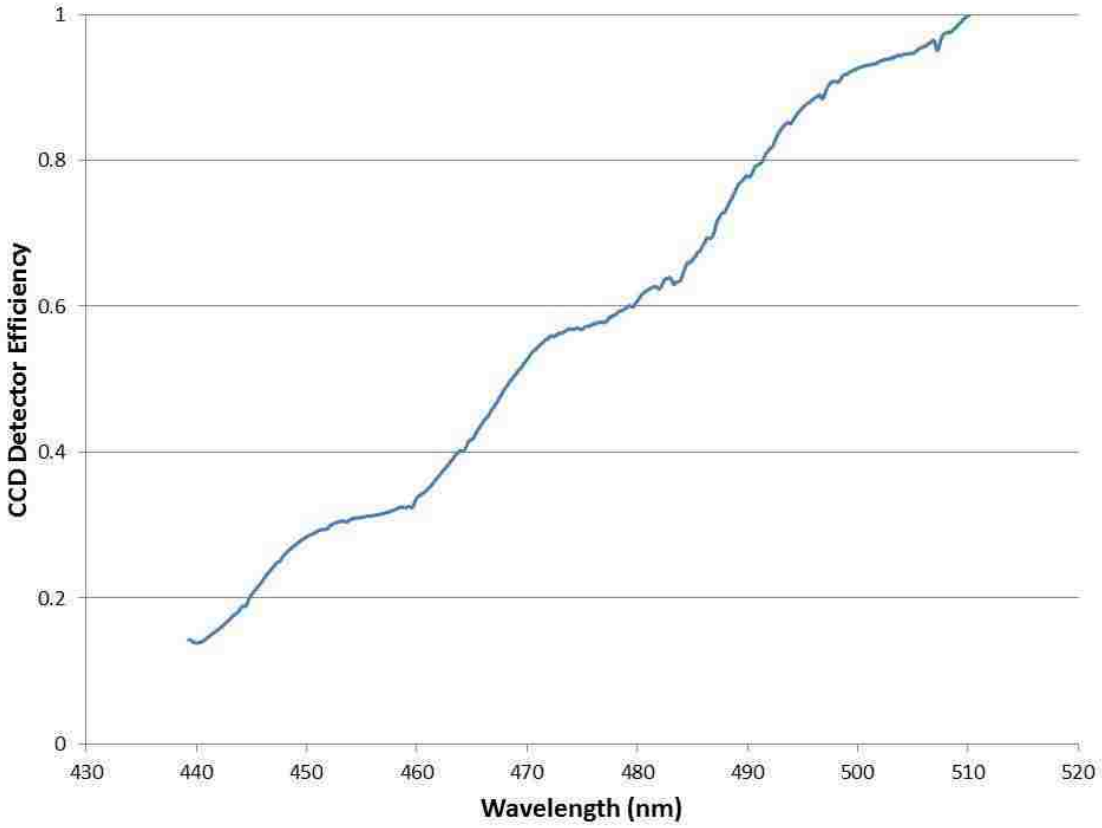

Figure 3.8: Relative efficiency of the detection system, which includes lenses, mirrors, windows, filters, monochromator grating and mirrors, and the CCD detector. Efficiency is scaled to have a maximum value of 1. Though the x-axis is given in wavelength units here, it is often more useful in correcting spectra to plot efficiency as a function of pixel number for a given grating position. The monochromator grating was set to 940nm and used in second order to produce this efficiency curve. The following filters were placed in front of the monochromator entrance slits: 395nm longpass, 540 shortpass, and 675 shortpass.

Chapter 4

Experimental Techniques

To investigate the high lying electronic states of NaCs, we employed the Optical-Optical Double Resonance (OODR) technique [34, 35, 36]. We used the dye and Ti:Sapphire lasers in a pump-probe scheme, as illustrated in Figure 4.1. The pump laser induced transitions from a thermally populated rovibrational level of the ground $1(X)^1\Sigma^+$ state to a selected level of the mixed $1(b)^3\Pi_{0^+} \sim 2(A)^1\Sigma^+$ states. Strong spin-orbit coupling causes every rovibrational level of the $1(b)^3\Pi_{0^+} \sim 2(A)^1\Sigma^+$ manifold to have both singlet and triplet character. Hence the laser in the probe step was able to induce transitions either to upper singlet states or to upper triplet states. Transitions were observed by detecting fluorescence corresponding to transitions from the upper state down to either the $1(a)^3\Sigma^+$ or $1(X)^1\Sigma^+$ state as a function of pump or probe laser frequency.

4.1 Pump Transitions

The first step was to identify pump transitions from thermally populated rovibrational levels of the $1(X)^1\Sigma^+$ state to levels of the $2(A)^1\Sigma^+$ state. Many of these transitions had previously been identified by Ashman *et al.* [3]; however, it was also necessary to identify several new pump transitions. New pump transitions were needed for three reasons: to be able to access a lower range of total energy; to be able to pump a different J quantum number for more coverage of rotational

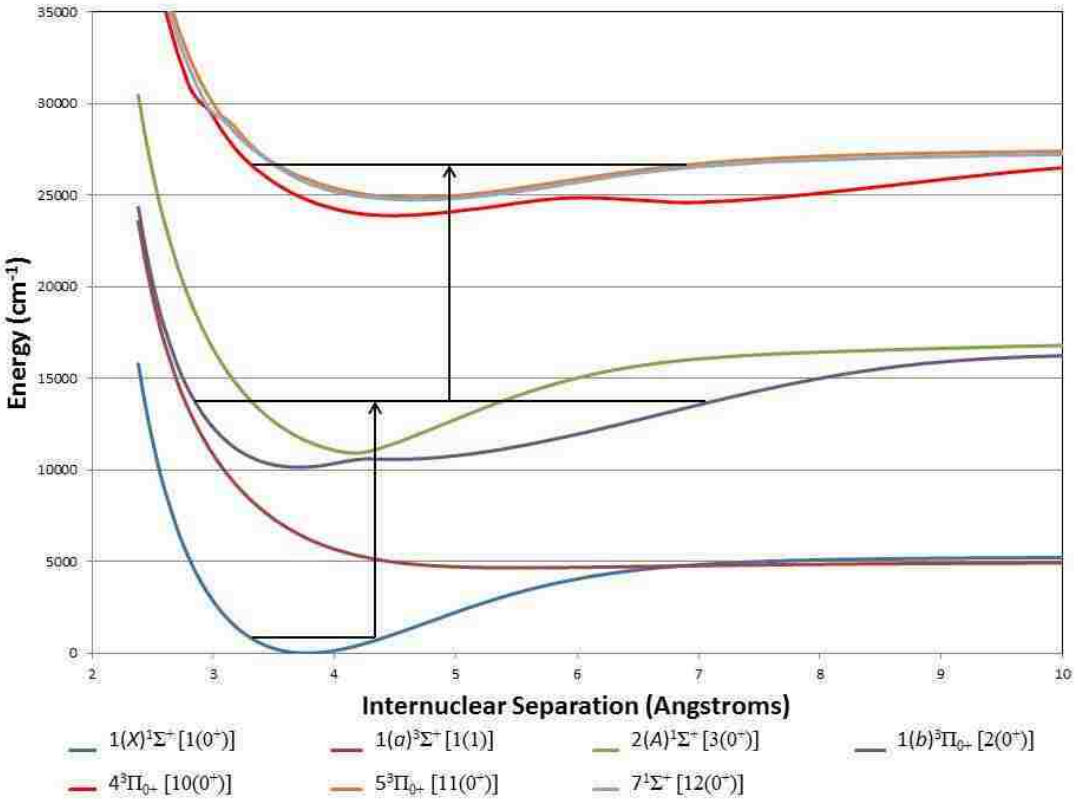

Figure 4.1: Schematic diagram of pump-probe OODR scheme. Only potentials relevant to this work are plotted here. Potentials are theoretical calculations from Korek *et al.* [12].

levels; and to be able to pump a different v in order to observe transitions with more favorable Franck-Condon factors. We scanned the frequency of the the pump (Ti:Sapphire) laser while monitoring the anode current from a freestanding PMT (Total Red PMT in Figure 3.1). When the frequency of the laser is resonant with a particular $2(A)^1\Sigma^+ (v', J') \leftarrow 1(X)^1\Sigma^+ (v'', J'')$ transition, red fluorescence is detected. Since only one laser is being used for this process the lines are Doppler broadened as shown in a typical scan in Fig. 4.2. This means that molecules with a velocity component in the direction of laser propagation absorb light of slightly lower frequency then those traveling perpendicular to the beam, since, in the frame of the molecule, the laser frequency is shifted to the blue by the Doppler effect. Similarly, molecules with a velocity component in the direction opposite the laser propagation direction absorb light of slightly higher frequency than those traveling perpendicular to the beam. The Doppler broadening results in lines that are approximately 1 GHz wide.

Once a scan like the one shown in Fig 4.2 has been recorded, the frequency of the pump laser was tuned and then fixed to the peak of one of the lines. The fluorescence was focused onto the entrance slits of the monochromator shown in Fig. 3.1 and an image, such as the one shown in Fig. 4.3, was recorded using the CCD diode array. In order to obtain good resolution for this spectrum, the entrance slits were set to a relatively small opening width of about 20 microns. If further resolution was required, the spectrum was recorded in second order. This spectrum is a good example of bound-bound fluorescence; a series of fluorescence doublets which correspond to downward transitions from the pumped $2(A)^1\Sigma^+$ rovibrational level (often referred to as the intermediate state) to all vibrational levels of the $1(X)^1\Sigma^+$ state subject to the selection rules $\Delta J = \pm 1$. The splitting between the two peaks of a particular doublet gives the rotational spacing of the ground state, while the splitting between two adjacent doublets gives the vibrational spacing of the ground state. The vibrational spacing identifies whether the molecule being excited is indeed NaCs. At lower pump frequencies, it is possible for the pump laser to induce Cs_2 transitions in addition to NaCs transitions. However, the two molecules can be distinguished since the ground state vibrational spacings for the two molecules are

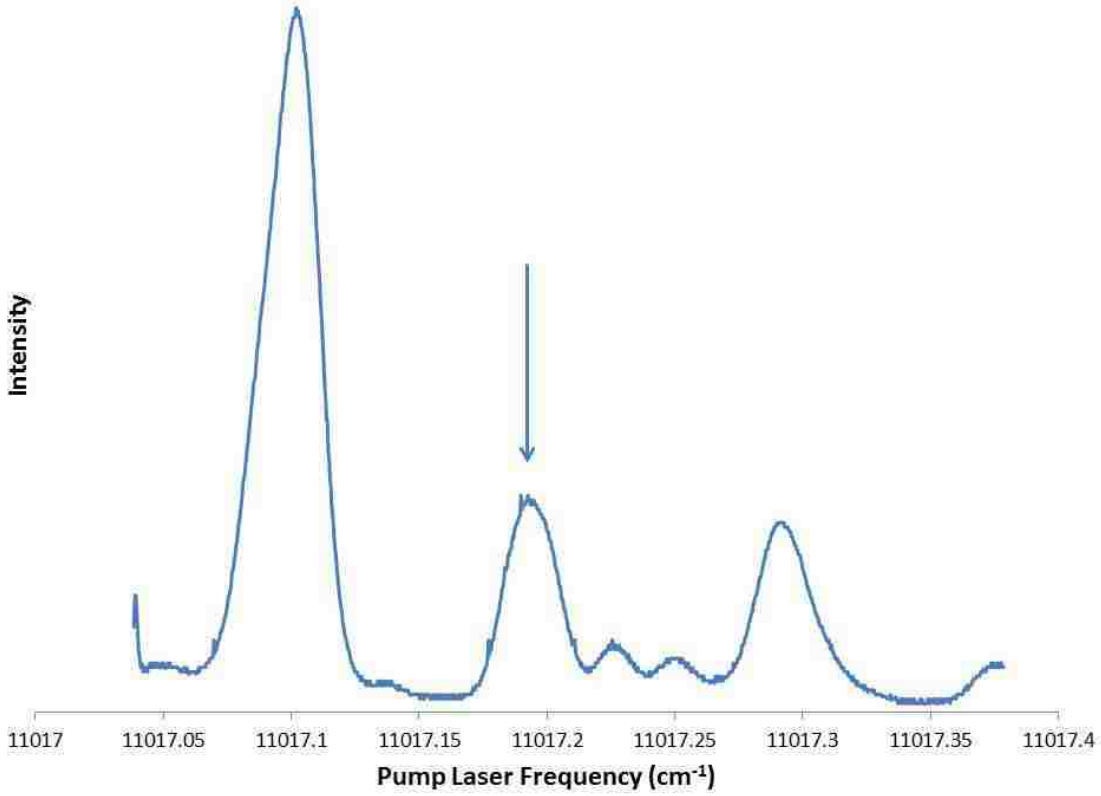

Figure 4.2: Typical pump laser excitation scan. Peaks in this type of scan are Doppler broadened so it is possible for more than one pump transition to lie within a Doppler width. The arrow indicates a peak resulting from two different pump transitions: $2(A)^1\Sigma^+\,(9,27) \leftarrow 1(X)^1\Sigma^+\,(0,26)$ and $2(A)^1\Sigma^+\,(9,17) \leftarrow 1(X)^1\Sigma^+\,(0,18)$.

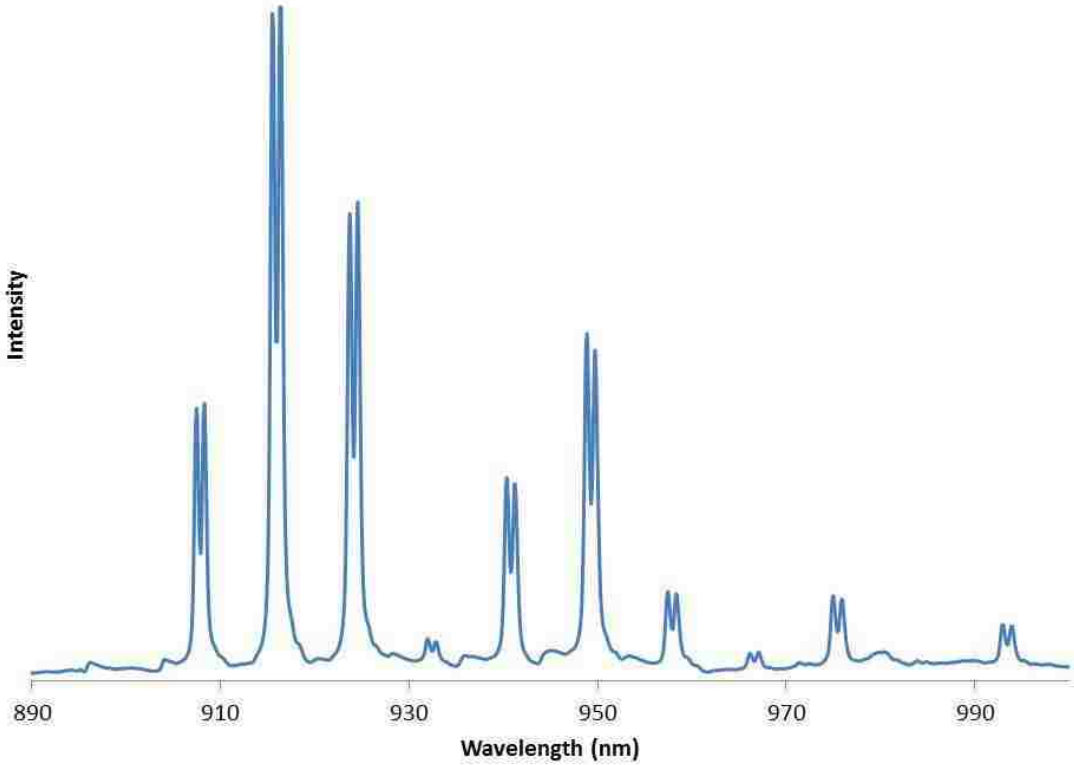

Figure 4.3: Resolved bound-bound fluorescence spectrum for transitions induced with the pump laser fixed at a particular frequency. The splitting of each doublet gives information about the rotational spacing of the ground state. The splitting between doublets gives information about the vibrational spacing of the ground state.

very different: ≈ 98 cm^{-1} for NaCs and ≈ 42 cm^{-1} for Cs_2. The $1(X)^1\Sigma^+$ state of NaCs is very well known from the work of Docenko *et al.* [15]. Therefore, we can compare the observed line splittings from a spectrum like this to known ground state splittings, allowing assignments to be made for values of the lower state vibrational and rotational quantum numbers, v'' and J'', for each line. Once the lower state J'' assignments are known, the $2(A)^1\Sigma^+$ rotational level assignment, J', is known also because of the $\Delta J = \pm 1$ selection rule. The value of the intermediate state vibrational quantum number, v', can be identified by calculating the total energy of the $2(A)^1\Sigma^+$ (v', J') rovibrational level and comparing it to levels in the database of Zaharova *et al.* [37]. Since the intermediate state vibration splitting is about 55 cm^{-1}, it is likely that there will only be one possibility for the assignment of v'. Once a particular pump transition was identified and properly assigned, the pump laser frequency was fixed to the peak of this transition. Though the line as observed on the red scan is Doppler broadened, the linewidth of the laser is significantly narrower (<1 MHz). Since the linewidth of the laser is less than the homogeneous linewidth, the laser effectively only excites molecules to the intermediate state with one particular component of velocity along the laser propagation axis. This causes the subsequent probe excitation scan to be Doppler-free.

4.2 Double Resonance

As described above, the pump laser frequency is fixed to a known pump transition populating a particular rovibrational level of the $1(b)^3\Pi_{0^+} \sim 2(A)^1\Sigma^+$ manifold. Spin-orbit coupling is sufficiently large in the heavy NaCs molecule that every level of these states is a singlet-triplet mixture. Due to the selection rules associated with the spin-orbit operator (see Sec. 6.1.1), the J' quantum number must be the same for both singlet and triplet components, but the v' quantum numbers of the two states need not be the same. For simplicity, all intermediate state v' quantum numbers in this dissertation refer to the vibrational level associated with the $2(A)^1\Sigma^+$ component.

The probe (dye) laser beam and pump laser beam were overlapped inside the oven by aligning both beams onto fixed apertures. The probe laser frequency was then scanned while monitoring the anode current of a second freestanding PMT (labeled "Total Green PMT" in Fig. 3.1), which is filtered to pass green/violet light. When the probe laser frequency was resonant with a transition out of the pumped $1(b)^3\Pi_{0^+}\ (v'_{\rm b}, J') \sim 2(A)^1\Sigma^+\ (v'_{\rm A}, J')$ level to an upper rovibrational level, downward fluorescence could be detected and recorded. Upper singlet electronic states radiate down to the $1(X)^1\Sigma^+$ state in the violet, and upper triplet electronic states radiate down to the $1(a)^3\Sigma^+$ state in the green. We record total (unresolved) violet or green emission as the probe laser is scanned over a transition. Such a scan, shown in Fig. 4.4, is called an "excitation scan". As mentioned above, these excitation lines are Doppler free since only the velocity group selected by the pump laser is excited by these transitions. It sometimes happens that more than one pump transition lies within one Doppler width of each other. In this case, more than one intermediate state rovibrational level is excited. Therefore, once a probe transition is identified, it is important to ensure that it corresponds to a transition out of the rovibrational level identified in the pump step. To do this, we fix the probe laser frequency on the peak and change the pump laser frequency by an amount corresponding to the difference between the $1(X)^1\Sigma^+\ (v'', J'' = J' - 1)$ and $1(X)^1\Sigma^+\ (v'', J'' = J' + 1)$ levels. This difference is known very accurately [15], so if the double resonance signal is reproduced with the new pump laser frequency, then we have confirmed that the probe transition is out of the identified $2(A)^1\Sigma^+\ (v', J')$ level. Pumping from a different ground state level in this way is also a valuable method to use if the v', J' assignment of the pump transition is not known precisely, since the laser frequency provides much more accurate energy differences than those obtained from the limited resolution of the resolved spectrum.

So far, no hyperfine structure has been observed in any of the electronic states of NaCs that we have studied. In studies of NaK [38, 39, 40] hyperfine structure took qualitatively different forms in states of different electronic symmetries and coupling regimes making it useful in identifying the different electronic states excited

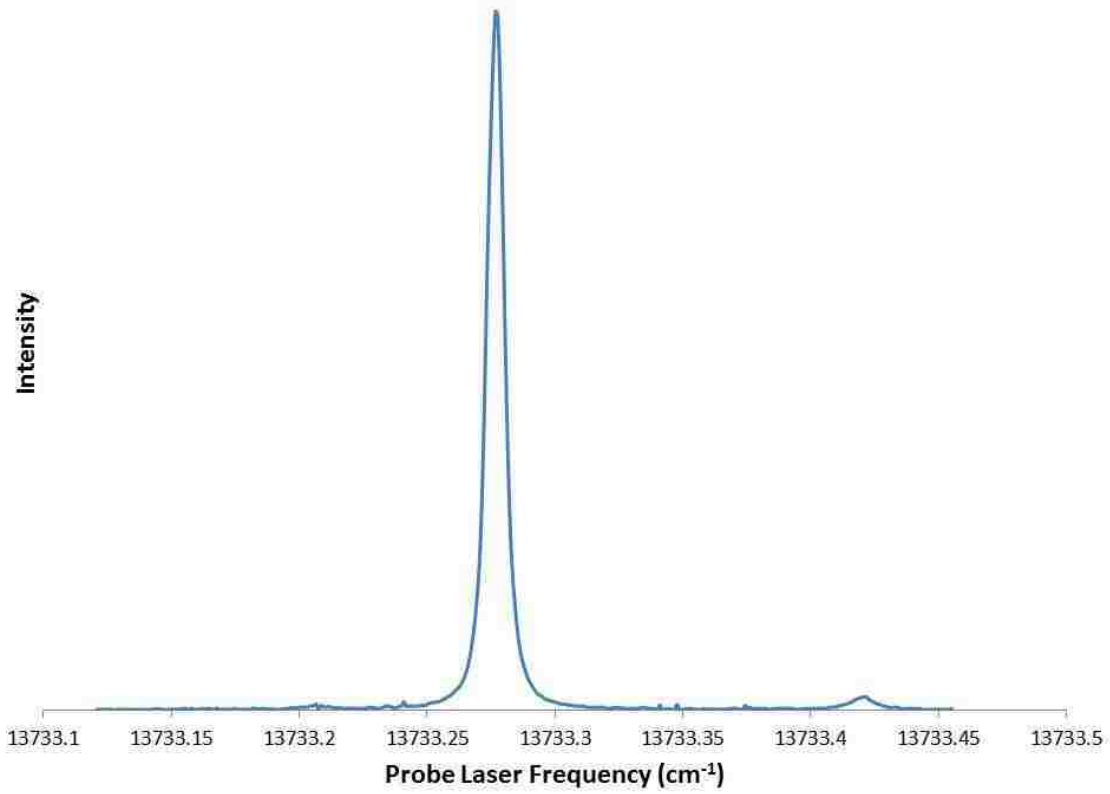

Figure 4.4: Typical probe laser excitation scan. The peak shown here corresponds to the double resonance transition $5^3\Pi_{0^+}\,(10,31) \leftarrow 1(b)^3\Pi_{0^+} \sim 2(A)^1\Sigma^+\,(14,32) \leftarrow 1(X)^1\Sigma^+\,(0,31)$.

by OODR transitions. The lack of observable hyperfine structure in our probe excitation scans of NaCs, which is explained in Ref. [3], means every double resonance signal is a single featureless peak (see Fig. 4.4). To identify the upper electronic state excited in the probe transition, we resolve the downward fluorescence. Both the pump and probe laser frequencies are fixed to pump a particular double resonance $^{1,3}\Lambda_\Omega(v, J) \leftarrow 1(b)^3\Pi_{0^+}\,(v'_{\rm b}, J') \sim 2(A)^1\Sigma^+\,(v'_{\rm A}, J') \leftarrow 1(X)^1\Sigma^+\,(v'', J'')$ transition. The fluorescence is filtered and focused onto the entrance slit of the monochromator. Upper triplet states radiate via transitions to the repulsive $1(a)^3\Sigma^+$ state. This bound-free emission gives rise to broad oscillatory spectra which are qualitatively different for different electronic states. Because the features in these spectra are quite broad, we use slit widths of approximately 200 microns in order to increase signal-to-noise. The resulting bound-free spectra serve as fingerprints for identifying the upper electronic state (as shown in Fig. 4.5). These spectra also allow for a tentative assignment of the upper state vibrational quantum number, v. As discussed in Sec. 2.4.1, for a monotonic difference potential the bound-free spectrum intensity can be considered to be a reflection of the square of the upper state vibrational wavefunction onto a wavelength grid. In such a case the spectrum should display v+1 bumps. Once a particular bound-free pattern was identified, the probe laser frequency was scanned so that rotational P and R pairs could be identified for many vibrational levels for an upper electronic state whose bound-free fluorescence exhibit this pattern. Coverage of vibrational levels is limited by the wavelength range of the probe laser and Franck-Condon factors between the intermediate state and the upper state. Both of these limitations can usually be partially circumvented by finding a different pump transition. Coverage of rotational levels is limited by the $\Delta J = \pm 1$ selection rule. Franck-Condon factors do not change very significantly with J, so typically both members of a P and R pair could be identified. To expand coverage of the J quantum number, a pump transition involving a different J must be used.

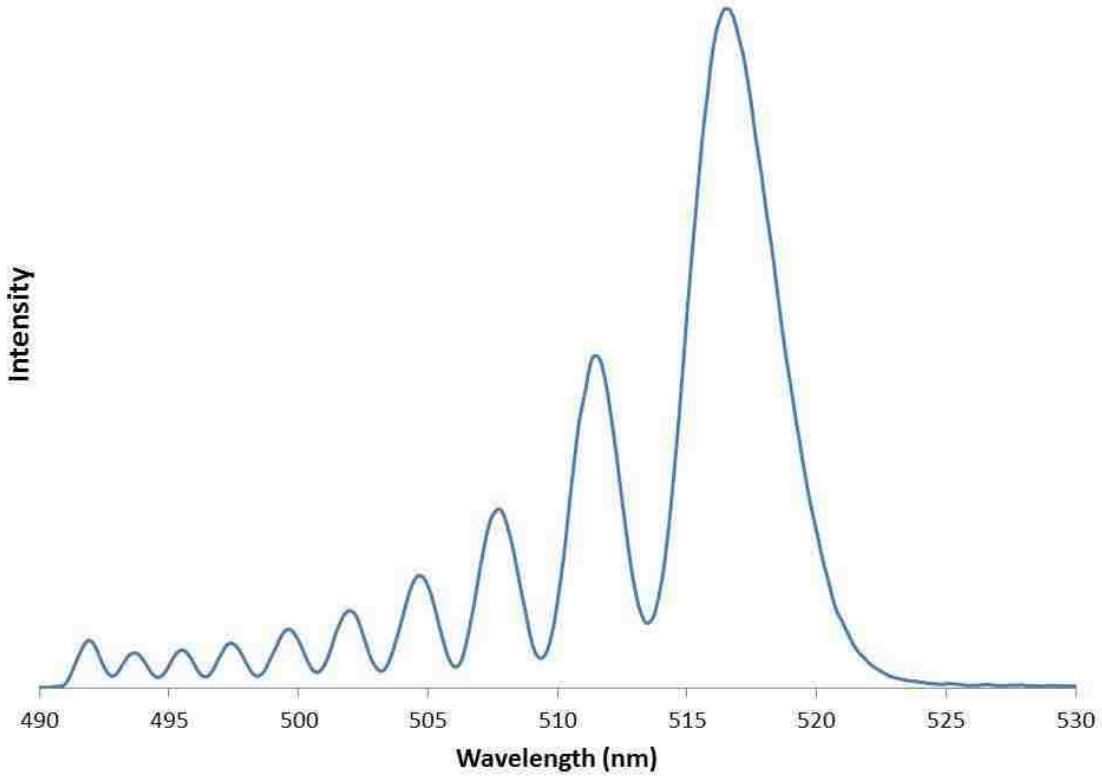

Figure 4.5: Resolved bound-free fluorescence spectrum of the double resonance signal shown in Fig. 4.4. Fluorescence shown here is due to downward transitions: $5^3\Pi_{0^+}\,(10, 31) \rightarrow 1(a)^3\Sigma^+$.

4.3 Collisional Satellite Lines

As described above, the number of rovibrational levels that can be probed from a given intermediate state level is limited by the selection rule $\Delta J = \pm 1$. Once the P and R probe transitions to levels of a given vibrational state have been found, a new pump transition must be identified and labeled to observe two more P and R probe transitions. One incredibly useful technique to get around this constraint is to use observations of collisional satellite lines to identify many rotational levels of a single vibrational state within one probe laser scan.

If the atomic (Ar or Cs) vapor pressure is sufficiently high, on either side of the direct P or R line in a pump or probe scan, one can observe regularly spaced satellite lines, which (in NaCs) decrease in intensity with increasing displacement in frequency from the direct line. Figure 4.6 shows a probe laser excitation spectrum with collisional lines. The direct P and R transitions in this figure are truncated and are actually approximately 10 times full scale. The satellite lines on either side of the direct lines are due to transitions out of collisionally populated levels near the rovibrational level involved in the direct transition. A collision of the molecule in the pumped intermediate level with an atomic collision partner causes the molecule to jump to a nearby rotational level. This collisional transfer is not limited by the usual $\Delta J = \pm 1$ selection rule. In experiments at Temple University, Salami *et al.* [41] observed collisional transfer of up to $\Delta J = -58$ in the ground state of Rb_2, and Wolfe *et al.* [42] observed transfer up to $|\Delta J| = 12$ in excited state NaK . The energy gaps between neighboring satellite lines in the spectrum shown in Fig. 4.6 are equal to the differences of the rotational energy level splittings of the upper and lower electronic states involved in the transition. Since these rotational gaps vary slowly with J, and are generally different for each electronic state, the satellite lines appear on either side of both the P and R direct transitions.

From a practical standpoint, we can take advantage of these satellite lines by using a two-step process to determine the level energies of the upper electronic state of interest. First, a direct transition to an upper state $^{1,3}\Lambda(v, J) \leftarrow 1(b)^3\Pi_{0^+}\,(v'_{\rm b}, J') \sim 2(A)^1\Sigma^+\,(v'_{\rm A}, J') \leftarrow 1(X)^1\Sigma^+\,(v'', J'')$ is found using the traditional pump/probe

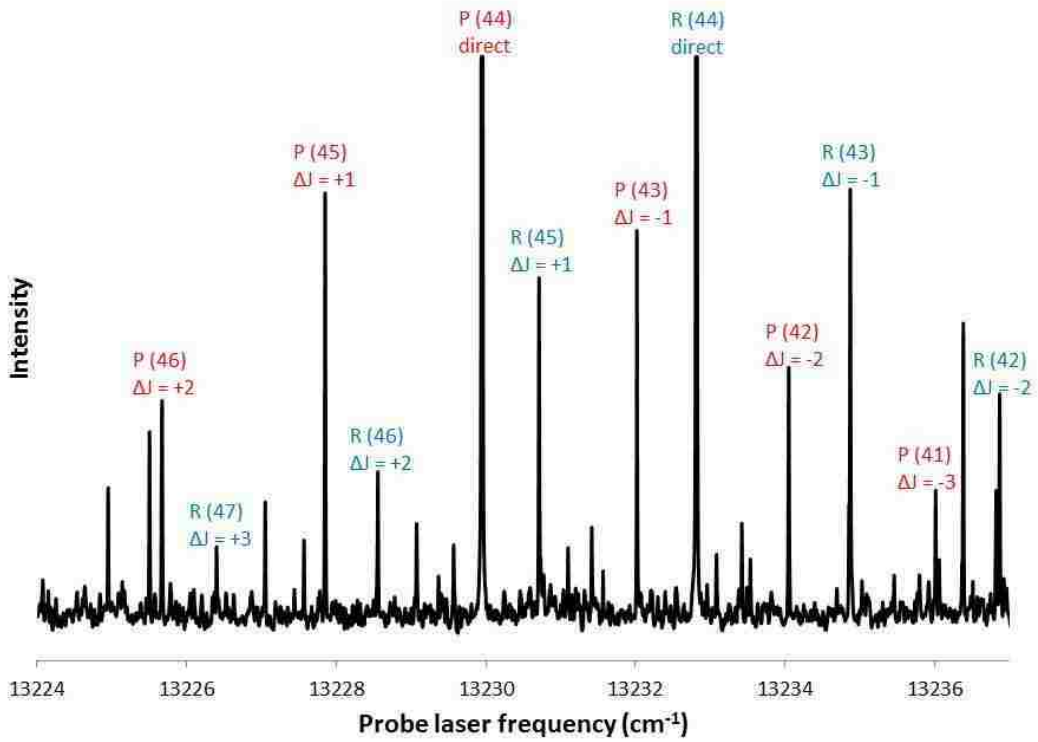

Figure 4.6: Example of collisional lines in an excitation spectrum obtained with the pump laser fixed on the NaCs $2(A)^1\Sigma^+\,(14, 44) \leftarrow 1(X)^1\Sigma^+\,(0, 45)$ transition. The direct P and R lines are truncated and are actually approximately 10 times full scale.

scheme. A particularly strong direct transition is favorable since a larger direct line signal typically means that a greater number of collisional lines with sufficient intensity will be observed. Once this direct transition is identified, the probe laser frequency is fixed on the peak of the $^{1,3}\Lambda(v, J) \leftarrow 2(A)^1\Sigma^+ (v'_A, J')$ transition and the pump laser frequency is scanned. Figure 4.7 shows a schematic diagram of transitions responsible for collisional lines in a scan of the pump laser. A pump excitation spectrum will show satellite collisional lines due to the pump transitions $2(A)^1\Sigma^+ (v'_A, J' \pm \Delta J) \leftarrow X(v'', J'' \pm \Delta J)$ followed by collisional transfer of population $2(A)^1\Sigma^+ (v'_A, J' \pm \Delta J) + (\text{Ar or Cs}) \rightarrow 2(A)^1\Sigma^+ (v'_A, J') + (\text{Ar or Cs})$. The frequencies of the collisional pump transitions resulting in $^{1,3}\Lambda(v, J) \rightarrow 1(a)^3\Sigma^+$, $1(X)^1\Sigma^+$ fluorescence depend on the difference between the rotational splittings of the intermediate state and the ground state. Thus these satellite lines provide the energies of the intermediate state levels relative to those of the ground state levels. Since the energies of the ro-vibrational levels of the ground electronic state are accurately known [15], the energies of the intermediate state levels can be determined to almost the same degree of accuracy (the laser frequencies are known to within 0.01 cm^{-1}). We then carry out a complementary experiment by fixing the pump laser frequency on the peak of the direct transition $2(A)^1\Sigma^+ (v'_A, J') \leftarrow 1(X)^1\Sigma^+ (v'', J'')$ and scanning the probe laser frequency. Figure 4.8 shows a schematic diagram of transitions responsible for collisional lines in a scan of the probe laser. Collisions in the intermediate state transfer population to neighboring rotational levels $2(A)^1\Sigma^+ (v'_A, J' \pm \Delta J)$ producing satellite lines due to probe transitions $^{1,3}\Lambda(v, J \pm \Delta J) \leftarrow 2(A)^1\Sigma^+ (v'_A, J' \pm \Delta J)$. The energies of the upper state ro-vibrational levels can now be determined relative to the intermediate state ro-vibrational levels with almost the same degree of accuracy as for the ground state level energies.

This process of identifying collisional lines greatly improves the efficiency with which one can determine level energies since it is possible to observe transitions to many rotational levels with a single scan. Splittings between rotational levels within an excited NaCs electronic state are typically about 2-6 cm^{-1}. However, the spacings between the collisional lines in a pump or probe laser scan are equal to the

difference in the rotational splittings between two different electronic states. These values are typically $\lesssim 1$ cm^{-1}. The collisional lines also allow one to make large jumps in J, which is done by fixing one of the laser frequencies on a collisional peak and scanning the other until it becomes resonant with the direct transition for that J. Now this new rotational transition becomes the direct line and new collisional lines are strong enough to identify and expand the rotational dataset.

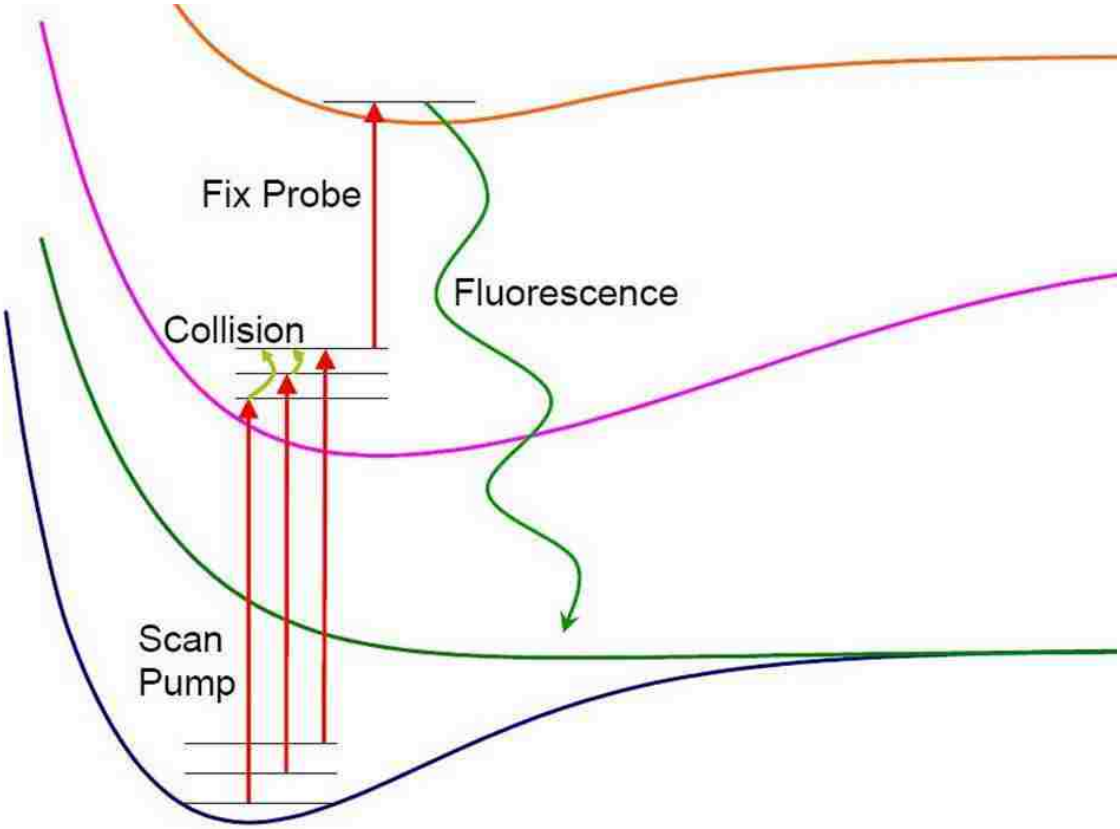

Figure 4.7: Schematic diagram of transitions resulting in collisional lines in pump scans. As the pump laser is scanned, collisions transfer population from the pump rotational levels to the lower rotational level associated with the probe transition. The frequencies of these collisional lines allow us to determine energies of the intermediate state relative to the ground state.

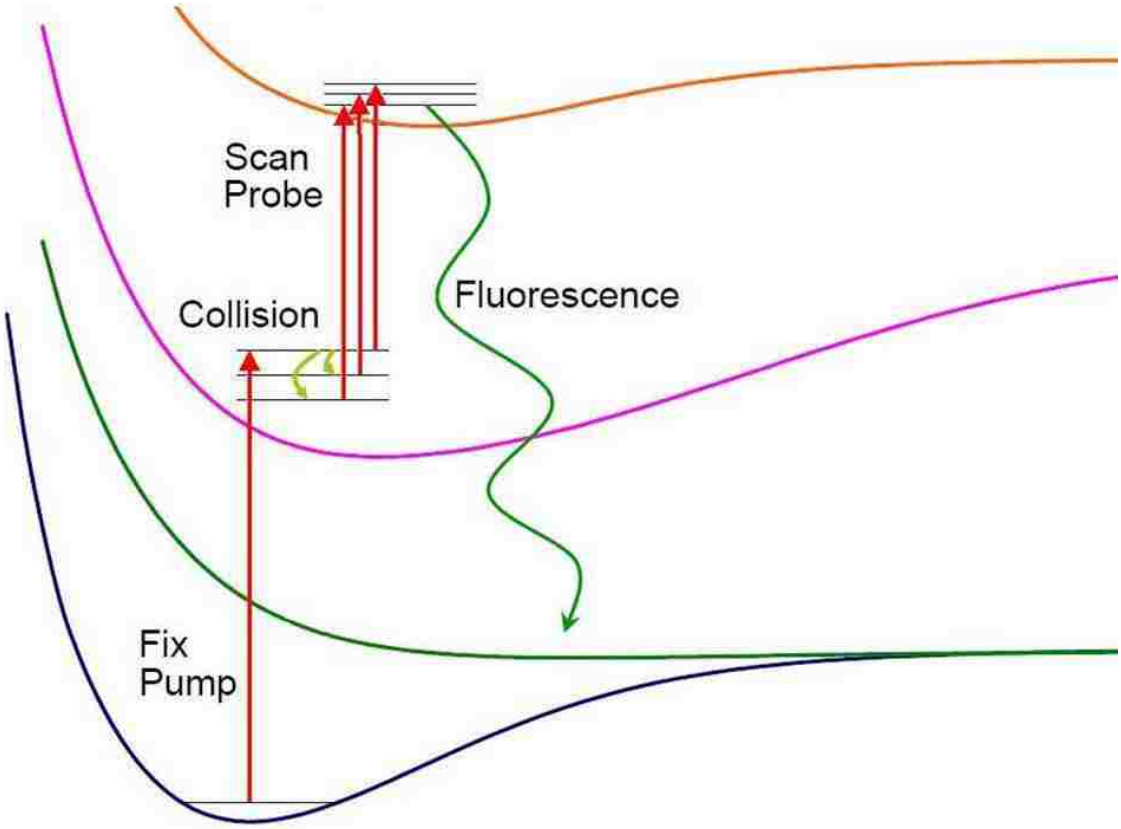

Figure 4.8: Schematic diagram of transitions resulting in collisional lines in probe scans. As the probe laser is scanned, collisions transfer population from the pumped rotational level to nearby rotational levels. The probe laser can then excite transition from the collisionally populated intermediate state levels to upper rotational levels. The frequencies of these collisional lines allow us to determine energies of the upper state relative to the intermediate state.

Chapter 5

Mapping the NaCs $12(0^+)$ Electronic Potential

In addition to the rovibrational levels from the NaCs $11(0^+)$ electronic state mapped out by previous work in this lab [3], we have been able to excite rovibrational levels from several other electronic states within the range of photon energies available to us with our lasers. This chapter describes the methods we use to identify and measure rovibrational level energies for the $12(0^+)$ electronic state of NaCs. Descriptions of how the electronic state was identified and how the RKR and IPA methods were used to produce a potential energy curve for this state from measured level energies are also presented. A table of measured rovibrational level energies is presented in Appendix B.

5.1 Identifying the Electronic State

The first step in the process of mapping out an electronic potential curve for a diatomic molecule involves measuring energies for many rotational and vibrational levels for that particular electronic state. In the present work, these measurements were done by finding double resonance transitions as described in Section 4.2. One challenge in this process is to identify the upper electronic state involved in these

transitions. In NaK, upper triplet states were identified relatively easily by the hyperfine structure that was observed in a probe excitation spectrum [38, 39, 40]. In that case, the hyperfine structure took a qualitatively different form in states of different symmetries. In our studies of NaCs thus far, we have not observed hyperfine structure. Arguments based on angular momenta vector coupling models provide an explanation for why we do not observe hyperfine structure in most electronic states of NaCs and these are presented in [3]. However, without observations of hyperfine structure, rovibrational levels must be assigned to their various electronic states by resolving their fluorescence as a function of wavelength. As described in Section 2.4.2, the overall intensity distribution within a resolved fluorescence spectrum depends on the shapes of the upper and lower state potentials. In particular, it is very sensitive to the upper state wavefunction, which is determined by the potential, and the transition dipole moment function between the upper and lower states involved in the transition. Therefore, rovibrational levels with similar resolved spectra (specifically bound-free spectra) are likely to belong to the same upper electronic state. Figure 5.1 shows several bound-free spectra for a particular electronic state that we were able to identify as the $12(0^+)$ state. Though the non-typical shapes of the bound-free spectra initially made assignment of the v quantum number difficult, it was clear that the levels associated with these spectra are low vibrational levels. These levels were found in the same energy region as the low lying vibrational levels of the $11(0^+)$ electronic state, which implies that the potential minimum of this new state must be relatively close, within a few hundred wavenumbers, to the bottom of the $11(0^+)$ potential.

A valuable piece of information when trying to identify the electronic state is the Ω quantum number. It is relatively easy to identify the Ω quantum number if rovibrational levels can be assigned for the lowest J's. In Hund's cases (a) and (c), as shown in Figure 2.1, the total angular momentum vector, $\vec{J}$, is made up of the nuclear rotation angular momentum, $\vec{R}$, and the total electronic angular momentum, $\vec{\Omega}$. Since $\vec{J} = \vec{R} + \vec{\Omega}$, and $\vec{R} \perp \vec{\Omega}$, $|\vec{J}| \geq |\vec{\Omega}|$. Therefore the lowest rotational level of a particular electronic state has the quantum number $J = \Omega$. To help determine the Ω quantum number for the $12(0^+)$ state, we succeeded in

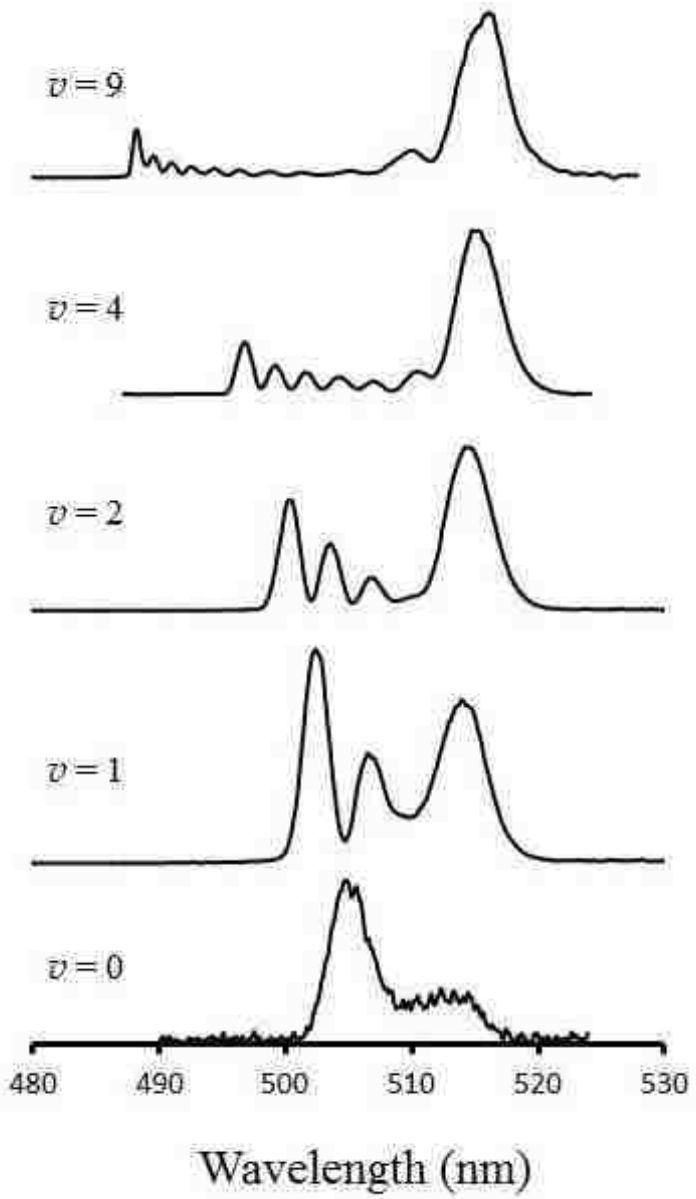

Figure 5.1: Experimental $12(0^+) \rightarrow 1(a)^3\Sigma^+$ bound-free spectra for several vibrational levels of the $12(0^+)$ electronic state. Vibrational quantum number assignments is explained in Sec. 5.2.

labeling a pump transition: $2(A)^1\Sigma^+(14,1) \leftarrow 1(X)^1\Sigma^+(0,2)$, which was done by making large jumps in the J quantum number using collisional -lines as described in Section 4.3. A probe laser excitation spectrum is shown in Figure 5.2 which shows the P and R lines associated with transitions to $J = 0$ and $J = 2$ of $v = 12$ of the $12(0^+)$ state. Collisional lines extend on only one side of the direct P line, indicating that the latter corresponds to the lowest rotational level of the upper state. We know that this lowest level is $J = 0$ because it is a P transition from the level $2(A)^1\Sigma^+(14,1)$. The pump transition assignment was confirmed by pumping the same intermediate state level with a transition from a different known ground state level, namely $2(A)^1\Sigma^+(14,1) \leftarrow 1(X)^1\Sigma^+(0,0)$. Since we observed a rotational level with the quantum number $J = 0$, we were able to confirm the assignment of $\Omega = 0$ for the upper electronic state.

By following progressions of rovibrational levels, which display bound-free spectra similar those shown in Figure 5.1, we were able to determine preliminary values for vibrational and rotational spectroscopic constants. We determined that this particular electronic state has an ω_e value (vibrational spacing) of approximately 54 cm^{-1}, a B_e value (rotational constant) of approximately 0.036 cm^{-1}, and a minimum (T_e) at $\approx$ 24670 cm^{-1} above the bottom of the ground $1(X)^1\Sigma^+$ state well. The rotational constant corresponds to an equilibrium separation of 4.9 Å. These preliminary constants are very similar to those of the $11(0^+)$ state where $\omega_e = 64.24$ cm^{-1}, $B_e = 0.03706$ cm^{-1}, and $T_e = 24511.8$ cm^{-1}, which were previously determined by Ashman *et al.* [3]. With this information we were able to examine the theoretical potentials calculated by Korek *et al.* [12] for an electronic state with $\Omega = 0$, and a minimum very close in energy and internuclear separation to that of the $11(0^+)$ electronic state. Figure 5.3 shows these potentials and indicates that the electronic state in question must be the $12(0^+)$ state.

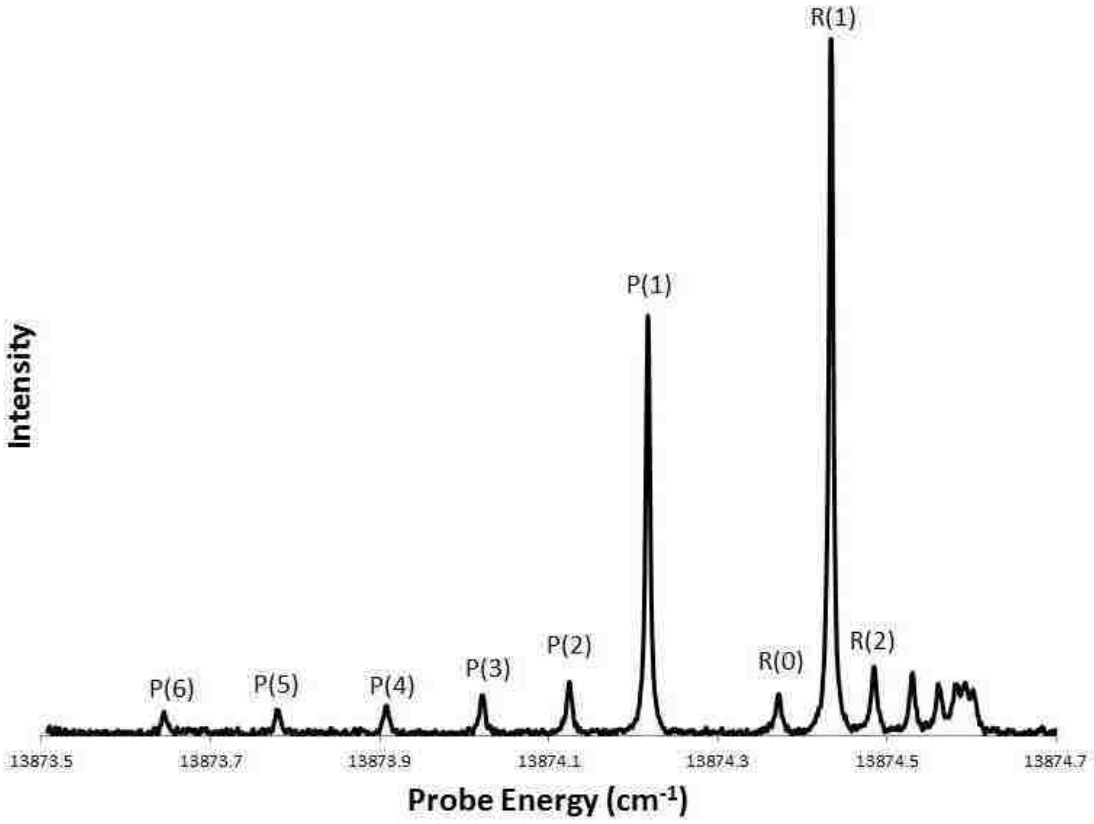

Figure 5.2: Probe laser excitation spectrum showing the transition [labeled P(1)] to a $J = 0$ level of the $12(0^+)$ electronic state. The pump laser frequency was fixed on the transition $2(A)^1\Sigma^+(14,1) \leftarrow 1(X)^1\Sigma^+(0,2)$. Collisional lines show transitions from nearby rotational levels due to population transfer. Note that there are no collisional lines associated with the P-series at energies above that of the P(1) line, indicating that the direct P-line [P(1)] corresponds to the lowest possible J, as expected.

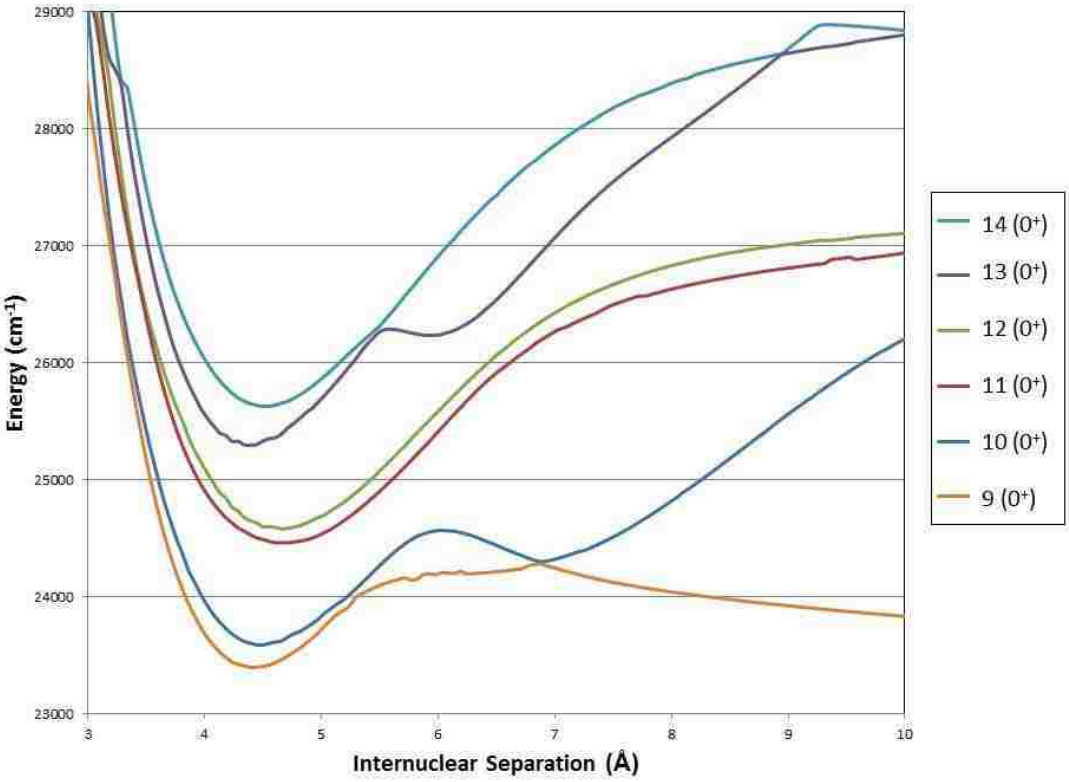

Figure 5.3: Electronic potential curves of NaCs calculated by Korek *et. al.* [12]. All potentials shown here have electronic symmetry 0^+ and have minima in the energy region of the $11(0^+)$ state. By comparing initial experimental data with these curves we were able to label a series of progressions as belonging to the $12(0^+)$ electronic state.

5.2 Energy Level Assignment and Analysis

Although preliminary spectroscopic constants, ω_e and B_e, were obtained for the $12(0^+)$ state, it is important that we have accurate assignments of the vibrational quantum number so that we can map the rovibrational levels of the electronic state down to the bottom of the well. In the $11(0^+)$ state, this assignment was relatively easy since the bound-free spectra, as seen in Figure 2.7, are not complicated. For transitions between states with a monotonic difference potential one could identify the vibrational quantum number since the square of the upper state wavefunction, and hence the bound-free spectrum, should have $v + 1$ peaks. However, the bound-free spectra associated with the $12(0^+)$ state were not so simple and an absolute vibrational numbering could not be confidently assigned using just the bound-free emission. The reason for this is explained in the next chapter. To be sure that we had an accurate assignment of the $12(0^+)$ vibrational quantum numbers, we analyzed the bound-bound parts of the resolved spectra from the lowest observed rovibrational levels. Figures 5.4, 5.5, and 5.6 show resolved spectra for the three lowest vibrational levels of the $12(0^+)$ state. These resolved spectra reveal that there is both bound-free emission to the repulsive $1(a)^3\Sigma^+$ state, and bound-bound emissions to the rovibrational levels of the ground $1(X)^1\Sigma^+$ state. Though the shape of the bound-free resolved fluorescence does not allow for easy assignment of the upper state vibrational quantum number, v, the envelope of the discrete bound-bound resolved fluorescence is more regular and conveys additional information about v. The envelope of the bound-bound fluorescence for the lowest measured rovibrational level has only one peak and can therefore be tentatively assigned $v = 0$ (see also Chapter 6). Once we established an absolute vibrational numbering for the low lying levels, we were able to make accurate quantum number assignments for all other measured rovibrational levels.

The ultimate goal in measuring many rovibrational levels associated with a single electronic state is to construct a relatively smooth potential energy curve that is able to reproduce the measured energy levels as well as possible and also reasonably predict the energies of unmeasured levels. The most common method of producing

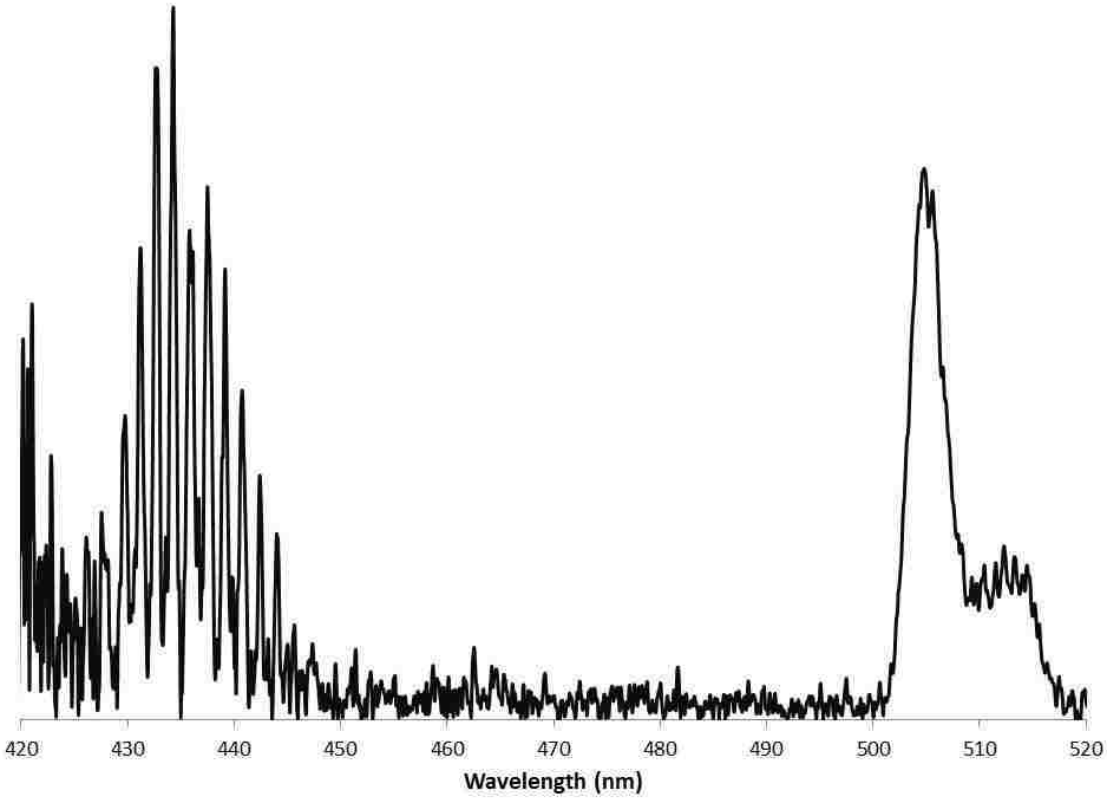

Figure 5.4: Resolved spectrum showing fluorescence due to bound-free transitions $12(0^+)(0,43) \rightarrow 1(a)^3\Sigma^+$ (500-520 nm) and bound-bound transitions $12(0^+)(0,43) \rightarrow 1(X)^1\Sigma^+ (v'', 42\,\&\,44)$ (425-450 nm). This spectrum has been corrected for the wavelength dependence of the detector efficiency (see Sec. 3.4.3) which results in the dramatic increase in the noise level at the short wavelength end of the spectrum (near 420 nm).

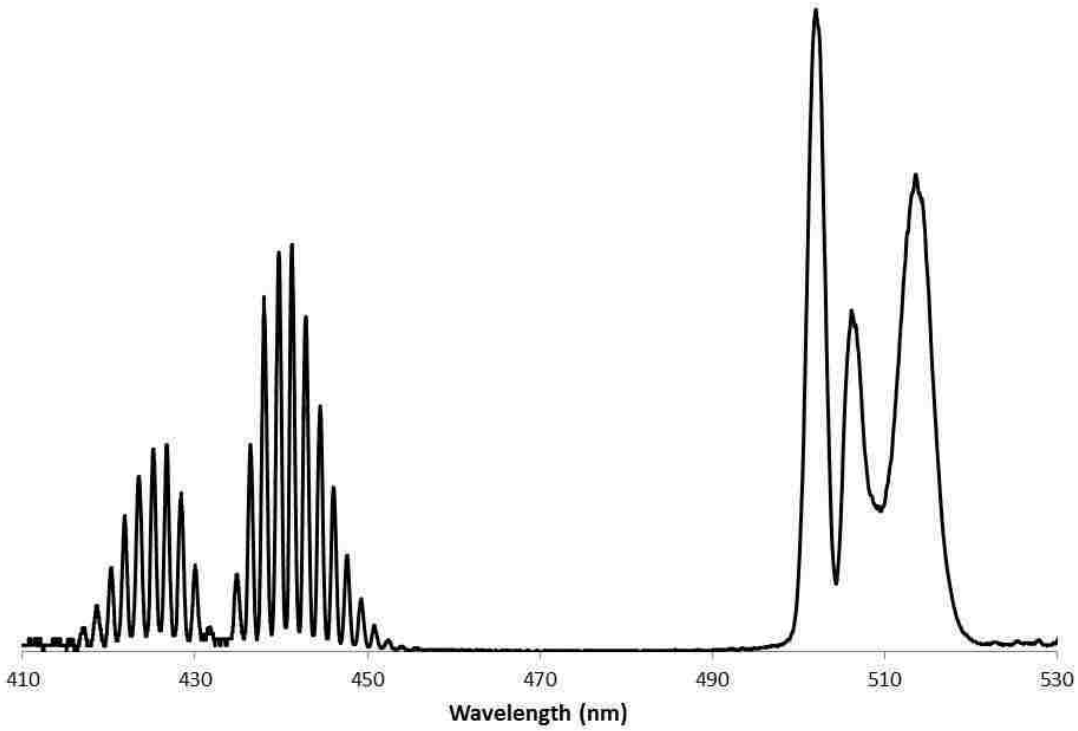

Figure 5.5: Resolved spectrum showing fluorescence due to bound-free transitions $12(0^+)(1,43) \rightarrow 1(a)^3\Sigma^+$ (500-520 nm) and bound-bound transitions $12(0^+)(1,43) \rightarrow 1(X)^1\Sigma^+$ $(v'', 42\,\&\,44)$(410-460 nm).

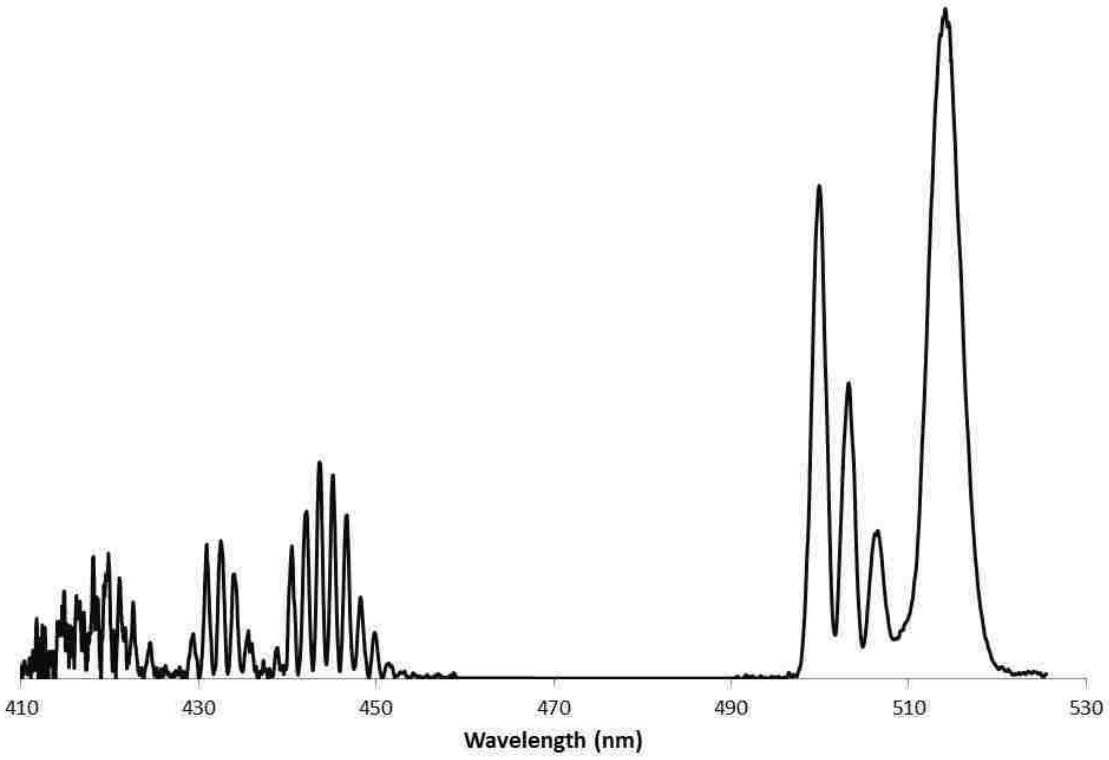

Figure 5.6: Resolved spectrum showing fluorescence due to bound-free transitions $12(0^+)(2,43) \rightarrow 1(a)^3\Sigma^+$ (500-520 nm) and bound-bound transitions $12(0^+)(2,43) \rightarrow 1(X)^1\Sigma^+$ $(v'', 42\,\&\,44)$(410-460 nm).

an experimental potential from energy level data is the Rydberg-Klein-Rees (RKR) method. This method requires an accurate set of spectroscopic constants determined from the measured energies, so the first task is to compile the measured level energies into a database and fit them using the Dunham expansion, which is described in Section 2.3.3. We obtain a set of Dunham coefficients using a program called DParFit developed by Robert Le Roy [21]. This program takes a list of assigned experimental energies along with experimental uncertainties and fits the constants $Y_{i,k}$ in Eq. (2.31) (see Sec. 5.3 below) to reproduce those energies in a least squares sense. The user must determine how many terms to keep in the Dunham expansion. If too few terms are used, the fit will not have enough flexibility to reproduce the measured energies. If too many terms are used, the error in the fit is smaller. However the constants may have been adjusted in a way that accommodates slightly perturbed energy levels as well as those following regular progressions. Constants produced from such a fit are often be less able to predict energies for levels that lie outside the range of experimental data than those obtained from a fit based on a smaller number of terms. In NaCs, spin-orbit interactions are very strong, and electronic states typically have global interactions with one another. This means that rather than having localized perturbations where one or two rotational levels may not fit into an otherwise regular progression, global perturbations can cause several sets of vibrational levels to interact with one another. These interactions result in level energies that tend to exhibit small oscillations about regular progressions. Because of this, it is important to decide first on a meaningful number of terms to keep in the Dunham expansion.

Therefore, I first examined individual rotational levels within a particular vibrational level. Initially, this was done for the $v = 2$ vibrational level since we have wide coverage of J. Figure 5.7 shows a plot of the rotational levels for the $v = 2$ vibrational level. Such levels should obey the rotational expansion:

$$E(v, J) = G_v + B_v J(J+1) - D_v[J(J+1)]^2 + \cdots , \tag{5.1}$$

where G_v is the energy of the $(v, 0)$ level for that particular vibrational state, B_v is

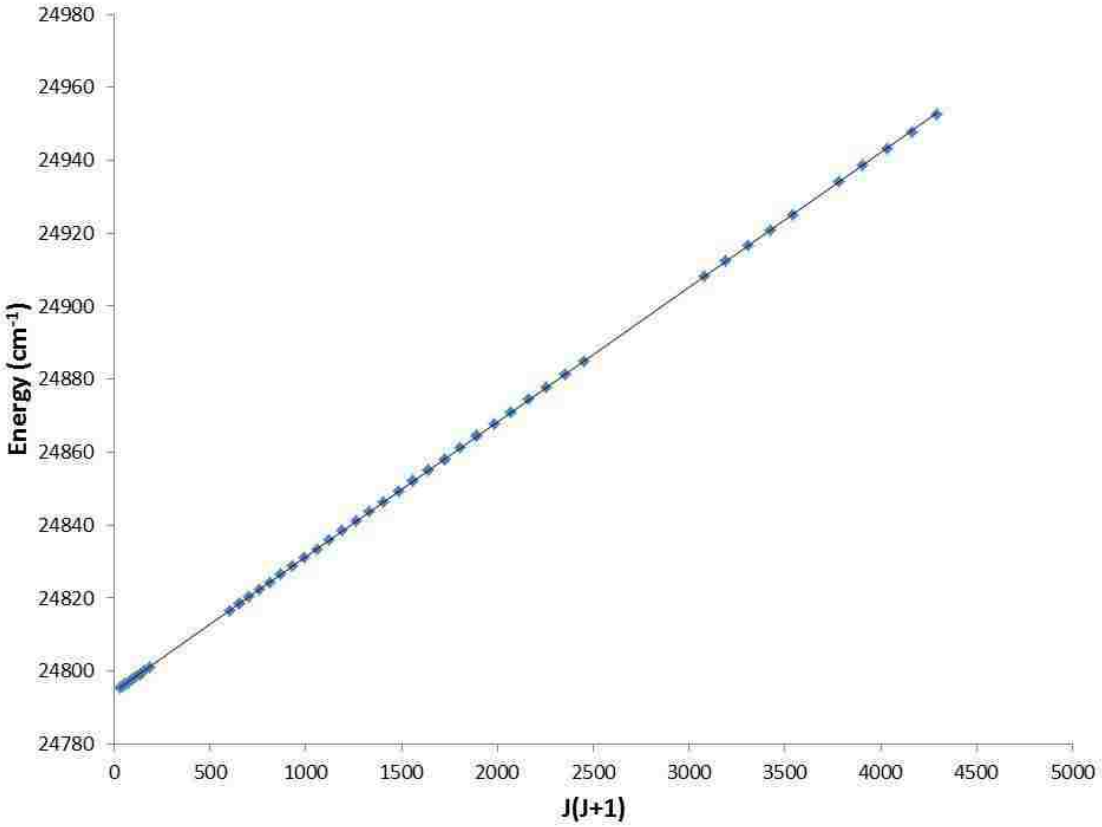

Figure 5.7: Linear fit of rotational levels for $v = 2$ of the $12(0^+)$ state to Eq. (5.1) (with D_v and higher order terms fixed to zero). Error bars associated with each measurement are 0.02 cm^{-1} and hence too small to see on this plot. The fit yields $G_v = (24794.44 \pm 0.02)$ cm^{-1} and $B_v = (0.03694 \pm 0.000011)$ cm^{-1}. Uncertainties in the coefficients are statistical.

the rotational constant described in Section 2.3.2, and D_v is the centrifugal distortion constant. The straight line fit to the data shown in Fig. 5.7 includes only the constant and linear terms in Eq. (5.1); i.e. D_v and all higher order terms were fixed to zero for this fit. Though the level energies appear to be well described with a linear fit, discrepancies arising from neglect of higher order terms in Eq. (5.1) are not easily seen due to the large scale of the vertical axis. To more clearly visualize any higher order dependency on $J(J+1)$ we plot the expression $\frac{E(v,J)-G_v}{J(J+1)}$ versus $J(J+1)$ for measured energy values and the G_v value obtained in the linear fit. Figure 5.8 shows this plot using the same data as Fig. 5.7. Smaller values of J were omitted from this plot since those points exaggerate small discrepancies [due to dividing by $J(J+1)$], which do not give any information about the systematic trend. From Eq. (5.1) we see that

$$\frac{E(v,J)-G_v}{J(J+1)} = B_v - D_v[J(J+1)] + \cdots . \tag{5.2}$$

Therefore, if no quadratic or higher order terms in $J(J+1)$ are needed to fit the data, the points would be observed to be randomly distributed around a constant value, with deviations consistent with experimental error bars. However a systematic slope or curvature in this plot, like the one shown in Figure 5.8, suggests that higher order terms are required.

The same process was repeated with the next higher order term in Eq. (5.1), namely $-D_v[J(J+1]^2$. This term accounts for centrifugal distortion, which means that as the molecule rotates faster, it stretches. The stretching increases the internuclear separation which results in a lower rotational energy, hence the minus sign included explicitly in this term. Again, to highlight any systematic dependencies on $J(J+1)$ after including the centrifugal distortion term in the fit, we plot the function $\frac{E(v,J)-G_v}{[J(J+1)]^2} - \frac{B_v}{J(J+1)}$ versus $J(J+1)$ using measure energies and the new fitted values of G_v and B_v. Figure 5.9 shows this plot for the data used in Fig 5.7. Since these values appear to be randomly distributed about a constant value, we assume that no additional higher order terms need to be included in the functional form of Eq. (5.1) used in the fit to reproduce the measured levels.

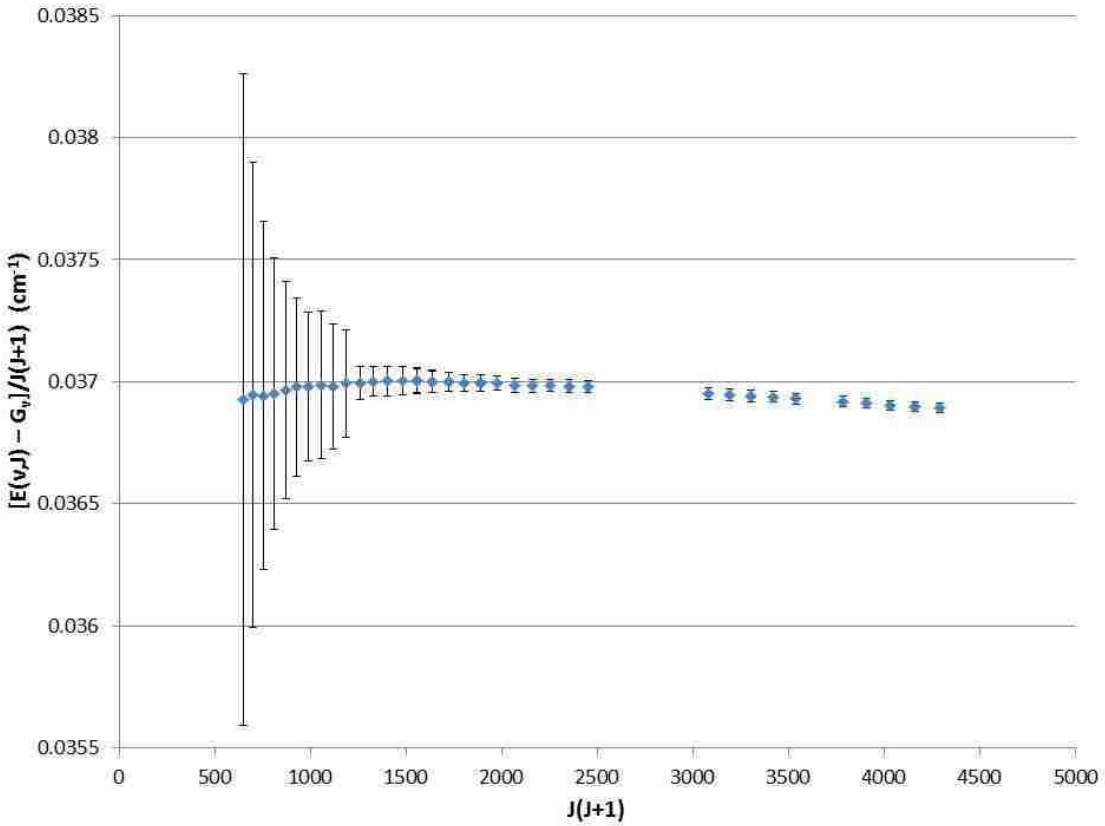

Figure 5.8: Plot of $\frac{E(v,J)-G_v}{J(J+1)}$ versus $J(J+1)$ for $v = 2$ levels of the $12(0^+)$ state using the G_v value from the linear fit. The systematic downward slope at high J implies that higher order terms are needed in Eq. (5.1) to accurately describe the level energies.

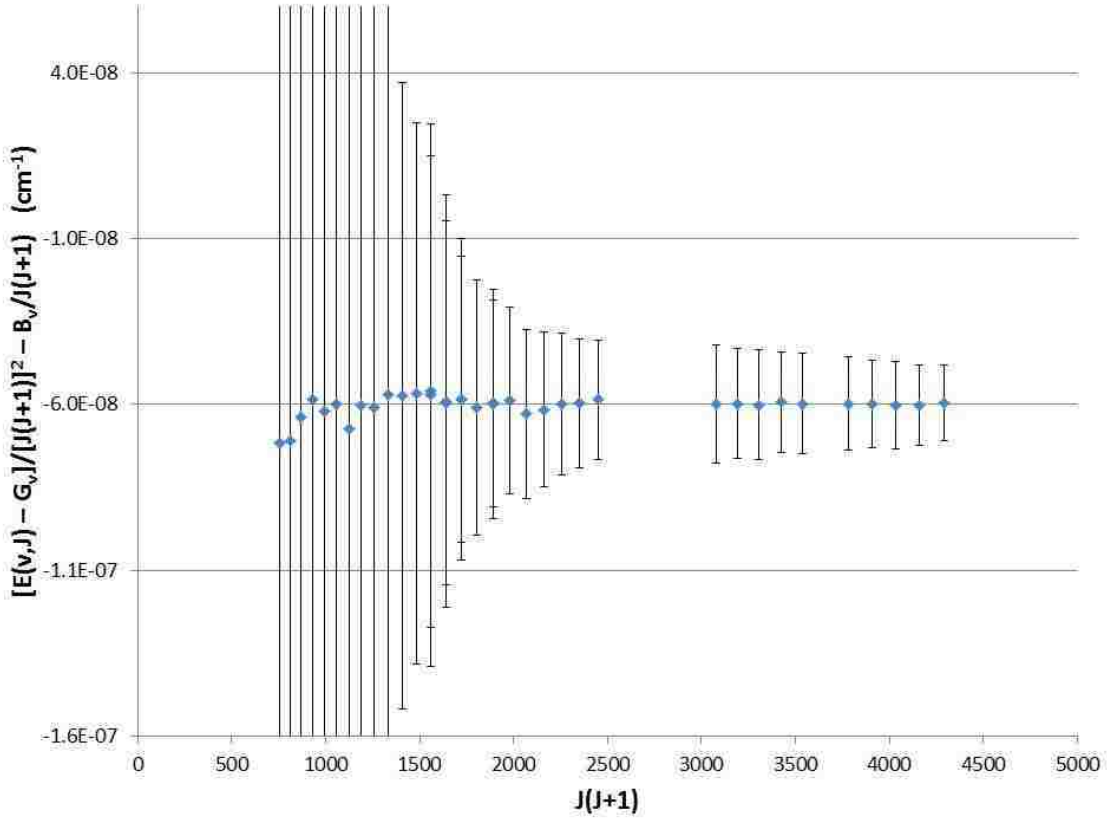

Figure 5.9: Plot of $\frac{E(v,J)-G_v}{[J(J+1)]^2} - \frac{B_v}{J(J+1)}$ versus $J(J+1)$ for $v = 2$ levels of the $12(0^+)$ state. The values of G_v and B_v for this vibrational level are taken from the quadratic fit of $E(v, J) = G_v + B_v[J(J + 1)] - D_v[J(J + 1)]^2$; $D_v = (6.0 \pm 0.2) \times 10^{-8}$ cm^{-1}, $B_v = (3.718 \pm 0.001) \times 10^{-2}$ cm^{-1}, and $G_v = 24794.312 \pm 0.008$ cm^{-1}.

v	G_v (cm^{-1})	$B_v(\mathrm{cm}^{-1})$	$D_v(\mathrm{cm}^{-1})$
1	24742.92	0.03704	6.8×10^{-8}
2	24794.31	0.03718	6.0×10^{-8}
4	24903.16	0.03730	5.5×10^{-8}
5	24958.31	0.03724	6.7×10^{-8}
6	25012.68	0.03704	5.7×10^{-8}

Table 5.1: Coefficients of quadratic fit of rotational levels. The vibrational levels chosen for the rotational fits have large coverage of J.

v	G_v (cm^{-1})	$B_v(\mathrm{cm}^{-1})$	$D_v(\mathrm{cm}^{-1})$ (fixed)
0	24693.308	0.036910	6.1×10^{-8}
1	24742.924	0.037027	6.1×10^{-8}
2	24794.308	0.037187	6.1×10^{-8}
3	24847.954	0.037366	6.1×10^{-8}
4	24903.149	0.037323	6.1×10^{-8}
5	24958.314	0.037220	6.1×10^{-8}
6	25012.676	0.037050	6.1×10^{-8}
7	25065.924	0.036824	6.1×10^{-8}
8	25118.023	0.036666	6.1×10^{-8}
10	25220.343	0.036368	6.1×10^{-8}
12	25312.896	0.038183	6.1×10^{-8}
13	25371.037	0.036079	6.1×10^{-8}
14	25421.054	0.035927	6.1×10^{-8}

Table 5.2: Coefficients of quadratic fit of rotational levels with D_v fixed at $6.1 \times 10^{-8}\mathrm{cm}^{-1}$. Although this D_v value was determined for vibrational levels with large coverage of J, it is fixed in the fit for all vibrational levels.

After fitting rotational progressions for many vibrational levels, we found that the centrifugal distortion constants were the same to within error bars for different vibrational states (see Table 5.1). Therefore, in subsequent analysis, the rotational constant D_v was fixed at $(6.1 \pm 0.7) \times 10^{-8}\text{cm}^{-1}$. This value is the average of the D_v constants obtained from the quadratic fits the of v=1, 2, 4, 5, and 6 level energies. These vibrational levels were chosen since they have very wide coverage of J. G_v and B_v values were then refitted for all v's using Eq. (5.1) with D_v fixed to $(6.1 \pm 0.7) \times 10^{-8}\text{cm}^{-1}$ and all higher terms set to zero. These values are given in Table 5.2.

Next we performed similar fits to determine how many vibrational terms are needed to describe G_v and B_v based on our data set. We fit rotationless vibrational level energies (G_v values from Table 5.2) to the expression

$$G_v = T_e + \omega_e(v+\frac{1}{2}) - \omega_e x_e(v+\frac{1}{2})^2 + \omega_e y_e(v+\frac{1}{2})^3 + \omega_e z_e(v+\frac{1}{2})^4 + \cdots , \quad (5.3)$$

and rotational constants (B_v values from Table 5.2) for each vibrational level to the expression

$$B_v = B_e - \alpha_e(v+\frac{1}{2}) + \gamma_e(v+\frac{1}{2})^2 + \cdots . \quad (5.4)$$

The G_v and B_v constants as a function of $(v+\frac{1}{2})$ can be analyzed using Eqs. (5.3) and (5.4) and a method similar to that used for the rotational energies described above. First we determine how many terms in Eq. (5.3) are needed to describe the G_v values within experimental uncertainties. Therefore, we plot G_v versus $v+\frac{1}{2}$ (Fig. 5.10) and fit with the linear function $G_v = T_e + \omega_e(v+\frac{1}{2})$. To determine if this linear fit is sufficient we plot $\frac{G_v - T_e}{v+\frac{1}{2}}$ versus $v+\frac{1}{2}$ using the T_e value from the linear fit (Fig. 5.11). Since, there is clearly a systematic dependence on $(v+\frac{1}{2})$, a quadratic term in Eq. (5.3) is needed. We then refit the G_v values with Eq. (5.3) including a quadratic term (but no higher terms). Figure 5.12 shows the plot of $\frac{G_v - T_e}{(v+\frac{1}{2})^2} - \frac{\omega_e}{v+\frac{1}{2}}$ versus $v+\frac{1}{2}$ using the T_e and ω_e values from the quadratic fit. This plot does not show any significant systematic dependence on $v+\frac{1}{2}$ which implies

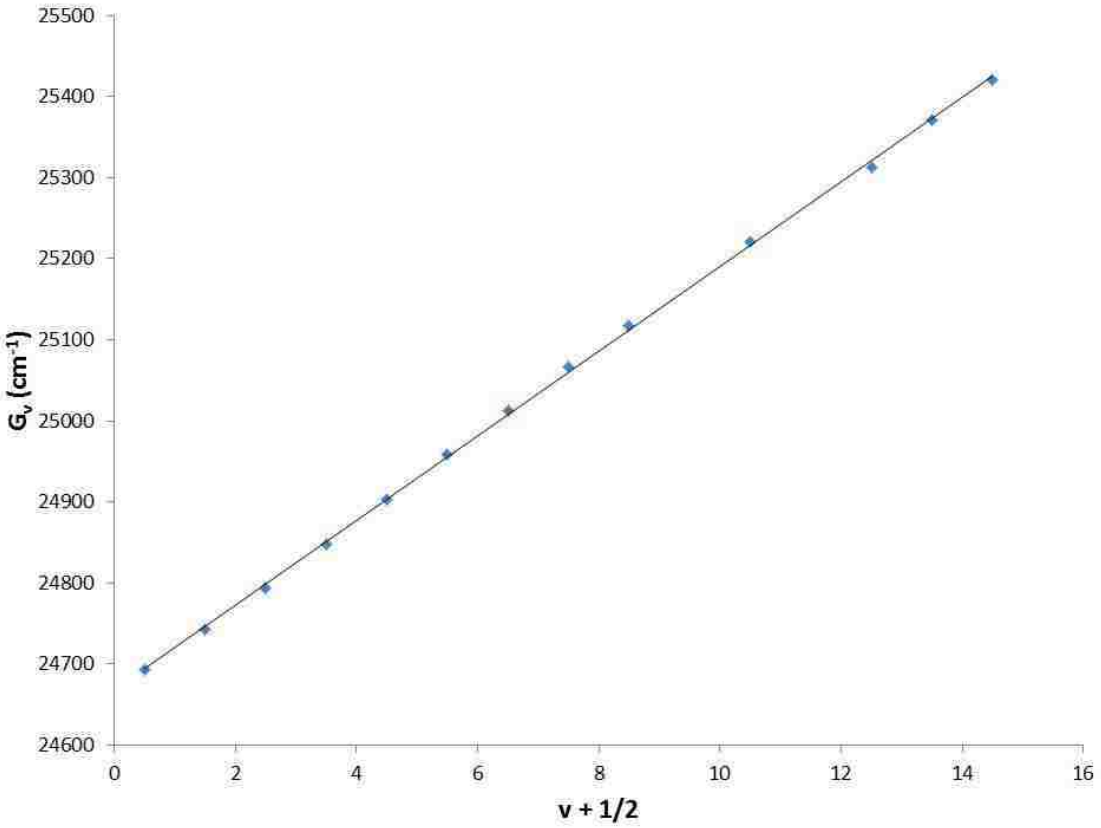

Figure 5.10: Plot of G_v versus $v + \frac{1}{2}$ for vibrational levels of the $12(0^+)$ state along with a linear fit to Eq. (5.3) (with $\omega_e x_e$ and higher order terms fixed to zero). Error bars associated with the values of G_v are too small to be seen on this plot. The fit yields $T_e = 24668 \pm 2$ cm^{-1} and $\omega_e = 52.1 \pm 0.3$ cm^{-1}.

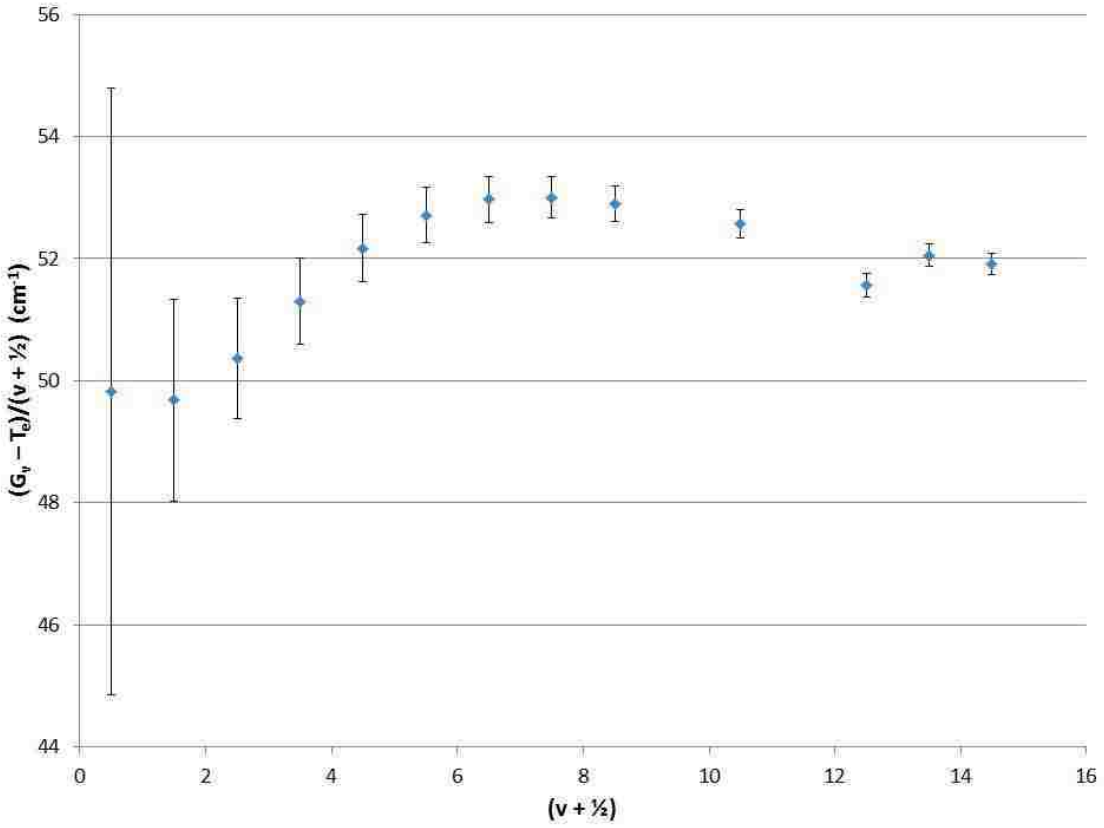

Figure 5.11: Plot of $\frac{G_v - T_e}{v+\frac{1}{2}}$ versus $v + \frac{1}{2}$ for vibrational levels of the $12(0^+)$ state. Values of G_v are taken from Table 5.2 and $T_e = 24668 \pm 2$ cm^{-1} was obtained from the fit of G_v values to the linear function $G_v = T_e + \omega_e(v + \frac{1}{2})$. There is clearly a systematic dependence on $(v + \frac{1}{2})$, which implies more than just the constant and linear terms in Eq. (5.3) are needed.

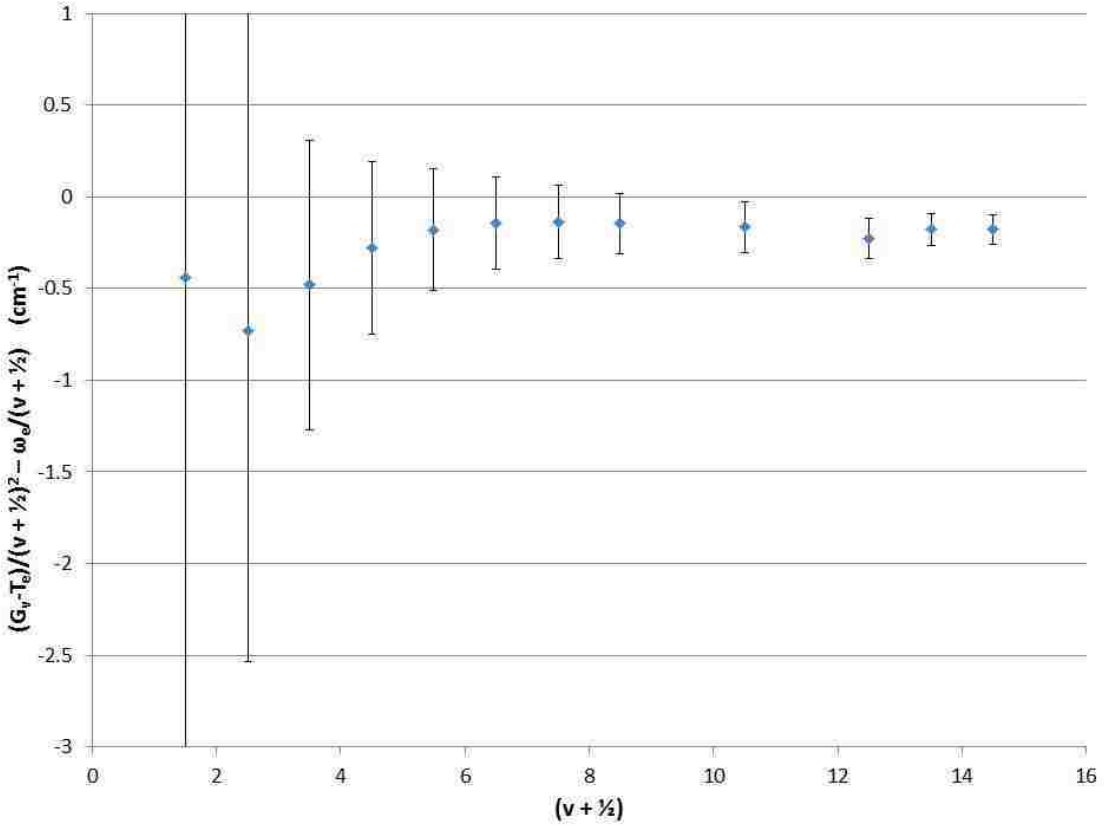

Figure 5.12: Plot of $\frac{G_v - T_e}{(v+\frac{1}{2})^2} - \frac{\omega_e}{v+\frac{1}{2}}$ versus $v + \frac{1}{2}$ for vibrational levels of the $12(0^+)$ state. Values of G_v are taken from Table 5.2 and $T_e = 24661 \pm 3$ cm^{-1}, $\omega_e = 55.0 \pm 0.9$ cm^{-1} were obtained from the fit of the G_v values to $G_v = T_e + \omega_e(v + \frac{1}{2}) - \omega_e x_e (v + \frac{1}{2})^2$. There does not seem to be any significant systematic dependence on $v + \frac{1}{2}$, which implies that no terms beyond the constant, linear, and quadratic terms in Eq. (5.3) are needed to describe G_v.

that no terms beyond the constant, linear, and quadratic terms in Eq. (5.3) need to be included in the description of G_v. Keeping more terms in Eq. (5.3) will increase the accuracy with which the experimental energies are described; however, keeping too many terms will make it unlikely that the constants can be used to accurately determine energies of levels beyond the range of the current dataset.

We plot rotational constants (B_v) from Table 5.2 versus $v + \frac{1}{2}$ in Fig. 5.13 and we fit them using constant and linear terms in Eq. (5.4), $B_v = B_e - \alpha_e(v + \frac{1}{2})$. To determine if a linear fit is sufficient, we plot $\frac{B_v - B_e}{v+\frac{1}{2}}$ versus $v + \frac{1}{2}$ using $B_e = 0.0374 \pm 0.0001$ cm^{-1} from the linear fit (Fig. 5.14). The dependence on $(v + \frac{1}{2})$ implies more than just the constant and linear terms in Eq. (5.4) are needed to describe B_v. Therefore we refit the B_v constants including the quadratic term in Eq. (5.4). To determine if this is sufficient we plot $\frac{B_v - B_e}{(v+\frac{1}{2})^2} + \frac{\alpha_e}{v+\frac{1}{2}}$ versus $v + \frac{1}{2}$ using $B_e = 0.0370 \pm 0.0001$ cm^{-1} and $\alpha_e = (6 \pm 4) \times 10^{-5}$ cm^{-1} from the quadratic fit (Fig. 5.15). This plot does not seem to show any significant systematic dependence on $v + \frac{1}{2}$, which implies that no terms beyond the constant, linear, and quadratic terms in Eq. (5.4) must be kept to describe the B_v values obtained in this work.

The best fit spectroscopic constants obtained from the the fitting methods presented here are listed in Table 5.3.

Spectroscopic Constant	Fit Value with Error (cm^{-1})
T_e	24661 ± 3
ω_e	55.0 ± 0.9
$\omega_e x_e$	-0.18 ± 0.06
B_e	$(3.71 \pm 0.01) \times 10^{-2}$
α_e	$(6 \pm 4) \times 10^{-5}$
γ_e	$(-1.0 \pm 0.3) \times 10^{-5}$
D_v	$(6.1 \pm 0.7) \times 10^{-8}$

Table 5.3: Spectroscopic constants for the NaCs 12(0^+) state

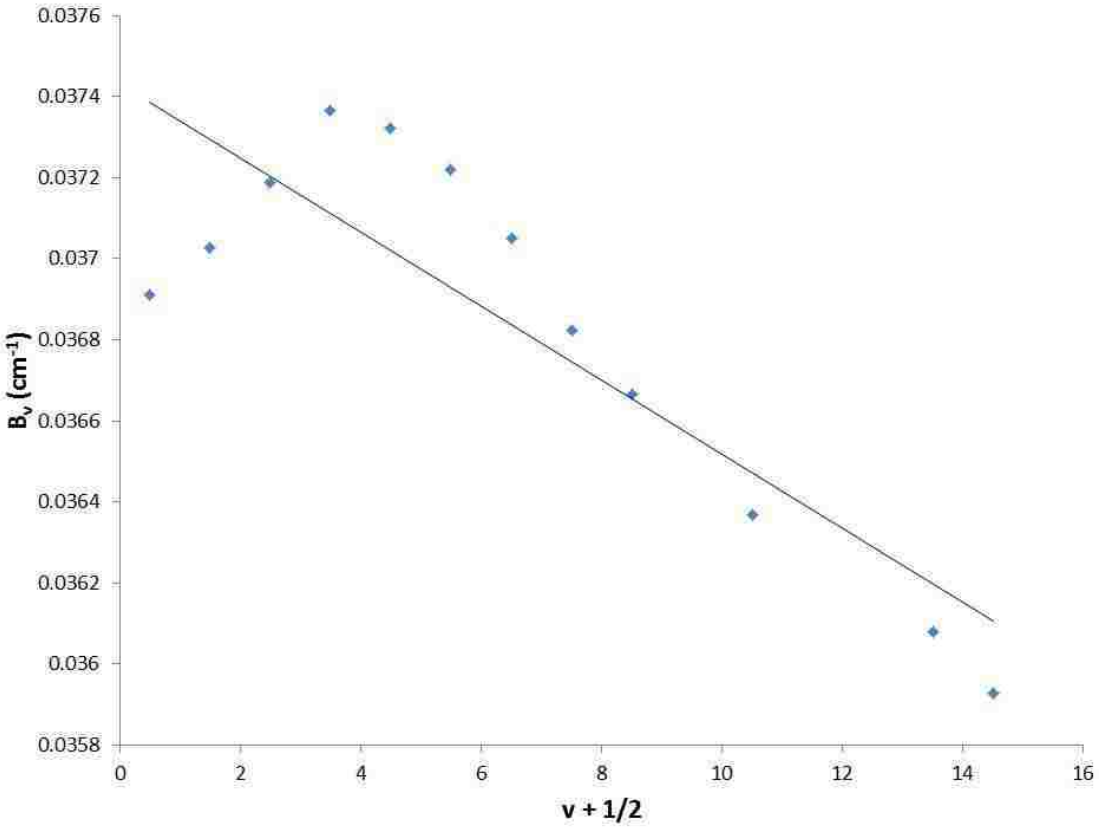

Figure 5.13: Plot of B_v versus $v + \frac{1}{2}$ for vibrational levels of the $12(0^+)$ state along with a linear fit to Eq. (5.4) (with γ_e and higher order terms fixed to zero). It is evident that the constant and linear terms in Eq. (5.4) are not sufficient to reproduce the B_v terms. Error bars associated with the values of B_v are too small to be seen on this plot. The fit yields $B_e = 0.0374 \pm 0.0001$ cm^{-1} and $\alpha_e = (9.1 \pm 1.7) \times 10^{-5}$ cm^{-1}.

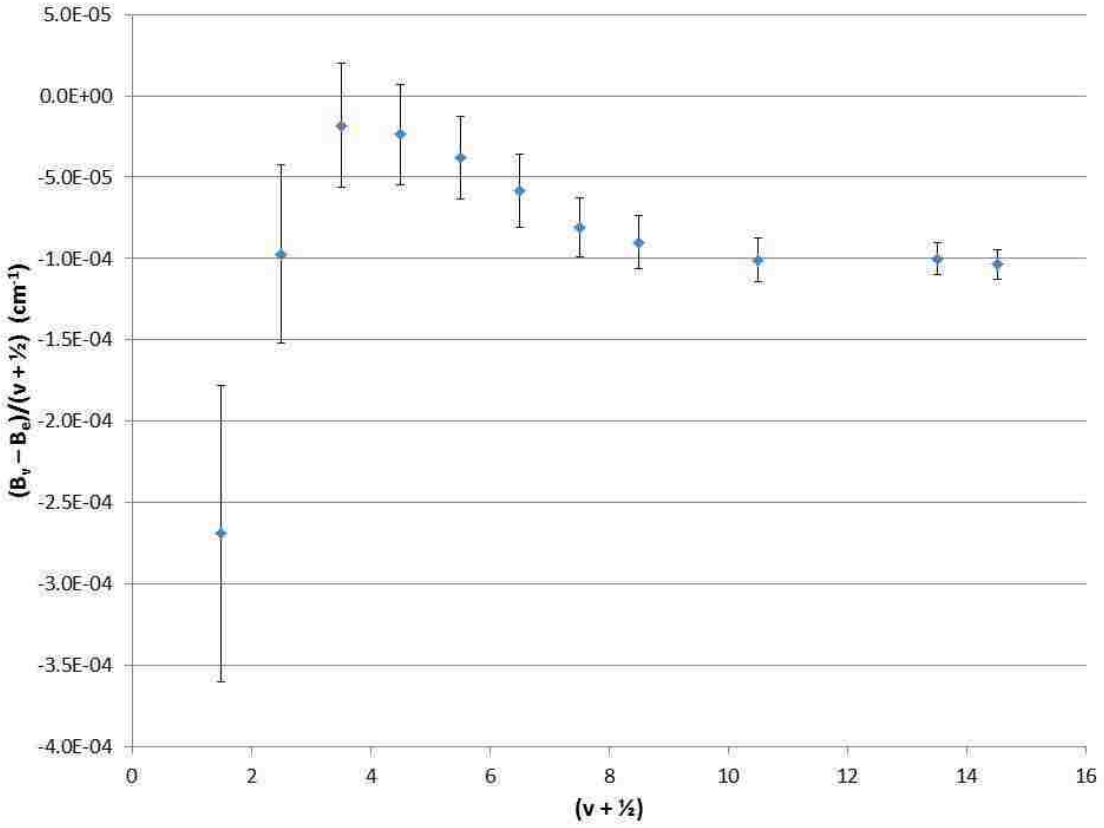

Figure 5.14: Plot of $\frac{B_v - B_e}{v+\frac{1}{2}}$ versus $v + \frac{1}{2}$ for vibrational levels of the $12(0^+)$ state. Values of B_v are taken from Table 5.2 and $B_e = 0.0374 \pm 0.0001$ cm^{-1} was obtained from the fit of B_v values to the linear function $B_v = B_e - \alpha_e(v + \frac{1}{2})$. There is clearly a systematic dependence on $v + \frac{1}{2}$, which implies that more than just the constant and linear terms in Eq. (5.4) are needed to describe B_v.

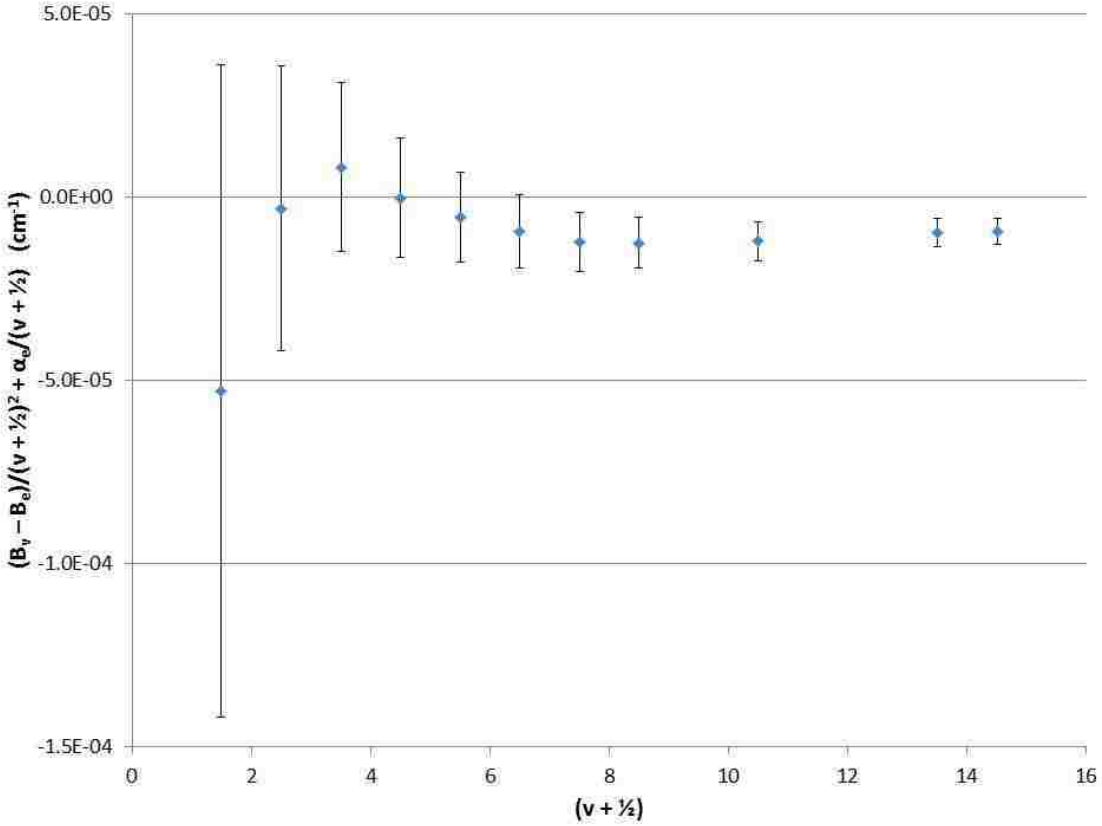

Figure 5.15: Plot of $\frac{B_v - B_e}{(v+\frac{1}{2})^2} + \frac{\alpha_e}{v+\frac{1}{2}}$ versus $v + \frac{1}{2}$ for vibrational levels of the $12(0^+)$ state. Values of B_v are taken from Table 5.2 and $B_e = 0.0370 \pm 0.0001$ cm^{-1} and $\alpha_e = (6 \pm 4) \times 10^{-5}$ cm^{-1} were obtained from the fit of B_v values to the quadratic function $B_v = B_e - \alpha_e(v + \frac{1}{2}) + \gamma_e(v + \frac{1}{2})^2$. There does not seem to be any significant systematic dependence on $v + \frac{1}{2}$, which implies that no terms beyond the constant, linear, and quadratic terms in Eq. (5.4) are needed to describe B_v.

5.3 Dunham coefficients

The program DParFit [21] by Robert Le Roy was used to fit all measured level energies to the global Dunham expansion:

$$E(v, J) = \sum_{i,k} Y_{i,k} \left(v + \frac{1}{2} \right)^i [J(J+1) - \Omega^2]^k. \tag{5.5}$$

This program takes an input file of experimental energies and uncertainties and determines the Dunham coefficients, $Y_{i,k}$, that best reproduce the experimental energies in a least squares sense. The user decides what is the highest value of i used in the fit for each value of k. As described by the analysis presented in Sec. 5.2, the rotational expansion should include terms up to $k = 2$. The centrifugal distortion constant, which is equivalent to $Y_{0,2}$, was fixed at the value $(6.1 \pm 0.7) \times 10^{-8} \text{cm}^{-1}$ as mentioned above. In the expansion of G_v, $Y_{i,0}$, should include terms up to at least $i = 2$. However, we found that including terms up to $i = 4$ significantly improved the fit to the experimental energies. Finally, in the expansion of B_v, $Y_{i,1}$, should include terms up to at least $i = 2$.

Dunham coefficients were fit to 214 level energies for the $12(0^+)$ state which spanned a range of vibrational levels $v = 0 - 14$. The best fit set of Dunham coefficients is listed in Table 5.4. These coefficients reproduce the level energies with an root mean square (RMS) deviation of 0.38 cm^{-1}. Figure 5.16 shows a plot of the difference between the observed energies and the ones calculated with the Dunham coefficients.

5.4 Potential Energy Curve

5.4.1 RKR Potential

Once we determined a reasonable set of Dunham coefficients, we used the coefficients to construct an NaCs $12(0^+)$ electronic potential energy curve using the Rydberg-Klein-Rees method [43, 44, 45, 46]. For this process we used the computer program

	$k=0$	1	2
$i=0$	24671.019 ± 0.57	$(3.683 \pm 0.021) \times 10^{-2}$	-6.14×10^{-8} (fixed)
1	44.24 ± 0.42	$(1.95 \pm 0.84) \times 10^{-4}$	-
2	2.694 ± 0.11	$(-2.41 \pm 0.68) \times 10^{-5}$	-
3	-0.273417 ± 0.011	-	-
4	$(8.57 \pm 0.37) \times 10^{-3}$	-	-

Table 5.4: NaCs $12(0^+)$ Dunham coefficients. All paramaters have units of cm^{-1}. More digits are reported than are statistically significant so that the coefficients can appropriately reproduce experimental energies.

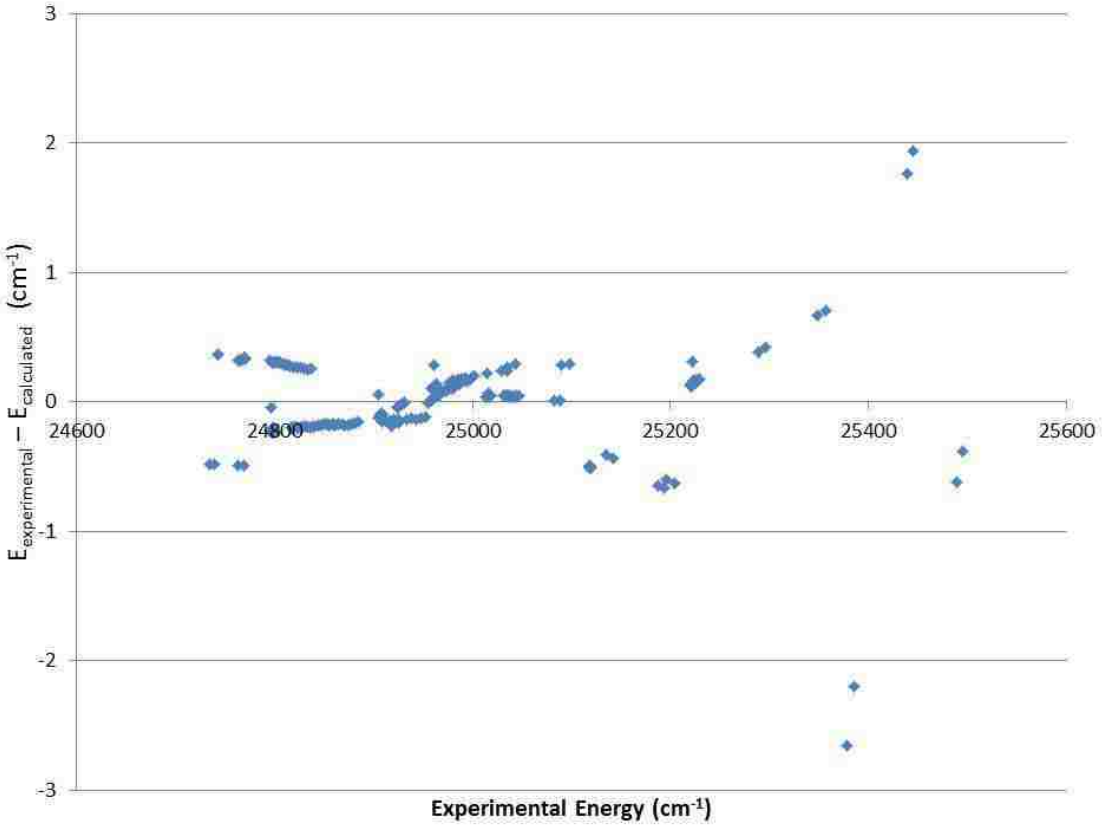

Figure 5.16: Differences of experimental energies and energies calculated using the Dunham coefficients listed in Table 5.4.

RKR1 2.0, developed by Robert Le Roy [1]. The program accepts spectroscopic constants or Dunham coefficients as input and uses them to evaluate the following two integrals:

$$R_2(v) - R_1(v) = 2\sqrt{\frac{C_u}{\mu}} \int_{v_{\min}}^{v} \frac{dv'}{[G_v - G_{v'}]^{\frac{1}{2}}} \equiv 2f, \tag{5.6}$$

and

$$\frac{1}{R_1(v)} - \frac{1}{R_2(v)} = 2\sqrt{\frac{\mu}{C_u}} \int_{v_{\min}}^{v} \frac{B_{v'}dv'}{[G_v - G_{v'}]^{\frac{1}{2}}} \equiv 2g. \tag{5.7}$$

In these equations $R_1(v)$ and $R_2(v)$ represent the turning points for the vibrational level v, G_v and B_v are the rotationless vibrational constant and rotational constant, respectively, for vibrational level v, μ is the reduced mass, and C_u is a constant equal to $\frac{\hbar^2}{2}$. The integrals are evaluated semi-classically, treating v as a continuous variable. The integrals are evaluated from $v' = v_{\min} = -\frac{1}{2}$, which takes into account the zero point energy of vibration, to $v' = v$, the level of interest. The user can select a size for dv', which sets the grid spacing for evaluation of these integrals. In addition, integer (and possibly non-integer) values of v are specified for the calculations such that the potential is accurately mapped over an energy range corresponding to the region of measured data. These two integrals give two equations, for a given v, that can be solved simultaneously to give turning points $R_1(v)$ and $R_2(v)$. Since these turning points are calculated as a function of rotationless vibrational level, and hence of energy, they can be interpolated to map out the potential energy curve. The RKR potential turning points that we have determined for the NaCs $12(0^+)$ state, as a function of v, are given in Table 5.5.

Figure 5.17 shows a plot of the RKR potential obtained from the Dunham coefficients listed in Table 5.4, along with the theoretically calculated $12(0^+)$ potential from [12]. When comparing the level energies calculated using this RKR potential with measured energy levels, we obtain an RMS deviation of 0.65 cm^{-1} for $v = 0-14$ vibrational levels. Figure 5.18 shows a plot of the difference between the observed energies and the ones calculated with LEVEL 8.0 [25] using the RKR potential.

v	R_1 (Å)	R_2 (Å)	Energy (cm^{-1})
-0.4	4.7447410889	4.9202362886	4.4507
-0.2	4.6818452619	4.9829621785	13.5071
0	4.6396580163	5.0250162234	22.7599
0.2	4.6061539547	5.0584362914	32.1963
0.4	4.5777813483	5.0867850321	41.8044
0.6	4.5528928465	5.1117194221	51.5724
0.8	4.5305601693	5.1341762800	61.4886
1	4.5101977177	5.1547488241	71.5421
1.2	4.4914075702	5.1738418139	81.7219
1.4	4.4739046972	5.1917464495	92.0177
1.6	4.4574767441	5.2086806827	102.4191
1.8	4.4419606147	5.2248127126	112.9164
2	4.4272279782	5.2402755431	123.5001
2.2	4.4131758566	5.2551764510	134.1610
2.4	4.3997202659	5.2696033906	144.8903
2.6	4.3867917793	5.2836294690	155.6794
2.8	4.3743323456	5.2973161597	166.5202
3	4.3622929548	5.3107156643	177.4048
3.2	4.3506318896	5.3238726832	188.3256
3.4	4.3393133947	5.3368257648	199.2755
3.6	4.3283066470	5.3496083505	210.2476
3.8	4.3175849494	5.3622495926	221.2354
4	4.3071250916	5.3747750031	232.2326
4.2	4.2969068384	5.3872069726	243.2334
4.4	4.2869125161	5.3995651878	254.2321
4.6	4.2771266764	5.4118669716	265.2237
5	4.2581281687	5.4363603284	287.1658
6	4.2135249311	5.4974657532	341.5923
7	4.1724675803	5.5590621112	395.1057
8	4.1346944715	5.6214178398	447.5052
9	4.1003799336	5.6842122943	498.7958
10	4.0700518128	5.7465776176	549.1880
11	4.0445157829	5.8071477571	599.0983
12	4.0247510099	5.8641739909	649.1484
13	4.0117636136	5.9157421724	700.1662
14	4.0064124165	5.9600803601	753.1850

Table 5.5: NaCs 12(0^+) RKR potential energy curve determined in this work. To obtain the total absolute potential curve, T_e = 24671.019 cm^{-1} must be added to each point.

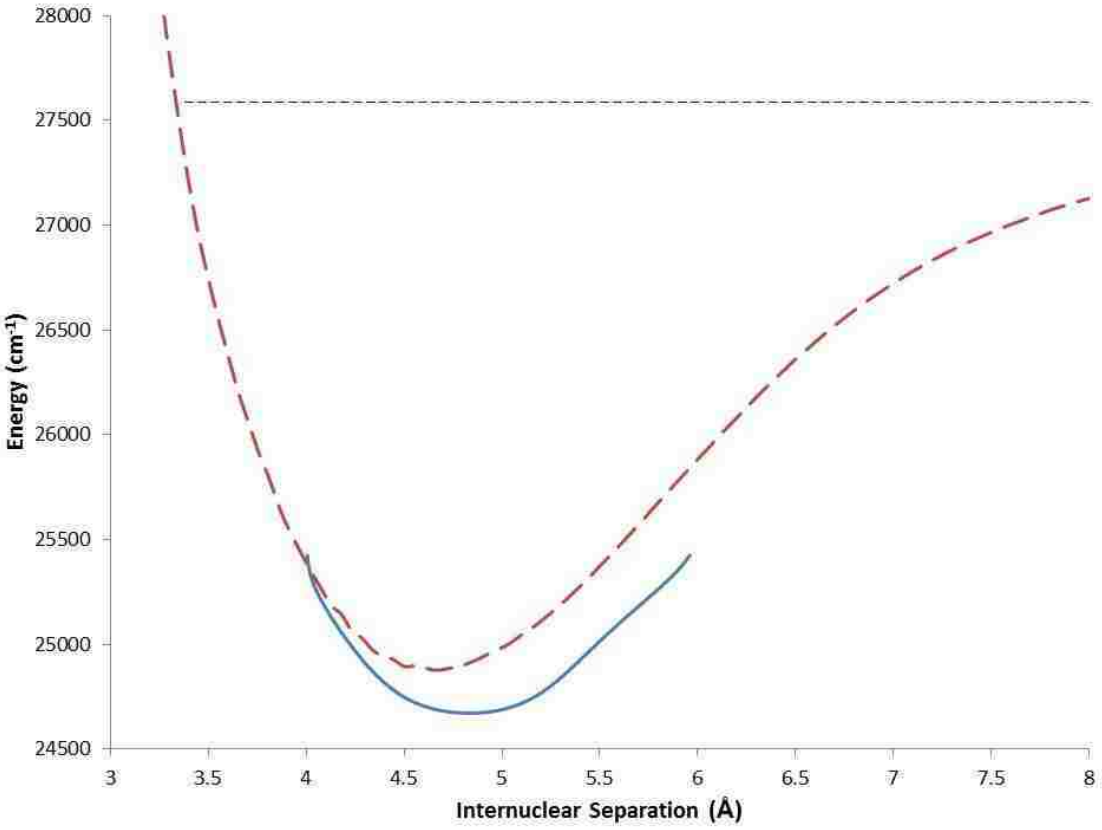

Figure 5.17: RKR potential (solid curve) calculated using the Dunham coefficients in Table 5.4. The theoretically calculated $12(0^+)$ potential curve (dashed curve) from [12] is also plotted for comparision with the horizontal dashed line corresponding to the $Na(3S_{1/2})$ + $Cs(6D_{5/2})$ atomic asymptote.

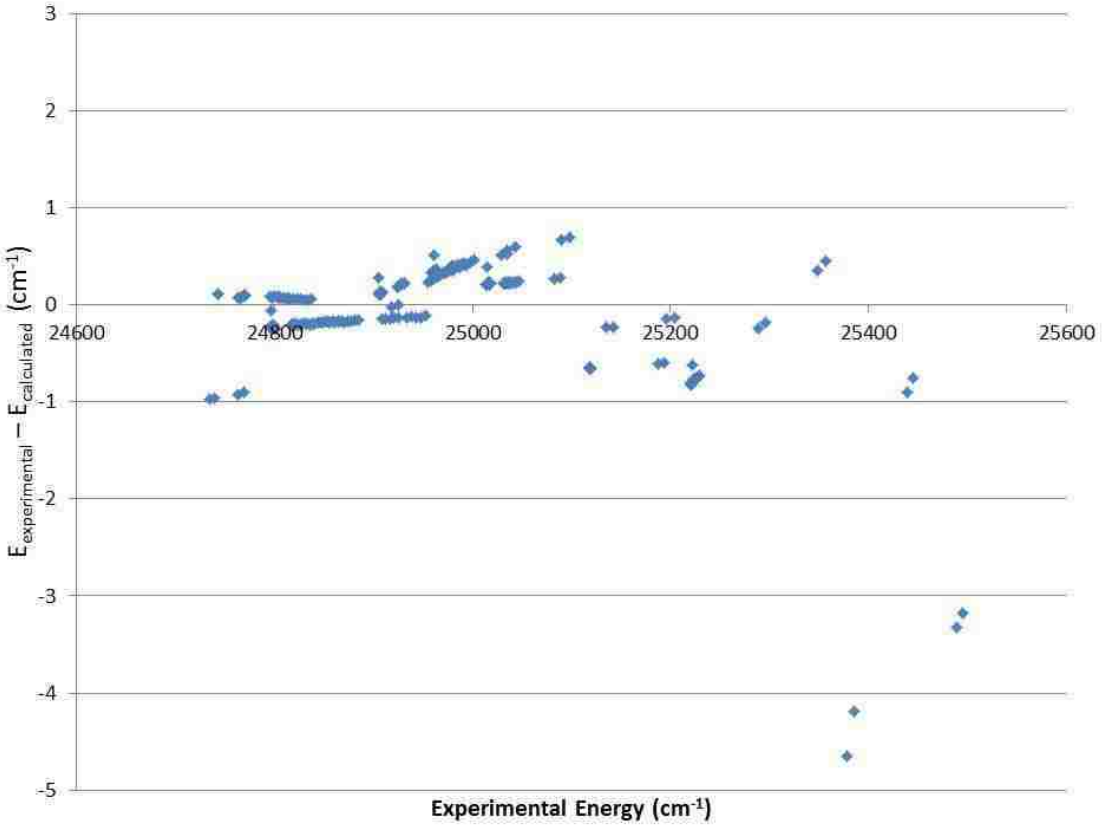

Figure 5.18: Differences of experimental level energies and energies calculated for the RKR potential determined in this work.

This RKR potential was used as the starting point to apply the Inverted Perturbation Approach (IPA) method to obtain a more accurate potential (as evidenced by better agreement with measured data).

5.4.2 IPA potential

Our calculated NaCs $12(0^+)$ RKR potential presented in the previous section is not of sufficient quality to reproduce the level energies to within the accuracy with which they were measured. To obtain a "better" potential, we used the IPA method [47] to adjust the potential so that it reproduces the level energies more accurately. To begin the process, the IPA program requires a potential, $V_0(R)$, which reproduces level energies reasonably well, to use as an initial guess. The RKR potential described in the previous section is sufficient for this purpose. A correction term, $\delta V(R)$, is then added to the initial potential. The Schrödinger equation is solved for this new potential, $V(R) = V_0(R) + \delta V(R)$, using first-order perturbation theory. Once the correction potential is determined, the energies of the new total potentials are evaluated exactly. This process is iterated until level energies calculated using the new $V(R)$, agree with measured level energies in a least squares sense. For each iteration, $V(R)$ from the previous round of fitting becoming the new initial potential for the next round of fitting.

In practice, we use a modified version of the IPA program written by Pashov *et al.* [2]. Pashov's IPA program requires several input files for each iteration. One file includes experimental energies for measured rovibrational levels along with experimental uncertainties. Another contains the initial potential energy curve as a function of internuclear separation to be used for that iteration. There is also an input file containing level energies calculated from xLEVEL using the initial potential. xLEVEL is a version of LEVEL written by Robert Le Roy [25], which has been modified by A. P. Hickman (details in Ref. [38]) to output level energies and wavefunctions for use as input to IPA. Finally, there is one additional input file that allows the user to describe how the $\delta V(R)$ function is to be varied. The user can choose the number of equally spaced points, and whether or not to vary each

point individually. After each iteration of the IPA program, xLEVEL must be run using the new IPA potential to obtain new energies and wavefunctions, and the new potential must replace the old potential as the initial guess for the next round. The number of grid points and whether or not to vary $\delta V(R)$ or to fix $\delta V(R) = 0$ at each individual grid point are also chosen by the user for each iteration.

The process by which the IPA program determines the correction potential, $\delta V(R) = 0$, is detailed in Ref. [2] as follows. The program treats the correction potential using first order perturbation theory, so that the correction to the energies of the initial potential, $\{E^0_{vJ}\}$ are given by

$$\delta E_{vJ} = \langle \xi^0_{vJ} | \, \delta V(R) \, | \xi^0_{vJ} \rangle \, , \tag{5.8}$$

where ξ^0_{vJ} is the vibrational wavefuntion associated with the level (v, J) of the inital potential. The correction potential is expressed as an expansion over a set of basis functions $\{f_i(R)\}$:

$$\delta V(R) = \sum_i c_i f_i(R), \tag{5.9}$$

where $\{c_i\}$ are the expansion coefficients. Using this expansion, the energy corrections become

$$\delta E_{vJ} = \sum_i c_i \, \langle \xi^0_{vJ} | \, f_i(R) \, | \xi^0_{vJ} \rangle = \sum_i c_i K_{i,vJ}. \tag{5.10}$$

The problem can now be expressed as a matrix equation:

$$\delta \mathbf{E} = \mathbf{K} \cdot \mathbf{c}. \tag{5.11}$$

The program determines the set of coefficients $\{c_i\}$ by replacing the energy correction with the known differences between the initial potential energies, $\{E^0_{vJ}\}$, and the known experimental energies, $\{E^{\rm exp}_{vJ}\}$, called $d\mathbf{E}$. Since $\mathbf{K}$ is a matrix of known $K_{i,vJ}$ coefficients calculated from the initial potential wavefunctions, the only unknown quantities are the expansion coefficients for the correction potential, $\{c_i\}$. Using the determined set of $\{c_i\}$, Eq. (5.11) is evaluated again and $d\mathbf{E}$ is compared to

the calculated $\delta\mathbf{E}$. The coefficients are varied such that the difference between the experimental $d\mathbf{E}$ and the calculated $\delta\mathbf{E}$ is minimized in a least squares sense.

Use of a finer and finer grid of points will continue to reduce discrepancies between calculated and measured energies, but at the expense of unphysical wiggles in the potential. The "best" fit IPA potential is determined by us as a trade-off between accurate reproduction of level energies while still maintaining a reasonably smooth potential. Using these criteria, we determined our best fit IPA potential for the NaCs $12(0^+)$ state, which is shown in Fig. 5.19 and listed in Table 5.6. The initial RKR potential was calculated with turning points up to $v = 14$. However, the levels for v=12, 13, and 14 appear to be strongly perturbed so they were not used for the fitting of the IPA potential. The IPA curve determined here reproduces measured level energies for $v = 0 - 10$ with an RMS deviation of 0.034 cm^{-1}. Figure 5.20 shows a plot of the differences between the observed energies and the ones calculated with the IPA potential. When comparing the IPA potential to the theoretical or RKR potentials, it is clear that the IPA potential is not a simple smooth curve. Some "wiggles" in the inner and outer IPA potential walls appear to be necessary in order to accurately reproduce the level energies. This is a result of the assumption we use that all the measured energy levels belonging to the $12(0^+)$ state can be described by a single potential energy curve. In reality, there are other NaCs electronic state potentials in this energy region that can interact with one another to influence the patterns of rovibrational level energies. Most prominently, the $11(0^+)$ electronic state is a state that was mapped out in a similar process in our lab by Ashman *et al.* [3]. The IPA potential for the $11(0^+)$ state shows similar fluctuations in the outer wall. Chapter 6 will describe in detail how these two states probably interact with each other and how this influences not only the level energies, but also the vibrational wavefunctions, and hence the resolved fluorescence spectra associated with these states.

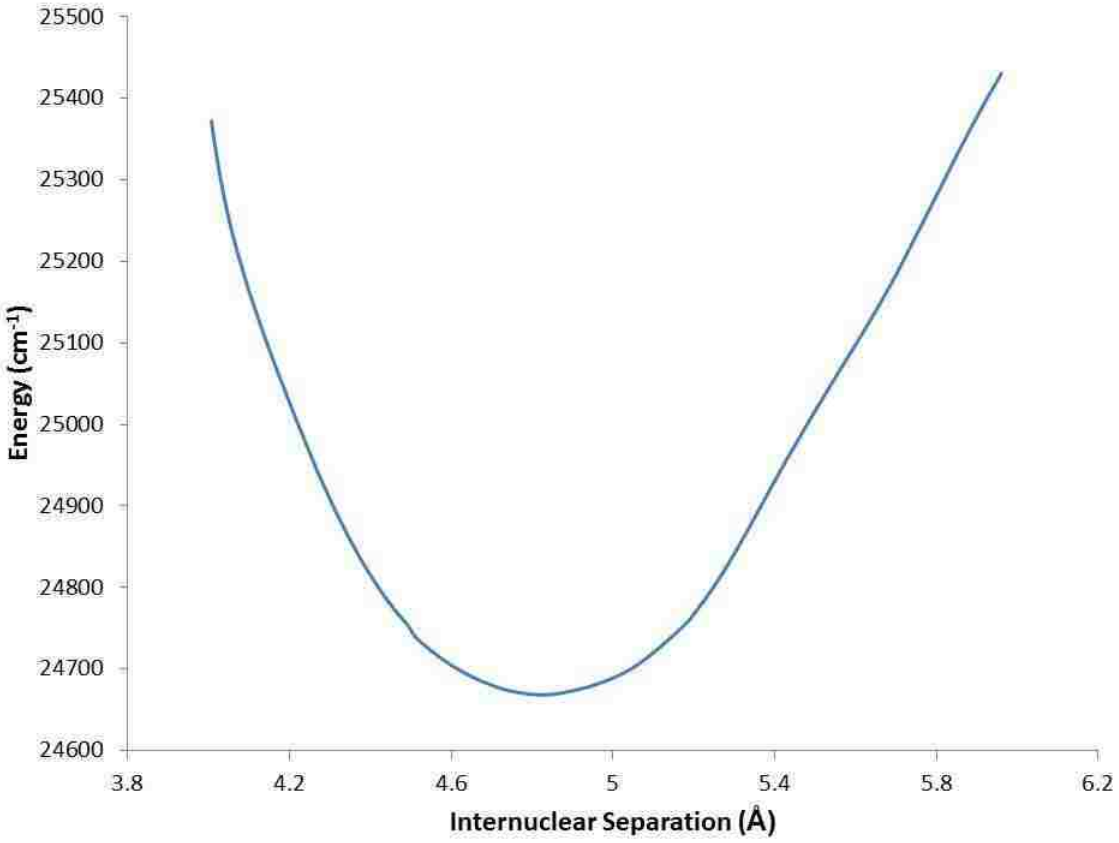

Figure 5.19: IPA potential for the NaCs 12(0^+) state determined in this work.

R (Å)	Energy (cm^-1)	R (Å)	Energy (cm^-1)
4.0066	25372.1902	4.9204	24675.7057
4.0120	25353.8388	4.9832	24685.5888
4.0249	25313.6700	5.0252	24694.8413
4.0447	25262.8959	5.0586	24704.7210
4.0702	25212.3998	5.0870	24715.0111
4.1006	25162.1021	5.1119	24725.0570
4.1349	25112.1539	5.1344	24734.6046
4.1727	25061.5645	5.1549	24743.7734
4.2137	25009.3151	5.1740	24752.9083
4.2583	24955.1027	5.1919	24762.1829
4.2773	24933.1528	5.2089	24773.3190
4.2871	24922.2078	5.2250	24783.9433
4.2971	24911.3020	5.2405	24794.7367
4.3073	24900.4408	5.2554	24805.6899
4.3178	24889.6251	5.2698	24816.7863
4.3285	24878.8374	5.2838	24828.0196
4.3395	24868.0960	5.2975	24839.3859
4.3508	24857.3999	5.3109	24850.8537
4.3625	24846.7576	5.3241	24862.3620
4.3745	24836.1676	5.3370	24873.8740
4.3870	24825.6479	5.3498	24885.3510
4.3999	24815.1958	5.3624	24896.7747
4.4134	24804.8180	5.3750	24908.1083
4.4274	24794.5197	5.3874	24919.3482
4.4422	24784.2999	5.3998	24930.4736
4.4577	24774.1712	5.4121	24941.4632
4.4741	24764.1546	5.4366	24962.9916
4.4916	24754.2386	5.4977	25014.7877
4.5104	24739.9024	5.5593	25065.4399
4.5308	24730.5804	5.6216	25115.7452
4.5531	24721.3148	5.6844	25169.3976
4.5780	24712.0850	5.7468	25228.9479
4.6064	24702.7850	5.8073	25288.2247
4.6399	24693.3421	5.8644	25344.1242
4.6820	24683.7029	5.9159	25391.9912
4.7449	24673.2199	5.9603	25430.4357
4.8327	24668.2803		

Table 5.6: NaCs 12(0^+) IPA potential energy curve determined in this work.

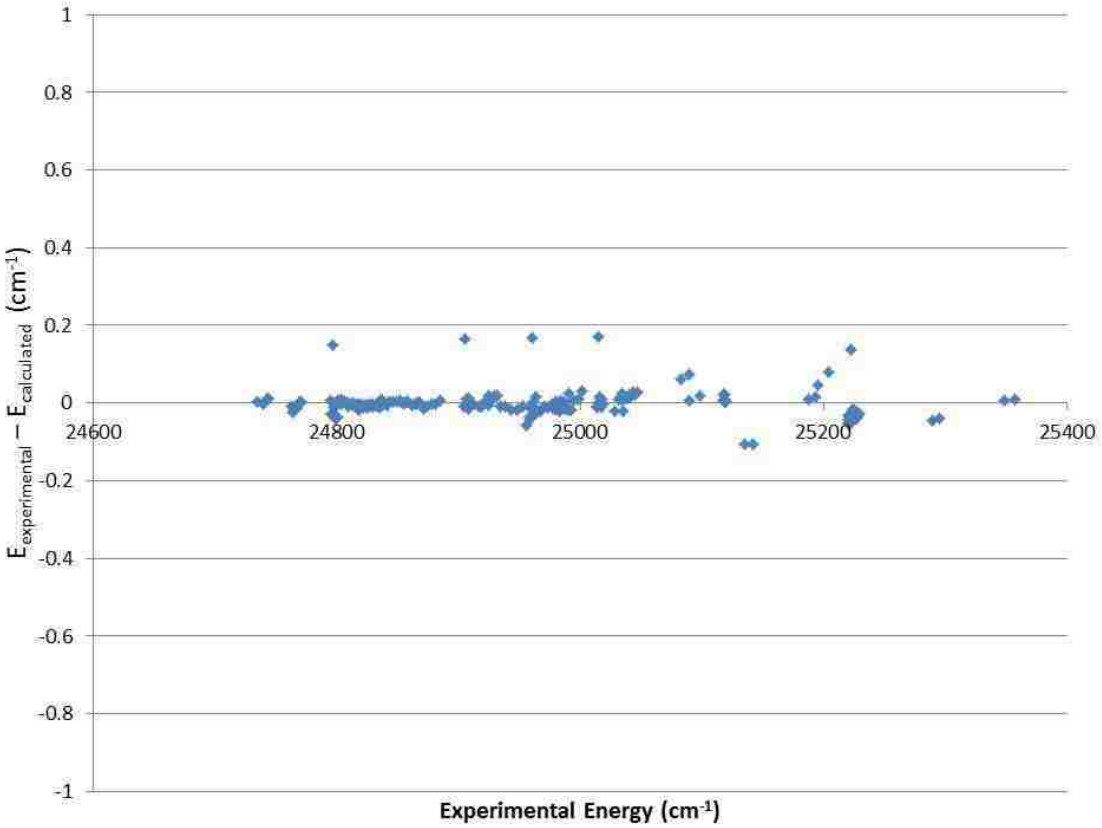

Figure 5.20: Differences of experimental level energies and energies calculated with the best fit IPA potential.

Chapter 6

Interactions between the NaCs $11(0^+)$ and $12(0^+)$ States

Although the $12(0^+)$ electronic state is believed to have predominantly singlet character, resolved spectra from this electronic state show strong bound-free emission to the $1(a)^3\Sigma^+$ electronic state. We believe this is due to coupling with the $11(0^+)$ state which has predominantly triplet character. However, spin-orbit coupling between these two states is not enough to describe and simulate the bound-free emission spectra from the $12(0^+)$ state. This chapter describes a model for certain types of interactions between electronic states that we believe to be responsible for the unique intensity distributions of the $12(0^+)$ bound-free emission. The model and method used to simulate the bound-free emission are explained. Results of fitting these simulations to experimental spectra will then be presented and interpreted.

6.1 Types of Interactions

There are several types of interactions that can cause coupling between the various rovibrational levels of the electronic states of a diatomic molecule. Experimentally, we measure the level energies that nature determines including all interactions. However, if we would like to model the spectra that we observe, we need to understand

specifically how the interactions affect the basic Hamiltonian presented in Section 2.1. Theoretically, coupling between states of the molecule arises because of terms that are neglected in the Hamiltonian. The four main types of perturbations that can arise are [19]: electrostatic perturbations due to terms left out of the electronic part of the Hamiltonian; nonadiabatic perturbations due to terms left out of the nuclear kinetic energy part of the Hamiltonian; rotational perturbations due to the dropped terms that are described at the end of Sec. 2.2; and spin-orbit perturbations due to relativistic terms that have been neglected because electron spin has been left out of the Hamiltonian. The two relevant interactions that we believe are responsible for coupling the $11(0^+)$ and $12(0^+)$ states are spin-orbit and nonadiabatic perturbations. These two perturbations are described in more detail below.

6.1.1 Spin-Orbit Interactions

In order to incorporate relativistic effects into the Hamiltonian, we need to take into account the effects that the spin of the electron has on the energy of the molecule. The dominant spin interaction is between the spin magnetic dipole moment of the electron and the magnetic field generated by the orbital angular momentum of the electron as it orbits the nuclei. In molecules, there are also effects due to the interaction of the electron spin with nuclear rotation and with other electronic spins. However, these effects are much smaller than the spin-orbit terms and generally can be neglected. The molecular spin-orbit operator is [19]:

$$\boldsymbol{H}_{\mathrm{SO}} = \frac{\alpha^2}{2}\sum_{i=1}^{N}\left(\frac{Z_{\mathrm{A}}}{r_{i\mathrm{A}}^3}\boldsymbol{l}_{i\mathrm{A}}\cdot\boldsymbol{s}_i + \frac{Z_{\mathrm{B}}}{r_{i\mathrm{B}}^3}\boldsymbol{l}_{i\mathrm{B}}\cdot\boldsymbol{s}_i\right) - \frac{\alpha^2}{2}\sum_{i=1}^{N}\sum_{j>i}^{N}\frac{1}{r_{ij}^3}(\boldsymbol{r}_{ij}\times\boldsymbol{p}_i)\cdot(\boldsymbol{s}_i+2\boldsymbol{s}_j). \quad (6.1)$$

Here α is the fine structure constant, $\alpha = e^2/\hbar c = 137.036$, $\boldsymbol{l}_{i\mathrm{A}}$ is the angular momentum of electron i with respect to nucleus A, $\boldsymbol{s}_i$ is the spin angular momentum of electron i, $(\boldsymbol{r}_{ij}\times\boldsymbol{p}_i)$ is the orbital angular momentum of electron i about electron j, and $\boldsymbol{p}_i$ is the momentum of electron i with respect to molecule fixed coordinates. The first term describes the sum of the individual electron spins interacting with their orbital angular momenta about each nucleus. The second term describes the

sum of the individual electron spins interacting with the orbital angular momentum of every other electron. Veseth [48] shows that the two-electron part of Eq. (6.1) can be incorporated into the one-electron part as a screening effect. This lets us write the spin-orbit Hamiltonian in a more compact form:

$$\boldsymbol{H}_{\mathrm{SO}} = \sum_i \hat{a}_i \boldsymbol{l}_i \cdot \boldsymbol{s}_i, \tag{6.2}$$

where

$$\hat{a}_i \boldsymbol{l}_i = \sum_K \frac{\alpha^2}{2} \frac{Z_{\mathrm{eff},K}}{r_{iK}^3} \boldsymbol{l}_{iK}, \tag{6.3}$$

and $Z_{\mathrm{eff},K}$ is the effective charge of nucleus K. Expanding the $\boldsymbol{l}_i \cdot \boldsymbol{s}_i$ term into components we find

$$\boldsymbol{l}_i \cdot \boldsymbol{s}_i = \boldsymbol{l}_{iz} \cdot \boldsymbol{s}_{iz} + \frac{1}{2}(\boldsymbol{l}_i^+ \boldsymbol{s}_i^- + \boldsymbol{l}_i^- \boldsymbol{s}_i^+). \tag{6.4}$$

This gives two terms that lead to spin-orbit coupling between electronic states. The $\boldsymbol{l}_{iz} \cdot \boldsymbol{s}_{iz}$ term couples states with the same Λ and Σ quantum numbers. The $(\boldsymbol{l}_i^+ \boldsymbol{s}_i^- + \boldsymbol{l}_i^- \boldsymbol{s}_i^+)$ term, which is the term most relevant for the present work, couples states where $\Delta\Lambda = -\Delta\Sigma = \pm 1$. This is a very common interaction that causes coupling between $^3\Pi$ and $^1\Sigma$ states in alkali diatomics. To summarize, the relevant selection rules for states coupling by this second spin-orbit interaction term are [19]:

$$\Delta J = 0,\ \Delta\Omega = 0,\ \Delta S = \pm 1,\ \Delta\Lambda = -\Delta\Sigma = \pm 1. \tag{6.5}$$

It is possible that nonrelativistic potential curves corresponding to states with the same Ω quantum number can cross as shown in Fig. 6.1. Including the relativistic spin-orbit terms in the Hamiltonian results in states where Ω is the only good quantum number and the potentials do not cross. The most common example in the alkali diatomic molecules is the spin-orbit coupling of the $A^1\Sigma^+$ and $b^3\Pi_0$ electronic states. When the spin-orbit coupling is taken into account, Hund's case (a) notation no longer applies because Λ and Σ can no longer be considered good quantum

numbers. Instead the electronic states are described only by their Ω quantum number, and hence they are referred to as the $2(0^+)$ and $3(0^+)$ electronic states. Figure 6.1 shows two sets of theoretically calculated electronic potential curves for NaCs. The dashed lines are potentials calculated without the spin-orbit effect [49] which are designated by Hund's case (a) notation. Since these curves have different electronic symmetry with respect to the non-relativistic Hamiltonian, they are allowed to cross one another. Solid curves represent potentials calculated with the spin-orbit effect [12]. These potentials are designated by Hund's case (c) notation. Note that the spin-orbit interaction, like all perturbations, should push the potentials apart at each value of R. The fact that this is not demonstrated by the potentials shown in Fig. 6.1 is due to different basis sets being used in the two calculations of Refs. [49] and [12]. The spin-orbit interaction is particularly important because it causes mixing between the singlet and triplet electronic states. This mixing leads to rovibrational levels that have both singlet and triplet character, which allows the $\Delta S = 0$ selection rule on electronic transitions to be circumvented. Since the ground $1(X)^1\Sigma^+$ state of all alkali molecules is a spin singlet, the only way to access upper triplet states is through mixed singlet-triplet levels, which in this context are called "window levels". In NaCs, the spin-orbit effect is so strong that nearly every $2(A)^1\Sigma^+$ rotational level is significantly perturbed by rotational levels belonging to several vibrational levels of the $1(b)^3\Pi_{0^+}$ state. This leads to a global mixture, which results in every $2(A)^1\Sigma^+$ rovibrational level having significant triplet amplitude in addition to its singlet amplitude.

6.1.2 Nonadiabatic Interactions

As mentioned in Sec. 2.1, Eq. (2.10) is valid when the solutions $[\Phi_n(\vec{r_i};\vec{R})]$ to the electronic Schrödinger equation vary slowly with internuclear distance. When the Born-Oppenheimer approximation breaks down, off-diagonal elements of the neglected nuclear kinetic energy terms couple electronic states of identical symmetry; this is called nonadiabatic coupling. The potentials calculated without consideration of these off-diagonal terms can have avoided crossings and are referred to as

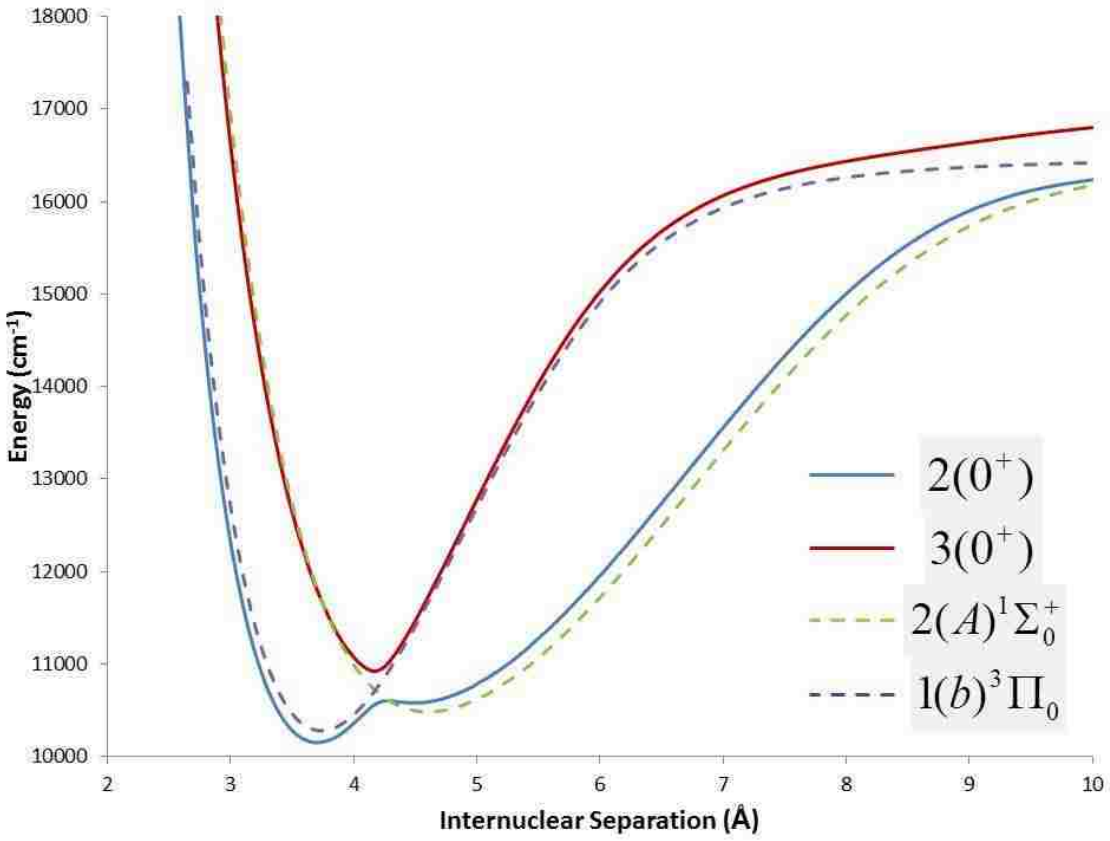

Figure 6.1: Theoretical calculations of electronic potential curves with and without the spin-orbit effect. Dashed curves represent potentials calculated without the spin-orbit effect [49] which are designated by Hund's case (a) notation. Solid curves represent potentials calculated with the spin-orbit effect [12] which are designated by Hund's case (c) notation. Perturbations should result in energies that are farther apart than before incorporating the interaction. However, this is not the case at all values of R for the potentials shown here. For example, the outer wall of the $2(0^+)$ state lies above that of the nonrelativistic $2(A)^1\Sigma^+$ state. This is a result of different theoretical basis sets used in the two calculations.

adiabatic potentials. Avoided crossings typically correspond to sudden changes in the electronic wavefunction over small ranges of R. Figure 6.2 shows a close up of the potential energy curves for the $3^3\Pi$ and $4^3\Pi$ electronic states of NaK. In cases such as this, it is sometimes convenient to determine a new set of solutions to the electronic part of the the Schrödinger equation such that the electronic wavefunction varies as little as possible with R. These potentials, which might cross each other, are known as diabatic potentials. A diabatic curve represents a state with the same electronic character for a large range of R. This representation is found by determining a new set of electronic wavefunctions which are diagonalized with respect to the nuclear kinetic energy term but not necessarily diagonalized with respect to the full electronic Hamiltonian.

The form of the off-diagonal matrix elements due to nonadiabatic coupling are found by looking at the matrix elements of the nuclear kinetic energy operator:

$$\hat{T}_{\text{nucl}} = -\frac{\hbar^2}{2\mu R^2}\left[\frac{\partial}{\partial R}\left(R^2\frac{\partial}{\partial R}\right)\right] + \frac{\boldsymbol{R}^2}{2\mu R^2}. \tag{6.6}$$

The second term in this expression involves the angular nuclear coordinates and describes the rotational nuclear kinetic energy. [Note again the possibly confusing notation. Here R is the internuclear separation coordinate while $\boldsymbol{R}^2$ is the operator representing the square of the nuclear rotational angular momentum.] The matrix elements of this second term can be evaluated separately and result in terms responsible for rotational coupling as described at the end of Section 2.2. In regard to nonadibatic coupling, this term can be ignored. We simplify the radial part of the nuclear kinetic energy operator using the chain rule:

$$\hat{T}_{\text{radial}} = -\frac{\hbar^2}{2\mu R^2}\left[2R\frac{\partial}{\partial R} + R^2\frac{\partial^2}{\partial R^2}\right] = -\frac{\hbar^2}{2\mu}\left[\frac{\partial^2}{\partial R^2} + \frac{2}{R}\frac{\partial}{\partial R}\right]. \tag{6.7}$$

Next, we determine the off-diagonal matrix elements that couple levels of two adiabatic electronic states. Recall that the total wavefunction, $\Psi(\vec{r}, R)$, excluding rotation, of the molecule in a particular rovibrational level, is a product function such that

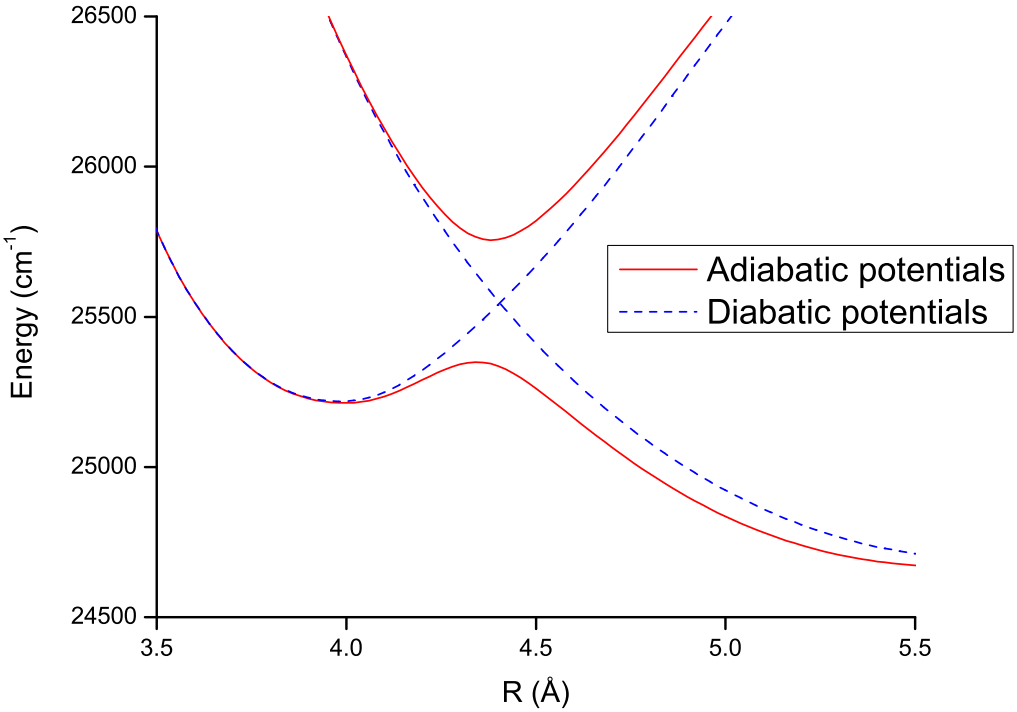

Figure 6.2: Adiabatic and diabatic states corresponding to the $3^3\Pi$ and $4^3\Pi$ electronic states of NaK. Figure reprinted from Ref. [50].

$$\Psi^{\rm ad}(\vec{r},R) = \chi(R)\Phi^{\rm ad}(\vec{r},R), \tag{6.8}$$

with

$$\int d^3r \Phi_a^{*\rm ad}\Phi_b^{\rm ad} = \delta_{ab}. \tag{6.9}$$

Here $\chi(R)$ is the nuclear vibrational wavefunction, $\Phi_a^{\rm ad}(\vec{q},R)$ and $\Phi_b^{\rm ad}(\vec{q},R)$ are the adiabatic electronic wavefunctions, and δ_{ab} is the Kronecker delta.

The matrix element of Eq. (6.7) is given by

$$\begin{aligned}\langle\Psi_1^{\rm ad}|\,\hat{T}_{\rm radial}\,|\Psi_2^{\rm ad}\rangle &= -\frac{\hbar^2}{2\mu}\int\int R^2 dR d^3r \chi_1^* \Phi_1^{*\rm ad}\left[\frac{\partial^2(\chi_2\Phi_2^{\rm ad})}{\partial R^2} + \frac{2}{R}\frac{\partial(\chi_2\Phi_2^{\rm ad})}{\partial R}\right] \\ &= -\frac{\hbar^2}{2\mu}\int\int R^2 dR d^3r \chi_1^* \Phi_1^{*\rm ad}\left[\left(\chi_2\frac{\partial^2\Phi_2^{\rm ad}}{\partial R^2} + \frac{d^2\chi_2}{dR^2}\Phi_2^{\rm ad} + 2\frac{d\chi_2}{dR}\frac{\partial\Phi_2^{\rm ad}}{\partial R}\right)\right. \\ &\left. + \left(\frac{2}{R}\chi_2\frac{\partial\Phi_2^{\rm ad}}{\partial R} + \frac{2}{R}\frac{d\chi_2}{dR}\Phi_2^{\rm ad}\right)\right]. \end{aligned} \tag{6.10}$$

Here d^3r indicates an integral over all electronic coordinates, while R^2dR indicates an integral over only the radial nuclear coordinate. The integral over angular nuclear coordinates is not included here but yields a factor of one for states of the same J. The second term on the second line and the second term on the last line of Eq. (6.10) are zero due to the orthogonality of the electron wavefunctions expressed in Eq. (6.9). We rewrite the vibrational wavefunction such that

$$\chi(R) = \frac{\xi(R)}{R}. \tag{6.11}$$

The functions $\chi(R)$ are normalized with respect to R^2dR, while the functions $\xi(R)$ are normalized with respect to dR.

With these substitutions the matrix element becomes

$$\langle \Psi_1^{\rm ad} | \, \hat{T}_{\rm radial} \, | \Psi_2^{\rm ad} \rangle = -\frac{\hbar^2}{2\mu} \int\int R^2 dR d^3r \left[\frac{\xi_1^* \xi_2}{R^2} \Phi_1^{*\rm ad} \frac{\partial^2 \Phi_2^{\rm ad}}{\partial R^2} + \frac{2\xi_1^*}{R} \frac{d\left(\frac{\xi_2}{R}\right)}{dR} \Phi_1^{*\rm ad} \frac{\partial \Phi_2^{\rm ad}}{\partial R} + \frac{2\xi_1^* \xi_2}{R^3} \Phi_1^{*\rm ad} \frac{\partial \Phi_2^{\rm ad}}{\partial R} \right]. \quad (6.12)$$

Using the chain rule to take the derivative of the vibrational function in the second term, we obtain

$$\langle \Psi_1^{\rm ad} | \, \hat{T}_{\rm radial} \, | \Psi_2^{\rm ad} \rangle = -\frac{\hbar^2}{2\mu} \int\int R^2 dR d^3r \left[\frac{\xi_1^* \xi_2}{R^2} \Phi_1^{*\rm ad} \frac{\partial^2 \Phi_2^{\rm ad}}{\partial R^2} + \frac{2\xi_1^*}{R^2} \frac{d\xi_2}{dR} \Phi_1^{*\rm ad} \frac{\partial \Phi_2^{\rm ad}}{\partial R} - \frac{2\xi_1^* \xi_2}{R^3} \Phi_1^{*\rm ad} \frac{\partial \Phi_2^{\rm ad}}{\partial R} + \frac{2\xi_1^* \xi_2}{R^3} \Phi_1^{*\rm ad} \frac{\partial \Phi_2^{\rm ad}}{\partial R} \right], \quad (6.13)$$

where the last two terms cancel. Finally we obtain

$$\langle \Psi_1^{\rm ad} | \, \hat{T}_{\rm radial} \, | \Psi_2^{\rm ad} \rangle = -\frac{\hbar^2}{2\mu} \int\int dR d^3r \left[\xi_1^* \xi_2 \Phi_1^{*\rm ad} \frac{\partial^2 \Phi_2^{\rm ad}}{\partial R^2} + 2\xi_1^* \frac{d\xi_2}{dR} \Phi_1^{*\rm ad} \frac{\partial \Phi_2^{\rm ad}}{\partial R} \right]. \quad (6.14)$$

Next, we proceed to evaluate the electronic part of the integral. We know that the adiabatic electronic wavefunctions depend on R and can change rapidly in regions near avoided crossings. If we assume that only two electronic states are coupled by this interaction (i.e. because other states of the same symmetry lie relatively far away in energy), we can write the adiabatic electronic wavefunctions in terms of diabatic electronic wavefunctions:

$$\Phi_1^{\rm ad}(\vec{r}, R) = \cos\varphi(R) \Phi_1^{\rm d}(\vec{r}) + \sin\varphi(R) \Phi_2^{\rm d}(\vec{r}), \quad (6.15)$$

$$\Phi_2^{\rm ad}(\vec{r}, R) = -\sin\varphi(R) \Phi_1^{\rm d}(\vec{r}) + \cos\varphi(R) \Phi_2^{\rm d}(\vec{r}), \quad (6.16)$$

where we use $\cos\varphi(R)$ and $\sin\varphi(R)$ as expansion coefficients to satisfy normalization, and $\Phi^{\rm d}(\vec{r})$ is a diabatic electronic wavefunction. Since the adiabatic electronic wavefunctions depend on R, we must assume that the mixing angle, φ, will also

depend on R. However the diabatic electronic wavefunctions are defined as wavefunctions that have a very weak dependence on R. Using Eqs. (6.15) and (6.16), we evaluate the derivatives of the electronic wavefunctions with respect to R:

$$\frac{\partial \Phi_1^{\rm ad}}{\partial R} = -\sin\varphi \frac{\partial \varphi}{\partial R}\Phi_1^{\rm d} + \cos\varphi \frac{\partial \varphi}{\partial R}\Phi_2^{\rm d} = \Phi_2^{\rm ad}\frac{\partial \varphi}{\partial R}, \tag{6.17}$$

$$\frac{\partial \Phi_2^{\rm ad}}{\partial R} = -\cos\varphi \frac{\partial \varphi}{\partial R}\Phi_1^{\rm d} - \sin\varphi \frac{\partial \varphi}{\partial R}\Phi_2^{\rm d} = -\Phi_1^{\rm ad}\frac{\partial \varphi}{\partial R}, \tag{6.18}$$

and

$$\frac{\partial^2 \Phi_1^{\rm ad}}{\partial R^2} = \frac{\partial}{\partial R}\left(\Phi_2^{\rm ad}\frac{\partial \varphi}{\partial R}\right) = -\left(\frac{\partial \varphi}{\partial R}\right)^2 \Phi_1^{\rm ad} + \left(\frac{\partial^2 \varphi}{\partial R^2}\right)\Phi_2^{\rm ad}, \tag{6.19}$$

$$\frac{\partial^2 \Phi_2^{\rm ad}}{\partial R^2} = \frac{\partial}{\partial R}\left(-\Phi_1^{\rm ad}\frac{\partial \varphi}{\partial R}\right) = -\left(\frac{\partial \varphi}{\partial R}\right)^2 \Phi_2^{\rm ad} - \left(\frac{\partial^2 \varphi}{\partial R^2}\right)\Phi_1^{\rm ad}. \tag{6.20}$$

Therefore, it follows that the electronic parts of the matrix elements are

$$\begin{aligned}
\langle \Phi_1^{\rm ad}| \frac{\partial}{\partial R} |\Phi_1^{\rm ad}\rangle_r &= 0, \\
\langle \Phi_1^{\rm ad}| \frac{\partial}{\partial R} |\Phi_2^{\rm ad}\rangle_r &= -\frac{\partial \varphi}{\partial R}, \\
\langle \Phi_2^{\rm ad}| \frac{\partial}{\partial R} |\Phi_1^{\rm ad}\rangle_r &= \frac{\partial \varphi}{\partial R}, \\
\langle \Phi_2^{\rm ad}| \frac{\partial}{\partial R} |\Phi_2^{\rm ad}\rangle_r &= 0,
\end{aligned} \tag{6.21}$$

and

$$\begin{aligned}
\langle \Phi_1^{\rm ad}| \frac{\partial^2}{\partial R^2} |\Phi_1^{\rm ad}\rangle_r &= -\left(\frac{\partial \varphi}{\partial R}\right)^2, \\
\langle \Phi_1^{\rm ad}| \frac{\partial^2}{\partial R^2} |\Phi_2^{\rm ad}\rangle_r &= -\frac{\partial^2 \varphi}{\partial R^2}, \\
\langle \Phi_2^{\rm ad}| \frac{\partial^2}{\partial R^2} |\Phi_1^{\rm ad}\rangle_r &= \frac{\partial^2 \varphi}{\partial R^2}, \\
\langle \Phi_2^{\rm ad}| \frac{\partial^2}{\partial R^2} |\Phi_2^{\rm ad}\rangle_r &= -\left(\frac{\partial \varphi}{\partial R}\right)^2.
\end{aligned} \tag{6.22}$$

We now evaluate the electronic integral in Eq. (6.14) by substituting Eqs. (6.21) and Eqs. (6.22):

$$\langle \Psi_1^{\rm ad} | \, \hat{T}_{\rm radial} \, | \Psi_2^{\rm ad} \rangle = -\frac{\hbar^2}{2\mu} \int dR \left[\xi_1^* \xi_2 \left(-\frac{\partial^2 \varphi}{\partial R^2} \right) + 2\xi_1^* \frac{\partial \xi_2}{\partial R} \left(-\frac{\partial \varphi}{\partial R} \right) \right]. \tag{6.23}$$

Integration of the first term by parts leads to

$$\langle \Psi_1^{\rm ad} | \, \hat{T}_{\rm radial} \, | \Psi_2^{\rm ad} \rangle = -\frac{\hbar^2}{2\mu} \left\{ - \xi_1^* \xi_2 \frac{\partial \varphi}{\partial R} \bigg|_0^\infty + \int dR \left[\frac{\partial (\xi_1^* \xi_2)}{\partial R} \frac{\partial \varphi}{\partial R} - 2\xi_1^* \frac{\partial \xi_2}{\partial R} \frac{\partial \varphi}{\partial R} \right] \right\}, \tag{6.24}$$

where the boundry term [first term in Eq. (6.24)] goes to zero since the vibrational wavefunctions must go to zero at zero and infinite internuclear separations. The derivative in the second term on the right hand side of Eq. (6.24) is evaluated using the chain rule:

$$\langle \Psi_1^{\rm ad} | \, \hat{T}_{\rm radial} \, | \Psi_2^{\rm ad} \rangle = -\frac{\hbar^2}{2\mu} \int dR \left[\left(\xi_1^* \frac{\partial \xi_2}{\partial R} + \frac{\partial \xi_1^*}{\partial R} \xi_2 \right) \frac{\partial \varphi}{\partial R} - 2\xi_1^* \frac{\partial \xi_2}{\partial R} \frac{\partial \varphi}{\partial R} \right]. \tag{6.25}$$

Finally, we combine terms to obtain the final expression for the off-diagonal matrix element of the nuclear kinetic energy operator:

$$\langle \Psi_1^{\rm ad} | \, \hat{T}_{\rm radial} \, | \Psi_2^{\rm ad} \rangle = -\frac{\hbar^2}{2\mu} \int dR \left[\frac{\partial \xi_1^*}{\partial R} \xi_2 - \xi_1^* \frac{\partial \xi_2}{\partial R} \right] \frac{\partial \varphi}{\partial R}. \tag{6.26}$$

This equation agrees with Eq. 9 in Ref. [50].

6.2 Two-stage coupling between the NaCs 11(0^+) and 12(0^+) states

As mentioned in Chapter 5, the $12(0^+) \rightarrow 1(a)^3\Sigma^+$ electronic transition displays very clean and unique resolved bound-free fluorescence spectra. However, the $12(0^+) \rightarrow 1(X)^1\Sigma^+$ electronic transition is also strong and gives clean bound-bound fluorescence spectra. The fact that the $12(0^+)$ state makes radiative transitions down to

both the triplet repulsive state, $2(A)^1\Sigma^+$, and the singlet ground state, $1(X)^1\Sigma^+$, indicates that the $12(0^+)$ state has both triplet and singlet character. This is most likely due to spin-orbit perturbations with the nearby $11(0^+)$ electronic state, which is labeled $5^3\Pi_{0^+}$ in Hund's case (a) notation. Based on theoretical calculations, which do not include the spin-orbit effect [49], in Hund's case (a) the $12(0^+)$ state is labeled the $7^1\Sigma^+$ state. Spin-orbit coupling between $^3\Pi$ and $^1\Sigma$ states is very common, so it is likely that each of the rovibrational levels of both states has significant singlet and triplet character due to the mixing of the electronic wavefunctions. However, it is clear from the intensity distribution of the $12(0^+)\rightarrow 1(a)^3\Sigma^+$ resolved bound-free fluorescence that the spin-orbit effect cannot be the only interaction responsible for the mixing of the levels of these two electronic states. For example, a contrasting case occurs in NaK, where spin-orbit coupling between the $2(A)^1\Sigma^+$ and $1(b)^3\Pi_{0^+}$ states is (16.33 ± 0.15) cm^{-1} [51]. Thus significant coupling occurs between levels of the same J that lie within a few cm^{-1} of each other. These levels are known as window levels [52]. Because of the Hund's case (a) dipole selection rule on spin, $\Delta S = 0$, resolved fluorescence intensity distributions corresponding to two such interacting levels should be identical except for an overall scaling factor. This will be verified experimentally by observing singlet emission from both components of NaK window levels. For either upper level, only the part of the mixed wavefunction with triplet electronic character give rise to allowed transitions to the repulsive $1(a)^3\Sigma^+$ state. Similarly, only the part of the mixed wavefunction with singlet electronic character give rise to allowed transitions to the bound $1(X)^1\Sigma^+$ state.

In the case of NaCs, the $11(0^+)\rightarrow 1(a)^3\Sigma^+$ and $12(0^+)\rightarrow 1(a)^3\Sigma^+$ resolved bound-free fluorescence is qualitatively very different for nearby rovibrational levels of the two upper states. To explain the intensity distribution of the bound-free emission, we developed a simple two-stage coupling model to describe how the various components of the mixed wavefunction result in the observed bound-free fluorescence spectra. First we consider the electronic part of the wavefunction describing levels of the $11(0^+)$ and $12(0^+)$ states. One key assumption of this model is that these are the only two electronic state interacting with one another. Discussion of the validity of assumptions is deferred to Sec. 6.4. However using this assumption, we can

write the relativistic [Hund's case (c), spin-orbit included] electronic wavefunctions $[\Phi_{11(0^+)}(\vec{r},R), \Phi_{12(0^+)}(\vec{r},R)]$ in terms of the non-relativistic [Hund's case (a), spin-orbit not included] electronic wavefunctions $[\Phi_{5^3\Pi_{0^+}}(\vec{r}), \Phi_{7^1\Sigma^+}(\vec{r})]$ as

$$\Phi_{12(0^+)}(\vec{q},R) = \cos\theta(R)\Phi_{7^1\Sigma^+}(\vec{q},R) + \sin\theta(R)\Phi_{5^3\Pi_{0^+}}(\vec{q},R) \tag{6.27}$$

and

$$\Phi_{11(0^+)}(\vec{q},R) = -\sin\theta(R)\Phi_{7^1\Sigma^+}(\vec{q},R) + \cos\theta(R)\Phi_{5^3\Pi_{0^+}}(\vec{q},R). \tag{6.28}$$

The expansion coefficients are written using sines and cosines so that normalization is automatically satisfied. This analysis of the mixing of the electronic wavefunctions emphasizes the fact that, in NaCs, the large spin-orbit effect causes global perturbations that affect all levels of both electronic states.

In addition to the mixing of the electronic state wavefunctions due to spin-orbit coupling, the individual rovibrational levels of the two electronic states can also interact via some separate interaction. Making the assumption that only two rovibrational levels of the same J (one from each electronic state) mix together, we obtain the following mixed total wavefunctions:

$$\Psi_{\rm A} = \cos\phi\frac{\xi^J_{v_{12(0^+)}}}{R}\Phi_{12(0^+)} + \sin\phi\frac{\xi^J_{v_{11(0^+)}}}{R}\Phi_{11(0^+)} \tag{6.29}$$

and

$$\Psi_{\rm B} = -\sin\phi\frac{\xi^J_{v_{12(0^+)}}}{R}\Phi_{12(0^+)} + \cos\phi\frac{\xi^J_{v_{11(0^+)}}}{R}\Phi_{11(0^+)}. \tag{6.30}$$

As in the previous expansion, sines and cosines are used to preserve normalization, and the signs here reflect the assumption that the predominantly $12(0^+)$ level A lies higher in energy than the predominantly $11(0^+)$ level B. However we introduce a different angle, ϕ, to represent the mixing angle for this second interaction. Note also that we have introduced a superscript J for the vibrational wavefunctions since these depend on J.

Now to simulate the resolved fluorescence spectra corresponding to these levels we first determine the Hund's case (a) singlet and triplet amplitudes of each upper

level wavefunction, since the bound-free and bound-bound fluorescence, due to transitions down to the ground triplet and singlet states, respectively, can be described in terms of Hund's case (a) wavefunctions and dipole selection rules. To do this we insert Eqs. (6.27) and (6.28) into Eqs. (6.29) and (6.30) to obtain

$$\begin{aligned}\Psi_{\rm A} = &\cos\phi\frac{\xi^J_{v_{12(0^+)}}}{R}[\cos\theta(R)\Phi_{7^1\Sigma^+} + \sin\theta(R)\Phi_{5^3\Pi_{0^+}}] \\ &+ \sin\phi\frac{\xi^J_{v_{11(0^+)}}}{R}[-\sin\theta(R)\Phi_{7^1\Sigma^+} + \cos\theta(R)\Phi_{5^3\Pi_{0^+}}],\end{aligned} \tag{6.31}$$

and

$$\begin{aligned}\Psi_{\rm B} = &-\sin\phi\frac{\xi^J_{v_{12(0^+)}}}{R}[\cos\theta(R)\Phi_{7^1\Sigma^+} + \sin\theta(R)\Phi_{5^3\Pi_{0^+}}] \\ &+ \cos\phi\frac{\xi^J_{v_{11(0^+)}}}{R}[-\sin\theta(R)\Phi_{7^1\Sigma^+} + \cos\theta(R)\Phi_{5^3\Pi_{0^+}}].\end{aligned} \tag{6.32}$$

It is convenient to use the non-relativistic electronic wavefunctions since it is then obvious which components of the wavefunction are responsible for the bound-free (triplet) emission and which are responsible for the bound-bound (singlet) emission. We can rearrange the equations to better show the singlet and triplet components:

$$\begin{aligned}\Psi_{\rm A} = &[\cos\phi\cos\theta(R)\frac{\xi^J_{v_{12(0^+)}}}{R} - \sin\phi\sin\theta(R)\frac{\xi^J_{v_{11(0^+)}}}{R}]\Phi_{7^1\Sigma^+} \\ &+ [\cos\phi\sin\theta(R)\frac{\xi^J_{v_{12(0^+)}}}{R} + \sin\phi\cos\theta(R)\frac{\xi^J_{v_{11(0^+)}}}{R}]\Phi_{5^3\Pi_{0^+}},\end{aligned} \tag{6.33}$$

and

$$\begin{aligned}\Psi_{\rm B} = &[-\sin\phi\cos\theta(R)\frac{\xi^J_{v_{12(0^+)}}}{R} - \cos\phi\sin\theta(R)\frac{\xi^J_{v_{11(0^+)}}}{R}]\Phi_{7^1\Sigma^+} \\ &+ [-\sin\phi\sin\theta(R)\frac{\xi^J_{v_{12(0^+)}}}{R} + \cos\phi\cos\theta(R)\frac{\xi^J_{v_{11(0^+)}}}{R}]\Phi_{5^3\Pi_{0^+}}.\end{aligned} \tag{6.34}$$

Assuming that the mixing angles, θ and ϕ, are small, the singlet emission from the state associated with $\Psi_{\rm A}$ is dominated by the $\xi^J_{v_{12(0^+)}}$ vibrational wavefunction.

Similarly, the triplet emission from the state associated with $\Psi_{\rm B}$ is dominated by the $\xi^J_{v_{11(0^+)}}$ vibrational wavefunction. For the purposes of this dissertation we will refer to these components as the direct components. This makes sense if we consider that the $11(0^+)$ and $12(0^+)$ states are predominantly triplet and singlet, respectively. This is also why it is reasonable to assign the vibrational quantum number for levels of the $12(0^+)$ state based on the intensity pattern of the resolved $12(0^+)\rightarrow 1(X)^1\Sigma^+$ bound-bound emission, rather than the $12(0^+)\rightarrow 1(a)^3\Sigma^+$ bound-free emission.

The cross term components show how the vibrational wavefunctions can mix together to produce an upper state wavefunction with unusual resolved fluorescence spectra. The triplet emission associated with $\Psi_{\rm A}$, and the singlet emission associated with $\Psi_{\rm B}$ are not dominated by either the $11(0^+)$ or $12(0^+)$ vibrational wavefunction, assuming the mixing angles are small and of comparable magnitudes. Rather, terms from each vibrational wavefunction contribute significantly to the sums, so that the resolved fluorescence spectra exhibit quantum interference. It is also important to note that this interference requires two stages of coupling between the interacting levels.

6.3 Resolved fluorescence from the $11(0^+)$ and $12(0^+)$ states

In order to test the model described by Eqs. (6.33) and (6.34), we simulated resolved fluorescence spectra for $11(0^+)$, $12(0^+) \rightarrow 1(X)^1\Sigma^+ , 1(a)^3\Sigma^+$ transitions. This was done for three pairs of $11(0^+)$ ($v_{11(0^+)}$, J) and $12(0^+)$ ($v_{12(0^+)}$, J) levels. The levels were chosen because their emission spectra are relatively strong and the intensity patterns in the parts of the spectra associated with the cross terms are distinct and fairly simple. To simulate the spectra, we first applied the model to vibrational levels that are nearest neighbors in terms of energy. In each of the cases we studied, the nearest neighbors satisfied $v_{12(0^+)} - v_{11(0^+)} = 2$. Figure 6.3 shows the results of one such mixing of wavefunctions. We used LEVEL [25] and a modified version of BCONT [18, 24] to carry out the simulations. First, level energies and wavefunctions

were calculated by LEVEL using experimental $11(0^+)$ and $12(0^+)$ potentials for the rovibrational levels of interest. The IPA potential of the present work (Table 5.6) was used for the $12(0^+)$ state and the experimental IPA potential presented in [3] was used for the $11(0^+)$ state. The wavefunctions calculated from these potentials were copied into an Excel spreadsheet and manipulated according to Eqs. (6.33) and (6.34) to form the singlet and triplet components of the interacting levels.

In this first "proof of principle" calculation of these mixed wavefunctions, we took the mixing angle θ to be constant; i.e. $\theta(R) = \theta_{\text{ave}}$. This approximation is discussed in Sec. 6.4 where we consider the effect of the actual dependence of θ on R and how such a dependence can be incorporated into the model. Once an appropriate pair of mixing angles was chosen, the custom wavefunction components were input to BCONT in order to simulate the spectra from these mixed levels. Using a custom wavefunction in BCONT allows the user to bypass the input of an initial upper state potential. Instead of having BCONT calculate the level energy and wavefunction from the desired upper state level, a separate input file provides the level energy and point-wise wavefunction. In order to fit the two mixing angles, θ and ϕ, calculated spectra were compared to experimental spectra in two stages. First, the shape of the cross term components was fit. We define K to be the ratio of the $\xi^J_{v_{11(0^+)}}$ amplitude to the $\xi^J_{v_{12(0^+)}}$ amplitude in the cross term component of Eq. (6.33):

$$K = \frac{\tan\phi}{\tan\theta}. \tag{6.35}$$

Therefore K gives a measure of how much the $\xi^J_{v_{11(0^+)}}$ vibrational wavefunction contributes to the cross term component relative to the $\xi^J_{v_{12(0^+)}}$ vibrational wavefunction in the level described by Ψ_{A} in Eq. (6.33); i.e. Eq. (6.33) becomes

$$\begin{aligned}\Psi_{\text{A}} = C\Big\{&[\cot\theta\xi^J_{v_{12(0^+)}} - \tan\phi\xi^J_{v_{11(0^+)}}]\Phi_{7^1\Sigma^+} \\ &+[\xi^J_{v_{12(0^+)}} + K\xi^J_{v_{11(0^+)}}]\Phi_{5^3\Pi_{0^+}}\Big\},\end{aligned} \tag{6.36}$$

with $C = \frac{\cos\phi\sin\theta}{R}$. The ratio K, therefore, has a large impact on the intensity

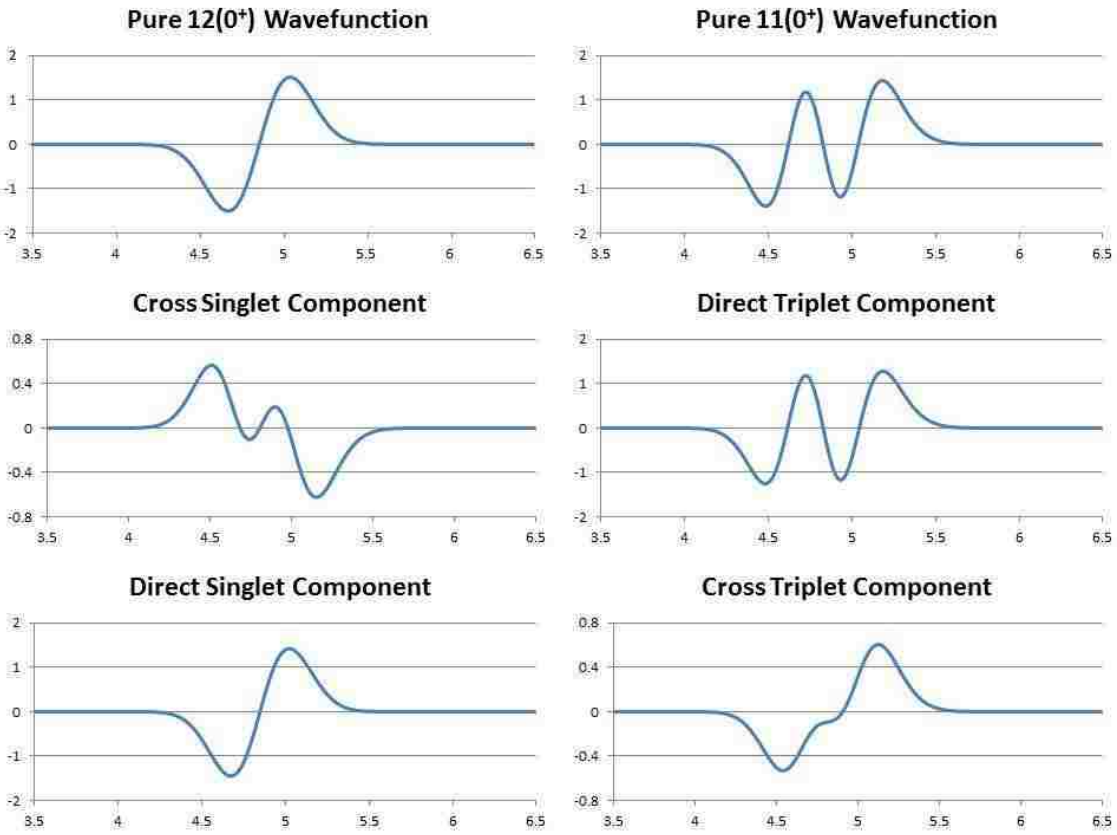

Figure 6.3: Pure and mixed components of wavefunctions as functions of internuclear separation (Å) for particular levels of the NaCs $11(0^+)$ and $12(0^+)$ states. The top row shows plots of pure wavefunctions for the $12(0^+)(1,\ 43)$ and $11(0^+)(3,\ 43)$ levels, respectively, calculated using the computer program LEVEL [25]. The second row shows the singlet and triplet wavefunction components for the state described by Eq. (6.34). The third row shows the singlet and triplet wavefunction components for the state described by Eq. (6.33). These mixed wavefunction components were calculated with $\theta = 0.311$ radians and $\phi = 0.209$ radians.

distribution in the part of the spectrum resulting from the cross term component. We varied K until the simulated triplet part of the $12(0^+)$ spectrum, corresponding to the triplet cross term component, matched the experimental spectrum as closely as possible in a least squares sense. The overall normalization factor was used to scale the simulations to ensure that the integrated areas of both the experimental and simulated spectra were the same. The scaled simulation was compared to the experimental spectrum at each point along the wavelength grid used in the BCONT calculation, and the RMS deviation was determined. The value of K was adjusted after each simulation to obtain new cross term wavefunction components that were given to BCONT for the next simulation. The value of K was varied with four significant digits until the RMS deviation was minimized for the bound-free fluorescence associated with each of the three $12(0^+)$ rovibrational levels studied. Figures 6.4, 6.5, and 6.6 show the bound-free (triplet) parts of the simulations associated with each optimized cross term component in Eq. (6.33) along with the experimental spectra associated with the corresponding $12(0^+) \rightarrow 1(a)^3\Sigma^+$ transitions. In these simulations the transition dipole moment function associated with the $5^3\Pi_{0^+} \rightarrow 1(a)^3\Sigma^+$ electronic transition determined in [3] was used, along with the $1(a)^3\Sigma^+$ potential curve determined by [3] and [15].

The parameter K also affects the shape of the singlet cross term component (the first term in Eq. (6.34)). The ratio of the amplitude of $\xi^J_{v_{11(0^+)}}$ to the amplitude of $\xi^J_{v_{12(0^+)}}$ in this term is simply $\frac{1}{K}$. Therefore, using K as the only free parameter we should be able to fit both cross term components simultaneously. Despite this, we only used the $12(0^+) \rightarrow 1(a)^3\Sigma^+$ spectra for the actual fitting because the $11(0^+) \rightarrow 1(X)^1\Sigma^+$ spectra are very weak and noisy in comparison.

Once the intensity distribution of the $12(0^+)$ triplet spectra associated with the cross term components was reproduced as closely as possible, we began the second stage of fitting. This involved varying the value of ϕ for each pair of mixed levels in order to best reproduce the relative total intensities of the singlet and triplet components for each of the levels with the value of K held fixed. For each value of ϕ, the corresponding θ was determined using the previously determined best fit K and Eq. (6.35). By examining Eqs. (6.33) and (6.34), we can see that, for small angles,

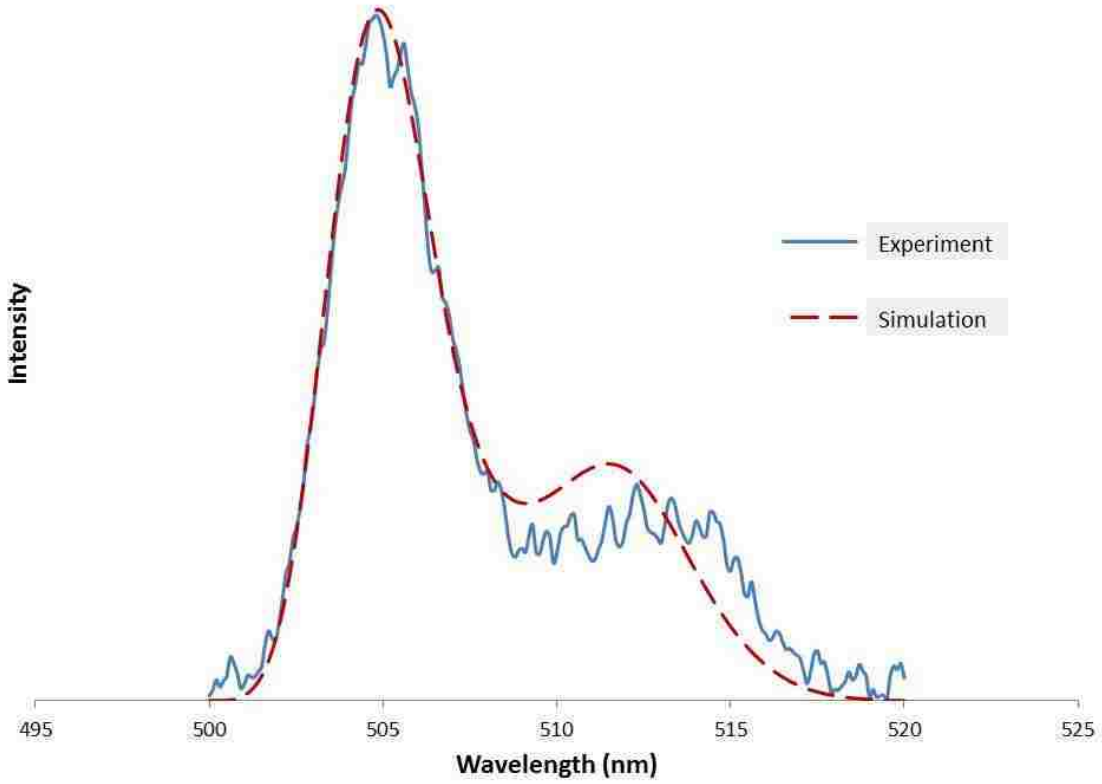

Figure 6.4: Experimental and simulated spectra of the $12(0^+)$ (0, 43) $\rightarrow$ $1(a)^3\Sigma^+$ transition. The simulated spectrum (dashed) is normalized to the experimental spectrum (solid) by a constant factor such that the total integrated area is the same for both. The value of K was varied in order to give the smallest RMS deviation between the experimental and normalized simulated spectra. The wavefunction component used for this simulation involved a mixture of pure $11(0^+)(2, 43)$ and $12(0^+)(0, 43)$ wavefunctions with the best fit value of $K = 0.4075 \pm 0.0001$.

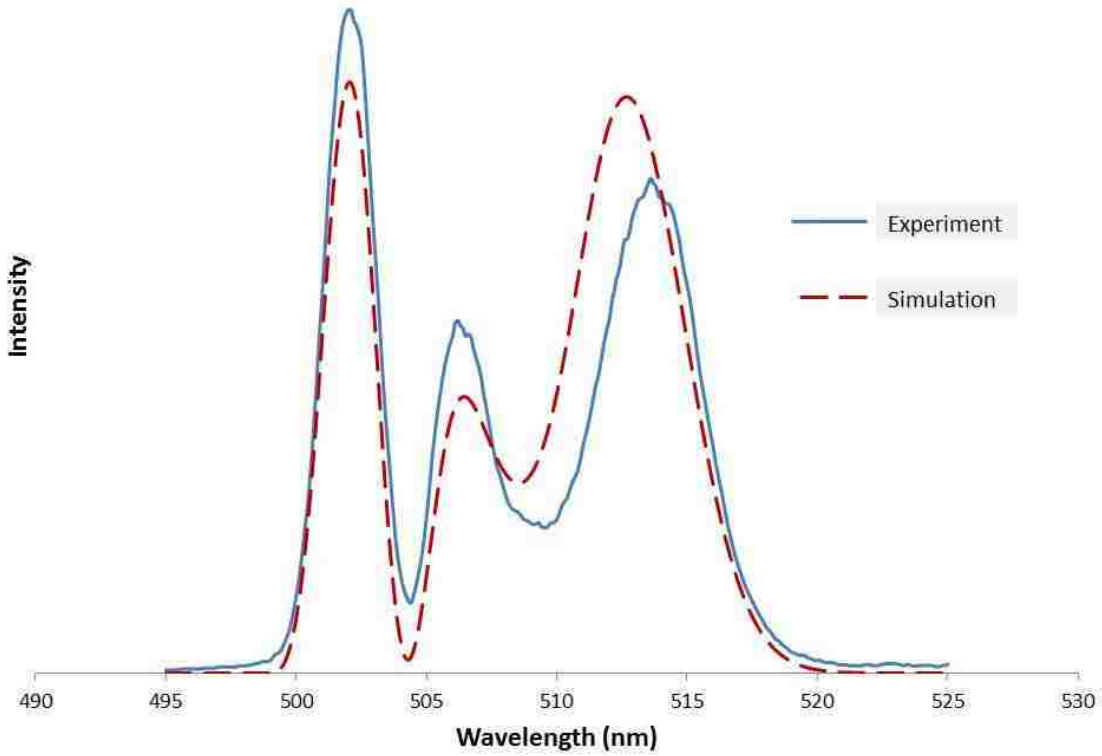

Figure 6.5: Experimental and simulated spectra of the $12(0^+)$ (1, 43) $\rightarrow$ $1(a)^3\Sigma^+$ transition. The simulated spectrum (dashed) is normalized to the experimental spectrum (solid) by a constant factor such that the total integrated area is the same for both. The value of K was varied in order to give the smallest RMS deviation between the experimental and normalized simulated spectra. The wavefunction component used for this simulation involved a mixture of pure $11(0^+)(3, 43)$ and $12(0^+)(1, 43)$ wavefunctions with the best fit value of $K = 0.6591 \pm 0.0001$.

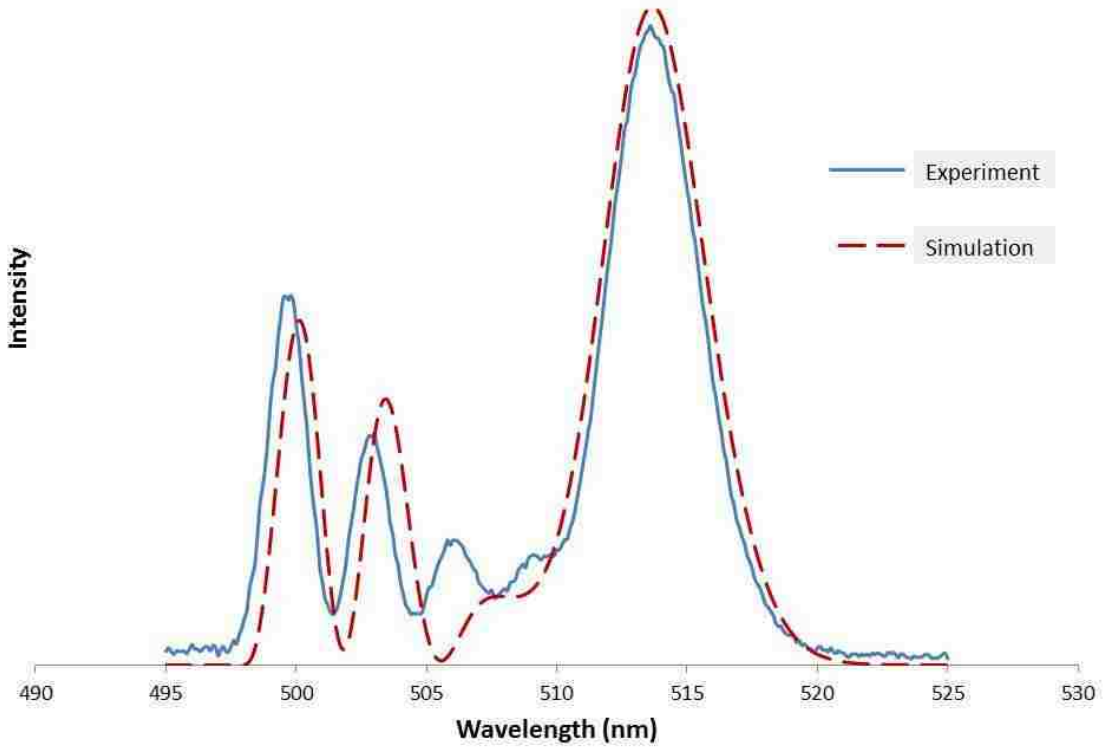

Figure 6.6: Experimental and simulated spectra of the $12(0^+)$ (2, 33) $\rightarrow$ $1(a)^3\Sigma^+$ transition. The simulated spectrum (dashed) is normalized to the experimental spectrum (solid) by a constant factor such that the total integrated area is the same for both. The value of K was varied in order to give the smallest RMS deviation between the experimental and normalized simulated spectra. The wavefunction component used for this simulation involved a mixture of pure $11(0^+)(4, 33)$ and $12(0^+)(2, 33)$ wavefunctions with the best fit value of $K = 0.8454 \pm 0.0001$.

an increase in both angles will result in little change to the overall magnitudes of the direct components, but will cause the overall magnitudes of the cross components to increase significantly. For the $12(0^+)$ levels, described by Eq. (6.33), a larger ϕ results in a greater amplitude of triplet relative to singlet emission. For the $11(0^+)$ levels, described by Eq. (6.34), a larger ϕ results in a greater amplitude of singlet relative to triplet emission. The relative singlet and triplet emission from a state is also heavily influenced by the transition dipole moment functions so it was important to have good transition dipole moment functions. For the triplet emission from both states, the experimental $5^3\Pi_{0^+} \rightarrow 1(a)^3\Sigma^+$ transition dipole moment function from [3] was used. For the singlet emission from both states, the theoretical $7^1\Sigma^+ \rightarrow 1(X)^1\Sigma^+$ transition dipole moment function from [17] was used. The observed ratio of singlet emission intensity to triplet emission intensity for a particular experimental spectrum is also affected by the efficiency of the detection system as a function of wavelength. Therefore all spectra used for fitting were first carefully corrected for the detection efficiency as described in Sec. 3.4.3. Finally, BCONT was used to simulate both the singlet and triplet emission for both states, even though the singlet emission is bound-bound. This is because the current version of LEVEL does not allow for a custom wavefunction to be used as input for the initial state. Since this feature is critical for this analysis, the version of BCONT modified by Brett McGeehan was used. This modified version calculates bound-bound transitions as a continuum by treating the discrete levels as a continuum described by a density of states. Just as important, the modified version of BCONT correctly treats the relative intensities of bound-free and bound-bound emission. Normalization is preserved by these calculations, so the experimental and simulated spectra were compared using total integrated area.

For a given pair of mixed $11(0^+)$ and $12(0^+)$ rovibrational levels, a value of ϕ was chosen and the value of K from the previous fitting of the $12(0^+)$ triplet emission was used. All components of the wavefunctions in Eqs. (6.33) and (6.34) were calculated and used as input for BCONT. The resulting singlet and triplet simulated spectra for both states were compared to experiment by first normalizing the simulated triplet emission spectra for both states by scaling them to match the total integrated

intensity of the experimental spectra. The simulated singlet emission spectra for both states were then scaled by the same factor used for the triplet emission for their respective states. Finally, the ratio of the total integrated areas of the singlet to triplet emission was calculated for the experimental and simulated spectra for both states. The RMS deviation between these simulated and experimental integrated intensity ratios for both states was calculated and ϕ was varied in order to minimize this RMS deviation. Table 6.1 lists the best fit parameters for each pair of levels studied here. Figures 6.7 - 6.12 show comparisons of the experimental and simulated spectra obtained from these fits. Note that the signal to noise ratio is low on the short wavelength end of several of the singlet spectra because the detector efficiency in the violet range of the spectrum is approximately six times lower at 420 nm than at 450 nm. The detector efficiency is about 22 times greater for the green region of the spectra associated with the bound-free emission than for the violet region. The relative CCD detector efficiency is shown in Fig. 6.13. The efficiency is normalized so the maximum value is one. Since the singlet portion of several of the spectra (especially those from $11(0^+)$ levels) is already very weak due to the relatively small $7^1\Sigma^+ \rightarrow 1(X)^1\Sigma^+$ transition dipole moment (shown in Fig. 6.14 compared with $5^3\Pi_{0^+} \rightarrow 1(a)^3\Sigma^+$ transition dipole moment function), the low efficiency at short wavelength can cause the noise to appear greatly enhanced relative to the signal in this spectral region.

$v_{11(0^+)}$	$v_{12(0^+)}$	J	K	ϕ (Radians)	θ (Radians)
0	2	43	0.4075 ± 0.0001	0.103 ± 0.001	0.248 ± 0.002
1	3	43	0.6591 ± 0.0001	0.209 ± 0.001	0.311 ± 0.002
2	4	33	0.8454 ± 0.0001	0.281 ± 0.001	0.329 ± 0.002

Table 6.1: Summary of best fit mixing angle parameters.

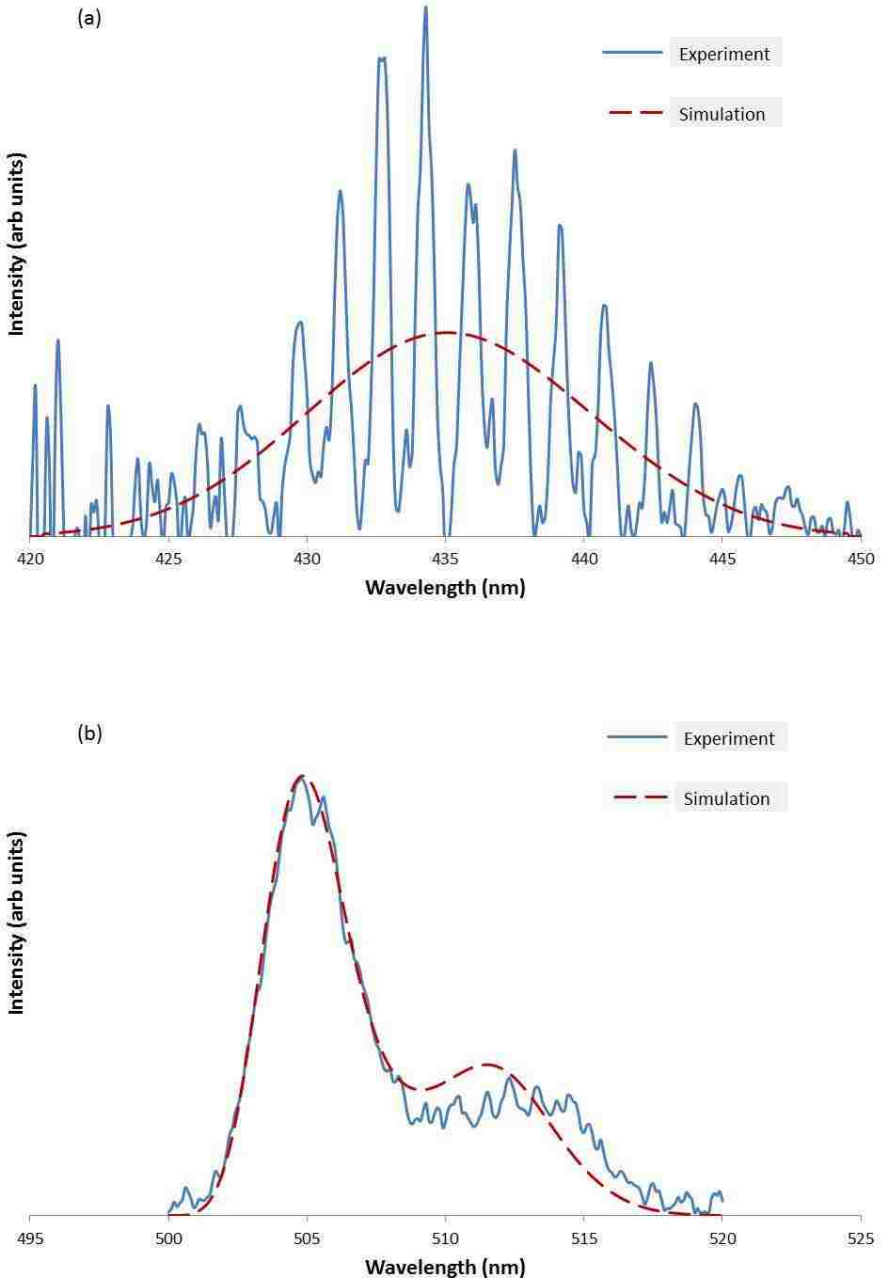

Figure 6.7: Comparison of experimental and simulated spectra for (a) $12(0^+)$ (0, 43) $\rightarrow 1(X)^1\Sigma^+$ and (b) $12(0^+)$ (0, 43) $\rightarrow 1(a)^3\Sigma^+$ transitions. The spectra are the result of mixing pure $11(0^+)$ (2, 43) and $12(0^+)$ (0, 43) wavefunctions according to Eqs. (6.33) and (6.34) where $\phi = 0.103 \pm 0.001$ radians and $\theta = 0.248 \pm 0.002$ radians.

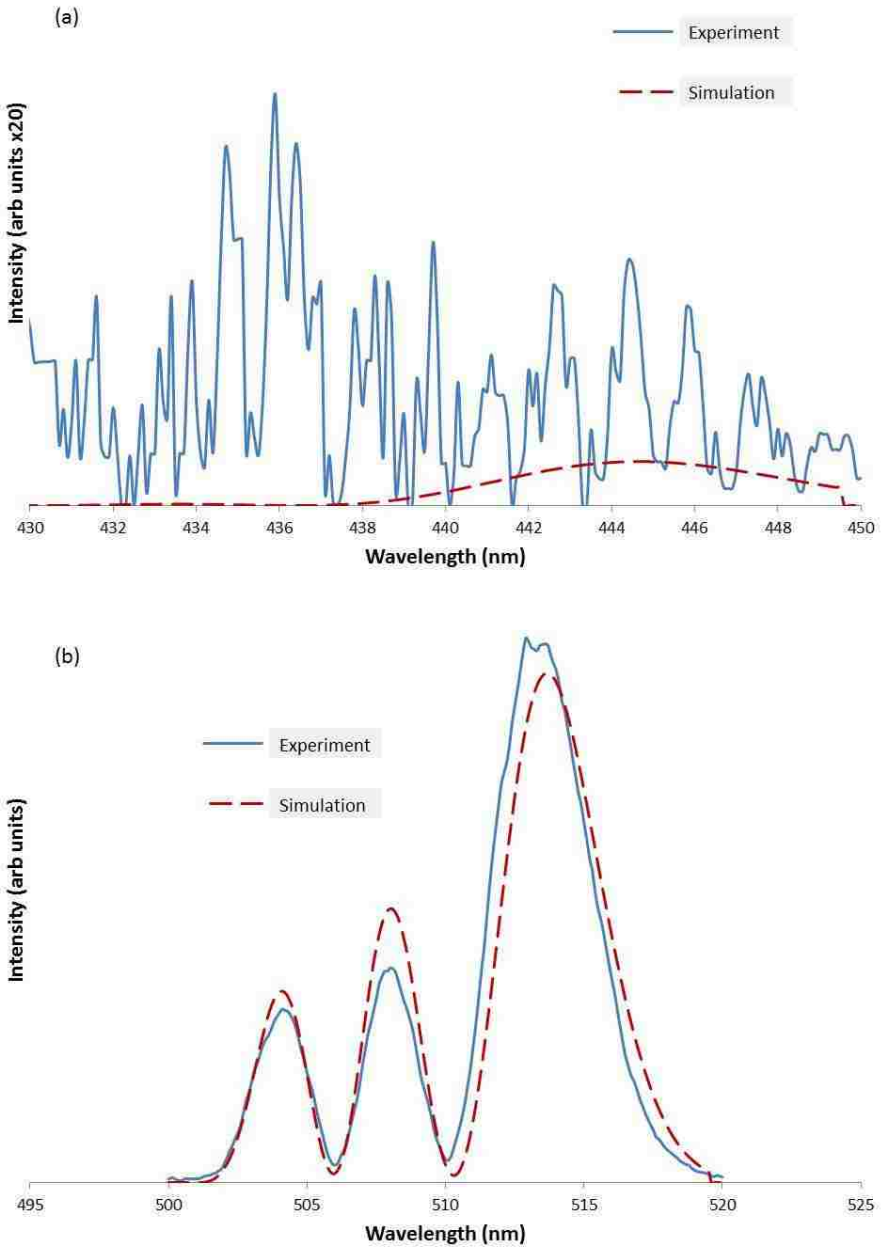

Figure 6.8: Comparison of experimental and simulated spectra for (a) $11(0^+)$ (2, 43) $\rightarrow 1(X)^1\Sigma^+$ and (b) $11(0^+)$ (2, 43) $\rightarrow 1(a)^3\Sigma^+$ transitions. The spectra are the result of mixing pure $11(0^+)$ (2, 43) and $12(0^+)$ (0, 43) wavefunctions according to Eqs. (6.33) and (6.34) where $\phi = 0.103 \pm 0.001$ radians and $\theta = 0.248 \pm 0.002$ radians.

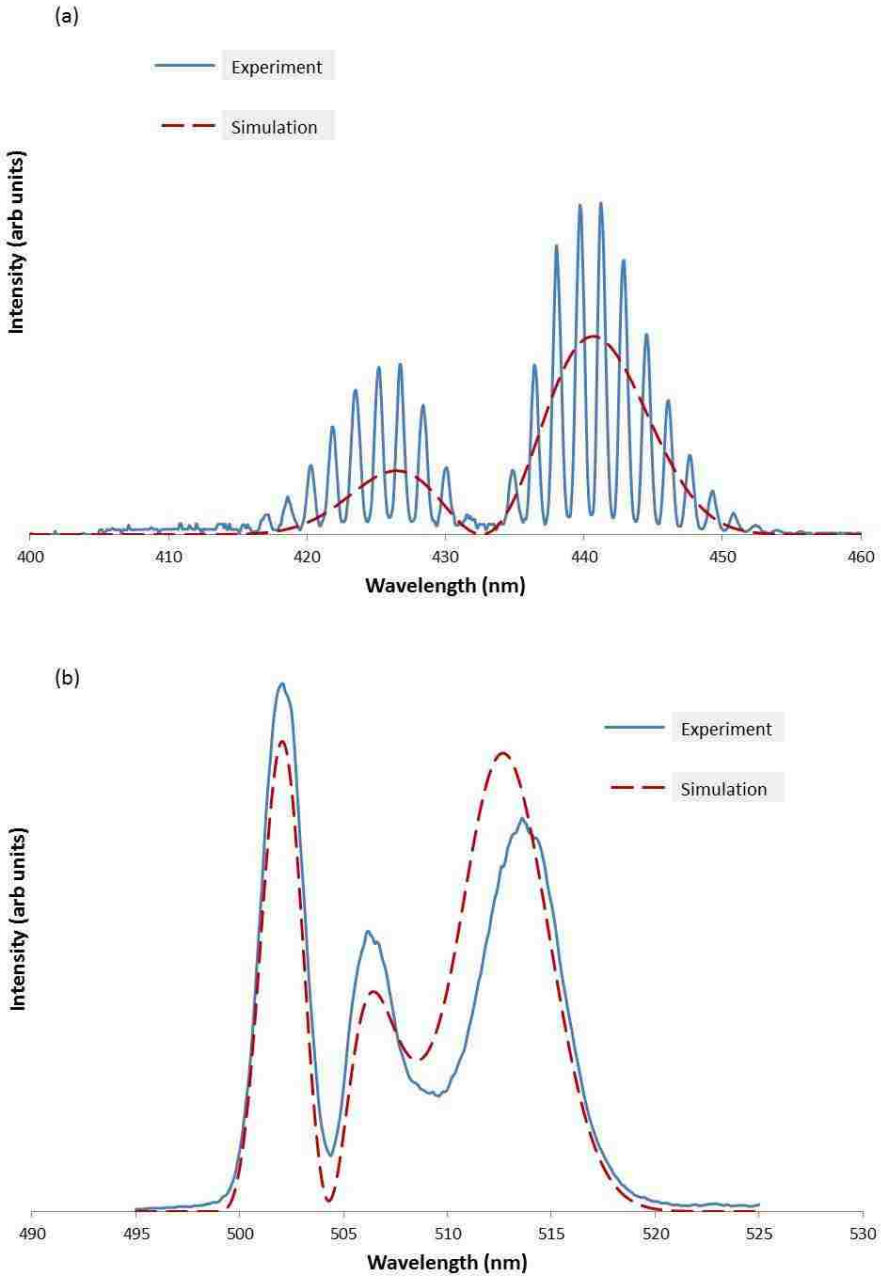

Figure 6.9: Comparison of experimental and simulated spectra for (a) $12(0^+)$ (1, 43) $\rightarrow 1(X)^1\Sigma^+$ and (b) $12(0^+)$ (1, 43) $\rightarrow 1(a)^3\Sigma^+$ transtions. The spectra are the result of mixing pure $11(0^+)$ (3, 43) and $12(0^+)$ (1, 43) wavefunctions according to Eqs. (6.33) and (6.34) where $\phi = 0.209 \pm 0.001$ radians and $\theta = 0.311 \pm 0.002$ radians.

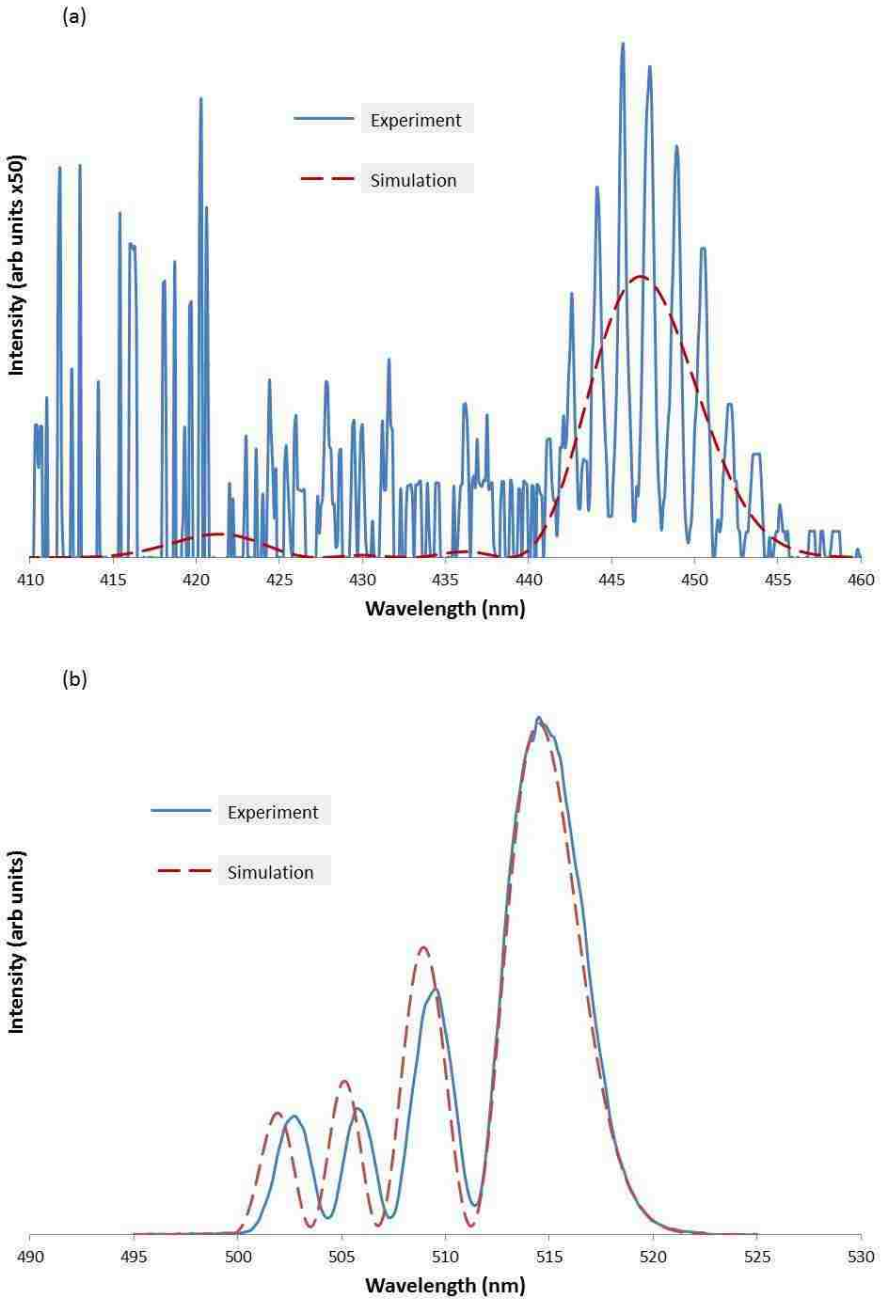

Figure 6.10: Comparison of experimental and simulated spectra for (a) $11(0^+)$ (3, 43) $\rightarrow 1(X)^1\Sigma^+$ and (b) $11(0^+)$ (3, 43) $\rightarrow 1(a)^3\Sigma^+$ transitions. The spectra are the result of mixing pure $11(0^+)$ (3, 43) and $12(0^+)$ (1, 43) wavefunctions according to Eqs. (6.33) and (6.34) where $\phi = 0.209 \pm 0.001$ radians and $\theta = 0.311 \pm 0.002$ radians.

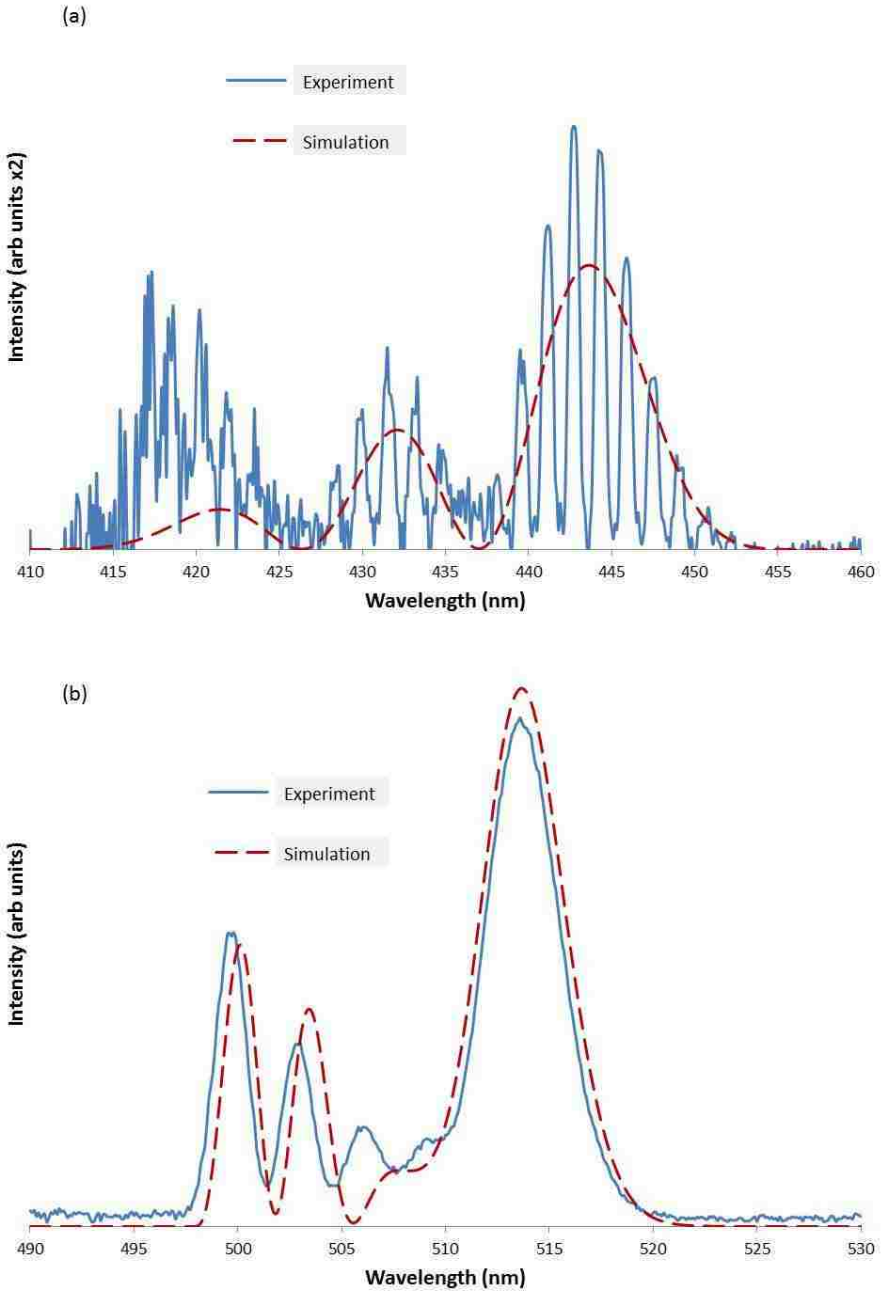

Figure 6.11: Comparison of experimental and simulated spectra for (a) $12(0^+)$ (2, 33) $\rightarrow 1(X)^1\Sigma^+$ and (b) $12(0^+)$ (2, 33) $\rightarrow 1(a)^3\Sigma^+$ transitions. The spectra are the result of mixing pure $11(0^+)$ (4, 33) and $12(0^+)$ (2, 33) wavefunctions according to Eqs. (6.33) and (6.34) where $\phi = 0.281 \pm 0.001$ radians and $\theta = 0.329 \pm 0.002$ radians.

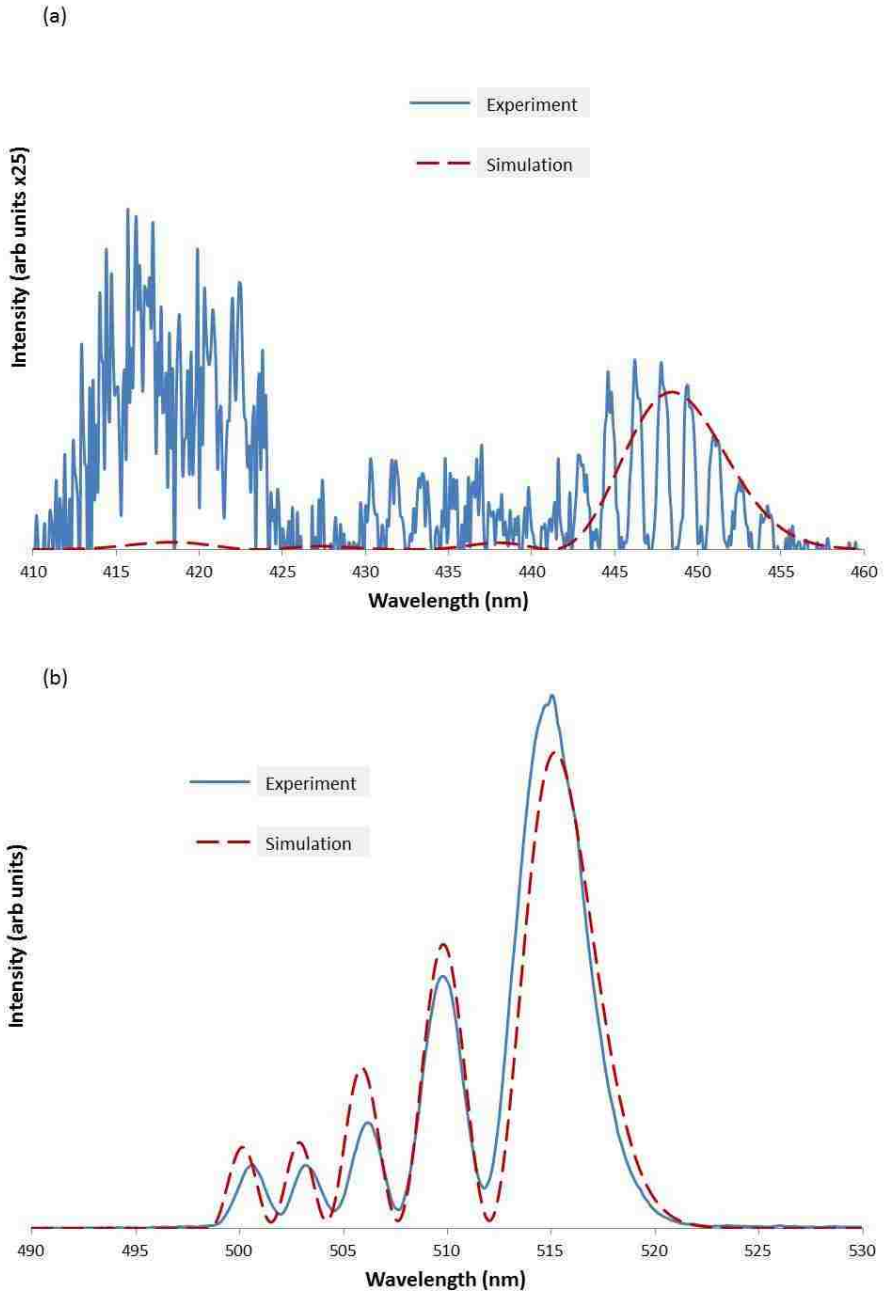

Figure 6.12: Comparison of experimental and simulated spectra for (a) $11(0^+)$ (4, 33) $\rightarrow 1(X)^1\Sigma^+$ and (b) $11(0^+)$ (4, 33) $\rightarrow 1(a)^3\Sigma^+$ transitions. The spectra are the result of mixing pure $11(0^+)$ (4, 33) and $12(0^+)$ (2, 33) wavefunctions according to Eqs. (6.33) and (6.34) where $\phi = 0.281 \pm 0.001$ radians and $\theta = 0.329 \pm 0.002$ radians.

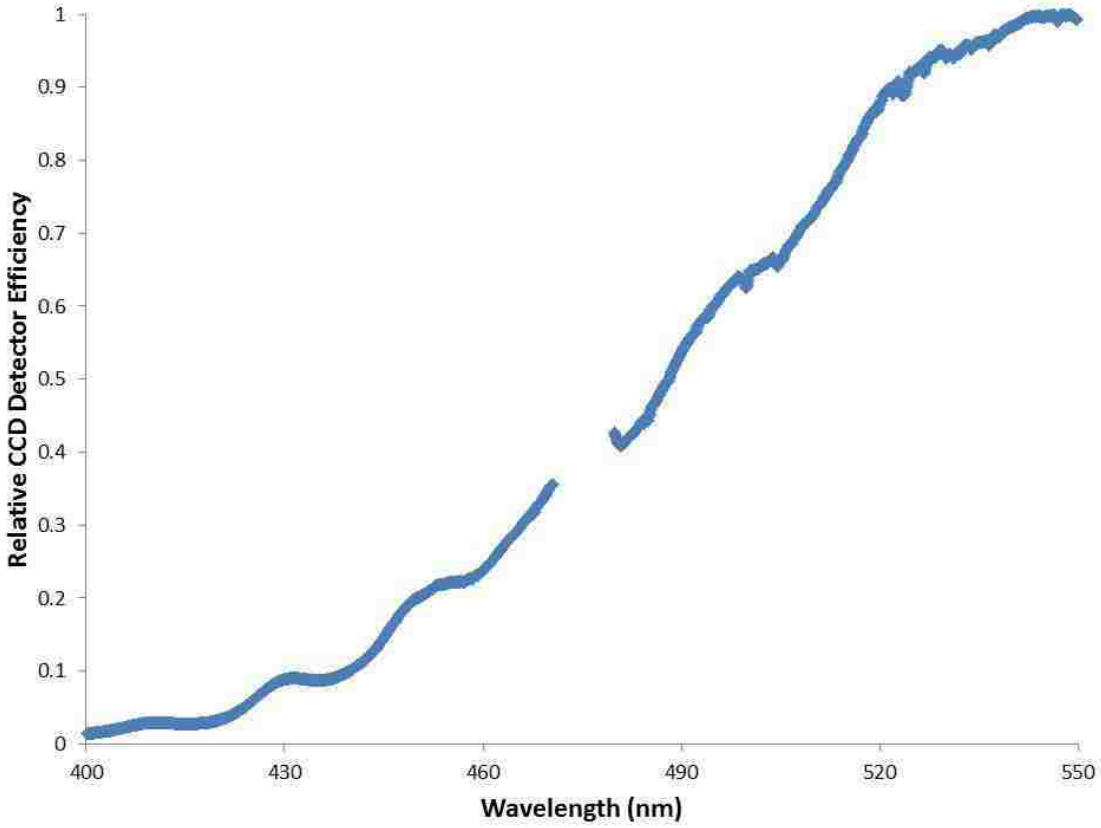

Figure 6.13: Relative CCD detector efficiency scaled such that the maximum is one.

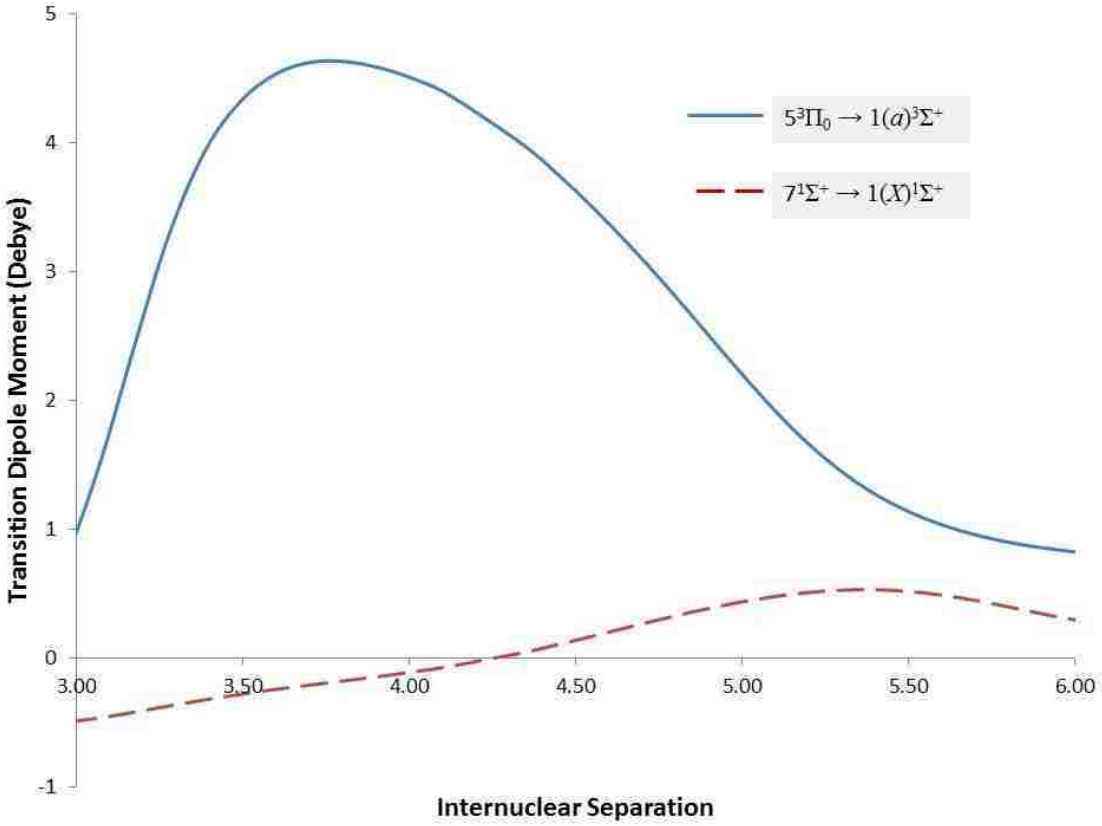

Figure 6.14: Theoretical $7^1\Sigma^+ \rightarrow 1(X)^1\Sigma^+$ and $5^3\Pi_{0^+} \rightarrow 1(a)^3\Sigma^+$ transition dipole moment functions calculated by Aymar and Dulieu [17].

6.4 Discussion of assumptions and approximations

For the model described in Sec. 6.2 to be able to reproduce the experimental spectra, it is essential that there be two stages of interactions between the states of the molecule. The first stage of coupling between these states is spin-orbit coupling, described in Sec. 6.1.1. This is evident because both electronic states involved in the coupling radiate to both lower triplet and lower singlet states.

The first simplifying assumption of our model is that in Eqs. (6.27) and (6.28) we have assumed that the spin-orbit interaction causes the electronic wavefunctions to mix such that relativistic wavefunctions can be written as a linear combination of nonrelativistic wavefunctions involving only two electronic states. However, there are many electronic states that can be excited in the energy region we can access with our laser systems. Figure 6.15 shows several theoretically calculated potentials in the energy region of the $11(0^+)$ and $12(0^+)$ states. The minimum of the $13(0^+)$ potential is much higher than the levels used to fit mixing angles for this work and likely does not contribute. However, it does seem to show an avoided crossing with the $12(0^+)$ state above 26,000 cm^{-1}. The $10(0^+)$ [$4^3\Pi_{0^+}$] electronic state has energy levels that can be excited in the same region as the $11(0^+)$ and $12(0^+)$ levels studied here. The fact that the $4^3\Pi_{0^+}$ theoretical potential shows a double minimum implies that it interacts strongly with one or more electronic states. In particular it almost certainly interacts with the $11(0^+)$ state in the region near $R \sim 6$ Å. If the spin-orbit interaction of the $11(0^+)$ and $12(0^+)$ electronic states with the $4^3\Pi_{0^+}$ state is significant, it should be included as an additional term in the expansion of the electronic wavefunctions. This would result in more terms in the final wavefunction, specifically ones that contribute to triplet emission. However, we believe that these terms are negligible because we should be able to see evidence of the mixing with the $4^3\Pi_{0^+}$ state in the experimental spectra. As discussed in Chapter 7, the intensity distribution of the $4^3\Pi_{0^+} \rightarrow 1(a)^3\Sigma^+$ bound-free emission is quite different from that of the $11(0^+) \rightarrow 1(a)^3\Sigma^+$ or $12(0^+) \rightarrow 1(a)^3\Sigma^+$ emission. In the energy region of the rovibrational levels studied here, $4^3\Pi_{0^+}$ energy levels span a very large range of R, and hence the bound-free emission spans a very wide range of wavelength. If there

are significant contributions to the mixed levels from the $4^3\Pi_{0^+}$ electronic state, the emission would extend to much longer wavelengths than have been observed. Localized perturbations involving individual rovibrational levels are also unlikely since the wavelength of the oscillations in the $4^3\Pi_{0^+}$ vibrational level wavefunctions are much smaller than those of the $11(0^+)$ or $12(0^+)$ vibrational wavefunctions. This means that there would be poor overlap between the vibrational wavefunctions and hence weak interactions. Since emission at longer wavelengths has not been detected, we conclude that any contributions to the mixing of the levels studied here from the $4^3\Pi_{0^+}$ electronic state is likely negligible.

The second stage of coupling is likely due to nonadiabatic interactions. Unlike the spin-orbit interaction, evidence of this interaction is much less direct. As described in Sec. 6.1.2, nonadiabatic coupling is a result of nuclear kinetic energy terms left out of the Hamiltonian. These terms specifically involve derivatives of the electronic wavefunction with respect to the internuclear separation, R. Such terms are large when the character of the electronic wavefunction changes suddenly with respect to R. Evidence of this sudden change of electronic character can be seen in the potential energy curves, as shown in Fig. 6.2, when avoided crossings are present. However, for the current work, avoided crossings are not apparent between the $11(0^+)$ and $12(0^+)$ states of NaCs because the potential energy curves are somewhat parallel as seen in Fig. 6.16. Although there is no obvious avoided crossing between these two potentials, electronic states of the same symmetry (0^{-1} in this case) can interact via nonadiabatic coupling.

If nonadiabatic coupling is indeed the interaction responsible for the second stage of coupling, as we have assumed, then our model utilizes several additional simplifying assumptions in order to calculate simulated spectra. First, in the derivation of the off-diagonal matrix elements of the nuclear kinetic energy operator, Eqs. (6.15) and (6.16) show that the adiabatic electronic wavefunctions, which depend on R, are expanded in terms of the diabatic electronic wavefunctions, which do not depend on R. All the R dependence of the adiabatic wavefunctions is then contained in the mixing angle, φ. However, in our case since the first stage of interaction between the electronic states is spin-orbit coupling rather than electrostatic interactions, instead

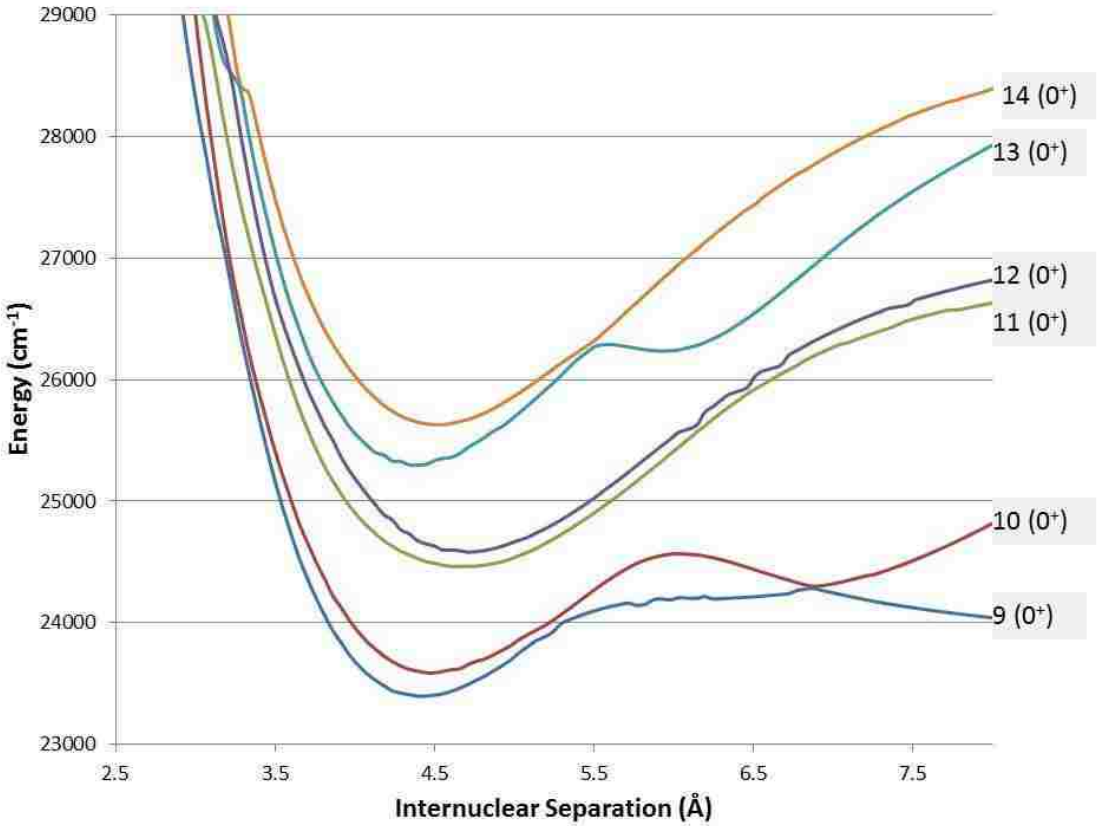

Figure 6.15: Theoretical potential energy curves in the region of the $11(0^+)$ and $12(0^+)$ states of NaCs. All curves shown here have 0^+ symmetry and were calculated by Korek *et al.* [12].

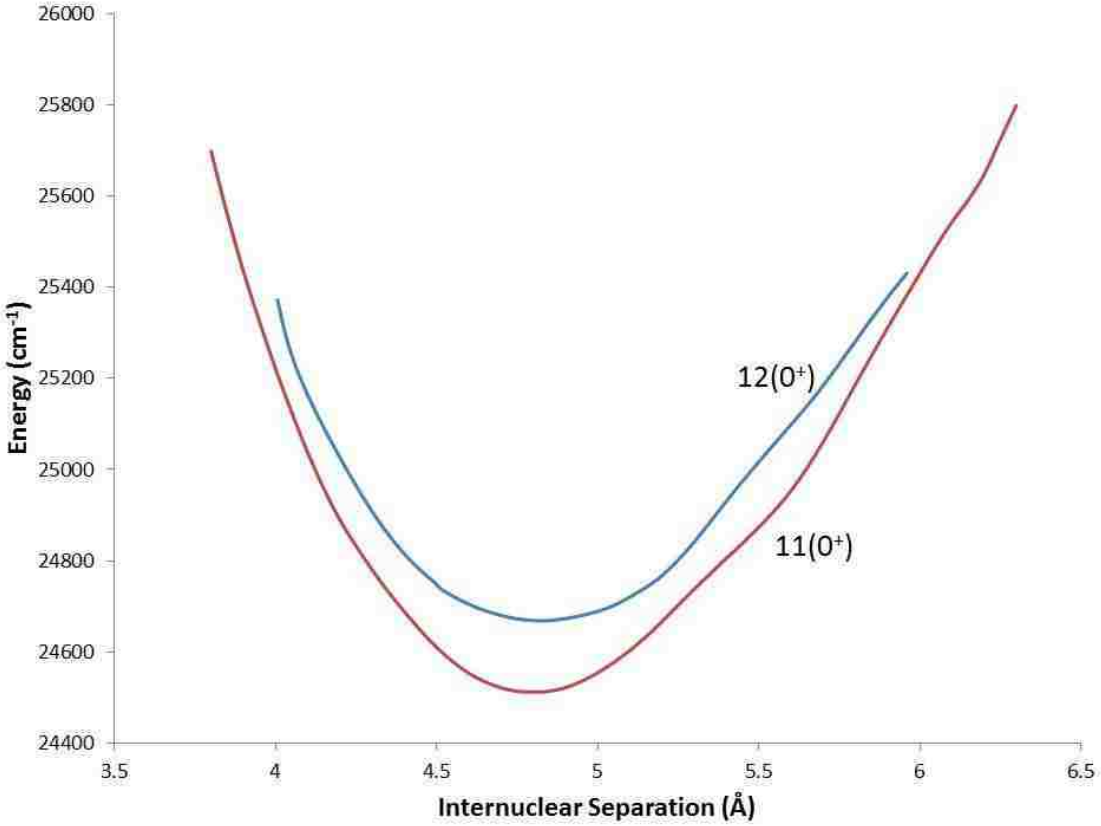

Figure 6.16: Experimental potential energy curves for the $11(0^+)$ and $12(0^+)$ states. The former is taken from [3], the latter is from the present work.

of expanding adiabatic wavefunctions in terms of diabatic wavefunctions, we expand relativistic wavefunctions in terms of nonrelativistic wavefunctions. In this expansion, as written in Eqs. (6.27) and (6.28), the relativistic electronic wavefunctions as well as θ depend on R. However, if we assume that the electronic wavefunctions do not depend significantly on R, the final matrix element for the nonadiabatic interaction is identical to Eq. (6.26) with $\theta(R)$ replacing $\varphi(R)$. If the character of the nonrelativistic electronic wavefunction changes significantly with R, then there would be an additional term in the final nonadiabatic matrix element involving a derivative of the electronic wavefunction with respect to R. This, in turn, would affect the final nonadiabatic interaction expansion coefficients, $\sin\phi$ and $\cos\phi$. Although the matrix element may have additional terms due to this non-zero derivative of the electronic wavefunction, the matrix element will still involve an integral over R which means the expansion coefficients will be independent of R. Because the mixing amplitudes in our model are fitted to the data, our results are not sensitive to a possible non-zero derivative of the electronic wavefunction.

In addition to assuming that only two electronic states contribute significantly to the character of the mixed levels, we have also made the assumption that only two rovibrational levels interact with one another through the second stage of coupling. Vibrational levels where $v_{12(0^+)} - v_{11(0^+)} = 2$ lie closest in energy with an average separation of about 20 cm^{-1}. Simulations based on mixed levels built from nearest neighbor pairs gave the best agreement with experimental spectra. The next nearest neighbor is not much farther away for most vibrational levels (usually approximately 30 cm^{-1}). So in order to test whether they contribute significantly, simulations were done with next nearest neighbor pairs. Figure 6.17 shows one such simulation with $12(0^+)$ (1, 43) interacting with $11(0^+)$ (2, 43) and it is evident that there is little to no agreement with the experimental spectrum. We also can be sure that there is no mixing with any higher vibrational levels by the same argument presented in the discussion of interactions involving the $10(0^+)$ state. Mixing with higher vibrational levels of either state would result in wavefunctions with a larger range of R and hence emission at longer wavelengths (see Fig. 6.18). Again, we do not observe any emission in longer wavelength regions, so we conclude that mixing with any higher

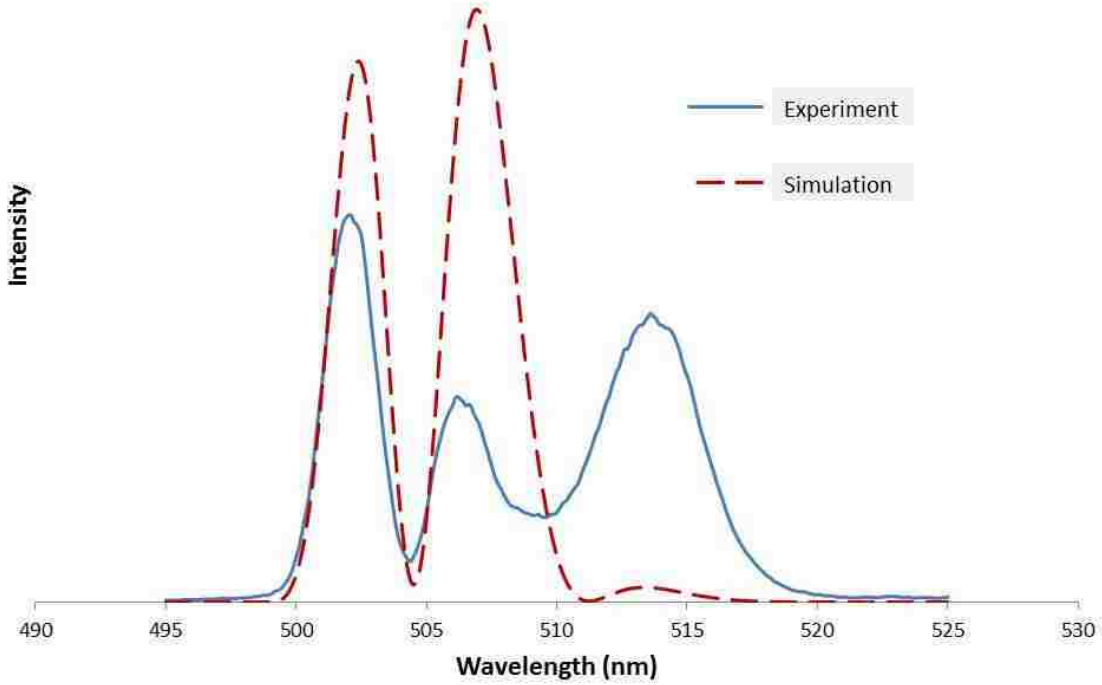

Figure 6.17: Simulation of triplet spectrum from next nearest neighbor pair of mixed levels. In this case, the simulated $12(0^+)$ (1, 43) $\rightarrow$ $1(a)^3\Sigma^+$ spectrum was computed using a mixture of pure $12(0^+)$ (1, 43) and $11(0^+)$ (2, 43) wavefunctions. The lack of agreement is evident regardless of the values of θ and ϕ chosen, which implies that the $12(0^+)$ (1, 43) and $11(0^+)$ (2, 43) levels do not appear to interact significantly.

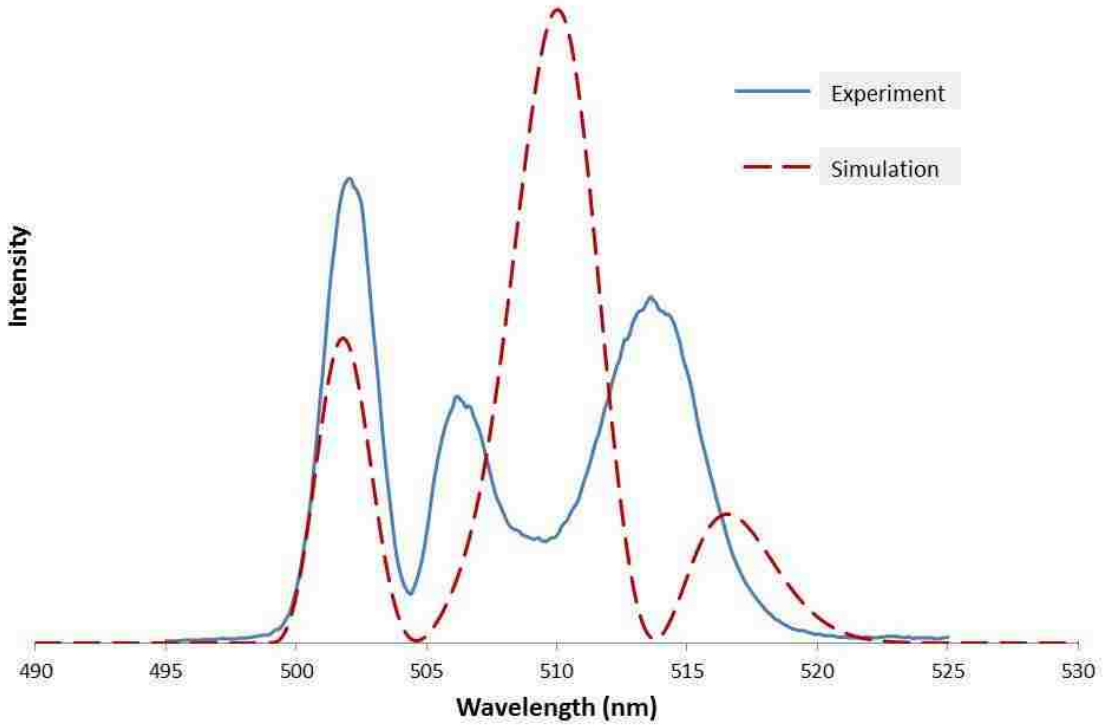

Figure 6.18: Simulated $12(0^+)$ (1, 43) $\rightarrow$ $1(a)^3\Sigma^+$ spectrum computed using a mixture of pure $12(0^+)$ (1, 43) and $11(0^+)$ (4, 43) wavefunctions. Not only does the simulated emission extend to longer wavelengths than in the experimental spectrum, but the overall intensity distribution resulting from the cross term component interference does not agree with observation. This implies that this $11(0^+)$ (4, 43) level and higher vibrational levels of the $11(0^+)$ state do not significantly interact with the $12(0^+)$ (1, 43) level.

vibrational levels is negligible.

The final assumption made in this model is that the mixing angle, θ, used for the expansion coefficients due to spin-orbit coupling can be described as a constant. In Eqs. (6.27) and (6.28), the R dependence of the relativistic electronic wavefunctions is contained in the mixing angle $\theta(R)$. However, we replaced $\theta(R)$ with an average θ for our simulations. A significant dependence of θ on R would result in a much different interference between the two mixed wavefunctions. Salami *et al.* [41] used Morse functions to describe empirical and *ab initio* spin-orbit functions for Rb_2. So it is very possible that θ could have a significant R dependence.

Although this dependence was not included in our fitting of the mixing angles, the agreement between the simulations and the experimental spectra is quite good. Systematic discrepancies can likely be attributed to neglecting the R dependence of θ. Because the emission resulting from the cross term components of the wavefunction is sensitive to the mixing angles, it is very likely that a more complicated fit could be done to determine the general dependence of θ on R. As an example, Fig. 6.19 shows a simulation of the triplet emission from the $12(0^+)$ (1, 43) level where θ is assumed to have a simple linear dependence on R,

$$\theta(R) = \theta_{\text{ave}} + m(R - R_0), \tag{6.37}$$

where θ_{ave} is the average value of θ as determined in the fit which produced the simulation shown in panel (b) of Fig. 6.9, m is the free parameter describing the slope, and R_0 is the internuclear separation associated with the midpoint of the wavefunctions. Comparison of panel (b) in Fig. 6.9 and Fig. 6.19 indicates that the linear $\theta(R)$ does a better job of fitting the spectrum than θ = constant. From Fig. 6.19 it appears that inclusion of a quadratic term in $\theta(R)$ would likely give even better agreement. More careful and complicated fitting of the R dependence of θ will be carried out in future work. Planned future efforts to include $\theta(R)$ in our model are described in Sec. 8.2.

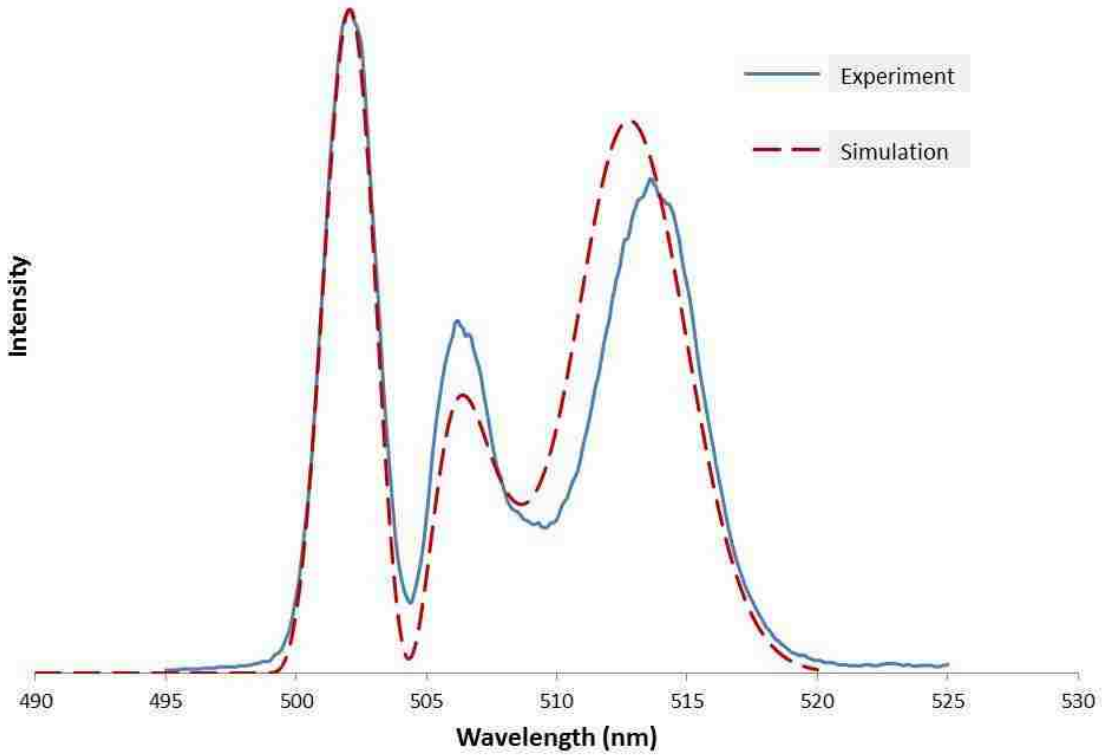

Figure 6.19: Simulation of the $12(0^+)$ $(1,\ 43) \rightarrow 1(a)^3\Sigma^+$ emission using a linear R dependence for θ. $\theta(R)$ was assumed to have a linear dependence on R with the constraint that the average value of θ over the relevant range of R remained fixed at the value determined in the fitting which produced the spectrum shown in panel (b) of Fig. 6.9. Comparing these two simulations, we find that the linear $\theta(R)$ does a better job at simulating the spectrum. Hence future work will involve careful fitting of a more complicated R dependence of θ.

Chapter 7

The NaCs $4^3\Pi_{0^+}$ State

As discussed in Chapter 5, we were able to excite rovibrational levels of several different high lying electronic states of NaCs in the present work. Levels belonging to the $4^3\Pi_{0^+}$ electronic state were identified and their energies measured. This electronic state is particularly interesting since it exhibits a double minimum potential. This double minimum potential results in patterns of rovibrational energy levels that are very different and more complicated than those of more regular potentials. The double minimum structure of the potential also produces quantum interference effects that can be observed in the bound-free fluorescence. This chapter describes how the $4^3\Pi_{0^+}$ electronic state was identified. Analysis of the vibrational and rotational progressions, and bound-free spectra are also discussed, and we qualitatively describe the shape and structure of the potential, based on our observations.

7.1 Identifying the $4^3\Pi_{0^+}$ state

As mentioned in Section 5.1, double resonance excitation signals corresponding to several different upper electronic states of NaCs can be observed for a given pump transition. However, due to the lack of observable unique hyperfine structure patterns, the fluorescence following a double resonance excitation must be resolved to determine the upper electronic state excited by the probe transition. Figure 7.1 shows a typical resolved bound-free spectrum for a transition to a state that we

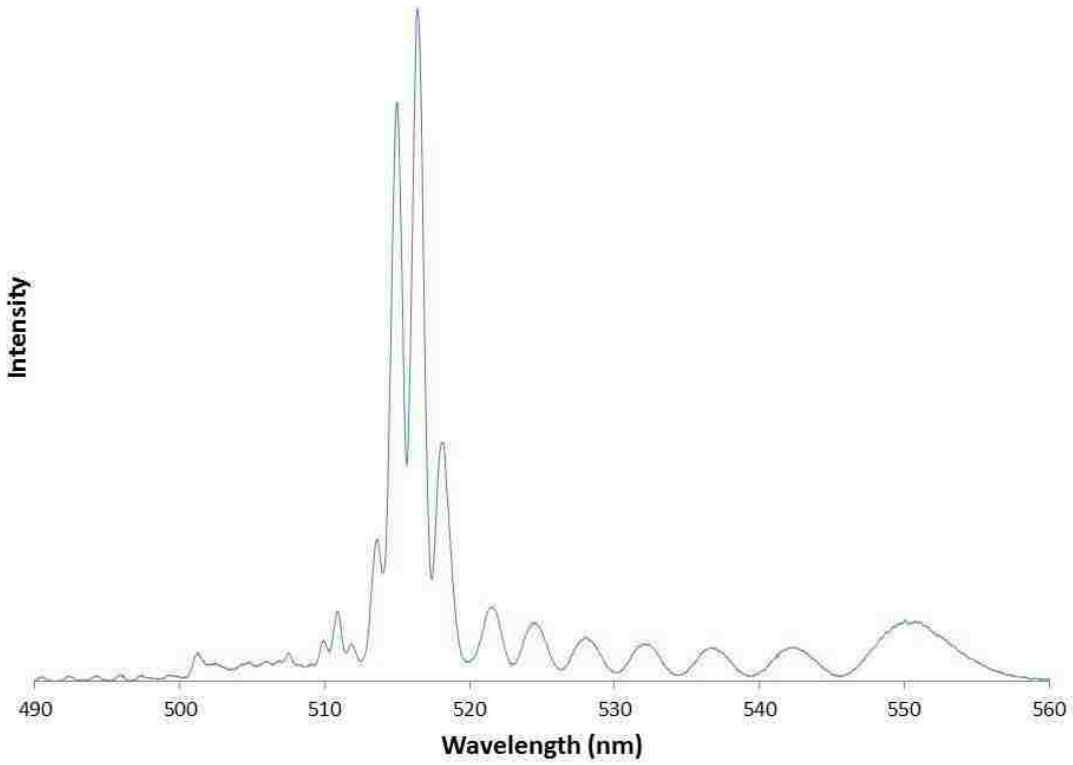

Figure 7.1: Resolved bound-free $4^3\Pi_{0^+}$ (v_0, 43) $\rightarrow 1(a)^3\Sigma^+$ fluorescence spectrum. The signature allowing us to identify this as $4^3\Pi_{0^+} \rightarrow 1(a)^3\Sigma^+$ fluorescence is the interference structure observed near 515 nm.

identified as the $4^3\Pi_{0^+}$ [or $10(0^+)$ in Hund's case (c) notation] electronic state of NaCs. In this dissertation we refer to this state as the $4^3\Pi_{0^+}$ electronic state, rather than as the $10(0^+)$ electronic state since, for our work, spin-orbit effects were not investigated. The most prominent feature of the $4^3\Pi_{0^+} \rightarrow 1(a)^3\Sigma^+$ bound-free spectra is the interference structure observed near 515 nm.

As discussed in Section 2.4.1, the Classical Franck-Condon Approximation (CFCA) is a good method to obtain a rough idea of the intensity distribution of a resolved bound-free fluorescence spectrum. In the CFCA, transitions take place instantaneously so they are represented by vertical lines connecting the potentials. In addition, momentum and hence kinetic energy are also conserved in this approximation. Therefore under this assumption, since the internuclear separation, R, does not change in a transition, one can calculate the difference potential between the two electronic states to obtain a $\lambda(R)$ function. This function gives a range of wavelengths over which the molecule can fluoresce and each wavelength is weighted by the probability that the two nuclei are separated by the corresponding R value. This probability is simply the square of the upper state nuclear radial (vibrational) wavefunction. If the potential is monotonic, then, under this approximation, we expect a simple reflection of the upper state wavefunction onto the wavelength grid according to $\lambda(R)$. However, if the difference potential is non-monotonic, then for some wavelengths there are contributions from more than one value of the internuclear separation, resulting in interference effects like those observed in Figure 7.1. To identify the upper electronic state responsible for this spectrum, we plotted several $^3\Lambda \rightarrow 1(a)^3\Sigma^+$ difference potentials, using the theoretical NaCs potentials of Korek *et al.* [12]. Figure 7.2 shows the function $\lambda(R)$ calculated from the difference potential $V_{4^3\Pi_{0^+}}(R) - V_{1(a)^3\Sigma^+}(R)$ [$\lambda(R) = \frac{hc}{[V_{4^3\Pi_{0^+}}(R) - V_{1(a)^3\Sigma^+}(R)]}$]. Clearly, there is a non-monotonic feature in the function $\lambda(R)$ in the region near where we observe interference structure. Furthermore, $\lambda(R)$ becomes monotonic at longer wavelengths which is consistent with the more simple and regular oscillating spectrum observed at longer wavelengths in Figure 7.1.

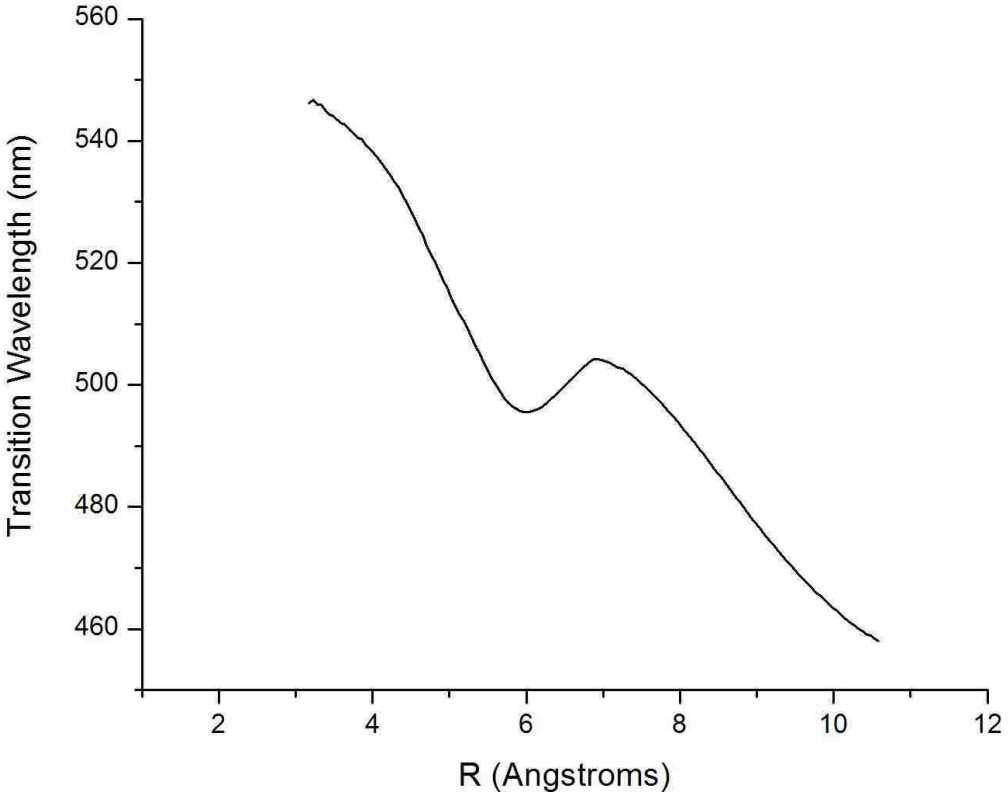

Figure 7.2: $\lambda(R)$ function corresponding to the difference potential, $V_{4^3\Pi_{0^+}}(R) - V_{1(a)^3\Sigma^+}(R)$. Theoretical potentials of Korek *et al.* [12] were used. The non-monotonic feature between 495 and 505 nm gives rises to the interference structure seen in Figure 7.1.

7.2 Rovibrational energies for the $4^3\Pi_{0^+}$ state

Once we identified the state responsible for the bound-free spectrum shown in Fig. 7.1 as the $4^3\Pi_{0^+}$ electronic state, rovibrational level energies were measured and collected into a database. Throughout the data collection process it was useful to have a reasonable idea of the region of the potential in which particular levels resided. Figure 7.3 shows the NaCs $4^3\Pi_{0^+}$ theoretical potential of Korek *et al.* [12]. Based on the sum of the energy of the initial ground-state rovibrational level and the two photon energies in the OODR excitation process, we determined that in the early stages of the experiment we probed levels of the $4^3\Pi_{0^+}$ state in the energy region above the barrier between the two minima. This was confirmed by preliminary measurements of vibrational and rotational splittings. Measured vibrational splittings in this energy region are approximately 8 cm^{-1}, which is much smaller than vibrational splittings of other nearby electronic states. For comparison, the $11(0^+)$ and $12(0^+)$ states both have vibrational splittings of approximately 55 cm^{-1}. The much smaller vibrational splitting for the $4^3\Pi_{0^+}$ state indicates that the potential is very wide in this region, and is consistent with vibrational splittings calculated for energies of the theoretical $4^3\Pi_{0^+}$ potential above the barrier. Rotational energy splittings also provide confirmation that we were exciting energy levels above the barrier. For one of the highest observed vibrational levels, we measured energies of many rotational levels using collisional spectra. The rotational constant for this vibrational state (later labeled $v_A + 1$) was determined to be $B_v = 0.01614$ cm^{-1}. This corresponds to an equilibrium separation of about 7.2 Å, which is consistent with the average internuclear separation of the theoretical potential in the region above the barrier.

One major challenge in the assignment of measured $4^3\Pi_{0^+}$ rovibrational levels is determining the vibrational quantum numbers. For the $11(0^+)$ and $12(0^+)$ electronic states, vibrational assignments were made by examining the resolved bound-free of bound-bound spectra corresponding to each of the various upper state vibrational levels such as those shown in Fig. 2.7 for the $11(0^+)$ state. However, the higher energy rovibrational levels of the $4^3\Pi_{0^+}$ state all produce resolved $4^3\Pi_{0^+} \rightarrow$

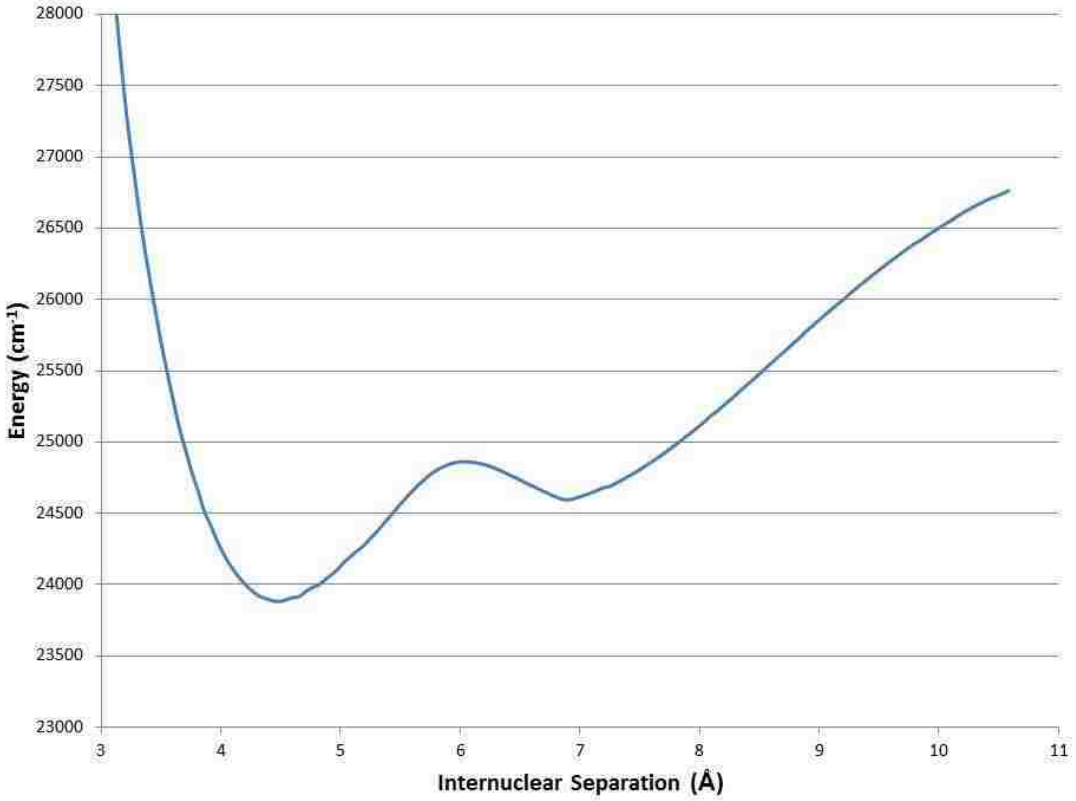

Figure 7.3: Theoretical NaCs $4^3\Pi_{0^+}$ potential energy curve from Korek *et al.* [12].

$1(a)^3\Sigma^+$ bound-free spectra that look almost identical to the one shown in Figure 7.1. The only difference between spectra originating in different $4^3\Pi_{0^+}$ vibrational levels are small variations in the interference structure. None of these variations give any indication of the correct vibrational numbering. Because of this, the best we could do was to assign a relative vibrational numbering for series of vibrational levels that were identified to be sequential. Throughout the course of identifying rovibrational levels, we made large downward jumps in energy in an effort to reach the barrier of the potential. Consequently there are some gaps in vibrational level coverage and hence the relative vibrational numbering scheme can only be given in sections. Further work is necessary to fill in these gaps and complete the relative vibrational numbering. This work in ongoing in our lab.

In order to map out any potential energy curve, coverage of rovibrational levels at the bottom of the potential well is needed. Unfortunately, the energy ranges that we can access with our lasers are limited, most importantly in the present case at lower energies. We have found that the lowest energy range available to us for NaCs OODR spectroscopy with our current lasers is not sufficiently low to excite rovibrational levels at the very bottom of the $4^3\Pi_{0^+}$ potential well. This prevents us from obtaining a complete picture of the potential since we cannot measure the energies of low lying rovibrational levels and we cannot assign an accurate vibrational numbering to the levels. Observing bound-free fluorescence from the lowest vibrational levels, where there will likely be little to no interference structure, would have allowed us to assign an absolute vibrational numbering based on node counting. In addition, when the lasers are operated at the very low ends of their tuning ranges, the calibration of the wavemeter becomes less reliable so level energies measured in these regions are likely to have large and undetermined errors. Because of these issues, we only present a summary of the data we have collected so far, in the form of a table of measured energies in Appendix C. We hope to conclude our study of the NaCs $4^3\Pi_{0^+}$ state when new laser equipment becomes available to us, possibly through collaboration with another research group.

Because the $4^3\Pi_{0^+}$ electronic potential is likely to be a double minimum potential, as indicated by the theoretical calculations and our data, we expect the energy level

structure to change dramatically as the barrier region is approached from above. To visualize this, we calculated rotational and vibrational constants for each observed vibrational level. By fitting the $4^3\Pi_{0^+}$ state rotational level energies to the function

$$E(v, J) = G_v + B_v J(J + 1), \tag{7.1}$$

we obtained values of G_v and B_v for each vibrational state. G_v represents the energy of the rotationless vibrational level while $B_v J(J + 1)$ is the rotational energy. The mean internuclear separation for that vibrational level is given by $R^v_{\rm eq} = \left(\frac{\hbar^2}{2\mu B_v}\right)^{\frac{1}{2}}$. We can also predict the G_v, B_v, and $R^v_{\rm eq}$ values for the theoretical double minimum state. Figure 7.4 shows a plot of G_v versus $R^v_{\rm eq}$, for vibrational levels determined using LEVEL 8.0 to calculate energy levels from the theoretical potential. The theoretical potential is plotted for reference. The calculated vibrational levels are clearly separated into three distinct regions: one set above the barrier, one set associated with the outer well, and one set associated with the inner well. Table 7.1 lists the G_v, B_v, and $R^v_{\rm eq}$ values calculated using the theoretical potential, which were used to generate Fig. 7.4.

In the region above the barrier, the calculations show more closely spaced G_v values because of the wide open nature of the potential well in this region and the $R^v_{\rm eq}$ values lie near the R value of the barrier. Below the barrier the calculations show vibrational levels associated with both the inner and outer wells. Because the potential is much narrower in the regions of each minimum compared to the region above the barrier, these vibrational levels have larger spacings than those above the barrier. The rotational constants, and hence equilibrium separations, for the calculations are also very different for vibrational levels associated with the inner and outer wells.

Figure 7.5 shows a similar plot for the measured vibrational levels of the $4^3\Pi_{0^+}$ state. The theoretical $4^3\Pi_{0^+}$ potential is also plotted for reference. Each point represents G_v versus $R^v_{\rm eq}$ for a single vibrational level whose rotational level energies were fit to Eq. (7.1). Green triangles represent vibrational levels where several rotational levels were observed, either through collisional spectra or by using more than one

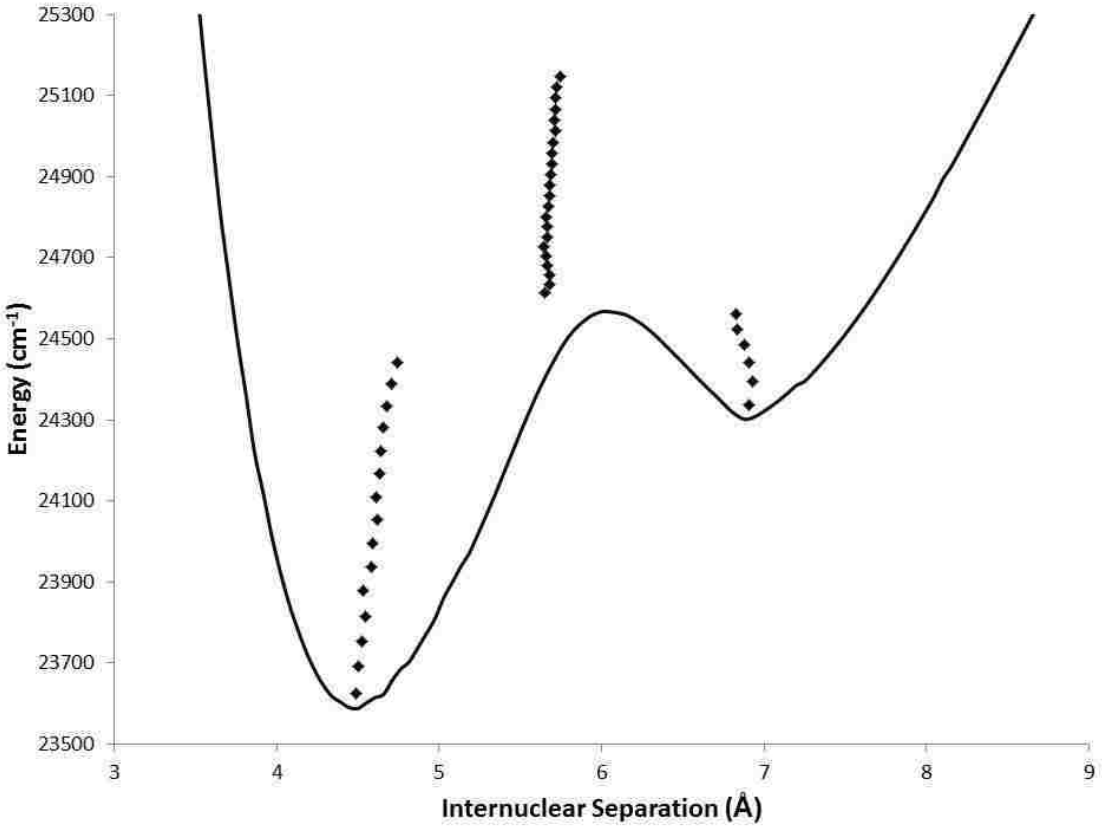

Figure 7.4: Plot of G_v versus R_{eq} for calculated vibrational levels of the $4^3\Pi_{0^+}$ state. The theoretical potential is also plotted for reference. The calculated vibrational levels are clearly separated into three distinct regions: one set above the barrier, one set associated with the outer well, and one set associated with the inner well.

v_{outer}	G_v (cm^{-1})	B_v (cm^{-1})	R_{eq}^v (Å)		v_{total}	G_v (cm^{-1})	B_v (cm^{-1})	R_{eq}^v (Å)
0	24337.4381	0.018047	6.905		25	24614.0418	0.026939	5.652
1	24396.0345	0.017937	6.927		26	24634.7537	0.026707	5.677
2	24441.5660	0.018036	6.908		27	24657.1106	0.026671	5.680
3	24483.8450	0.018182	6.880		28	24679.7406	0.026796	5.667
4	24523.9806	0.018437	6.832		29	24703.2069	0.026867	5.660
5	24561.6423	0.018469	6.826		30	24727.1343	0.027006	5.645
v_{inner}	G_v (cm^{-1})	B_v (cm^{-1})	R_{eq}^v (Å)		31	24751.4003	0.026834	5.663
0	23624.6562	0.042781	4.485		32	24776.1600	0.026783	5.668
1	23691.1061	0.042392	4.506		33	24801.2379	0.026883	5.658
2	23754.4020	0.042065	4.523		34	24826.7395	0.026765	5.670
3	23815.6921	0.041630	4.547		35	24852.5027	0.026652	5.682
4	23877.9722	0.041851	4.534		36	24878.4586	0.026678	5.680
5	23937.8853	0.041004	4.581		37	24904.9648	0.026580	5.690
6	23996.4644	0.040825	4.591		38	24931.4299	0.026568	5.691
7	24052.6102	0.040318	4.620		39	24958.0601	0.026570	5.691
8	24110.4187	0.040518	4.609		40	24984.9303	0.026458	5.703
9	24167.7223	0.040051	4.635		41	25011.7180	0.026357	5.714
10	24224.2281	0.039995	4.639		42	25038.7145	0.026391	5.710
11	24279.8984	0.039643	4.659		43	25065.8534	0.026361	5.714
12	24334.8748	0.039353	4.676		44	25093.2027	0.026323	5.718
13	24388.6662	0.038848	4.707		45	25120.7388	0.026251	5.726
14	24440.6931	0.038292	4.741		46	25148.3128	0.026051	5.748

Table 7.1: G_v, B_v, and R_{eq}^v values calculated from the theoretical $4^3\Pi_{0^+}$ potential of [12].

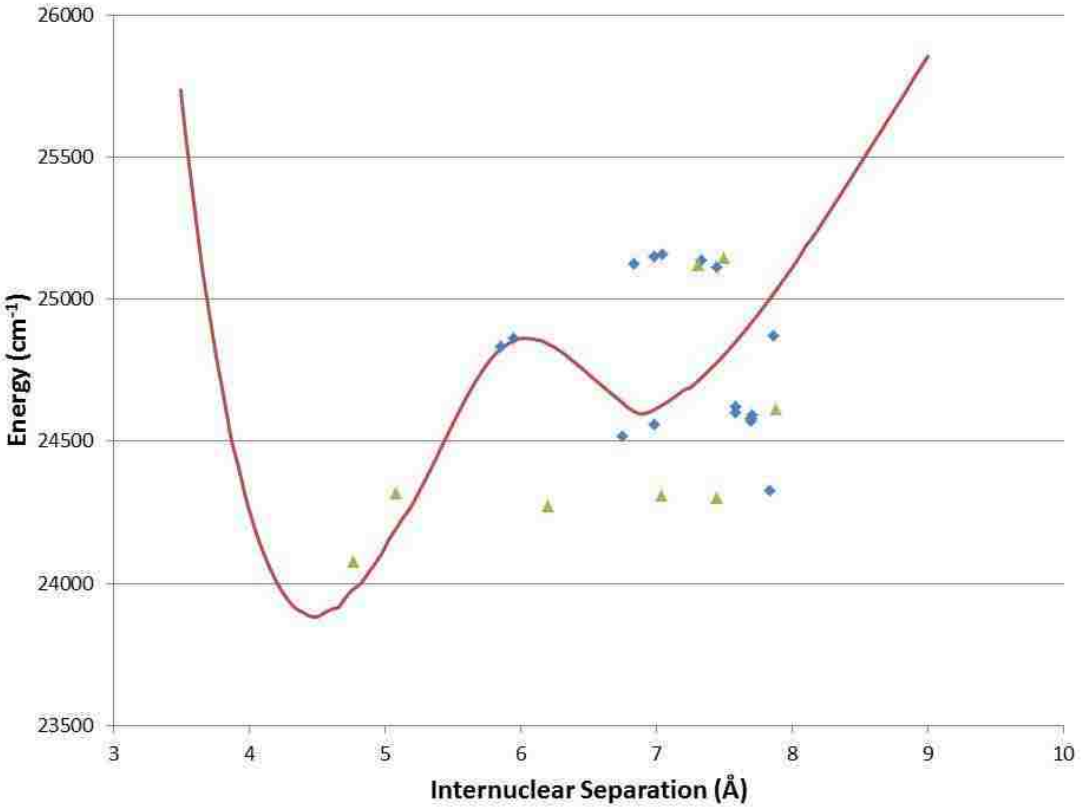

Figure 7.5: Plot of G_v versus $R_{\rm eq}^v$ for measured vibrational levels of the $4^3\Pi_{0^+}$ state. The theoretical potential is also plotted for reference. Green triangles represent vibrational levels for which several different rotational levels were observed, while blue diamonds represent vibrational levels for which only two rotational levels (one P line and one R line from a single intermediate state level) were observed.

pump transition. Blue diamonds represent vibrational levels for which we only have two measured rotational level energies, corresponding to one P and one R line from a single intermediate level. The G_v and $R^v_{\rm eq}$ values for these latter vibrational levels are not as accurate since any small perturbation in one or both of the levels could dramatically affect the G_v and B_v constants. From what we see in Figure 7.5, it is likely that the theoretical potential would need to be shifted to larger R and lower energy to accommodate the measured levels. However, the positions of points associated with vibrational levels in the region where there should be both inner and outer well levels imply discrepancies that no adjustment of the potential would be able to accommodate. For example, there are energy levels that seem to lie well above the barrier but still have large $R_{\rm eq}$ values that are more suggestive of the outer well position. To understand these issues we need a more complete picture of the energy level structure of the $4^3\Pi_{0^+}$ state, most critically near the bottom of the potential. However, at the moment this is not possible in our lab because this lower region of the potential lies in an energy range that cannot be reached with our current laser systems.

Since we are unable to determine an accurate potential energy curve for the $4^3\Pi_{0^+}$ state with our current limited dataset, it is best to summarize the observed level energies by reporting the G_v and B_v constants calculated from the data as described above. These are given in Table 7.2 for all measured vibrational levels along, with the relative vibrational numbering. Appendix C gives a full list of measured level energies.

7.3 Bound-free fluorescence spectra

As mentioned above, the resolved bound-free fluorescence spectra from the higher rovibrational levels of the NaCs $4^3\Pi_{0^+}$ state are very similar in appearance, including the number of broad oscillations. Only small variations in the interference structure distinguish the individual spectra associated with different vibrational levels. However, lower lying levels with energies approaching the barrier region and below,

v_{rel}	G_v	B_v	R^v_{eq}
v_{A}+6	25157.95	0.01736	7.04
v_{A}+5	25150.57	0.01765	6.98
v_{A}+4	25146.43	0.01535	7.49
v_{A}+3	25135.79	0.01601	7.33
v_{A}+2	25123.50	0.01844	6.83
v_{A}+1	25120.49	0.01614	7.30
v_{A}	25112.38	0.01553	7.44
v_{B}+2	24873.05	0.01395	7.86
v_{B}	24833.35	0.02518	5.85
v_{C}+10	24622.46	0.01498	7.58
v_{C}+9	24613.92	0.01387	7.88
v_{C}+8	24601.94	0.01497	7.58
v_{C}+7	24592.40	0.01451	7.70
v_{C}+6	24582.15	0.01454	7.69
v_{C}+5	24571.97	0.01456	7.69
v_{C}+4	24558.70	0.01766	6.98
v_{C}	24517.48	0.01889	6.75
v_{D}	24079.43	0.03802	4.76
v_{E}	24317.14	0.03336	5.08
v_{F}+3	24326.25	0.01403	7.83
v_{F}+2	24308.77	0.01741	7.03
v_{F}+1	24302.12	0.01553	7.44
v_{F}	24274.16	0.02240	6.20

Table 7.2: Results of least squares fits of rotational progression data to Eq. (7.1) for each observed vibrational state of the NaCs $4^3\Pi_{0^+}$ state.

display spectra that look quite different. Figure 7.6 shows several resolved bound-free spectra from some of the lowest studied rovibrational levels of the $4^3\Pi_{0^+}$ state. The top spectrum in an example of the resolved bound-free fluorescence seen from levels that lie above the barrier. The most useful information to be gathered from the three lower spectra is the absolute vibrational numbering. The lowest spectrum almost certainly corresponds to the $v = 4$ vibrational level, with the second one likely corresponding to $v = 6$. These vibrational levels likely lie below the barrier such that there is little to no interference structure. In principle, one should be able to now assign an absolute vibrational numbering to all the levels that lie higher in energy, which were previously only labeled with relative v's. Unfortunately, these particular spectra were taken with our lasers at the absolute end of their tuning ranges and as a result the wavemeter calibration is not valid. Because of this, the levels associated with these spectra do not appear in Table 7.2.

Figure 7.7 shows BCONT simulations of resolved bound-free fluorescence from levels approximately corresponding to those shown in Figure 7.6. These simulations use the theoretical $4^3\Pi_{0^+}$ potential of Korek *et al.* [12], the experimental $1(a)^3\Sigma^+$ potential of Ashman *et al.* [3], and the theoretical $4^3\Pi_{0^+} \rightarrow 1(a)^3\Sigma^+$ transition dipole moment function of Aymar and Dulieu [17]. Comparing the simulations of Fig. 7.7 to the experimental spectra of Fig. 7.6 we see that the long wavelength end of the simulations extend much farther to the red than the experimental spectra, by as much as 20 nm or more. By looking at the difference potential, Figure 7.2, the CFCA suggests that the long wavelength end of the bound-free fluorescence corresponds to the smallest internuclear separations. This implies that the inner wall of the theoretical $4^3\Pi_{0^+}$ potential needs to be shifted to larger R (or that the repulsive wall of the experimental$1(a)^3\Sigma^+$ potential is too steep). The cutoffs at the short wavelength end of the experimental spectra and simulations are in fairly good agreement, as is expected based on energy constraints. Obtaining additional bound-free spectra from the lowest levels of the $4^3\Pi_{0^+}$ state could give us more insight into the shape of the potential and a more reliable assignment of the vibrational quantum number.

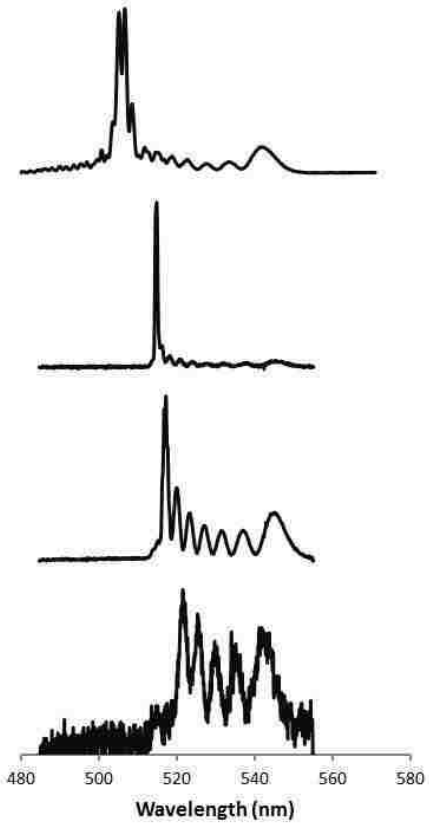

Figure 7.6: Resolved bound-free fluorescence spectra for several different vibrational levels of the $4^3\Pi_{0^+}$ state. From top to bottom, these spectra show bound-free emission to the $1(a)^3\Sigma^+$ state from $4^3\Pi_{0^+}$ ($v_A + 1$, 43), ($v_C + 1$, 26), (6, 16), and (4, 16 or 18). Vibrational quantum number assignments are tentative.

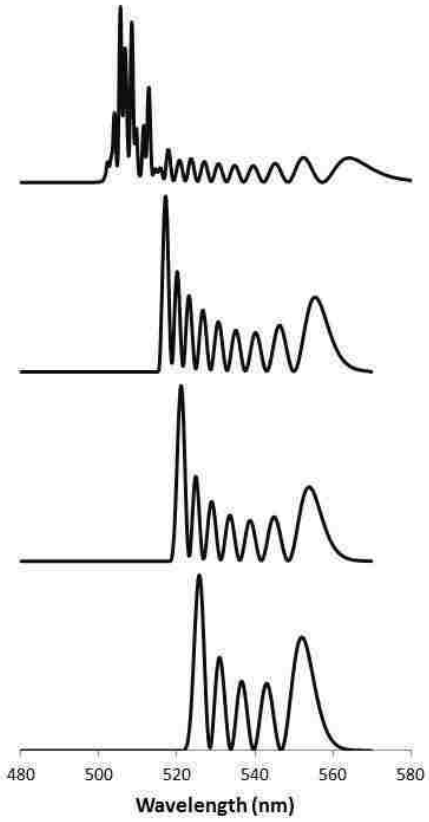

Figure 7.7: BCONT simulations of bound-free spectra for several different vibrational levels of the $4^3\Pi_{0^+}$ state. From top to bottom , these simulations show bound-free emission to the $1(a)^3\Sigma^+$ state from $4^3\Pi_{0^+}$ (32, 43), (8, 26), (6, 16), and (4, 16). The vibrational number for the top spectrum was chosen such that the calculated total energy was as close as possible to the measured energy of the top spectrum shown in Fig. 7.6.

Chapter 8

Conclusions and Future Work

8.1 Conclusions

The work presented in this dissertation was undertaken in order to increase our knowledge of high lying electronic states in NaCs. Our lab's first study of these states was carried out by Ashman *et al.* who mapped out the $5^3\Pi_{0^+}$ potential well [3]. He also mapped the $5^3\Pi_{0^+} \rightarrow 1(a)^3\Sigma^+$ transition dipole moment function along with the repulsive wall of the $1(a)^3\Sigma^+$ potential by comparing simulated and experimental bound-free emission spectra. It was evident from the experimental $5^3\Pi_{0^+}$ IPA potential obtained by Ashman that other nearby electronic states interact with the $5^3\Pi_{0^+}$ state [3]. The work presented here focuses on understanding the interactions between the $11(0^+)$ [$5^3\Pi_{0^+}$] and $12(0^+)$ [$7^1\Sigma^+$] states of NaCs.

Upper state rovibrational levels of several electronic states were identified and categorized based on the resolved bound-free spectra. One such grouping of rovibrational levels corresponds to the $12(0^+)$ electronic state of NaCs. We made use of a change-coupled device (CCD) array detector to identify these rovibrational levels by observing the resulting $12(0^+) \rightarrow 1(a)^3\Sigma^+$ bound-free resolved fluorescence spectra. The CCD detector greatly reduced the amount of time required to obtain such spectra compared to the previously used setup consisting of a monochromator and photomultiplier tube. We measured energies of 184 $12(0^+)$ rovibrational levels

covering a vibrational level range of $v = 0 - 14$. These level energies were used to construct an experimental potential by first fitting the energies to Dunham coefficients. The Dunham coefficients were then used to construct a Rydberg-Klein-Rees potential which was used as a starting point for applying the Inverted Perturbation Approach (IPA). The final IPA potential reproduces the measured level energies for $v = 0 - 10$ with an RMS deviation of 0.034 cm^{-1}.

Analysis of the intensity patterns in the $12(0^+) \rightarrow 1(a)^3\Sigma^+$ bound-free emission showed distinct features that could not be reproduced when using the experimental potential to simulate spectra. We determined that these features are the result of two stages of interactions between the $11(0^+)$ and $12(0^+)$ electronic states. First, the electronic states interact via the spin-orbit effect. In Hund's case (a) notation the $11(0^+)$ and $12(0^+)$ states are labeled as the $5^3\Pi_{0^+}$ and $7^1\Sigma^+$ states, respectively. Spin-orbit interactions between a $^1\Sigma^+$ state and a $^3\Pi_{0^+}$ state are very common and result in individual levels of the two states that have both singlet and triplet character. However, this interaction alone is not enough to explain the intensity patterns we observe for the $12(0^+) \rightarrow 1(a)^3\Sigma^+$ bound-free spectra. A second interaction, which we believe to be non-adiabatic coupling, is necessary to produce the type of quantum interference that results in the resolved spectra we observe.

We determined a model for the form of the wavefunction for a particular energy level which is mixed via this two stage coupling. The resulting mixed wavefunctions have direct and cross term components of both singlet and triplet character. The program BCONT was used to simulate bound-bound and bound-free resolved spectra resulting from these wavefunctions. The expansion coefficients describing the mixing between the electronic states and the individual rovibrational levels were adjusted so that the simulations matched the experimental spectra as closely as possible. From the fitted coefficients, we obtain information about these interactions. This information, gained from the studies of mixed wavefunctions, leading to quantum interference effects on the bound-bound and bound-free emission intensity patterns, is a different and more sensitive method of studying such small interactions compared to the more usual way of studying perturbations through energy level shifts.

In this work, we also began studies of the $4^3\Pi_{0^+}$ state of NaCs. The $4^3\Pi_{0^+}$ electronic state exhibits a double minimum potential energy curve. The barrier in the potential is evidence of an avoided crossing with higher electronic states, most likely the $11(0^+)$ and $12(0^+)$ states. Since the $4^3\Pi_{0^+}$ state is likely to interact with the other electronic states studied in this work, we also sought to map out the $4^3\Pi_{0^+}$ potential. The $4^3\Pi_{0^+} \rightarrow 1(a)^3\Sigma^+$ bound-free resolved fluorescence is particularly interesting since it shows strong interference features. However, the nature of the quantum interference observed in the resolved $4^3\Pi_{0^+} \rightarrow 1(a)^3\Sigma^+$ fluorescence is different from that of the $11(0^+)$ and $12(0^+)$ states described above. The double minimum in the $4^3\Pi_{0^+}$ potential energy curve results in a non-monotonic difference potential. Under the Classical Franck-Condon Approximation, this means that molecules at more than one value of the internuclear separation contribute to the fluorescence at a particular wavelength. Quantum mechanically, one would say that the wavefunction overlap integral has significant contributions from two separate regions of R space.

By identifying levels with these distinct bound-free spectra, we compiled a set of 112 rovibrational levels of the $4^3\Pi_{0^+}$ state. Unfortunately, restrictions on laser wavelengths currently available in our lab prevent us from carrying out a complete analysis of the $4^3\Pi_{0^+}$ electronic state at this time.

8.2 Future Work

The work presented here has greatly expanded our knowledge of small interactions between molecular electronic states in general, and high lying electronic states of NaCs in particular, and of how to obtain information about these interactions through observations of resolved bound-free and bound-bound spectra. Although we believe the basic two-stage coupling model presented in this dissertation contains the essential physics to explain our observations, there are still ways that the model can be improved to give a more complete description of the interactions. Such improvements will be the subject of future work.

The most prominent feature left out of the current model is the dependence of

the spin-orbit mixing angle, θ, on R. As mentioned in Sec. 6.4, the expansion coefficients used to express the relativistic electronic wavefunctions in terms of the non-relativistic electronic wavefunctions should depend on the internuclear separation coordinate, R. The fitting of bound-free and bound-bound spectra described in Sec. 6.3 was carried out assuming a constant value for θ [which probably best represents the average value of $\theta(R)$ over the relevant range of R]. Figure 6.19 shows that a preliminary rough adjustment of an assumed linear $\theta(R)$ dependence can give better agreement between the simulated and experimental spectra.

Figures 8.1 and 8.2 show a rough preliminary fit of simulations of resolved fluorescence from the $11(0^+)$ (6, 45) and $12(0^+)$ (4, 45) levels. These levels lie above those that were studied in the work presented in Chapter 6. The fitted values for θ and ϕ for the $11(0^+)$ (6, 45) and $12(0^+)$ (4, 45) pair are 0.56 radians and 0.6 radians, respectively. Since the levels involved in these new fits are higher vibrational levels, the wavefunctions span a larger range of R. Therefore, if θ does have a significant R dependence, it will likely become more and more important for higher vibrational levels. This appears to be the case, since we find that the fits displayed in Figs. 8.1 and 8.2 are not very good. We believe that these fits can be improved dramatically by incorporating an R dependent θ.

A second issue that we wish to explore in the future involves the magnitude of θ and ϕ, for higher vibrational levels. We note that the average θ and ϕ values used to obtain the "best fit" simulations shown in Figs. 8.1 and 8.2 are a factor of 2-3 times larger than those used in the fits described in Sec. 6.3. When the values of θ and ϕ are larger, the $\sin\theta \sin\phi$ terms in the direct components become relatively more significant and have a greater effect on the intensity distributions seen in the resolved fluorescence. Ashman *et al.* [3] mention that one oscillation at the short wavelength end of the bound-free emission from $11(0^+)$ (v=6) levels seemed to be washed out in their spectra, for reasons that they attribute to resolution issues. Since we now know that the $11(0^+)$ and $12(0^+)$ states interact in a complicated way, we may be able to explain the suppressed peak in the bound-free spectrum due to interference in what we call the direct component of the wavefunction. Fitting higher vibrational levels, which may have more significant direct term interference,

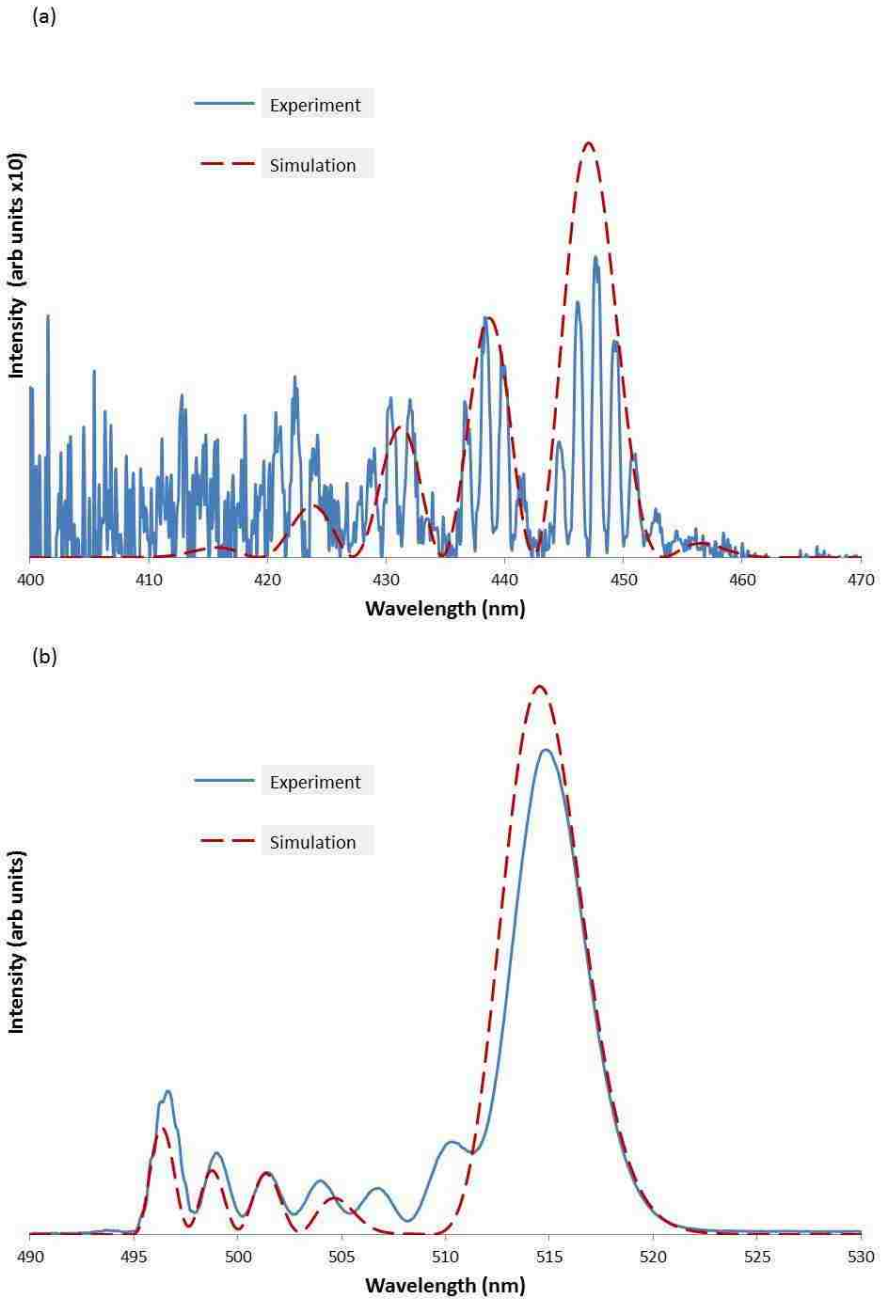

Figure 8.1: Comparison of experimental and simulated spectra for $12(0^+)$ (4, 45) $\rightarrow$ $1(X)^1\Sigma^+$, $1(a)^3\Sigma^+$ transitions. These spectra result from a mixture of pure $11(0^+)$ (6, 45) and $12(0^+)$ (4, 45) wavefunctions according to Eqs. (6.33) and (6.34), with $\phi = 0.6$ radians and $\theta = 0.56$ radians. (a) $12(0^+)$ (4, 45) $\rightarrow$ $1(X)^1\Sigma^+$ emission, and (b) $12(0^+)$ (4, 45) $\rightarrow$ $1(a)^3\Sigma^+$ emission.

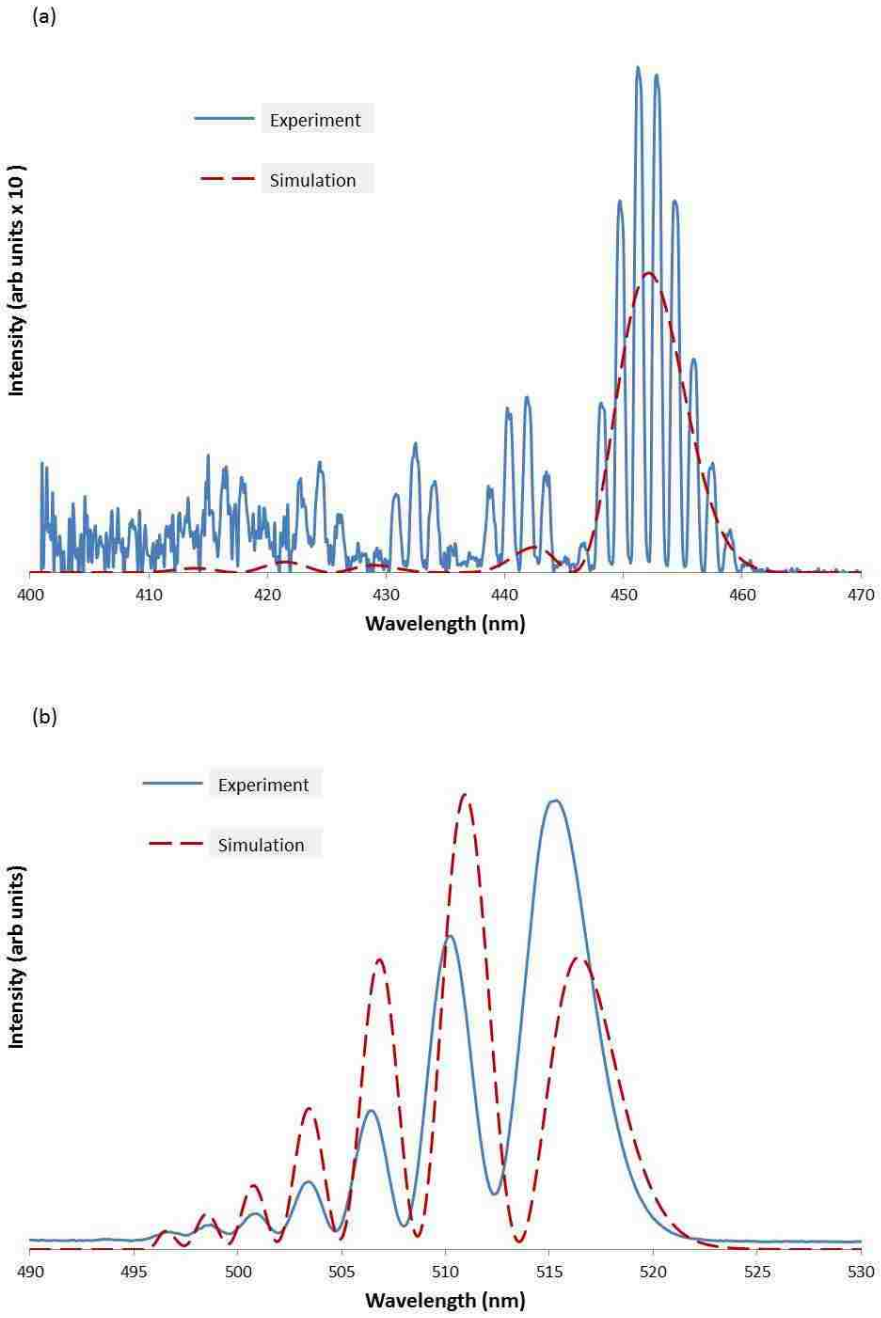

Figure 8.2: Comparison of experimental and simulated spectra for $11(0^+)$ (6, 45) $\rightarrow$ $1(X)^1\Sigma^+$, $1(a)^3\Sigma^+$ transitions. These spectra result from a mixture of pure $11(0^+)$ (6, 45) and $12(0^+)$ (4, 45) wavefunctions according to Eqs. (6.33) and (6.34), with $\phi = 0.6$ radians and $\theta = 0.56$ radians. (a) $11(0^+)$ (4, 45) $\rightarrow$ $1(X)^1\Sigma^+$ emission, and (b) $11(0^+)$ (4, 45) $\rightarrow$ $1(a)^3\Sigma^+$ emission.

could give more insight into how θ depends on R, but also on subtle changes in the resolved bound-free and bound-bound emission.

Interference in the direct components of the wavefunctions also influences another aspect that we would like to address in future work. For the simulations shown in this dissertation, the theoretical $7^1\Sigma^+ \rightarrow 1(X)^1\Sigma^+$ transition dipole moment (TDM) function was used. A more accurate fit requires the use of an experimentally determined $7^1\Sigma^+ \rightarrow 1(X)^1\Sigma^+$ TDM function. This can determined by adjusting parameters describing the TDM function in order to give good agreement between simulations and bound-bound $7^1\Sigma^+ \rightarrow 1(X)^1\Sigma^+$ resolved fluorescence. However, since the $12(0^+)$ state undergoes mixing with the $11(0^+)$ state as described here, the component of the wavefunction with $7^1\Sigma^+$ character is not necessarily simply the $12(0^+)$ wavefunction. This means that the wavefunction component fitting and the $7^1\Sigma^+ \rightarrow 1(X)^1\Sigma^+$ TDM function fitting to reproduce the bound-free and bound-bound spectra should be carried out simultaneously.

All the fits described in this dissertation were done by manually adjusting the mixing angle parameters. Future work on the interactions of these two states will likely involve more complicated global fitting of the resolved spectra. Since $\theta(R)$ is associated with the spin-orbit mixing of the electronic states, as opposed to the individual rovibrational levels, it should be treated as a global parameter. A more sophisticated fit would involve several parameters to describe the functional form for the global $\theta(R)$ function, which would then be used in the same way for each vibrational level, along with local mixing parameters, ϕ_v, which could vary from one vibrational level to the next.

Finally, work will continue to map out the $4^3\Pi_{0^+}$ electronic state of NaCs. In order to have the most complete picture of the $4^3\Pi_{0^+}$ potential, it is critical to acquire rovibrational level data down to the bottom of the well. Extension of the dataset in this regard is currently not possible since the lowest energy region that we can access with our lasers is limited. The dataset presented here is compiled with the intent that it will be used someday as a part of a more complete study of the $4^3\Pi_{0^+}$ state when new laser equipment becomes available to us, possibly through collaboration with another research group.

Appendix A

$2(A)^1\Sigma^+$ Experimental Data

The following table compiles measured $2(A)^1\Sigma^+$ level energies determined in this work and work done by Ashman *et al.* [3]. v' and J' denote the $2(A)^1\Sigma^+$ state vibrational and rotational quantum numbers, respectively. v'' and J'' denote the ground $1(X)^1\Sigma^+$ state vibrational and rotational quantum numbers, respectively. $E_{\rm gs}$ is the energy of the $1(X)^1\Sigma^+$ rovibrational level, calculated with experimental Dunham coefficients from Docenko *et al.* [15], which are reported to be accurate to $\pm$ 0.003 cm^{-1}. $E_{2(A)^1\Sigma^+\,(v',J')}$ is the total energy of the $2(A)^1\Sigma^+$ rovibrational level. We assign a laser frequency calibration error of $\pm$ 0.01 cm^{-1}, hence $E_{\rm pump}$, and $E_{2(A)^1\Sigma^+\,(v',J')}$ should be assigned an uncertainty of $\pm$ 0.01 cm^{-1}. The final column distinguishes whether the level was measured in this work (*) or in Ref. [3] (blank).

v'	J'	v''	J''	$E_{\rm gs}$ (cm^{-1})	$E_{\rm pump}$ (cm^{-1})	$E_{2(A)^1\Sigma^+\,(v',J')}$ (cm^{-1})	Note
9	13	0	14	61.513	11019.23	11080.74	*
9	14	0	15	63.249	11018.76	11082.01	*
9	14	0	13	59.893	11022.11	11082.00	*

v'	J'	v''	J''	E_{gs} (cm^{-1})	E_{pump} (cm^{-1})	$E_{2(A)^1\Sigma^+\,(v',J')}$ (cm^{-1})	Note
9	15	0	16	65.100	11018.27	11083.36	*
9	15	0	14	61.513	11021.85	11083.36	*
9	16	0	17	67.067	11017.75	11084.82	*
9	16	0	15	63.249	11021.57	11084.82	*
9	17	0	18	69.149	11017.22	11086.37	*
9	17	0	16	65.100	11021.26	11086.36	*
9	17	0	18	69.149	11017.21	11086.36	*
9	17	0	16	65.100	11021.26	11086.36	*
9	18	0	19	71.347	11016.66	11088.00	*
9	18	0	17	67.067	11020.94	11088.01	*
9	19	0	20	73.660	11016.08	11089.74	*
9	19	0	18	69.149	11020.59	11089.74	*
9	20	0	0	71.347	11020.23	11091.58	*
9	22	0	21	76.089	11019.45	11095.54	*
9	23	0	22	78.633	11019.03	11097.67	*
9	23	0	24	84.066	11013.60	11097.67	*
9	24	0	23	81.292	11018.60	11099.89	*
9	24	0	25	86.956	11012.93	11099.89	*
9	25	0	24	84.066	11018.15	11102.22	*
9	25	0	26	89.961	11012.26	11102.22	*

v'	J'	v''	J''	E_{gs} (cm^{-1})	E_{pump} (cm^{-1})	$E_{2(A)^1\Sigma^+\,(v',J')}$ (cm^{-1})	Note
9	26	0	25	86.956	11017.69	11104.64	*
9	26	0	27	93.081	11011.56	11104.64	*
9	27	0	26	89.961	11017.22	11107.18	*
9	27	0	28	96.316	11010.86	11107.17	*
9	28	0	27	93.081	11016.73	11109.81	*
9	28	0	29	99.666	11010.14	11109.81	*
9	29	0	28	96.316	11016.23	11112.55	*
9	29	0	30	103.131	11009.41	11112.54	*
9	30	0	29	99.666	11015.73	11115.39	*
9	30	0	31	106.711	11008.68	11115.39	*
9	31	0	30	103.131	11015.21	11118.34	*
9	31	0	32	110.406	11007.93	11118.34	*
9	32	0	33	114.215	11007.18	11121.40	*
9	33	0	34	118.140	11006.43	11124.57	*
12	22	0	21	76.089	11171.51	11247.60	*
12	23	0	22	78.633	11171.18	11249.81	*
12	24	0	23	81.292	11170.79	11252.08	*
12	26	0	27	93.081	11163.70	11256.78	*
12	26	0	25	86.956	11169.82	11256.77	*
12	27	0	28	96.316	11162.89	11259.20	*

v'	J'	v''	J''	E_{gs} (cm^{-1})	E_{pump} (cm^{-1})	$E_{2(A)^1\Sigma^+\,(v',J')}$ (cm^{-1})	Note
12	27	0	26	89.961	11169.24	11259.20	*
12	28	0	29	99.666	11162.01	11261.68	*
12	28	0	27	93.081	11168.59	11261.67	*
12	29	0	30	103.131	11161.07	11264.20	*
12	29	0	28	96.316	11167.88	11264.20	*
12	30	0	31	106.711	11160.06	11266.78	*
12	30	0	29	99.666	11167.11	11266.78	*
12	31	0	32	110.406	11159.01	11269.41	*
12	31	0	30	103.131	11166.28	11269.41	*
12	32	0	33	114.215	11157.89	11272.11	*
12	32	0	31	106.711	11165.40	11272.11	*
12	33	0	32	110.406	11164.46	11274.87	*
12	33	0	34	118.140	11156.73	11274.87	*
12	34	0	35	122.179	11155.49	11277.67	*
12	34	0	33	114.215	11163.45	11277.67	*
12	35	0	36	126.332	11154.25	11280.59	*
12	35	0	34	118.140	11162.45	11280.59	*
12	36	0	37	130.600	11152.95	11283.55	*
12	36	0	35	122.179	11161.38	11283.56	*
12	37	0	38	134.982	11151.61	11286.59	*

v'	J'	v''	J''	E_{gs} (cm^{-1})	E_{pump} (cm^{-1})	$E_{2(A)^1\Sigma^+\,(v',J')}$ (cm^{-1})	Note
12	37	0	36	126.332	11160.26	11286.59	*
12	38	0	39	139.479	11150.23	11289.70	*
12	38	0	37	130.600	11159.11	11289.71	*
12	39	0	40	144.090	11148.80	11292.89	*
12	39	0	38	134.982	11157.91	11292.90	*
12	40	0	41	148.816	11147.34	11296.16	*
12	40	0	39	139.479	11156.69	11296.17	*
12	41	0	42	153.655	11145.85	11299.51	*
12	41	0	40	144.090	11155.42	11299.51	*
12	41	0	42	153.655	11145.85	11299.50	*
12	42	0	41	148.816	11154.12	11302.93	*
12	42	0	43	158.609	11144.32	11302.93	*
12	43	0	42	153.655	11152.79	11306.44	*
12	43	0	44	163.676	11142.76	11306.43	*
12	44	0	43	158.609	11151.42	11310.03	*
12	44	0	45	168.858	11141.17	11310.02	*
12	45	0	44	163.676	11150.03	11313.71	*
12	45	0	46	174.153	11139.55	11313.70	*
12	46	0	45	168.858	11148.60	11317.46	*
12	46	0	47	179.562	11137.89	11317.45	*

v'	J'	v''	J''	E_{gs} (cm^{-1})	E_{pump} (cm^{-1})	$E_{2(A)^1\Sigma^+\,(v',J')}$ (cm^{-1})	Note
12	47	0	46	174.153	11147.15	11321.30	*
12	47	0	48	185.085	11136.21	11321.30	*
12	48	0	47	179.562	11145.67	11325.23	*
12	48	0	47	179.562	11145.66	11325.23	*
12	49	0	48	185.085	11144.16	11329.24	*
12	50	0	49	190.721	11142.63	11333.35	*
12	51	0	50	196.470	11141.08	11337.55	*
12	52	0	51	202.333	11139.51	11341.84	*
12	53	0	52	208.310	11137.92	11346.23	*
12	54	0	53	214.399	11136.31	11350.71	*
14	1	0	2	49.706	11296.42	11346.13	*
14	2	0	3	50.053	11296.22	11346.27	*
14	3	0	4	50.517	11296.01	11346.53	*
14	4	0	5	51.095	11295.76	11346.86	*
14	5	0	6	51.790	11295.48	11347.27	*
14	6	0	7	52.601	11295.17	11347.77	*
14	7	0	8	53.527	11294.83	11348.36	*
14	8	0	9	54.569	11294.63	11349.20	*
14	9	0	10	55.726	11294.05	11349.78	*
14	10	0	9	54.569	11296.06	11350.63	

v'	J'	v''	J''	E_{gs} (cm^{-1})	E_{pump} (cm^{-1})	$E_{2(A)^1\Sigma^+\,(v',J')}$ (cm^{-1})	Note
14	10	0	9	54.569	11296.06	11350.63	*
14	11	0	10	55.726	11295.80	11351.52	
14	12	0	11	56.999	11295.52	11352.52	
14	13	0	12	58.388	11295.22	11353.61	
14	13	0	14	61.513	11292.10	11353.61	
14	14	0	13	59.893	11294.89	11354.78	
14	14	0	15	63.249	11291.54	11354.79	
14	15	0	14	61.513	11294.53	11356.04	
14	15	0	16	65.100	11290.94	11356.04	
14	16	0	15	63.249	11294.14	11357.39	
14	16	0	17	67.067	11290.32	11357.38	
14	17	0	16	65.100	11293.71	11358.81	
14	17	0	18	69.149	11289.66	11358.81	
14	18	0	17	67.067	11293.26	11360.32	
14	18	0	19	71.347	11288.98	11360.32	
14	19	0	18	69.149	11292.78	11361.92	
14	19	0	20	73.660	11288.26	11361.92	
14	20	0	19	71.347	11292.27	11363.61	
14	20	0	21	76.089	11287.52	11363.61	
14	21	0	20	73.660	11291.73	11365.39	

v'	J'	v''	J''	E_{gs} (cm^{-1})	E_{pump} (cm^{-1})	$E_{2(A)^1\Sigma^+\,(v',J')}$ (cm^{-1})	Note
14	21	0	22	78.633	11286.76	11365.39	
14	22	0	21	76.089	11291.17	11367.26	
14	22	0	23	81.292	11285.97	11367.26	
14	23	0	22	78.633	11290.58	11369.21	
14	23	0	24	84.066	11285.15	11369.22	
14	24	0	23	81.292	11289.97	11371.26	
14	24	0	25	86.956	11284.31	11371.27	
14	25	0	24	84.066	11289.34	11373.41	
14	25	0	24	84.066	11289.34	11373.41	
14	25	0	26	89.961	11283.45	11373.41	
14	26	0	25	86.956	11288.69	11375.64	
14	26	0	25	86.956	11288.69	11375.65	
14	26	0	27	93.081	11282.56	11375.64	
14	26	0	27	93.081	11282.57	11375.65	
14	27	0	26	89.961	11288.02	11377.98	
14	27	0	26	89.961	11288.02	11377.98	
14	27	0	28	96.316	11281.67	11377.98	
14	28	0	27	93.081	11287.34	11380.42	
14	28	0	27	93.081	11287.34	11380.42	
14	28	0	29	99.666	11280.75	11380.42	

v'	J'	v''	J''	E_{gs} (cm^{-1})	E_{pump} (cm^{-1})	$E_{2(A)^1\Sigma^+\,(v',J')}$ (cm^{-1})	Note
14	28	0	29	99.666	11280.75	11380.42	
14	29	0	28	96.316	11286.64	11382.96	
14	29	0	28	96.316	11286.64	11382.96	
14	29	0	30	103.131	11279.83	11382.96	
14	29	0	30	103.131	11279.83	11382.96	
14	30	0	29	99.666	11285.94	11385.60	
14	30	0	29	99.666	11285.94	11385.61	
14	30	0	31	106.711	11278.89	11385.60	
14	30	0	31	106.711	11278.89	11385.60	
14	31	0	30	103.131	11285.22	11388.35	
14	31	0	30	103.131	11285.23	11388.36	
14	31	0	32	110.406	11277.95	11388.35	
14	31	0	32	110.406	11277.95	11388.36	
14	32	0	31	106.711	11284.51	11391.22	
14	32	0	31	106.711	11284.51	11391.22	
14	33	0	32	110.406	11283.80	11394.20	
14	33	0	32	110.406	11283.80	11394.20	
14	34	0	33	114.215	11283.09	11397.30	
14	34	0	35	122.179	11275.12	11397.30	
14	35	0	34	118.140	11282.39	11400.53	

v'	J'	v''	J''	E_{gs} (cm^{-1})	E_{pump} (cm^{-1})	$E_{2(A)^1\Sigma^+\,(v',J')}$ (cm^{-1})	Note
14	35	0	36	126.332	11274.19	11400.52	
14	36	0	35	122.179	11281.71	11403.88	
14	36	0	37	130.600	11273.28	11403.88	
14	37	0	36	126.332	11281.04	11407.37	
14	37	0	38	134.983	11272.38	11407.37	
14	38	0	37	130.600	11280.39	11410.99	
14	38	0	39	139.479	11271.51	11410.99	
14	39	0	38	134.983	11279.75	11414.73	
14	39	0	40	144.090	11270.65	11414.74	
14	40	0	39	139.479	11279.15	11418.63	
14	40	0	41	148.816	11269.81	11418.63	
14	41	0	40	144.090	11278.57	11422.66	
14	41	0	42	153.655	11269.00	11422.66	
14	42	0	41	148.816	11278.02	11426.83	
14	42	0	43	158.609	11268.22	11426.83	
14	43	0	42	153.655	11277.49	11431.15	
14	43	0	44	163.676	11267.47	11431.14	
14	43	0	44	163.676	11267.47	11431.15	
14	44	0	43	158.609	11276.99	11435.60	
14	44	0	45	168.858	11266.74	11435.60	

v'	J'	v''	J''	E_{gs} (cm^{-1})	E_{pump} (cm^{-1})	$E_{2(A)^1\Sigma^+\,(v',J')}$ (cm^{-1})	Note
14	44	0	45	168.858	11266.74	11435.60	
14	45	0	44	163.676	11276.51	11440.19	
14	45	0	46	174.153	11266.03	11440.19	
14	45	0	46	174.153	11266.04	11440.19	
14	46	0	45	168.858	11276.06	11444.92	
14	46	0	47	179.562	11265.35	11444.91	
14	47	0	46	174.153	11275.62	11449.78	
14	47	0	48	185.085	11264.69	11449.78	
14	47	0	48	185.085	11264.70	11449.78	
14	47	0	48	185.085	11264.70	11449.78	
14	48	0	47	179.562	11275.21	11454.78	
14	48	0	49	190.721	11264.05	11454.77	
14	48	0	49	190.721	11264.06	11454.78	
14	48	0	49	190.721	11264.06	11454.78	
14	49	0	48	185.085	11274.82	11459.91	
14	49	0	50	196.470	11263.44	11459.91	
14	49	0	50	196.470	11263.44	11459.91	
14	49	0	50	196.470	11263.46	11459.93	
14	50	0	49	190.721	11274.46	11465.18	
14	50	0	51	202.333	11262.84	11465.18	

v'	J'	v''	J''	E_{gs} (cm^{-1})	E_{pump} (cm^{-1})	$E_{2(A)^1\Sigma^+\,(v',J')}$ (cm^{-1})	Note
14	50	0	51	202.333	11262.85	11465.18	
14	50	0	51	202.333	11262.85	11465.18	
14	51	0	50	196.470	11274.12	11470.59	
14	51	0	52	208.310	11262.28	11470.59	
14	51	0	52	208.310	11262.29	11470.59	
14	51	0	52	208.310	11262.29	11470.60	
14	52	0	51	202.333	11273.83	11476.17	
14	52	0	53	214.399	11261.77	11476.16	
14	52	0	53	214.399	11261.77	11476.17	
14	52	0	53	214.399	11261.77	11476.17	
14	53	0	52	208.310	11272.48	11480.79	
14	53	0	54	220.602	11260.20	11480.80	
14	53	0	54	220.602	11260.20	11480.80	
14	54	0	53	214.399	11272.32	11486.72	
14	54	0	53	214.399	11272.33	11486.73	
14	54	0	55	226.917	11259.81	11486.72	
14	54	0	55	226.917	11259.81	11486.73	
14	55	0	54	220.602	11272.08	11492.68	
14	55	0	54	220.602	11272.08	11492.68	
14	55	0	56	233.345	11259.33	11492.68	

v'	J'	v''	J''	E_{gs} (cm^{-1})	E_{pump} (cm^{-1})	$E_{2(A)^1\Sigma^+\,(v',J')}$ (cm^{-1})	Note
14	55	0	56	233.345	11259.33	11492.68	
14	56	0	55	226.917	11271.76	11498.68	
14	56	0	55	226.917	11271.76	11498.68	
14	56	0	57	239.886	11258.79	11498.68	
14	56	0	57	239.886	11258.79	11498.68	
14	57	0	56	233.345	11271.41	11504.76	
14	57	0	56	233.345	11271.41	11504.76	
14	57	0	58	246.540	11258.22	11504.76	
14	57	0	58	246.540	11258.22	11504.76	
14	58	0	57	239.886	11271.04	11510.92	
14	58	0	57	239.886	11271.04	11510.92	
14	58	0	59	253.306	11257.61	11510.92	
14	58	0	59	253.306	11257.61	11510.92	
14	59	0	58	246.540	11270.63	11517.17	
14	59	0	58	246.540	11270.63	11517.17	
14	59	0	60	260.185	11256.98	11517.17	
14	59	0	60	260.185	11256.98	11517.17	
14	60	0	59	253.306	11270.19	11523.50	
14	60	0	59	253.306	11270.19	11523.50	
14	60	0	61	267.176	11256.32	11523.50	

v'	J'	v''	J''	E_{gs} (cm^{-1})	E_{pump} (cm^{-1})	$E_{2(A)^1\Sigma^+\,(v',J')}$ (cm^{-1})	Note
14	60	0	61	267.176	11256.33	11523.50	
14	61	0	60	260.185	11269.72	11529.91	
14	61	0	62	274.279	11255.63	11529.90	
14	62	0	61	267.176	11269.19	11536.37	
14	62	0	63	281.494	11254.87	11536.37	
14	63	0	62	274.279	11268.59	11542.87	
14	63	0	64	288.822	11254.05	11542.87	
14	64	0	63	281.494	11267.90	11549.39	
14	64	0	65	296.261	11253.13	11549.39	
14	65	0	64	288.822	11267.06	11555.88	
14	65	0	66	303.811	11252.07	11555.88	
14	66	0	65	296.261	11266.04	11562.30	
14	66	0	67	311.474	11250.83	11562.30	
14	67	0	68	319.248	11249.36	11568.60	
14	67	0	68	319.248	11249.36	11568.60	
14	68	0	69	327.133	11247.63	11574.76	
14	68	0	69	327.133	11247.63	11574.77	
14	69	0	70	335.129	11245.67	11580.80	
14	70	0	71	343.237	11243.52	11586.75	
14	71	0	72	351.455	11241.20	11592.66	

v'	J'	v''	J''	E_{gs} (cm^{-1})	E_{pump} (cm^{-1})	$E_{2(A)^1\Sigma^+\,(v',J')}$ (cm^{-1})	Note
16	44	0	45	168.858	11375.67	11544.52	
18	1	0	2	49.706	11524.80	11574.50	
18	2	0	3	50.054	11524.61	11574.66	
18	2	0	3	50.054	11524.61	11574.66	
18	3	0	2	49.706	11525.18	11574.89	
18	3	0	4	50.517	11524.38	11574.89	
18	3	0	4	50.517	11524.38	11574.89	
18	4	0	3	50.054	11525.15	11575.20	
18	4	0	5	51.096	11524.11	11575.21	
18	4	0	5	51.096	11524.11	11575.21	
18	5	0	4	50.517	11525.08	11575.60	
18	5	0	6	51.790	11523.81	11575.60	
18	5	0	6	51.790	11523.81	11575.60	
18	6	0	5	51.096	11524.97	11576.07	
18	6	0	7	52.601	11523.46	11576.06	
18	6	0	7	52.601	11523.47	11576.07	
18	7	0	6	51.790	11524.82	11576.61	
18	7	0	6	51.790	11524.83	11576.62	
18	7	0	8	53.527	11523.09	11576.61	
18	7	0	8	53.527	11523.09	11576.61	

v'	J'	v''	J''	E_{gs} (cm^{-1})	E_{pump} (cm^{-1})	$E_{2(A)^1\Sigma^+\,(v',J')}$ (cm^{-1})	Note
18	8	0	7	52.601	11524.64	11577.24	
18	8	0	7	52.601	11524.64	11577.24	
18	8	0	9	54.569	11522.67	11577.24	
18	8	0	9	54.569	11522.67	11577.24	
18	9	0	8	53.527	11524.42	11577.95	
18	9	0	8	53.527	11524.42	11577.95	
18	9	0	10	55.726	11522.22	11577.95	
18	9	0	10	55.726	11522.22	11577.95	
18	10	0	9	54.569	11524.16	11578.73	
18	10	0	9	54.569	11524.16	11578.73	
18	10	0	11	56.999	11521.73	11578.73	
18	10	0	11	56.999	11521.73	11578.73	
18	11	0	10	55.726	11523.87	11579.59	
18	11	0	10	55.726	11523.87	11579.59	
18	11	0	12	58.388	11521.20	11579.59	
18	11	0	12	58.388	11521.21	11579.60	
18	12	0	11	56.999	11523.53	11580.53	
18	12	0	11	56.999	11523.54	11580.53	
18	12	0	13	59.893	11520.64	11580.53	
18	12	0	13	59.893	11520.65	11580.54	

v'	J'	v''	J''	E_{gs} (cm^{-1})	E_{pump} (cm^{-1})	$E_{2(A)^1\Sigma^+\,(v',J')}$ (cm^{-1})	Note
18	13	0	12	58.388	11523.16	11581.55	
18	13	0	12	58.388	11523.16	11581.55	
18	13	0	14	61.513	11520.04	11581.55	
18	13	0	14	61.513	11520.04	11581.55	
18	14	0	13	59.893	11522.75	11582.65	
18	14	0	13	59.893	11522.75	11582.65	
18	14	0	15	63.249	11519.40	11582.65	
18	14	0	15	63.249	11519.40	11582.65	
18	15	0	14	61.513	11522.31	11583.82	
18	15	0	14	61.513	11522.31	11583.82	
18	15	0	16	65.100	11518.73	11583.83	
18	15	0	16	65.100	11518.73	11583.83	
18	16	0	15	63.249	11521.83	11585.08	
18	16	0	15	63.249	11521.83	11585.08	
18	16	0	17	67.067	11518.01	11585.08	
18	16	0	17	67.067	11518.01	11585.08	
18	17	0	16	65.100	11521.31	11586.41	
18	17	0	16	65.100	11521.31	11586.41	
18	17	0	18	69.149	11517.26	11586.41	
18	17	0	18	69.149	11517.26	11586.41	

v'	J'	v''	J''	E_{gs} (cm^{-1})	E_{pump} (cm^{-1})	$E_{2(A)^1\Sigma^+\,(v',J')}$ (cm^{-1})	Note
18	18	0	17	67.067	11520.76	11587.82	
18	18	0	17	67.067	11520.76	11587.83	
18	18	0	19	71.347	11516.48	11587.82	
18	18	0	19	71.347	11516.48	11587.83	
18	19	0	18	69.149	11520.16	11589.31	
18	19	0	18	69.149	11520.17	11589.31	
18	19	0	20	73.660	11515.65	11589.31	
18	19	0	20	73.660	11515.65	11589.31	
18	20	0	19	71.347	11519.53	11590.88	
18	20	0	19	71.347	11519.54	11590.88	
18	20	0	21	76.089	11514.79	11590.88	
18	20	0	21	76.089	11514.80	11590.89	
18	21	0	20	73.660	11518.87	11592.53	
18	21	0	20	73.660	11518.87	11592.53	
18	21	0	22	78.633	11513.89	11592.52	
18	22	0	21	76.089	11518.17	11594.26	
18	22	0	21	76.089	11518.17	11594.26	
18	22	0	23	81.292	11512.96	11594.25	
18	23	0	22	78.633	11517.43	11596.06	
18	23	0	22	78.633	11517.43	11596.07	

v'	J'	v''	J''	E_{gs} (cm^{-1})	E_{pump} (cm^{-1})	$E_{2(A)^1\Sigma^+\,(v',J')}$ (cm^{-1})	Note
18	23	0	24	84.066	11511.99	11596.06	
18	24	0	23	81.292	11516.66	11597.95	
18	24	0	23	81.292	11516.66	11597.95	
18	24	0	25	86.956	11510.98	11597.94	
18	24	0	25	86.956	11510.99	11597.95	
18	25	0	24	84.066	11515.85	11599.92	
18	25	0	24	84.066	11515.85	11599.92	
18	25	0	26	89.961	11509.95	11599.91	
18	25	0	26	89.961	11509.95	11599.91	
18	26	0	25	86.956	11515.00	11601.95	
18	26	0	25	86.956	11515.01	11601.96	
18	26	0	27	93.081	11508.87	11601.95	
18	26	0	27	93.081	11508.88	11601.96	
18	27	0	26	89.961	11514.12	11604.08	
18	27	0	28	96.316	11507.76	11604.08	
18	27	0	28	96.316	11507.77	11604.09	
18	28	0	27	93.081	11513.20	11606.28	
18	28	0	29	99.666	11506.62	11606.28	
18	28	0	29	99.666	11506.63	11606.29	
18	29	0	28	96.316	11512.25	11608.57	

v'	J'	v''	J''	E_{gs} (cm^{-1})	E_{pump} (cm^{-1})	$E_{2(A)^1\Sigma^+\,(v',J')}$ (cm^{-1})	Note
18	29	0	30	103.131	11505.44	11608.57	
18	29	0	30	103.131	11505.45	11608.58	
18	30	0	29	99.666	11511.27	11610.94	
18	30	0	29	99.666	11511.28	11610.95	
18	30	0	31	106.711	11504.23	11610.94	
18	31	0	30	103.131	11510.26	11613.39	
18	31	0	30	103.131	11510.26	11613.40	
18	31	0	32	110.406	11502.98	11613.39	
18	32	0	31	106.711	11509.21	11615.92	
18	32	0	31	106.711	11509.21	11615.92	
18	32	0	33	114.215	11501.71	11615.92	
18	33	0	32	110.406	11508.13	11618.53	
18	33	0	32	110.406	11508.13	11618.53	
18	33	0	34	118.140	11500.39	11618.53	
18	34	0	33	114.215	11507.01	11621.22	
18	34	0	33	114.215	11507.01	11621.23	
18	34	0	35	122.179	11499.05	11621.22	
18	35	0	34	118.140	11505.86	11624.00	
18	35	0	34	118.140	11505.87	11624.01	
18	35	0	36	126.332	11497.67	11624.00	

v'	J'	v''	J''	E_{gs} (cm^{-1})	E_{pump} (cm^{-1})	$E_{2(A)^1\Sigma^+\,(v',J')}$ (cm^{-1})	Note
18	36	0	35	122.179	11504.68	11626.86	
18	36	0	37	130.600	11496.26	11626.86	
18	37	0	36	126.332	11503.48	11629.81	
18	37	0	38	134.983	11494.82	11629.80	
18	38	0	37	130.600	11502.23	11632.83	
18	38	0	39	139.479	11493.36	11632.84	
18	39	0	38	134.983	11500.97	11635.95	
18	39	0	40	144.090	11491.86	11635.95	
18	40	0	39	139.479	11499.67	11639.15	
18	40	0	41	148.816	11490.34	11639.15	
18	41	0	40	144.090	11498.35	11642.44	
18	41	0	42	153.655	11488.79	11642.44	
18	42	0	41	148.816	11497.00	11645.82	
18	42	0	43	158.609	11487.21	11645.82	
18	43	0	42	153.655	11495.63	11649.29	
18	43	0	44	163.676	11485.61	11649.29	
18	44	0	43	158.609	11494.24	11652.85	
18	44	0	45	168.858	11483.99	11652.85	
18	45	0	44	163.676	11492.83	11656.50	
18	45	0	46	174.153	11482.35	11656.50	

v'	J'	v''	J''	E_{gs} (cm^{-1})	E_{pump} (cm^{-1})	$E_{2(A)^1\Sigma^+\,(v',J')}$ (cm^{-1})	Note
18	46	0	45	168.858	11491.40	11660.26	
18	46	0	47	179.562	11480.69	11660.25	
18	47	0	46	174.153	11489.95	11664.10	
18	47	0	48	185.085	11479.02	11664.10	
18	48	0	47	179.562	11488.48	11668.05	
18	48	0	49	190.721	11477.33	11668.05	
18	49	0	48	185.085	11487.01	11672.09	
18	49	0	50	196.470	11475.62	11672.09	
18	50	0	49	190.721	11485.52	11676.25	
18	50	0	51	202.333	11473.92	11676.25	
18	51	0	50	196.470	11484.04	11680.51	
18	51	0	52	208.310	11472.20	11680.51	
18	52	0	51	202.333	11482.55	11684.88	
18	52	0	53	214.399	11470.49	11684.88	
18	53	0	52	208.310	11481.06	11689.37	
18	54	0	53	214.399	11479.58	11693.98	
18	55	0	54	220.602	11478.10	11698.71	
18	56	0	55	226.917	11476.64	11703.56	
18	57	0	56	233.345	11475.20	11708.54	
18	58	0	57	239.886	11473.78	11713.66	

v'	J'	v''	J''	E_{gs} (cm^{-1})	E_{pump} (cm^{-1})	$E_{2(A)^1\Sigma^+\,(v',J')}$ (cm^{-1})	Note
18	59	0	58	246.540	11472.38	11718.92	
18	60	0	59	253.306	11471.01	11724.32	
21	4	0	3	50.054	11685.40	11735.45	
21	5	0	4	50.517	11685.34	11735.86	
21	6	0	5	51.096	11685.26	11736.36	
21	6	0	7	52.601	11683.76	11736.36	
21	7	0	6	51.790	11685.15	11736.94	
21	7	0	8	53.527	11683.41	11736.93	
21	8	0	7	52.601	11685.00	11737.60	
21	8	0	9	54.569	11683.03	11737.60	
21	9	0	8	53.527	11684.81	11738.34	
21	9	0	10	55.726	11682.61	11738.34	
21	10	0	9	54.569	11684.60	11739.17	
21	10	0	11	56.999	11682.17	11739.16	
21	11	0	10	55.726	11684.34	11740.07	
21	11	0	12	58.388	11681.68	11740.07	
21	12	0	11	56.999	11684.06	11741.06	
21	12	0	13	59.893	11681.16	11741.05	
21	13	0	12	58.388	11683.73	11742.12	
21	13	0	14	61.513	11680.61	11742.12	

v'	J'	v''	J''	$E_{\rm gs}$ ($\rm cm^{-1}$)	$E_{\rm pump}$ ($\rm cm^{-1}$)	$E_{2(A)^1\Sigma^+\,(v',J')}$ ($\rm cm^{-1}$)	Note
21	14	0	13	59.893	11683.37	11743.26	
21	14	0	13	59.893	11683.37	11743.27	
21	14	0	15	63.249	11680.01	11743.26	
21	14	0	15	63.249	11680.02	11743.27	
21	15	0	14	61.513	11682.98	11744.50	
21	15	0	16	65.100	11679.39	11744.49	
21	16	0	15	63.249	11682.55	11745.80	
21	16	0	17	67.067	11678.73	11745.80	
21	17	0	16	65.100	11682.09	11747.19	
21	18	0	17	67.067	11681.59	11748.65	
21	19	0	18	69.149	11681.05	11750.19	
21	20	0	19	71.347	11680.47	11751.82	
21	21	0	20	73.660	11679.86	11753.52	
21	22	0	21	76.089	11679.21	11755.30	
21	23	0	22	78.633	11678.52	11757.15	
21	35	0	36	126.332	11659.00	11785.33	
21	36	0	37	130.600	11657.57	11788.17	
21	37	0	38	134.983	11656.10	11791.09	
21	38	0	39	139.479	11654.60	11794.08	
21	39	0	40	144.090	11653.05	11797.14	

v'	J'	v''	J''	E_{gs} (cm^{-1})	E_{pump} (cm^{-1})	$E_{2(A)^1\Sigma^+\,(v',J')}$ (cm^{-1})	Note
21	40	0	41	148.816	11651.47	11800.29	
21	41	0	40	144.090	11659.42	11803.51	
21	41	0	42	153.655	11649.85	11803.50	
21	42	0	41	148.816	11657.99	11806.80	
21	42	0	43	158.609	11648.19	11806.80	
21	43	0	42	153.655	11656.52	11810.18	
21	43	0	44	163.676	11646.50	11810.18	
21	44	0	43	158.609	11655.01	11813.62	
21	44	0	43	158.609	11655.02	11813.63	
21	44	0	45	168.858	11644.76	11813.62	
21	44	0	45	168.858	11644.77	11813.63	
21	45	0	44	163.676	11653.49	11817.17	
21	45	0	46	174.153	11643.01	11817.16	
21	46	0	45	168.858	11651.93	11820.79	
21	46	0	47	179.562	11641.22	11820.78	
21	47	0	46	174.153	11650.33	11824.49	
21	48	0	47	179.562	11648.71	11828.27	
21	49	0	48	185.085	11647.07	11832.16	
21	50	0	49	190.721	11645.41	11836.13	
21	51	0	50	196.470	11643.73	11840.20	

v'	J'	v''	J''	E_{gs} (cm^{-1})	E_{pump} (cm^{-1})	$E_{2(A)^1\Sigma^+\,(v',J')}$ (cm^{-1})	Note
21	52	0	51	202.333	11642.06	11844.39	
23	32	0	43	106.711	11762.49	11883.78	*
23	33	0	43	110.406	11762.49	11886.52	*
23	34	0	43	114.215	11762.49	11889.33	*
23	35	0	43	118.140	11762.49	11892.20	*
23	36	0	43	122.179	11762.49	11895.15	*
23	37	0	43	126.332	11762.49	11898.16	*
23	38	0	43	130.600	11762.49	11901.24	*
23	39	0	43	134.982	11762.49	11904.39	*
23	40	0	43	139.479	11762.49	11907.60	*
23	41	0	43	144.090	11762.49	11910.87	*
23	42	0	43	148.816	11762.49	11914.22	*
23	43	0	43	153.655	11762.49	11917.63	*
23	44	0	43	158.609	11762.49	11921.10	*
23	45	0	43	163.676	11762.49	11924.65	*
23	46	0	43	168.858	11762.49	11928.26	*
23	47	0	43	174.153	11762.49	11931.94	*
23	48	0	43	179.562	11762.48	11935.68	*
23	49	0	43	185.085	11762.49	11939.50	*
23	50	1	49	288.375	11655.01	11943.38	

v'	J'	v''	J''	E_{gs} (cm^{-1})	E_{pump} (cm^{-1})	$E_{2(A)^1\Sigma^+\,(v',J')}$ (cm^{-1})	Note
23	50	1	51	299.940	11643.43	11943.37	
23	50	0	43	190.721	11762.49	11943.38	*
23	51	0	43	196.470	11762.49	11947.32	*
23	52	0	43	202.333	11762.49	11951.33	*
25	9	1	8	151.740	11787.99	11939.73	
25	10	1	9	152.777	11787.94	11940.71	
25	11	1	10	153.930	11787.87	11941.80	
25	12	1	11	155.198	11787.79	11942.99	
25	13	1	12	156.582	11787.69	11944.27	
25	14	1	13	158.080	11787.57	11945.65	
25	15	1	14	159.694	11787.43	11947.13	
25	15	1	16	163.266	11783.86	11947.13	
25	16	1	15	161.422	11787.28	11948.70	
25	16	1	17	165.225	11783.48	11948.70	
25	17	1	16	163.266	11787.11	11950.37	
25	17	1	18	167.299	11783.07	11950.37	
25	18	0	17	67.067	11885.08	11952.14	
25	18	1	17	165.225	11786.91	11952.14	
25	18	1	19	169.488	11782.65	11952.14	
25	19	0	18	69.149	11884.85	11954.00	

v'	J'	v''	J''	E_{gs} (cm^{-1})	E_{pump} (cm^{-1})	$E_{2(A)^1\Sigma^+\,(v',J')}$ (cm^{-1})	Note
25	19	1	18	167.299	11786.70	11954.00	
25	20	0	19	71.347	11884.61	11955.96	
25	20	0	21	76.089	11879.87	11955.96	
25	20	1	19	169.488	11786.47	11955.96	
25	20	1	21	174.210	11781.75	11955.96	
25	21	0	20	73.660	11884.35	11958.01	
25	21	0	22	78.633	11879.37	11958.00	
25	21	1	20	171.792	11786.21	11958.00	
25	21	1	22	176.744	11781.26	11958.00	
25	22	0	21	76.089	11884.06	11960.15	
25	22	0	23	81.292	11878.86	11960.15	
25	22	1	21	174.210	11785.94	11960.15	
25	22	1	23	179.393	11780.75	11960.14	
25	23	0	22	78.633	11883.75	11962.38	
25	23	0	24	84.066	11878.31	11962.38	
25	23	1	22	176.744	11785.63	11962.38	
25	23	1	24	182.156	11780.22	11962.38	
25	24	0	23	81.292	11883.41	11964.70	
25	24	0	25	86.956	11877.75	11964.70	
25	24	1	23	179.393	11785.31	11964.70	

v'	J'	v''	J''	E_{gs} (cm^{-1})	E_{pump} (cm^{-1})	$E_{2(A)^1\Sigma^+\,(v',J')}$ (cm^{-1})	Note
25	24	1	25	185.034	11779.67	11964.70	
25	25	0	24	84.066	11883.05	11967.11	
25	25	0	26	89.961	11877.15	11967.11	
25	25	1	24	182.156	11784.95	11967.11	
25	25	1	26	188.026	11779.08	11967.11	
25	25	1	24	182.156	11817.35	11999.50	
25	26	0	25	86.956	11882.66	11969.61	
25	26	0	27	93.081	11876.53	11969.61	
25	26	1	25	185.034	11784.58	11969.61	
25	26	1	27	191.134	11778.48	11969.61	
25	27	0	26	89.961	11882.24	11972.20	
25	27	0	28	96.316	11875.88	11972.20	
25	27	0	28	96.316	11875.88	11972.20	
25	27	1	26	188.026	11784.17	11972.19	
25	27	1	28	194.356	11777.77	11972.12	
25	28	0	27	93.081	11881.79	11974.87	
25	28	0	29	99.666	11875.20	11974.86	
25	28	1	27	191.134	11783.73	11974.86	
25	28	1	29	197.692	11777.17	11974.87	
25	29	0	28	96.316	11881.30	11977.62	

v'	J'	v''	J''	E_{gs} (cm^{-1})	E_{pump} (cm^{-1})	$E_{2(A)^1\Sigma^+\,(v',J')}$ (cm^{-1})	Note
25	29	0	30	103.131	11874.49	11977.62	
25	29	1	28	194.356	11783.26	11977.61	
25	29	1	30	201.143	11776.47	11977.62	
25	30	0	29	99.666	11880.78	11980.45	
25	30	0	31	106.711	11873.74	11980.45	
25	30	1	29	197.692	11782.76	11980.45	
25	31	0	32	110.406	11872.95	11983.36	
25	31	1	30	201.143	11782.21	11983.36	
25	32	0	31	106.711	11879.64	11986.35	
25	32	0	33	114.215	11872.13	11986.35	
25	32	1	31	204.708	11781.64	11986.35	
25	33	0	32	110.406	11879.00	11989.41	
25	33	0	32	110.406	11879.01	11989.41	
25	33	0	34	118.140	11871.27	11989.41	
25	33	1	32	208.388	11781.02	11989.41	
25	34	0	33	114.215	11878.33	11992.54	
25	34	0	33	114.215	11878.33	11992.54	
25	34	0	35	122.179	11870.36	11992.54	
25	34	1	33	212.182	11780.36	11992.54	
25	35	0	34	118.140	11877.61	11995.75	

v'	J'	v''	J''	E_{gs} (cm^{-1})	E_{pump} (cm^{-1})	$E_{2(A)^1\Sigma^+\,(v',J')}$ (cm^{-1})	Note
25	35	0	34	118.140	11877.61	11995.75	
25	35	0	36	126.332	11869.41	11995.74	
25	36	0	35	122.179	11876.84	11999.02	
25	36	0	35	122.179	11876.84	11999.02	
25	36	0	37	130.600	11868.42	11999.02	
25	37	0	36	126.332	11876.02	12002.36	
25	37	0	36	126.332	11876.02	12002.36	
25	37	0	38	134.983	11867.37	12002.36	
25	38	0	37	130.600	11875.16	12005.76	
25	38	0	39	139.479	11866.28	12005.76	
25	39	0	38	134.983	11874.24	12009.22	
25	39	0	40	144.090	11865.13	12009.22	
25	40	0	39	139.479	11873.26	12012.74	
25	40	0	41	148.816	11863.92	12012.74	
25	41	0	40	144.090	11872.23	12016.32	
25	41	0	42	153.655	11862.66	12016.32	
25	42	0	41	148.816	11871.14	12019.96	
25	42	0	43	158.609	11861.35	12019.96	
25	43	0	42	153.655	11869.99	12023.65	
25	44	0	43	158.609	11868.78	12027.39	

v'	J'	v''	J''	E_{gs} (cm^{-1})	E_{pump} (cm^{-1})	$E_{2(A)^1\Sigma^+\,(v',J')}$ (cm^{-1})	Note
25	45	0	44	163.676	11867.37	12031.05	
25	46	0	45	168.858	11866.18	12035.04	
25	47	0	46	174.153	11864.79	12038.94	
25	48	0	47	179.562	11863.33	12042.89	
27	11	0	10	55.726	12189.13	12244.85	
27	11	0	12	58.388	12186.47	12244.85	
27	11	1	10	153.930	12090.93	12244.86	
27	11	1	12	156.582	12088.27	12244.85	
27	33	1	32	208.388	11877.40	12085.78	
27	34	1	33	212.182	11877.03	12089.21	
27	35	1	34	216.091	11876.64	12092.73	
27	36	1	35	220.113	11876.23	12096.34	
27	36	1	37	228.500	11867.84	12096.34	
27	37	1	36	224.250	11875.79	12100.04	
27	37	1	38	232.865	11867.17	12100.04	
27	38	1	37	228.500	11875.33	12103.83	
27	38	1	39	237.343	11866.49	12103.83	
27	39	1	38	232.865	11874.84	12107.70	
27	39	1	40	241.936	11865.77	12107.70	
27	40	1	39	237.343	11874.31	12111.66	

v'	J'	v''	J''	E_{gs} (cm^{-1})	E_{pump} (cm^{-1})	$E_{2(A)^1\Sigma^+\,(v',J')}$ (cm^{-1})	Note
27	40	1	41	246.642	11865.01	12111.66	
27	41	1	40	241.936	11873.75	12115.69	
27	41	1	42	251.461	11864.22	12115.68	
27	42	1	41	246.642	11873.15	12119.79	
27	42	1	43	256.395	11863.40	12119.79	
27	43	1	42	251.461	11872.51	12123.97	
27	43	1	44	261.442	11862.53	12123.97	
27	44	1	43	256.395	11871.82	12128.21	
27	44	1	45	266.602	11861.61	12128.21	
27	45	1	44	261.442	11871.08	12132.52	
27	45	1	46	271.875	11860.64	12132.52	
27	46	1	45	266.602	11870.28	12136.88	
27	46	1	47	277.262	11859.62	12136.89	
27	47	1	46	271.875	11869.43	12141.30	
27	47	1	48	282.762	11858.54	12141.30	
27	48	1	47	277.262	11868.51	12145.77	
27	48	1	49	288.375	11857.39	12145.77	
27	49	1	48	282.762	11867.52	12150.28	
27	49	1	50	294.101	11856.18	12150.28	
27	50	1	49	288.375	11866.45	12154.83	

v'	J'	v''	J''	E_{gs} (cm^{-1})	E_{pump} (cm^{-1})	$E_{2(A)^1\Sigma^+\,(v',J')}$ (cm^{-1})	Note
27	50	1	51	299.940	11854.89	12154.83	
27	51	1	50	294.101	11865.31	12159.42	
27	51	1	52	305.892	11853.52	12159.41	
27	52	1	51	299.940	11864.10	12164.04	
27	52	1	53	311.956	11852.08	12164.04	
27	53	1	52	305.892	11862.80	12168.69	
27	53	1	54	318.133	11850.56	12168.69	
27	54	1	53	311.956	11861.42	12173.38	
27	55	1	54	318.133	11859.96	12178.09	
27	56	1	55	324.423	11858.40	12182.83	
27	81	0	80	421.181	11900.11	12321.29	
27	81	0	82	439.712	11881.58	12321.29	
27	81	1	80	517.878	11803.42	12321.29	
27	81	1	82	536.331	11784.96	12321.29	
27	83	0	82	439.712	11897.41	12337.12	
27	83	0	84	458.680	11878.44	12337.12	
27	83	1	82	536.331	11800.79	12337.12	
27	83	1	84	555.219	11781.90	12337.12	
30	11	1	10	153.930	12260.46	12414.39	
30	11	1	12	156.582	12257.80	12414.38	

v'	J'	v''	J''	E_{gs} (cm^{-1})	E_{pump} (cm^{-1})	$E_{2(A)^1\Sigma^+\,(v',J')}$ (cm^{-1})	Note
30	11	2	10	251.477	12162.91	12414.39	
30	11	2	12	254.118	12160.27	12414.38	
31	61	0	60	260.185	12146.13	12406.32	
31	61	0	62	274.279	12132.04	12406.32	
31	61	1	60	357.553	12048.76	12406.32	
31	61	1	62	371.589	12034.73	12406.32	
31	61	2	60	454.256	11952.06	12406.32	
31	61	2	62	468.232	11938.08	12406.32	
31	61	3	60	550.286	11856.03	12406.32	
31	61	3	62	564.204	11842.11	12406.32	
31	61	4	60	645.641	11760.68	12406.32	
31	61	4	62	659.498	11746.82	12406.31	
32	46	1	45	266.602	12144.79	12411.39	
32	47	1	46	271.875	12144.43	12416.31	
32	47	1	48	282.762	12133.54	12416.31	
32	48	1	47	277.262	12144.07	12421.34	
32	48	1	49	288.375	12132.96	12421.33	
32	49	1	48	282.762	12143.71	12426.47	
32	49	1	50	294.101	12132.37	12426.47	
32	50	1	49	288.375	12143.35	12431.72	

v'	J'	v''	J''	E_{gs} (cm^{-1})	E_{pump} (cm^{-1})	$E_{2(A)^1\Sigma^+\,(v',J')}$ (cm^{-1})	Note
32	50	1	51	299.940	12131.78	12431.72	
32	51	1	50	294.101	12142.97	12437.07	
32	51	1	52	305.892	12131.18	12437.07	
32	52	1	51	299.940	12142.60	12442.54	
32	52	1	53	311.956	12130.58	12442.54	
32	53	1	52	305.892	12142.22	12448.11	
33	11	2	10	251.477	12268.51	12519.98	
33	11	2	12	254.118	12265.87	12519.98	
33	11	3	10	348.361	12171.61	12519.98	
33	11	3	12	350.991	12168.98	12519.97	
34	28	2	27	288.528	12193.34	12481.86	
34	28	2	29	295.059	12186.81	12481.86	
34	36	2	37	325.740	12176.98	12502.72	
34	37	2	38	330.086	12175.54	12505.62	
34	38	2	39	334.546	12174.04	12508.58	
34	39	2	40	339.120	12172.49	12511.61	
34	40	2	41	343.806	12170.89	12514.70	
34	41	2	42	348.606	12169.24	12517.85	
34	42	2	41	343.806	12177.25	12521.06	
34	42	2	43	353.519	12167.54	12521.06	

v'	J'	v''	J''	E_{gs} (cm^{-1})	E_{pump} (cm^{-1})	$E_{2(A)^1\Sigma^+\,(v',J')}$ (cm^{-1})	Note
34	43	2	42	348.606	12175.73	12524.34	
34	43	2	44	358.545	12165.79	12524.34	
34	44	2	43	353.519	12174.16	12527.68	
34	44	2	45	363.684	12163.99	12527.68	
34	44	2	45	363.684	12163.99	12527.68	
34	45	2	44	358.545	12172.54	12531.08	
34	45	2	46	368.935	12162.14	12531.08	
34	45	2	46	368.935	12162.14	12531.08	
34	46	2	45	363.684	12170.87	12534.55	
34	46	2	47	374.300	12160.25	12534.55	
34	46	2	47	374.300	12160.25	12534.55	
34	47	2	46	368.935	12169.14	12538.08	
34	47	2	48	379.777	12158.30	12538.08	
34	47	2	48	379.777	12158.30	12538.08	
34	47	2	48	379.777	12158.30	12538.08	
34	48	2	47	374.300	12167.37	12541.67	
34	48	2	49	385.367	12156.30	12541.67	
34	49	2	48	379.777	12165.55	12545.33	
34	49	2	50	391.069	12154.26	12545.33	
34	50	2	49	385.367	12163.69	12549.05	

v'	J'	v''	J''	E_{gs} (cm^{-1})	E_{pump} (cm^{-1})	$E_{2(A)^1\Sigma^+\,(v',J')}$ (cm^{-1})	Note
34	50	2	49	385.367	12163.69	12549.06	
34	50	2	51	396.883	12152.17	12549.05	
34	51	2	50	391.069	12161.77	12552.84	
34	51	2	50	391.069	12161.77	12552.84	
34	51	2	52	402.810	12150.03	12552.84	
34	52	2	51	396.883	12159.82	12556.70	
34	52	2	51	396.883	12159.81	12556.70	
34	52	2	53	408.849	12147.85	12556.70	
34	53	2	52	402.810	12157.81	12560.62	
34	53	2	54	415.000	12145.62	12560.62	
34	54	2	53	408.849	12155.76	12564.61	
34	54	2	55	421.264	12143.34	12564.61	
34	55	2	54	415.000	12153.66	12568.66	
34	55	2	56	427.639	12141.02	12568.66	
34	56	0	55	226.917	12345.87	12572.79	
34	56	0	57	239.886	12332.90	12572.78	
34	56	1	55	324.423	12248.36	12572.78	
34	56	1	57	337.339	12235.44	12572.78	
34	56	2	55	421.264	12151.52	12572.78	
34	56	2	55	421.264	12151.52	12572.78	

v'	J'	v''	J''	E_{gs} (cm^{-1})	E_{pump} (cm^{-1})	$E_{2(A)^1\Sigma^+\,(v',J')}$ (cm^{-1})	Note
34	56	2	57	434.125	12138.66	12572.78	
34	56	2	57	434.125	12138.66	12572.78	
34	56	3	55	517.434	12055.35	12572.78	
34	56	3	57	530.242	12042.54	12572.78	
34	57	2	56	427.639	12149.33	12576.97	
34	57	2	58	440.724	12136.25	12576.97	
34	58	2	57	434.125	12147.12	12581.24	
34	58	2	59	447.434	12133.81	12581.24	
34	59	2	58	440.724	12144.86	12585.58	
34	59	2	58	440.724	12144.86	12585.59	
34	60	2	59	447.434	12142.58	12590.01	
34	61	2	60	454.256	12140.28	12594.54	
34	62	2	61	461.188	12138.05	12599.24	
35	15	2	16	260.775	12263.38	12524.16	
35	15	3	14	354.077	12170.08	12524.16	
35	15	3	16	357.620	12166.54	12524.16	
35	68	2	67	505.117	12173.94	12679.05	
35	68	2	69	520.645	12158.41	12679.06	
35	87	1	86	574.542	12204.37	12778.91	
35	87	1	88	594.298	12184.62	12778.91	

v'	J'	v''	J''	E_{gs} (cm^{-1})	E_{pump} (cm^{-1})	$E_{2(A)^1\Sigma^+\,(v',J')}$ (cm^{-1})	Note
35	87	1	88	594.298	12184.62	12778.92	
35	87	2	86	670.323	12108.59	12778.91	
35	87	2	88	689.993	12088.92	12778.92	
37	43	0	42	153.655	12538.36	12692.01	
37	43	0	44	163.676	12528.34	12692.01	
37	43	1	42	251.461	12440.55	12692.01	
37	43	1	44	261.442	12430.57	12692.01	
37	43	2	42	348.606	12343.40	12692.00	
37	43	2	44	358.545	12333.46	12692.00	
37	43	3	42	445.084	12246.92	12692.00	
37	43	3	44	454.981	12237.02	12692.00	
37	43	4	42	540.891	12151.11	12692.00	
37	43	4	44	550.745	12141.27	12692.01	
37	43	4	44	550.745	12141.27	12692.01	
37	43	5	42	636.022	12055.99	12692.01	
37	43	5	44	645.834	12046.18	12692.01	
37	43	6	42	730.474	11961.54	12692.01	
37	43	6	44	740.242	11951.77	12692.01	
37	43	7	42	824.241	11867.77	12692.01	
37	43	7	44	833.966	11858.04	12692.01	

v'	J'	v''	J''	E_{gs} (cm^{-1})	E_{pump} (cm^{-1})	$E_{2(A)^1\Sigma^+\,(v',J')}$ (cm^{-1})	Note
37	43	8	42	917.319	11774.69	12692.01	
37	43	8	44	927.000	11765.01	12692.01	
37	43	9	42	1009.702	11682.31	12692.01	
37	43	9	44	1019.338	11672.68	12692.01	
37	43	10	42	1101.385	11590.63	12692.02	
37	43	10	44	1110.976	11581.04	12692.01	
37	43	11	42	1192.362	11499.65	12692.01	
37	43	11	44	1201.907	11490.11	12692.01	
37	43	12	42	1282.627	11409.39	12692.01	
37	43	12	44	1292.127	11399.89	12692.01	
37	43	13	42	1372.175	11319.84	12692.02	
37	43	13	44	1381.627	11310.39	12692.01	
37	43	15	42	1549.090	11142.92	12692.01	
37	43	15	44	1558.447	11133.57	12692.01	
37	68	2	69	520.645	12261.47	12782.11	
37	68	3	67	600.930	12181.19	12782.12	
37	68	3	69	616.392	12165.72	12782.11	
39	68	3	67	600.930	12301.67	12902.60	
39	68	3	69	616.392	12286.20	12902.60	
40	84	3	85	755.790	12275.74	13031.53	

v'	J'	v''	J''	E_{gs} (cm^{-1})	E_{pump} (cm^{-1})	$E_{2(A)^1\Sigma^+\,(v',J')}$ (cm^{-1})	Note
40	84	4	83	831.390	12200.15	13031.54	
40	84	4	85	850.247	12181.29	13031.53	
41	108	3	107	992.190	12248.18	13240.37	
41	108	3	109	1016.194	12224.18	13240.37	
41	108	4	107	1085.587	12154.78	13240.36	
41	108	4	109	1109.481	12130.89	13240.37	

Appendix B

$12(0^+)$ Experimental Data

The following table compiles measured $12(0^+)$ level energies determined in this work. v and J denote the vibrational and rotational quantum numbers for a particular state, respectively. The primes follow the typical convention where unprimed quantum numbers correspond to the upper state [the $12(0^+)$ state], single prime quantum numbers correspond to the intermediate state [the $2(A)^1\Sigma^+$ state], and double prime quantum numbers correspond to the ground state [the $1(X)^1\Sigma^+$ state]. If a particular transition involved a collision, the quantum numbers of collisionall populated intermediate state level are denoted with a subscript c. $E_{\rm gs}$ is the energy of the $1(X)^1\Sigma^+$ rovibrational level, calculated with experimental Dunham coefficients from Docenko *et al.* [15], which are reported to be accurate to $\pm$ 0.003 cm^{-1}. $E_{\rm pump}$ and $E_{\rm probe}$ are the photon energies of the pump and probe laser, respectively, which we assign an uncertainty of $\pm$ 0.01 cm^{-1}. $E_{\rm coll}$ is the energy associated with the collision which transferred population to the nearby rotational level. A positive $E_{\rm coll}$ indicates a collision which transferred population to a higher

rotational level, while a negative E_{coll} indicates a collision which transferred population to a lower rotational level. Finally, $E_{12(0^+)(v,J)}$ is the total energy of the $12(0^+)$ rovibrational level. Since these total energies are a result of photons from both lasers, we assign uncertainties of $\pm$ 0.02 cm^{-1} to each of the total energies.

v	J	v'	J'	v'_c	J'_c	v''	J''	E_{gs} (cm^{-1})	E_{pump} (cm^{-1})	E_{coll} (cm^{-1})	E_{probe} (cm^{-1})	$E_{12(0^+)(v,J)}$ (cm^{-1})
0	33	12	34			0	33	114.215	11163.45		13456.98	24734.65
0	35	12	34			0	33	114.215	11163.45		13462.05	24739.72
0	43	14	44			0	45	168.858	11266.74		13327.32	24762.92
0	45	14	44			0	45	168.858	11266.74		13333.86	24769.45
1	0	14	1			0	2	49.706	11296.42		13396.80	24742.93
1	2	14	1			0	2	49.706	11296.42		13397.02	24743.15
1	23	14	26	14	24	0	25	86.956	11288.69	-4.38	13392.06	24763.32
1	24	14	26	14	25	0	25	86.956	11288.69	-2.24	13391.70	24765.10
1	25	14	26			0	25	86.956	11288.69		13391.31	24766.95
1	26	14	26	14	27	0	25	86.956	11288.69	2.34	13390.91	24768.89
1	27	14	26	14	28	0	25	86.956	11288.69	4.77	13390.47	24770.89
1	27	14	26			0	25	86.956	11288.69		13395.24	24770.88
1	37	14	44	14	38	0	45	168.858	11266.74	-24.61	13383.89	24794.88
1	38	14	44	14	39	0	45	168.858	11266.74	-20.86	13382.93	24797.67
1	39	14	44	14	38	0	45	168.858	11266.74	-24.61	13389.56	24800.55
1	39	14	44	14	40	0	45	168.858	11266.74	-16.97	13381.91	24800.55
1	40	14	44	14	41	0	45	168.858	11266.74	-12.94	13380.83	24803.49
1	40	14	44	14	39	0	45	168.858	11266.74	-20.86	13388.76	24803.50
1	41	14	44	14	40	0	45	168.858	11266.74	-16.97	13387.88	24806.51
1	42	14	44	14	41	0	45	168.858	11266.74	-12.94	13386.93	24809.59
1	42	14	44	14	43	0	45	168.858	11266.74	-4.45	13378.45	24809.60

v	J	v'	J'	v'_c	J'_c	v''	J''	E_{gs} (cm^{-1})	E_{pump} (cm^{-1})	E_{coll} (cm^{-1})	E_{probe} (cm^{-1})	$E_{12(0^+)(v,J)}$ (cm^{-1})
1	43	14	44			0	45	168.858	11266.74		13377.16	24812.76
1	43	14	44	14	42	0	45	168.858	11266.74	-8.76	13385.93	24812.76
1	44	14	44	14	45	0	45	168.858	11266.74	4.59	13375.81	24815.99
1	44	14	44	14	43	0	45	168.858	11266.74	-4.45	13384.85	24815.99
1	45	14	44			0	45	168.858	11266.74		13383.70	24819.30
1	46	14	44	14	45	0	45	168.858	11266.74	4.59	13382.50	24822.68
1	47	14	44	14	46	0	45	168.858	11266.74	9.32	13381.22	24826.14
1	48	14	44	14	47	0	45	168.858	11266.74	14.18	13379.88	24829.66
1	49	14	44	14	48	0	45	168.858	11266.74	19.18	13378.48	24833.26
1	50	14	44	14	49	0	45	168.858	11266.74	24.33	13377.02	24836.95
2	5	14	10	14	6	0	9	54.569	11296.06	-2.85	13447.63	24795.41
2	6	14	10	14	7	0	9	54.569	11296.06	-2.27	13447.50	24795.86
2	7	14	10	14	8	0	9	54.569	11296.06	-1.42	13447.35	24796.56
2	8	14	10	14	9	0	9	54.569	11296.06	-0.85	13447.19	24796.97
2	9	14	10			0	9	54.569	11296.06		13447.03	24797.66
2	10	14	10	14	11	0	9	54.569	11296.06	0.90	13446.85	24798.37
2	11	14	10	14	12	0	9	54.569	11296.06	1.89	13446.67	24799.19
2	11	14	10	14		0	9	54.569	11296.06		13448.60	24799.22
2	12	14	10	14	13	0	9	54.569	11296.06	2.99	13446.47	24800.08
2	13	14	10	14	14	0	9	54.569	11296.06	4.16	13446.26	24801.05
2	24	14	26	14	23	0	25	86.956	11288.69	-6.43	13447.39	24816.60
2	25	14	26			0	25	86.956	11288.69		13442.80	24818.44
2	25	14	26	14	24	0	25	86.956	11288.69	-4.38	13447.19	24818.45
2	26	14	26	14	25	0	25	86.956	11288.69	-2.24	13446.98	24820.39
2	27	14	26			0	25	86.956	11288.69		13446.74	24822.38
2	28	14	26	14	27	0	25	86.956	11288.69	2.34	13446.47	24824.46
2	29	14	26	14	28	0	25	86.956	11288.69	4.77	13446.19	24826.61
2	30	14	26	14	29	0	25	86.956	11288.69	7.31	13445.88	24828.84
2	31	14	39	14	30	0	40	144.090	11270.65	-29.13	13445.53	24831.13

v	J	v'	J'	v'_c	J'_c	v''	J''	E_{gs} (cm^{-1})	E_{pump} (cm^{-1})	E_{coll} (cm^{-1})	E_{probe} (cm^{-1})	$E_{12(0^+)(v,J)}$ (cm^{-1})
2	32	14	39	14	31	0	40	144.090	11270.65	-26.38	13445.15	24833.51
2	33	14	39	14	32	0	40	144.090	11270.65	-23.52	13444.72	24835.94
2	34	14	39	14	33	0	40	144.090	11270.65	-20.53	13444.27	24838.47
2	35	14	39	14	34	0	40	144.090	11270.65	-17.43	13443.76	24841.06
2	36	14	39	14	35	0	40	144.090	11270.65	-14.21	13443.21	24843.74
2	37	14	39	14	36	0	40	144.090	11270.65	-10.85	13442.59	24846.47
2	38	14	39	14	37	0	40	144.090	11270.65	-7.37	13441.92	24849.29
2	39	14	39	14	38	0	40	144.090	11270.65	-3.75	13441.19	24852.17
2	39	14	44	14	38	0	45	168.858	11266.74	-24.61	13441.19	24852.18
2	40	14	39			0	40	144.090	11270.65		13440.39	24855.13
2	40	14	44	14	39	0	45	168.858	11266.74	-20.86	13440.39	24855.13
2	41	14	39	14	40	0	40	144.090	11270.65	3.89	13439.53	24858.16
2	41	14	44	14	40	0	45	168.858	11266.74	-16.97	13439.53	24858.16
2	42	14	44	14	41	0	45	168.858	11266.74	-12.94	13438.60	24861.26
2	43	14	44			0	45	168.858	11266.74		13428.85	24864.44
2	43	14	44	14	42	0	45	168.858	11266.74	-8.76	13437.61	24864.44
2	44	14	44	14	43	0	45	168.858	11266.74	-4.45	13436.55	24867.70
2	45	14	44			0	45	168.858	11266.74		13435.41	24871.01
2	46	14	44	14	45	0	45	168.858	11266.74	4.59	13434.22	24874.41
2	47	14	44	14	46	0	45	168.858	11266.74	9.32	13432.97	24877.89
2	48	14	44	14	47	0	45	168.858	11266.74	14.18	13431.65	24881.43
2	49	14	44	14	48	0	45	168.858	11266.74	19.18	13430.28	24885.05
2	55	14	60	14	56	0	59	253.306	11270.20	-24.82	13409.58	24908.26
2	56	14	60	14	57	0	59	253.306	11270.20	-18.74	13407.63	24912.38
2	57	14	60	14	58	0	59	253.306	11270.20	-12.58	13405.65	24916.57
2	58	14	60	14	59	0	59	253.306	11270.20	-6.33	13403.68	24920.85
2	59	14	60			0	59	253.306	11270.20		13401.68	24925.18
2	61	14	60			0	59	253.306	11270.20		13410.57	24934.07
2	62	14	60	14	61	0	59	253.306	11270.20	6.40	13408.72	24938.63

v	J	v'	J'	v'_c	J'_c	v''	J''	E_{gs} (cm^{-1})	E_{pump} (cm^{-1})	E_{coll} (cm^{-1})	E_{probe} (cm^{-1})	$E_{12(0^+)(v,J)}$ (cm^{-1})
2	63	14	60	14	62	0	59	253.306	11270.20	12.87	13406.88	24943.25
2	64	14	60	14	63	0	59	253.306	11270.20	19.37	13405.07	24947.94
2	65	14	60	14	64	0	59	253.306	11270.20	25.89	13403.33	24952.72
3	43	12	44			0	43	158.609	11151.39		13608.43	24918.43
3	45	12	44			0	43	158.609	11151.39		13615.04	24925.04
4	6	14	10	14	7	0	9	54.569	11296.06	-2.27	13556.33	24904.69
4	7	14	10	14	8	0	9	54.569	11296.06	-1.42	13556.19	24905.39
4	8	14	10	14	9	0	9	54.569	11296.06	-0.85	13556.04	24905.82
4	9	14	10			0	9	54.569	11296.06		13555.88	24906.50
4	10	14	10	14	11	0	9	54.569	11296.06	0.90	13555.71	24907.23
4	11	14	10			0	9	54.569	11296.06		13557.45	24908.07
4	11	14	10	14	12	0	9	54.569	11296.06	1.89	13555.53	24908.05
4	12	14	10	14	13	0	9	54.569	11296.06	2.99	13555.34	24908.95
4	23	14	26	14	24	0	25	86.956	11288.69	-4.38	13552.47	24923.73
4	24	14	26	14	25	0	25	86.956	11288.69	-2.24	13552.12	24925.53
4	25	14	26			0	25	86.956	11288.69		13551.75	24927.39
4	26	14	26	14	27	0	25	86.956	11288.69	2.34	13551.35	24929.34
4	27	14	26	14	28	0	25	86.956	11288.69	4.77	13550.93	24931.35
4	27	14	26			0	25	86.956	11288.69		13555.70	24931.35
4	37	14	44	14	38	0	45	168.858	11266.74	-24.61	13544.46	24955.45
4	38	14	39			0	40	144.090	11270.65		13543.56	24958.29
4	38	14	44	14	39	0	45	168.858	11266.74	-20.86	13543.55	24958.29
4	39	14	39	14	40	0	40	144.090	11270.65	3.89	13542.57	24961.20
4	39	14	44	14	40	0	45	168.858	11266.74	-16.97	13542.57	24961.20
4	40	14	44	14	41	0	45	168.858	11266.74	-12.94	13541.52	24964.18
4	41	14	44	14	42	0	45	168.858	11266.74	-8.76	13540.39	24967.22
4	42	14	44	14	43	0	45	168.858	11266.74	-4.45	13539.20	24970.35
4	43	14	44			0	45	168.858	11266.74		13537.94	24973.54
4	44	14	44	14	45	0	45	168.858	11266.74	4.59	13536.62	24976.81

v	J	v'	J'	v'_c	J'_c	v''	J''	E_{gs} (cm^{-1})	E_{pump} (cm^{-1})	E_{coll} (cm^{-1})	E_{probe} (cm^{-1})	$E_{12(0^+)(v,J)}$ (cm^{-1})
4	45	14	44	14	46	0	45	168.858	11266.74	9.32	13535.24	24980.15
4	45	14	44			0	45	168.858	11266.74		13544.54	24980.13
4	46	14	44	14	47	0	45	168.858	11266.74	14.18	13533.79	24983.57
4	47	14	44	14	48	0	45	168.858	11266.74	19.18	13532.27	24987.04
4	48	14	44	14	49	0	45	168.858	11266.74	24.33	13530.69	24990.62
4	49	14	44	14	50	0	45	168.858	11266.74	29.58	13529.05	24994.23
4	50	14	44	14	51	0	45	168.858	11266.74	34.99	13527.34	24997.93
4	51	14	44	14	52	0	45	168.858	11266.74	40.57	13525.56	25001.73
4	59	14	60			0	59	253.306	11270.20		13511.01	25034.51
4	61	14	60			0	59	253.306	11270.20		13519.93	25043.43
5	4	14	10	14	5	0	9	54.569	11296.06	-3.36	13611.76	24959.03
5	5	14	10	14	6	0	9	54.569	11296.06	-2.85	13611.63	24959.41
5	6	14	10	14	7	0	9	54.569	11296.06	-2.27	13611.50	24959.85
5	7	14	10	14	8	0	9	54.569	11296.06	-1.42	13611.35	24960.55
5	8	14	10	14	9	0	9	54.569	11296.06	-0.85	13611.19	24960.97
5	9	14	10			0	9	54.569	11296.06		13611.03	24961.65
5	10	14	10	14	11	0	9	54.569	11296.06	0.90	13610.86	24962.38
5	11	14	10			0	9	54.569	11296.06		13612.60	24963.23
5	11	14	10	14	12	0	9	54.569	11296.06	1.89	13610.67	24963.19
5	12	14	10	14	13	0	9	54.569	11296.06	2.99	13610.48	24964.09
5	22	14	26	14	21	0	25	86.956	11288.69	-10.25	13611.74	24977.13
5	23	14	26	14	24	0	25	86.956	11288.69	-4.38	13607.58	24978.85
5	23	14	26	14	22	0	25	86.956	11288.69	-8.39	13611.58	24978.84
5	24	14	26	14	25	0	25	86.956	11288.69	-2.24	13607.22	24980.63
5	24	14	26	14	23	0	25	86.956	11288.69	-6.43	13611.41	24980.62
5	25	14	26			0	25	86.956	11288.69		13606.83	24982.47
5	26	14	26	14	25	0	25	86.956	11288.69	-2.24	13611.01	24984.42
5	26	14	26	14	27	0	25	86.956	11288.69	2.34	13606.44	24984.42
5	27	14	26			0	25	86.956	11288.69		13610.78	24986.42

v	J	v'	J'	v'_c	J'_c	v''	J''	E_{gs} (cm^{-1})	E_{pump} (cm^{-1})	E_{coll} (cm^{-1})	E_{probe} (cm^{-1})	$E_{12(0^+)(v,J)}$ (cm^{-1})
5	27	14	26	14	28	0	25	86.956	11288.69	4.77	13606.00	24986.42
5	28	14	26	14	27	0	25	86.956	11288.69	2.34	13610.52	24988.50
5	29	14	26	14	28	0	25	86.956	11288.69	4.77	13610.24	24990.66
5	30	14	26	14	29	0	25	86.956	11288.69	7.31	13609.92	24992.88
5	43	14	44			0	45	168.858	11266.74		13592.94	25028.53
5	45	14	44			0	45	168.858	11266.74		13599.52	25035.11
5	59	14	60			0	59	253.306	11270.20		13565.79	25089.30
5	61	14	60			0	59	253.306	11270.20		13574.69	25098.19
6	5	14	10	14	6	0	9	54.569	11296.06	-2.85	13665.98	25013.76
6	6	14	10	14	7	0	9	54.569	11296.06	-2.27	13665.85	25014.21
6	7	14	10	14	8	0	9	54.569	11296.06	-1.42	13665.70	25014.90
6	8	14	10	14	9	0	9	54.569	11296.06	-0.85	13665.55	25015.33
6	9	14	10			0	9	54.569	11296.06		13665.38	25016.01
6	10	14	10	14	11	0	9	54.569	11296.06	0.90	13665.20	25016.73
6	11	14	10			0	9	54.569	11296.06		13666.93	25017.56
6	11	14	10	14	12	0	9	54.569	11296.06	1.89	13665.02	25017.54
6	12	14	10	14	13	0	9	54.569	11296.06	2.99	13664.82	25018.44
6	22	14	26	14	21	0	25	86.956	11288.69	-10.25	13666.01	25031.40
6	23	14	26	14	22	0	25	86.956	11288.69	-8.39	13665.85	25033.10
6	23	14	26	14	24	0	25	86.956	11288.69	-4.38	13661.84	25033.11
6	24	14	26	14	23	0	25	86.956	11288.69	-6.43	13665.66	25034.88
6	24	14	26	14	25	0	25	86.956	11288.69	-2.24	13661.48	25034.88
6	25	14	26	14	24	0	25	86.956	11288.69	-4.38	13665.47	25036.73
6	25	14	26			0	25	86.956	11288.69		13661.09	25036.73
6	26	14	26	14	25	0	25	86.956	11288.69	-2.24	13665.25	25038.66
6	26	14	26	14	27	0	25	86.956	11288.69	2.34	13660.67	25038.65
6	27	14	26			0	25	86.956	11288.69		13665.01	25040.65
6	28	14	26	14	27	0	25	86.956	11288.69	2.34	13664.74	25042.73
6	29	14	26	14	28	0	25	86.956	11288.69	4.77	13664.45	25044.87

v	J	v'	J'	v'_c	J'_c	v''	J''	E_{gs} (cm^{-1})	E_{pump} (cm^{-1})	E_{coll} (cm^{-1})	E_{probe} (cm^{-1})	$E_{12(0^+)(v,J)}$ (cm^{-1})
6	30	14	26	14	29	0	25	86.956	11288.69	7.31	13664.13	25047.09
6	43	14	44			0	45	168.858	11266.74		13646.96	25082.56
6	45	14	44			0	45	168.858	11266.74		13653.51	25089.11
7	43	11	44			0	43	158.609	11107.34		13869.43	25135.38
7	45	11	44			0	43	158.609	11107.34		13875.93	25141.88
7	59	14	60			0	59	253.306	11270.20		13672.01	25195.51
7	61	14	60			0	59	253.306	11270.20		13680.81	25204.31
8	0	14	1			0	2	49.706	11296.42		13771.91	25118.04
8	1	14	1	14	2	0	2	49.706	11296.42	0.15	13771.82	25118.09
8	2	14	1	14	3	0	2	49.706	11296.42	0.40	13771.71	25118.24
8	2	14	1			0	2	49.706	11296.42		13772.13	25118.26
8	3	14	1	14	2	0	2	49.706	11296.42	0.15	13772.18	25118.46
8	4	14	1	14	3	0	2	49.706	11296.42	0.40	13772.22	25118.75
8	5	14	1	14	4	0	2	49.706	11296.42	0.73	13772.26	25119.12
8	43	18	44			0	43	158.609	11494.24		13534.33	25187.18
8	45	18	44			0	43	158.609	11494.24		13540.81	25193.66
10	0	14	1			0	2	49.706	11296.42		13874.22	25220.34
10	1	14	1	14	2	0	2	49.706	11296.42	0.15	13874.12	25220.40
10	2	14	1	14	3	0	2	49.706	11296.42	0.40	13874.02	25220.55
10	2	14	1			0	2	49.706	11296.42		13874.43	25220.56
10	3	14	1	14	4	0	2	49.706	11296.42	0.73	13873.91	25220.77
10	3	14	1	14	2	0	2	49.706	11296.42	0.15	13874.48	25220.76
10	4	14	1	14	5	0	2	49.706	11296.42	1.14	13873.78	25221.05
10	4	14	10	14	5	0	9	54.569	11296.06	-3.36	13873.78	25221.06
10	4	14	1	14	3	0	2	49.706	11296.42	0.40	13874.53	25221.06
10	5	14	1	14	6	0	2	49.706	11296.42	1.65	13873.64	25221.42
10	5	14	10	14	6	0	9	54.569	11296.06	-2.85	13873.65	25221.42
10	5	14	1	14	4	0	2	49.706	11296.42	0.73	13874.56	25221.42
10	6	14	10	14	7	0	9	54.569	11296.06	-2.27	13873.50	25221.86

v	J	v'	J'	v'_c	J'_c	v''	J''	E_{gs} (cm^{-1})	E_{pump} (cm^{-1})	E_{coll} (cm^{-1})	E_{probe} (cm^{-1})	$E_{12(0^+)(v,J)}$ (cm^{-1})
10	7	14	10	14	8	0	9	54.569	11296.06	-1.42	13873.35	25222.55
10	8	14	10	14	9	0	9	54.569	11296.06	-0.85	13873.18	25222.96
10	9	14	10			0	9	54.569	11296.06		13873.00	25223.63
10	10	14	10	14	9	0	9	54.569	11296.06	-0.85	13874.56	25224.34
10	11	14	10			0	9	54.569	11296.06		13874.53	25225.16
10	12	14	10	14	11	0	9	54.569	11296.06	0.90	13874.48	25226.01
10	13	14	10	14	12	0	9	54.569	11296.06	1.89	13874.43	25226.95
10	14	14	10	14	13	0	9	54.569	11296.06	2.99	13874.36	25227.98
10	15	14	10	14	14	0	9	54.569	11296.06	4.16	13874.29	25229.07
10	43	14	44			0	45	168.858	11266.74		13853.31	25288.90
10	45	14	44			0	45	168.858	11266.74		13859.74	25295.34
10	59	14	60			0	59	253.306	11270.20		13824.83	25348.33
10	61	14	60			0	59	253.306	11270.20		13833.52	25357.02
12	41	18	42			0	41	148.816	11497.00		13732.65	25378.47
12	43	18	42			0	41	148.816	11497.00		13739.11	25384.92
13	43	18	44			0	43	158.609	11494.24		13786.23	25439.08
13	45	18	44			0	43	158.609	11494.24		13792.61	25445.46
14	43	18	44			0	43	158.609	11494.24		13835.96	25488.81
14	45	18	44			0	43	158.609	11494.24		13842.31	25495.16
22	43	29	44			1	45	266.602	11994.95		13653.82	25915.37
22	45	29	44			1	45	266.602	11994.95		13659.80	25921.35

Appendix C

$4^3\Pi_{0^+}$ Experimental Data

The following table compiles measured $4^3\Pi_{0^+}$ level energies determined in this work. v and J denote the vibrational and rotational quantum numbers for a particular state, respectively. The primes follow the typical convention where unprimed quantum numbers correspond to the upper state [the $12(0^+)$ state], single prime quantum numbers correspond to the intermediate state [the $2(A)^1\Sigma^+$ state], and double prime quantum numbers correspond to the ground state [the $1(X)^1\Sigma^+$ state]. Since an absolute vibrational numbering scheme could not be determined, relative vibrational numbers are given. If a particular transition involved a collision, the quantum numbers of collisionall populated intermediate state level are denoted with a subscript c. $E_{\rm gs}$ is the energy of the $1(X)^1\Sigma^+$ rovibrational level, calculated with experimental Dunham coefficients from Docenko *et al.* [15], which are reported to be accurate to $\pm$ 0.003 cm^{-1}. $E_{\rm pump}$ and $E_{\rm probe}$ are the photon energies of the pump and probe laser, respectively, which we assign an uncertainty of $\pm$ 0.01 cm^{-1}. $E_{\rm coll}$ is the energy associated with the collision which transferred population to the

nearby rotational level. A positive $E_{\rm coll}$ indicates a collision which transferred population to a higher rotational level, while a negative $E_{\rm coll}$ indicates a collision which transferred population to a lower rotational level. Finally, $E_{4^3\Pi_{0^+}\,(v,J)}$ is the total energy of the $4^3\Pi_{0^+}$ rovibrational level. Since these total energies are a result of photons from both lasers, we assign uncertainties of $\pm$ 0.02 cm^{-1} to each of the total energies.

v	J	v'	J'	$v'_{\rm c}$	$J'_{\rm c}$	v''	J''	$E_{\rm gs}$ (cm^{-1})	$E_{\rm pump}$ (cm^{-1})	$E_{\rm coll}$ (cm^{-1})	$E_{\rm probe}$ (cm^{-1})	$E_{4^3\Pi_{0^+}\,(v,J)}$ (cm^{-1})
$v_{\rm A}$+7	43	23	44			0	43	158.609	11762.50		13278.66	25199.77
$v_{\rm A}$+6	45	23	44			0	43	158.609	11762.50		13272.78	25193.89
$v_{\rm A}$+6	43	23	44			0	43	158.609	11762.50		13269.69	25190.80
$v_{\rm A}$+5	45	23	44			0	43	158.609	11762.50		13266.01	25187.11
$v_{\rm A}$+5	43	23	44			0	43	158.609	11762.50		13262.86	25183.97
$v_{\rm A}$+4	47	23	44	23	48	0	43	158.609	11762.50	14.57	13245.34	25181.02
$v_{\rm A}$+4	46	23	44	23	47	0	43	158.609	11762.50	10.83	13247.67	25179.61
$v_{\rm A}$+4	45	23	44			0	45	168.858	11752.25		13257.10	25178.21
$v_{\rm A}$+4	45	23	44	23	46	0	43	158.609	11762.50	7.16	13249.96	25178.23
$v_{\rm A}$+4	44	23	44	23	45	0	43	158.609	11762.50	3.54	13252.22	25176.87
$v_{\rm A}$+4	44	23	44	23	43	0	43	158.609	11762.50	-3.48	13259.22	25176.85
$v_{\rm A}$+4	43	23	44			0	45	168.858	11752.25		13254.39	25175.50
$v_{\rm A}$+4	43	23	44	23	42	0	43	158.609	11762.50	-6.89	13261.29	25175.51
$v_{\rm A}$+4	42	23	44	23	43	0	43	158.609	11762.50	-3.48	13256.55	25174.18
$v_{\rm A}$+4	41	23	44	23	42	0	43	158.609	11762.50	-6.89	13258.66	25172.88
$v_{\rm A}$+4	40	23	44	23	41	0	43	158.609	11762.50	-10.24	13260.74	25171.62
$v_{\rm A}$+4	39	23	44	23	40	0	43	158.609	11762.50	-13.51	13262.73	25170.32
$v_{\rm A}$+3	45	23	44			0	43	158.609	11762.50		13247.82	25168.93
$v_{\rm A}$+3	43	23	44			0	43	158.609	11762.50		13244.97	25166.08
$v_{\rm A}$+2	45	23	44			0	43	158.609	11762.50		13240.57	25161.68

v	J	v'	J'	v'_c	J'_c	v''	J''	E_{gs} (cm^{-1})	E_{pump} (cm^{-1})	E_{coll} (cm^{-1})	E_{probe} (cm^{-1})	$E_{4^3\Pi_{0+}\ (v,J)}$ (cm^{-1})
v_A+2	43	23	44			0	43	158.609	11762.50		13237.29	25158.39
v_A+1	47	23	44	23	46	0	43	158.609	11762.50	7.16	13228.56	25156.82
v_A+1	46	23	44	23	45	0	43	158.609	11762.50	3.54	13230.71	25155.36
v_A+1	45	23	44			0	43	158.609	11762.50		13232.79	25153.90
v_A+1	45	23	44	23	46	0	43	158.609	11762.50	7.16	13225.67	25153.93
v_A+1	44	23	44	23	43	0	43	158.609	11762.50	-3.48	13234.87	25152.50
v_A+1	44	23	44	23	45	0	43	158.609	11762.50	3.54	13227.85	25152.50
v_A+1	43	23	44			0	43	158.609	11762.50		13229.94	25151.04
v_A+1	43	23	44	23	42	0	43	158.609	11762.50	-6.89	13236.83	25151.05
v_A+1	42	23	44	23	41	0	43	158.609	11762.50	-10.24	13238.77	25149.64
v_A+1	42	23	44	23	43	0	43	158.609	11762.50	-3.48	13232.02	25149.65
v_A+1	41	23	44	23	42	0	43	158.609	11762.50	-6.89	13234.05	25148.27
v_A+1	40	23	44	23	41	0	43	158.609	11762.50	-10.24	13236.02	25146.89
v_A	45	23	44			0	43	158.609	11762.50		13223.41	25144.51
v_A	43	23	44			0	43	158.609	11762.50		13220.64	25141.75
v_B+3	45	18	44			0	43	158.609	11494.24		13258.88	24911.73
v_B+3	43	18	44			0	43	158.609	11494.24		13254.56	24907.41
v_B+2	45	18	44			0	43	158.609	11494.24		13249.07	24901.92
v_B+2	43	18	44			0	43	158.609	11494.24		13246.59	24899.44
v_B	45	18	44			0	43	158.609	11494.24		13232.63	24885.48
v_B	43	18	44			0	43	158.609	11494.24		13228.15	24881.00
v_C+10	35	12	34			0	33	114.215	11163.45		13363.67	24641.33
v_C+10	33	12	34			0	33	114.215	11163.45		13361.60	24639.27
v_C+9	45	12	44			0	43	158.609	11151.40		13332.71	24642.72
v_C+9	43	12	44			0	43	158.609	11151.40		13330.01	24640.02
v_C+9	35	12	34			0	33	114.215	11163.45		13353.85	24631.52
v_C+9	33	12	34			0	33	114.215	11163.45		13351.73	24629.40
v_C+8	35	12	34			0	33	114.215	11163.45		13343.12	24620.79
v_C+8	33	12	34			0	33	114.215	11163.45		13341.06	24618.73

v	J	v'	J'	v'_c	J'_c	v''	J''	E_{gs} (cm^{-1})	E_{pump} (cm^{-1})	E_{coll} (cm^{-1})	E_{probe} (cm^{-1})	$E_{4^3\Pi_{0+}\ (v,J)}$ (cm^{-1})
v_C+7	35	12	34			0	33	114.215	11163.45		13333.02	24610.69
v_C+7	33	12	34			0	33	114.215	11163.45		13331.01	24608.68
v_C+6	35	12	34			0	33	114.215	11163.45		13322.81	24600.47
v_C+6	33	12	34			0	33	114.215	11163.45		13320.80	24598.47
v_C+5	35	12	34			0	33	114.215	11163.45		13312.65	24590.32
v_C+5	33	12	34			0	33	114.215	11163.45		13310.64	24588.31
v_C+4	35	12	34			0	35	122.179	11155.49		13303.29	24580.96
v_C+4	33	12	34			0	35	122.179	11155.49		13300.85	24578.52
v_C+2	35	12	34			0	35	122.179	11155.49		13283.44	24561.11
v_C	35	12	34			0	35	122.179	11155.49		13263.62	24541.29
v_C	33	12	34			0	35	122.179	11155.49		13261.01	24538.68
v_D	31	9	27	9	30	0	26	89.961	11017.22	8.21	13001.71	24117.10
v_D	30	9	27	9	29	0	26	89.961	11017.22	5.37	13002.22	24114.77
v_D	29	9	27	9	28	0	26	89.961	11017.22	2.63	13002.69	24112.49
v_D	28	9	27			0	26	89.961	11017.22		13003.13	24110.30
v_D	27	9	27	9	26	0	26	89.961	11017.22	-2.53	13003.54	24108.19
v_D	26	9	27	9	25	0	26	89.961	11017.22	-4.96	13003.92	24106.14
v_D	25	9	27	9	24	0	26	89.961	11017.22	-7.28	13004.28	24104.17
v_D	20	9	17	9	19	0	18	69.149	11017.22	3.38	13005.67	24095.42
v_D	19	9	17	9	18	0	18	69.149	11017.22	1.64	13005.89	24093.90
v_D	19	9	17	9	20	0	18	69.149	11017.22	5.21	13002.32	24093.90
v_D	18	9	17			0	18	69.149	11017.22		13006.08	24092.44
v_D	18	9	17	9	19	0	18	69.149	11017.22	3.38	13002.69	24092.44
v_D	17	9	17	9	16	0	18	69.149	11017.22	-1.55	13006.25	24091.07
v_D	17	9	17	9	18	0	18	69.149	11017.22	1.64	13003.06	24091.06
v_D	16	9	17			0	18	69.149	11017.22		13003.40	24089.77
v_D	16	9	17	9	15	0	18	69.149	11017.22	-3.00	13006.40	24089.76
v_D	15	9	17	9	14	0	18	69.149	11017.22	-4.36	13006.54	24088.54
v_D	15	9	17	9	16	0	18	69.149	11017.22	-1.55	13003.72	24088.54

v	J	v'	J'	v'_c	J'_c	v''	J''	E_{gs} (cm^{-1})	E_{pump} (cm^{-1})	E_{coll} (cm^{-1})	E_{probe} (cm^{-1})	$E_{4^3\Pi_{0+}\ (v,J)}$ (cm^{-1})
v_D	14	9	17	9	13	0	18	69.149	11017.22	-5.63	13006.65	24087.39
v_D	14	9	17	9	15	0	18	69.149	11017.22	-3.00	13004.03	24087.39
v_D	13	9	17	9	14	0	18	69.149	11017.22	-4.36	13004.33	24086.34
v_E	31	9	27	9	30	0	26	89.961	11017.22	8.21	13234.30	24349.69
v_E	30	9	27	9	29	0	26	89.961	11017.22	5.37	13235.24	24347.79
v_E	29	9	27	9	28	0	26	89.961	11017.22	2.63	13236.18	24345.99
v_E	28	9	27			0	26	89.961	11017.22		13237.03	24344.21
v_E	28	9	27	9	29	0	26	89.961	11017.22	5.37	13231.66	24344.21
v_E	27	9	27	9	28	0	26	89.961	11017.22	2.63	13232.66	24342.47
v_E	27	9	27	9	26	0	26	89.961	11017.22	-2.53	13237.83	24342.47
v_E	26	9	27			0	26	89.961	11017.22		13233.64	24340.81
v_E	26	9	27	9	25	0	26	89.961	11017.22	-4.96	13238.60	24340.82
v_E	25	9	27	9	26	0	26	89.961	11017.22	-2.53	13234.59	24339.23
v_E	25	9	27	9	24	0	26	89.961	11017.22	-7.28	13239.34	24339.23
v_E	24	9	27	9	25	0	26	89.961	11017.22	-4.96	13235.58	24337.79
v_E	19	9	17	9	20	0	18	69.149	11017.22	5.21	13237.63	24329.21
v_E	18	9	17	9	19	0	18	69.149	11017.22	3.38	13238.32	24328.06
v_E	17	9	17	9	18	0	18	69.149	11017.22	1.64	13239.60	24327.61
v_E	16	9	17			0	18	69.149	11017.22		13239.60	24325.97
v_F+3	28	9	27			0	26	89.961	11017.22		13230.46	24337.64
v_F+3	26	9	27			0	26	89.961	11017.22		13228.92	24336.10
v_F+2	28	9	27			0	26	89.961	11017.22		13215.65	24322.83
v_F+2	26	9	27			0	26	89.961	11017.22		13213.91	24321.08
v_F+2	18	9	17			0	18	69.149	11017.22		13228.38	24314.75
v_F+2	16	9	17			0	18	69.149	11017.22		13227.10	24313.47
v_F+1	28	9	27			0	26	89.961	11017.22		13207.50	24314.68
v_F+1	26	9	27			0	26	89.961	11017.22		13205.92	24313.09
v_F+1	18	9	17			0	18	69.149	11017.22		13221.04	24307.41
v_F+1	16	9	17			0	18	69.149	11017.22		13219.99	24306.35

v	J	v'	J'	v'_c	J'_c	v''	J''	E_{gs} (cm^{-1})	E_{pump} (cm^{-1})	E_{coll} (cm^{-1})	E_{probe} (cm^{-1})	$E_{4^3\Pi_{0+}\ (v,J)}$ (cm^{-1})
v_F	28	9	27			0	26	89.961	11017.22		13184.81	24291.99
v_F	26	9	27			0	26	89.961	11017.22		13183.18	24290.36
v_F	18	9	17			0	18	69.149	11017.22		13195.28	24281.64
v_F	16	9	17			0	18	69.149	11017.22		13193.94	24280.30

Appendix D

CCD Detector Efficiency Data

The following table compiles CCD detector efficiency curves for various monochromator grating settings used in this work. The efficiencies are given as a function of pixel number, as opposed to wavelength, so that if a spectrum is taken at one of the grating positions given here, the intensity can be easily corrected by dividing by the efficiency pixel by pixel. The efficiencies are normalized so that the maximum value is one. For the efficiencies shown here, the monochromator was used in second order with 395nm longpass, 540 shortpass, and 675 shortpass filters placed in front of the entrance slit. Figure D.1 and Table D.1 give the relative detector efficiency at a grating position of 860 nm. Figure D.2 and Table D.2 give the relative detector efficiency at a grating position of 940 nm. Figure D.2 and Table D.2 give the relative detector efficiency at a grating position of 1020 nm. Note that the given pixel numbers are 4-1039 as opposed to the total number of pixels which are numbered 0-1043. This is because the the first and last four pixels on the array do not produce signal and hence are removed from both the efficiencies and spectra.

Pixel	Efficiency	Pixel	Efficiency	Pixel	Efficiency	Pixel	Efficiency
4	0.0401	263	0.0789	522	0.2438	781	0.6032
5	0.0404	264	0.0789	523	0.2435	782	0.6040
6	0.0401	265	0.0789	524	0.2437	783	0.6043
7	0.0400	266	0.0789	525	0.2433	784	0.6080
8	0.0399	267	0.0795	526	0.2437	785	0.6079
9	0.0395	268	0.0794	527	0.2434	786	0.6088
10	0.0393	269	0.0797	528	0.2439	787	0.6098
11	0.0394	270	0.0802	529	0.2442	788	0.6109
12	0.0392	271	0.0802	530	0.2448	789	0.6122
13	0.0392	272	0.0803	531	0.2442	790	0.6130
14	0.0392	273	0.0804	532	0.2449	791	0.6135
15	0.0395	274	0.0806	533	0.2444	792	0.6149
16	0.0390	275	0.0806	534	0.2449	793	0.6151
17	0.0391	276	0.0809	535	0.2449	794	0.6154
18	0.0393	277	0.0810	536	0.2454	795	0.6154
19	0.0392	278	0.0816	537	0.2458	796	0.6161
20	0.0395	279	0.0817	538	0.2459	797	0.6158
21	0.0392	280	0.0818	539	0.2464	798	0.6160
22	0.0395	281	0.0821	540	0.2464	799	0.6156
23	0.0400	282	0.0821	541	0.2459	800	0.6155
24	0.0401	283	0.0824	542	0.2463	801	0.6151
25	0.0402	284	0.0832	543	0.2468	802	0.6153
26	0.0404	285	0.0831	544	0.2468	803	0.6166
27	0.0401	286	0.0835	545	0.2474	804	0.6165
28	0.0402	287	0.0833	546	0.2476	805	0.6179
29	0.0411	288	0.0831	547	0.2482	806	0.6187
30	0.0411	289	0.0837	548	0.2477	807	0.6188
31	0.0414	290	0.0837	549	0.2487	808	0.6183
32	0.0416	291	0.0839	550	0.2490	809	0.6203
33	0.0420	292	0.0838	551	0.2489	810	0.6205
34	0.0421	293	0.0844	552	0.2487	811	0.6221
35	0.0425	294	0.0849	553	0.2495	812	0.6218
36	0.0424	295	0.0849	554	0.2490	813	0.6216
37	0.0426	296	0.0852	555	0.2496	814	0.6221
38	0.0425	297	0.0859	556	0.2501	815	0.6228
39	0.0436	298	0.0854	557	0.2507	816	0.6237

Pixel	Efficiency	Pixel	Efficiency	Pixel	Efficiency	Pixel	Efficiency
40	0.0437	299	0.0856	558	0.2511	817	0.6225
41	0.0435	300	0.0855	559	0.2528	818	0.6235
42	0.0437	301	0.0864	560	0.2532	819	0.6239
43	0.0443	302	0.0869	561	0.2540	820	0.6243
44	0.0444	303	0.0880	562	0.2545	821	0.6244
45	0.0443	304	0.0889	563	0.2547	822	0.6241
46	0.0448	305	0.0894	564	0.2553	823	0.6242
47	0.0447	306	0.0900	565	0.2564	824	0.6243
48	0.0447	307	0.0904	566	0.2568	825	0.6248
49	0.0449	308	0.0911	567	0.2571	826	0.6235
50	0.0453	309	0.0914	568	0.2579	827	0.6235
51	0.0458	310	0.0916	569	0.2582	828	0.6239
52	0.0459	311	0.0928	570	0.2590	829	0.6246
53	0.0459	312	0.0928	571	0.2601	830	0.6252
54	0.0463	313	0.0931	572	0.2610	831	0.6249
55	0.0465	314	0.0937	573	0.2618	832	0.6250
56	0.0468	315	0.0942	574	0.2628	833	0.6257
57	0.0469	316	0.0950	575	0.2638	834	0.6248
58	0.0472	317	0.0954	576	0.2641	835	0.6257
59	0.0477	318	0.0959	577	0.2645	836	0.6256
60	0.0476	319	0.0965	578	0.2656	837	0.6255
61	0.0482	320	0.0972	579	0.2662	838	0.6258
62	0.0484	321	0.0976	580	0.2669	839	0.6268
63	0.0487	322	0.0983	581	0.2675	840	0.6264
64	0.0493	323	0.0985	582	0.2686	841	0.6250
65	0.0492	324	0.0995	583	0.2694	842	0.6239
66	0.0495	325	0.0999	584	0.2703	843	0.6217
67	0.0497	326	0.1009	585	0.2711	844	0.6214
68	0.0496	327	0.1014	586	0.2718	845	0.6218
69	0.0499	328	0.1022	587	0.2730	846	0.6236
70	0.0506	329	0.1034	588	0.2743	847	0.6258
71	0.0504	330	0.1043	589	0.2748	848	0.6270
72	0.0508	331	0.1049	590	0.2751	849	0.6299
73	0.0515	332	0.1056	591	0.2754	850	0.6307
74	0.0517	333	0.1065	592	0.2757	851	0.6318
75	0.0524	334	0.1072	593	0.2769	852	0.6333
76	0.0526	335	0.1083	594	0.2776	853	0.6343

Pixel	Efficiency	Pixel	Efficiency	Pixel	Efficiency	Pixel	Efficiency
77	0.0524	336	0.1089	595	0.2793	854	0.6344
78	0.0521	337	0.1098	596	0.2805	855	0.6355
79	0.0524	338	0.1105	597	0.2818	856	0.6362
80	0.0529	339	0.1117	598	0.2827	857	0.6368
81	0.0533	340	0.1124	599	0.2831	858	0.6360
82	0.0536	341	0.1136	600	0.2855	859	0.6376
83	0.0547	342	0.1145	601	0.2869	860	0.6378
84	0.0553	343	0.1152	602	0.2875	861	0.6374
85	0.0558	344	0.1160	603	0.2898	862	0.6367
86	0.0564	345	0.1174	604	0.2913	863	0.6370
87	0.0565	346	0.1182	605	0.2916	864	0.6368
88	0.0570	347	0.1189	606	0.2931	865	0.6385
89	0.0572	348	0.1202	607	0.2946	866	0.6393
90	0.0573	349	0.1209	608	0.2961	867	0.6422
91	0.0584	350	0.1223	609	0.2968	868	0.6432
92	0.0586	351	0.1235	610	0.2980	869	0.6443
93	0.0591	352	0.1245	611	0.2993	870	0.6462
94	0.0590	353	0.1256	612	0.3004	871	0.6478
95	0.0599	354	0.1268	613	0.3018	872	0.6490
96	0.0601	355	0.1277	614	0.3029	873	0.6498
97	0.0604	356	0.1293	615	0.3039	874	0.6513
98	0.0604	357	0.1307	616	0.3055	875	0.6517
99	0.0610	358	0.1315	617	0.3073	876	0.6516
100	0.0615	359	0.1333	618	0.3083	877	0.6529
101	0.0620	360	0.1341	619	0.3093	878	0.6554
102	0.0623	361	0.1353	620	0.3112	879	0.6566
103	0.0633	362	0.1363	621	0.3119	880	0.6581
104	0.0633	363	0.1378	622	0.3131	881	0.6599
105	0.0636	364	0.1384	623	0.3144	882	0.6609
106	0.0640	365	0.1397	624	0.3152	883	0.6622
107	0.0644	366	0.1405	625	0.3161	884	0.6641
108	0.0654	367	0.1412	626	0.3170	885	0.6660
109	0.0654	368	0.1422	627	0.3181	886	0.6674
110	0.0660	369	0.1436	628	0.3193	887	0.6686
111	0.0658	370	0.1452	629	0.3217	888	0.6703
112	0.0667	371	0.1465	630	0.3239	889	0.6720
113	0.0672	372	0.1482	631	0.3267	890	0.6729

Pixel	Efficiency	Pixel	Efficiency	Pixel	Efficiency	Pixel	Efficiency
114	0.0677	373	0.1500	632	0.3289	891	0.6757
115	0.0678	374	0.1516	633	0.3312	892	0.6777
116	0.0682	375	0.1532	634	0.3330	893	0.6800
117	0.0687	376	0.1545	635	0.3347	894	0.6806
118	0.0691	377	0.1559	636	0.3369	895	0.6824
119	0.0696	378	0.1569	637	0.3382	896	0.6851
120	0.0698	379	0.1577	638	0.3396	897	0.6861
121	0.0704	380	0.1590	639	0.3416	898	0.6877
122	0.0706	381	0.1604	640	0.3433	899	0.6902
123	0.0707	382	0.1623	641	0.3451	900	0.6928
124	0.0713	383	0.1639	642	0.3466	901	0.6944
125	0.0710	384	0.1656	643	0.3474	902	0.6955
126	0.0719	385	0.1670	644	0.3482	903	0.6973
127	0.0725	386	0.1687	645	0.3486	904	0.6992
128	0.0727	387	0.1701	646	0.3492	905	0.7012
129	0.0734	388	0.1714	647	0.3507	906	0.7034
130	0.0736	389	0.1731	648	0.3536	907	0.7059
131	0.0744	390	0.1743	649	0.3559	908	0.7078
132	0.0745	391	0.1761	650	0.3577	909	0.7100
133	0.0746	392	0.1774	651	0.3595	910	0.7117
134	0.0749	393	0.1795	652	0.3613	911	0.7136
135	0.0757	394	0.1805	653	0.3630	912	0.7161
136	0.0761	395	0.1823	654	0.3658	913	0.7177
137	0.0763	396	0.1840	655	0.3675	914	0.7197
138	0.0768	397	0.1850	656	0.3703	915	0.7222
139	0.0772	398	0.1862	657	0.3737	916	0.7239
140	0.0773	399	0.1876	658	0.3767	917	0.7265
141	0.0779	400	0.1893	659	0.3797	918	0.7296
142	0.0778	401	0.1907	660	0.3826	919	0.7320
143	0.0786	402	0.1922	661	0.3855	920	0.7346
144	0.0789	403	0.1939	662	0.3889	921	0.7367
145	0.0792	404	0.1954	663	0.3912	922	0.7388
146	0.0794	405	0.1967	664	0.3936	923	0.7414
147	0.0795	406	0.1978	665	0.3969	924	0.7442
148	0.0798	407	0.2001	666	0.3977	925	0.7466
149	0.0802	408	0.2012	667	0.4000	926	0.7485
150	0.0804	409	0.2026	668	0.4014	927	0.7518

Pixel	Efficiency	Pixel	Efficiency	Pixel	Efficiency	Pixel	Efficiency
151	0.0803	410	0.2043	669	0.4045	928	0.7537
152	0.0807	411	0.2054	670	0.4062	929	0.7556
153	0.0812	412	0.2070	671	0.4097	930	0.7580
154	0.0813	413	0.2080	672	0.4120	931	0.7603
155	0.0813	414	0.2093	673	0.4152	932	0.7628
156	0.0817	415	0.2115	674	0.4172	933	0.7645
157	0.0819	416	0.2125	675	0.4194	934	0.7680
158	0.0818	417	0.2140	676	0.4219	935	0.7694
159	0.0818	418	0.2152	677	0.4252	936	0.7713
160	0.0820	419	0.2165	678	0.4281	937	0.7734
161	0.0823	420	0.2183	679	0.4305	938	0.7745
162	0.0827	421	0.2196	680	0.4327	939	0.7779
163	0.0830	422	0.2207	681	0.4352	940	0.7790
164	0.0825	423	0.2221	682	0.4381	941	0.7813
165	0.0830	424	0.2229	683	0.4410	942	0.7829
166	0.0824	425	0.2242	684	0.4436	943	0.7849
167	0.0829	426	0.2254	685	0.4467	944	0.7871
168	0.0828	427	0.2263	686	0.4494	945	0.7886
169	0.0830	428	0.2279	687	0.4522	946	0.7915
170	0.0830	429	0.2286	688	0.4550	947	0.7918
171	0.0828	430	0.2300	689	0.4586	948	0.7940
172	0.0833	431	0.2308	690	0.4614	949	0.7960
173	0.0831	432	0.2317	691	0.4638	950	0.7983
174	0.0829	433	0.2325	692	0.4646	951	0.8010
175	0.0829	434	0.2337	693	0.4663	952	0.8029
176	0.0830	435	0.2350	694	0.4678	953	0.8037
177	0.0831	436	0.2361	695	0.4701	954	0.8066
178	0.0833	437	0.2365	696	0.4715	955	0.8085
179	0.0829	438	0.2372	697	0.4738	956	0.8107
180	0.0830	439	0.2385	698	0.4758	957	0.8122
181	0.0834	440	0.2390	699	0.4789	958	0.8137
182	0.0830	441	0.2403	700	0.4828	959	0.8148
183	0.0825	442	0.2400	701	0.4860	960	0.8166
184	0.0827	443	0.2409	702	0.4902	961	0.8189
185	0.0820	444	0.2418	703	0.4939	962	0.8217
186	0.0819	445	0.2432	704	0.4965	963	0.8223
187	0.0820	446	0.2434	705	0.4988	964	0.8250

Pixel	Efficiency	Pixel	Efficiency	Pixel	Efficiency	Pixel	Efficiency
188	0.0817	447	0.2443	706	0.5018	965	0.8267
189	0.0819	448	0.2453	707	0.5037	966	0.8290
190	0.0817	449	0.2461	708	0.5059	967	0.8315
191	0.0822	450	0.2464	709	0.5072	968	0.8346
192	0.0821	451	0.2468	710	0.5093	969	0.8358
193	0.0821	452	0.2470	711	0.5102	970	0.8386
194	0.0824	453	0.2485	712	0.5121	971	0.8408
195	0.0823	454	0.2490	713	0.5122	972	0.8430
196	0.0822	455	0.2493	714	0.5131	973	0.8453
197	0.0815	456	0.2501	715	0.5147	974	0.8471
198	0.0816	457	0.2509	716	0.5172	975	0.8495
199	0.0816	458	0.2510	717	0.5202	976	0.8517
200	0.0812	459	0.2507	718	0.5229	977	0.8537
201	0.0815	460	0.2514	719	0.5260	978	0.8562
202	0.0807	461	0.2511	720	0.5276	979	0.8580
203	0.0810	462	0.2517	721	0.5302	980	0.8597
204	0.0809	463	0.2519	722	0.5325	981	0.8628
205	0.0808	464	0.2520	723	0.5334	982	0.8653
206	0.0805	465	0.2527	724	0.5349	983	0.8671
207	0.0804	466	0.2527	725	0.5369	984	0.8696
208	0.0802	467	0.2525	726	0.5395	985	0.8721
209	0.0802	468	0.2533	727	0.5417	986	0.8742
210	0.0795	469	0.2536	728	0.5433	987	0.8765
211	0.0797	470	0.2535	729	0.5456	988	0.8785
212	0.0793	471	0.2534	730	0.5476	989	0.8810
213	0.0791	472	0.2535	731	0.5489	990	0.8841
214	0.0791	473	0.2530	732	0.5507	991	0.8862
215	0.0787	474	0.2534	733	0.5523	992	0.8865
216	0.0791	475	0.2534	734	0.5536	993	0.8853
217	0.0792	476	0.2539	735	0.5544	994	0.8835
218	0.0787	477	0.2543	736	0.5556	995	0.8836
219	0.0785	478	0.2531	737	0.5564	996	0.8837
220	0.0791	479	0.2530	738	0.5571	997	0.8867
221	0.0788	480	0.2527	739	0.5579	998	0.8911
222	0.0789	481	0.2534	740	0.5603	999	0.8971
223	0.0787	482	0.2540	741	0.5615	1000	0.9016
224	0.0785	483	0.2529	742	0.5624	1001	0.9058

Pixel	Efficiency	Pixel	Efficiency	Pixel	Efficiency	Pixel	Efficiency
225	0.0785	484	0.2529	743	0.5633	1002	0.9083
226	0.0783	485	0.2527	744	0.5627	1003	0.9121
227	0.0780	486	0.2518	745	0.5631	1004	0.9140
228	0.0780	487	0.2514	746	0.5632	1005	0.9167
229	0.0780	488	0.2515	747	0.5638	1006	0.9185
230	0.0779	489	0.2508	748	0.5645	1007	0.9214
231	0.0778	490	0.2504	749	0.5660	1008	0.9236
232	0.0776	491	0.2506	750	0.5678	1009	0.9251
233	0.0777	492	0.2508	751	0.5693	1010	0.9264
234	0.0778	493	0.2506	752	0.5708	1011	0.9269
235	0.0776	494	0.2502	753	0.5724	1012	0.9277
236	0.0778	495	0.2504	754	0.5737	1013	0.9292
237	0.0776	496	0.2499	755	0.5743	1014	0.9312
238	0.0779	497	0.2496	756	0.5747	1015	0.9340
239	0.0776	498	0.2490	757	0.5755	1016	0.9371
240	0.0777	499	0.2488	758	0.5770	1017	0.9407
241	0.0777	500	0.2485	759	0.5773	1018	0.9437
242	0.0778	501	0.2484	760	0.5777	1019	0.9475
243	0.0778	502	0.2484	761	0.5781	1020	0.9497
244	0.0776	503	0.2483	762	0.5793	1021	0.9520
245	0.0779	504	0.2479	763	0.5798	1022	0.9567
246	0.0777	505	0.2482	764	0.5814	1023	0.9584
247	0.0779	506	0.2479	765	0.5831	1024	0.9622
248	0.0781	507	0.2474	766	0.5850	1025	0.9651
249	0.0779	508	0.2477	767	0.5864	1026	0.9669
250	0.0780	509	0.2478	768	0.5872	1027	0.9696
251	0.0776	510	0.2471	769	0.5889	1028	0.9743
252	0.0780	511	0.2468	770	0.5897	1029	0.9774
253	0.0784	512	0.2465	771	0.5901	1030	0.9800
254	0.0783	513	0.2464	772	0.5915	1031	0.9828
255	0.0784	514	0.2459	773	0.5927	1032	0.9863
256	0.0781	515	0.2457	774	0.5941	1033	0.9888
257	0.0785	516	0.2457	775	0.5942	1034	0.9910
258	0.0785	517	0.2450	776	0.5952	1035	0.9923
259	0.0787	518	0.2456	777	0.5963	1036	0.9946
260	0.0785	519	0.2450	778	0.5981	1037	0.9974
261	0.0784	520	0.2448	779	0.5984	1038	0.9984

Pixel	Efficiency	Pixel	Efficiency	Pixel	Efficiency	Pixel	Efficiency
262	0.0789	521	0.2442	780	0.6015	1039	1.0000

Table D.1: Efficiency as a function of pixel number for a grating position of 860 nm

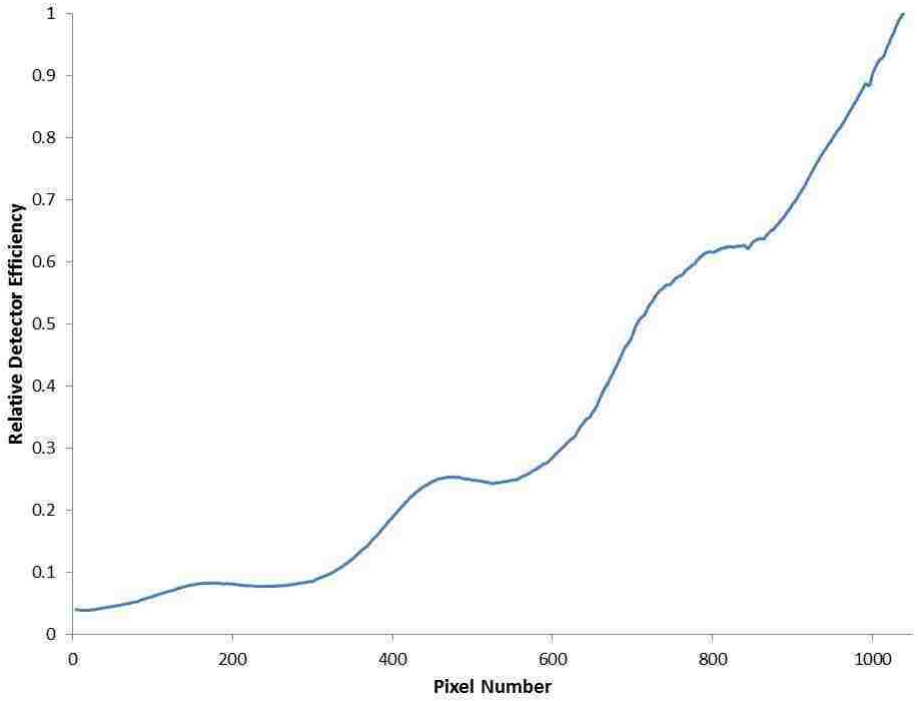

Figure D.1: Efficiency as a function of pixel number for a grating position of 860 nm.

Pixel	Efficiency	Pixel	Efficiency	Pixel	Efficiency	Pixel	Efficiency
4	0.1435	263	0.3162	522	0.5694	781	0.8280
5	0.1432	264	0.3167	523	0.5686	782	0.8299
6	0.1426	265	0.3172	524	0.5688	783	0.8324
7	0.1420	266	0.3179	525	0.5686	784	0.8352
8	0.1413	267	0.3179	526	0.5693	785	0.8368
9	0.1409	268	0.3175	527	0.5698	786	0.8381
10	0.1399	269	0.3179	528	0.5707	787	0.8397
11	0.1391	270	0.3186	529	0.5718	788	0.8416
12	0.1389	271	0.3186	530	0.5725	789	0.8431
13	0.1387	272	0.3197	531	0.5726	790	0.8449
14	0.1389	273	0.3200	532	0.5725	791	0.8458
15	0.1387	274	0.3203	533	0.5727	792	0.8475
16	0.1389	275	0.3206	534	0.5734	793	0.8484
17	0.1390	276	0.3208	535	0.5733	794	0.8488
18	0.1393	277	0.3213	536	0.5733	795	0.8501
19	0.1392	278	0.3217	537	0.5739	796	0.8509
20	0.1401	279	0.3222	538	0.5753	797	0.8512
21	0.1403	280	0.3226	539	0.5748	798	0.8519
22	0.1405	281	0.3232	540	0.5759	799	0.8515
23	0.1411	282	0.3239	541	0.5752	800	0.8504
24	0.1418	283	0.3241	542	0.5766	801	0.8501
25	0.1427	284	0.3243	543	0.5763	802	0.8507
26	0.1434	285	0.3248	544	0.5762	803	0.8520
27	0.1441	286	0.3254	545	0.5775	804	0.8538
28	0.1452	287	0.3247	546	0.5778	805	0.8562
29	0.1458	288	0.3246	547	0.5780	806	0.8577
30	0.1466	289	0.3244	548	0.5779	807	0.8592
31	0.1476	290	0.3244	549	0.5782	808	0.8605
32	0.1484	291	0.3240	550	0.5788	809	0.8620
33	0.1493	292	0.3240	551	0.5790	810	0.8634
34	0.1497	293	0.3248	552	0.5783	811	0.8660
35	0.1510	294	0.3248	553	0.5782	812	0.8669
36	0.1515	295	0.3255	554	0.5773	813	0.8667
37	0.1522	296	0.3255	555	0.5778	814	0.8686
38	0.1531	297	0.3255	556	0.5785	815	0.8695
39	0.1538	298	0.3247	557	0.5790	816	0.8715

Pixel	Efficiency	Pixel	Efficiency	Pixel	Efficiency	Pixel	Efficiency
40	0.1549	299	0.3244	558	0.5803	817	0.8715
41	0.1554	300	0.3240	559	0.5821	818	0.8729
42	0.1564	301	0.3253	560	0.5831	819	0.8739
43	0.1568	302	0.3273	561	0.5848	820	0.8749
44	0.1579	303	0.3303	562	0.5853	821	0.8756
45	0.1587	304	0.3331	563	0.5845	822	0.8768
46	0.1594	305	0.3356	564	0.5856	823	0.8776
47	0.1602	306	0.3372	565	0.5869	824	0.8786
48	0.1612	307	0.3384	566	0.5874	825	0.8791
49	0.1620	308	0.3394	567	0.5872	826	0.8795
50	0.1627	309	0.3402	568	0.5880	827	0.8800
51	0.1639	310	0.3407	569	0.5884	828	0.8813
52	0.1651	311	0.3412	570	0.5893	829	0.8820
53	0.1659	312	0.3421	571	0.5899	830	0.8834
54	0.1667	313	0.3425	572	0.5913	831	0.8838
55	0.1678	314	0.3435	573	0.5923	832	0.8845
56	0.1687	315	0.3441	574	0.5932	833	0.8855
57	0.1696	316	0.3448	575	0.5934	834	0.8859
58	0.1706	317	0.3460	576	0.5938	835	0.8870
59	0.1715	318	0.3473	577	0.5942	836	0.8870
60	0.1729	319	0.3477	578	0.5947	837	0.8883
61	0.1736	320	0.3490	579	0.5948	838	0.8890
62	0.1747	321	0.3501	580	0.5954	839	0.8896
63	0.1760	322	0.3508	581	0.5962	840	0.8898
64	0.1774	323	0.3519	582	0.5967	841	0.8881
65	0.1780	324	0.3527	583	0.5968	842	0.8860
66	0.1786	325	0.3538	584	0.5980	843	0.8848
67	0.1790	326	0.3549	585	0.5990	844	0.8846
68	0.1796	327	0.3565	586	0.5995	845	0.8861
69	0.1805	328	0.3577	587	0.6008	846	0.8891
70	0.1818	329	0.3592	588	0.6012	847	0.8918
71	0.1827	330	0.3604	589	0.6011	848	0.8950
72	0.1848	331	0.3619	590	0.6002	849	0.8977
73	0.1863	332	0.3633	591	0.5993	850	0.9000
74	0.1877	333	0.3646	592	0.5991	851	0.9013
75	0.1889	334	0.3658	593	0.5996	852	0.9031
76	0.1892	335	0.3674	594	0.6005	853	0.9048

Pixel	Efficiency	Pixel	Efficiency	Pixel	Efficiency	Pixel	Efficiency
77	0.1892	336	0.3683	595	0.6026	854	0.9061
78	0.1885	337	0.3693	596	0.6049	855	0.9062
79	0.1888	338	0.3706	597	0.6060	856	0.9078
80	0.1897	339	0.3720	598	0.6073	857	0.9083
81	0.1912	340	0.3739	599	0.6081	858	0.9083
82	0.1935	341	0.3748	600	0.6095	859	0.9086
83	0.1965	342	0.3760	601	0.6114	860	0.9085
84	0.1990	343	0.3765	602	0.6126	861	0.9087
85	0.2013	344	0.3777	603	0.6144	862	0.9071
86	0.2033	345	0.3788	604	0.6166	863	0.9069
87	0.2044	346	0.3802	605	0.6167	864	0.9067
88	0.2060	347	0.3816	606	0.6178	865	0.9077
89	0.2071	348	0.3833	607	0.6187	866	0.9083
90	0.2085	349	0.3842	608	0.6193	867	0.9105
91	0.2098	350	0.3862	609	0.6199	868	0.9119
92	0.2110	351	0.3873	610	0.6209	869	0.9132
93	0.2124	352	0.3886	611	0.6218	870	0.9160
94	0.2135	353	0.3896	612	0.6222	871	0.9165
95	0.2148	354	0.3912	613	0.6226	872	0.9174
96	0.2159	355	0.3919	614	0.6235	873	0.9173
97	0.2172	356	0.3942	615	0.6245	874	0.9184
98	0.2186	357	0.3956	616	0.6250	875	0.9186
99	0.2198	358	0.3968	617	0.6253	876	0.9178
100	0.2209	359	0.3984	618	0.6260	877	0.9189
101	0.2228	360	0.3990	619	0.6262	878	0.9201
102	0.2244	361	0.3996	620	0.6267	879	0.9203
103	0.2258	362	0.4008	621	0.6271	880	0.9214
104	0.2270	363	0.4018	622	0.6269	881	0.9218
105	0.2283	364	0.4022	623	0.6271	882	0.9223
106	0.2300	365	0.4018	624	0.6267	883	0.9228
107	0.2312	366	0.4015	625	0.6254	884	0.9231
108	0.2329	367	0.4009	626	0.6246	885	0.9241
109	0.2339	368	0.4014	627	0.6235	886	0.9248
110	0.2349	369	0.4025	628	0.6239	887	0.9246
111	0.2363	370	0.4040	629	0.6254	888	0.9252
112	0.2375	371	0.4063	630	0.6269	889	0.9252
113	0.2390	372	0.4087	631	0.6295	890	0.9258

Pixel	Efficiency	Pixel	Efficiency	Pixel	Efficiency	Pixel	Efficiency
114	0.2405	373	0.4110	632	0.6321	891	0.9270
115	0.2416	374	0.4134	633	0.6342	892	0.9274
116	0.2430	375	0.4149	634	0.6364	893	0.9276
117	0.2441	376	0.4161	635	0.6368	894	0.9275
118	0.2456	377	0.4172	636	0.6382	895	0.9287
119	0.2463	378	0.4167	637	0.6373	896	0.9286
120	0.2478	379	0.4173	638	0.6377	897	0.9285
121	0.2487	380	0.4182	639	0.6388	898	0.9287
122	0.2494	381	0.4194	640	0.6391	899	0.9296
123	0.2496	382	0.4207	641	0.6400	900	0.9296
124	0.2502	383	0.4231	642	0.6393	901	0.9305
125	0.2509	384	0.4249	643	0.6378	902	0.9299
126	0.2519	385	0.4265	644	0.6353	903	0.9304
127	0.2541	386	0.4293	645	0.6328	904	0.9306
128	0.2554	387	0.4304	646	0.6305	905	0.9309
129	0.2570	388	0.4320	647	0.6300	906	0.9307
130	0.2586	389	0.4335	648	0.6307	907	0.9308
131	0.2597	390	0.4352	649	0.6323	908	0.9313
132	0.2606	391	0.4366	650	0.6327	909	0.9321
133	0.2617	392	0.4383	651	0.6336	910	0.9317
134	0.2626	393	0.4403	652	0.6337	911	0.9323
135	0.2640	394	0.4418	653	0.6338	912	0.9321
136	0.2650	395	0.4434	654	0.6341	913	0.9321
137	0.2659	396	0.4446	655	0.6344	914	0.9321
138	0.2668	397	0.4453	656	0.6372	915	0.9336
139	0.2674	398	0.4467	657	0.6397	916	0.9329
140	0.2688	399	0.4478	658	0.6423	917	0.9340
141	0.2698	400	0.4488	659	0.6452	918	0.9351
142	0.2701	401	0.4503	660	0.6479	919	0.9359
143	0.2717	402	0.4519	661	0.6506	920	0.9365
144	0.2720	403	0.4539	662	0.6539	921	0.9358
145	0.2728	404	0.4561	663	0.6562	922	0.9365
146	0.2732	405	0.4576	664	0.6577	923	0.9370
147	0.2744	406	0.4593	665	0.6598	924	0.9383
148	0.2749	407	0.4603	666	0.6600	925	0.9381
149	0.2760	408	0.4618	667	0.6604	926	0.9380
150	0.2769	409	0.4632	668	0.6603	927	0.9383

Pixel	Efficiency	Pixel	Efficiency	Pixel	Efficiency	Pixel	Efficiency
151	0.2775	410	0.4648	669	0.6617	928	0.9383
152	0.2784	411	0.4666	670	0.6610	929	0.9387
153	0.2792	412	0.4681	671	0.6635	930	0.9383
154	0.2797	413	0.4694	672	0.6645	931	0.9390
155	0.2805	414	0.4712	673	0.6657	932	0.9385
156	0.2812	415	0.4742	674	0.6678	933	0.9397
157	0.2818	416	0.4751	675	0.6683	934	0.9401
158	0.2827	417	0.4771	676	0.6695	935	0.9406
159	0.2831	418	0.4785	677	0.6715	936	0.9410
160	0.2837	419	0.4806	678	0.6740	937	0.9413
161	0.2846	420	0.4820	679	0.6740	938	0.9401
162	0.2848	421	0.4840	680	0.6748	939	0.9422
163	0.2858	422	0.4854	681	0.6760	940	0.9423
164	0.2862	423	0.4872	682	0.6774	941	0.9430
165	0.2867	424	0.4886	683	0.6795	942	0.9430
166	0.2872	425	0.4903	684	0.6809	943	0.9441
167	0.2880	426	0.4910	685	0.6832	944	0.9430
168	0.2882	427	0.4928	686	0.6855	945	0.9443
169	0.2882	428	0.4953	687	0.6866	946	0.9440
170	0.2889	429	0.4962	688	0.6881	947	0.9432
171	0.2900	430	0.4983	689	0.6913	948	0.9434
172	0.2901	431	0.4987	690	0.6932	949	0.9441
173	0.2913	432	0.4997	691	0.6936	950	0.9455
174	0.2911	433	0.5015	692	0.6931	951	0.9455
175	0.2918	434	0.5029	693	0.6936	952	0.9456
176	0.2927	435	0.5038	694	0.6927	953	0.9453
177	0.2929	436	0.5058	695	0.6938	954	0.9455
178	0.2933	437	0.5069	696	0.6937	955	0.9459
179	0.2938	438	0.5076	697	0.6950	956	0.9460
180	0.2942	439	0.5102	698	0.6959	957	0.9466
181	0.2941	440	0.5105	699	0.6986	958	0.9465
182	0.2942	441	0.5120	700	0.7018	959	0.9460
183	0.2940	442	0.5134	701	0.7054	960	0.9461
184	0.2944	443	0.5138	702	0.7096	961	0.9468
185	0.2945	444	0.5148	703	0.7134	962	0.9474
186	0.2947	445	0.5168	704	0.7170	963	0.9470
187	0.2951	446	0.5180	705	0.7185	964	0.9469

Pixel	Efficiency	Pixel	Efficiency	Pixel	Efficiency	Pixel	Efficiency
188	0.2955	447	0.5198	706	0.7210	965	0.9471
189	0.2966	448	0.5222	707	0.7225	966	0.9483
190	0.2981	449	0.5229	708	0.7244	967	0.9489
191	0.2989	450	0.5242	709	0.7261	968	0.9508
192	0.2998	451	0.5252	710	0.7269	969	0.9504
193	0.3005	452	0.5265	711	0.7279	970	0.9520
194	0.3012	453	0.5281	712	0.7286	971	0.9532
195	0.3019	454	0.5297	713	0.7284	972	0.9535
196	0.3020	455	0.5315	714	0.7289	973	0.9535
197	0.3025	456	0.5329	715	0.7306	974	0.9537
198	0.3033	457	0.5343	716	0.7329	975	0.9552
199	0.3036	458	0.5360	717	0.7355	976	0.9551
200	0.3040	459	0.5365	718	0.7369	977	0.9561
201	0.3041	460	0.5375	719	0.7397	978	0.9562
202	0.3042	461	0.5386	720	0.7418	979	0.9564
203	0.3044	462	0.5401	721	0.7436	980	0.9563
204	0.3052	463	0.5409	722	0.7456	981	0.9577
205	0.3054	464	0.5411	723	0.7467	982	0.9585
206	0.3056	465	0.5427	724	0.7483	983	0.9592
207	0.3057	466	0.5436	725	0.7510	984	0.9603
208	0.3059	467	0.5448	726	0.7534	985	0.9603
209	0.3053	468	0.5455	727	0.7556	986	0.9607
210	0.3051	469	0.5468	728	0.7577	987	0.9622
211	0.3045	470	0.5478	729	0.7609	988	0.9628
212	0.3046	471	0.5484	730	0.7625	989	0.9632
213	0.3047	472	0.5496	731	0.7647	990	0.9645
214	0.3046	473	0.5505	732	0.7664	991	0.9648
215	0.3050	474	0.5509	733	0.7677	992	0.9624
216	0.3065	475	0.5521	734	0.7696	993	0.9590
217	0.3069	476	0.5534	735	0.7702	994	0.9551
218	0.3074	477	0.5545	736	0.7706	995	0.9521
219	0.3077	478	0.5546	737	0.7717	996	0.9502
220	0.3088	479	0.5556	738	0.7731	997	0.9528
221	0.3091	480	0.5553	739	0.7743	998	0.9559
222	0.3094	481	0.5569	740	0.7760	999	0.9606
223	0.3091	482	0.5585	741	0.7773	1000	0.9641
224	0.3098	483	0.5587	742	0.7782	1001	0.9674

Pixel	Efficiency	Pixel	Efficiency	Pixel	Efficiency	Pixel	Efficiency
225	0.3097	484	0.5597	743	0.7788	1002	0.9696
226	0.3101	485	0.5593	744	0.7779	1003	0.9717
227	0.3104	486	0.5592	745	0.7782	1004	0.9721
228	0.3098	487	0.5586	746	0.7777	1005	0.9733
229	0.3105	488	0.5595	747	0.7777	1006	0.9743
230	0.3101	489	0.5589	748	0.7776	1007	0.9747
231	0.3101	490	0.5600	749	0.7799	1008	0.9751
232	0.3108	491	0.5599	750	0.7816	1009	0.9757
233	0.3111	492	0.5612	751	0.7839	1010	0.9755
234	0.3106	493	0.5622	752	0.7869	1011	0.9756
235	0.3111	494	0.5623	753	0.7886	1012	0.9751
236	0.3113	495	0.5634	754	0.7907	1013	0.9756
237	0.3115	496	0.5633	755	0.7920	1014	0.9760
238	0.3120	497	0.5636	756	0.7927	1015	0.9769
239	0.3123	498	0.5630	757	0.7937	1016	0.9783
240	0.3128	499	0.5636	758	0.7939	1017	0.9790
241	0.3125	500	0.5642	759	0.7945	1018	0.9802
242	0.3125	501	0.5645	760	0.7953	1019	0.9816
243	0.3129	502	0.5656	761	0.7954	1020	0.9824
244	0.3125	503	0.5663	762	0.7961	1021	0.9826
245	0.3130	504	0.5669	763	0.7971	1022	0.9844
246	0.3129	505	0.5672	764	0.7986	1023	0.9852
247	0.3128	506	0.5681	765	0.8008	1024	0.9865
248	0.3129	507	0.5687	766	0.8038	1025	0.9874
249	0.3133	508	0.5691	767	0.8056	1026	0.9880
250	0.3132	509	0.5692	768	0.8080	1027	0.9890
251	0.3139	510	0.5692	769	0.8102	1028	0.9906
252	0.3137	511	0.5690	770	0.8107	1029	0.9919
253	0.3139	512	0.5687	771	0.8119	1030	0.9932
254	0.3140	513	0.5691	772	0.8131	1031	0.9937
255	0.3148	514	0.5689	773	0.8148	1032	0.9948
256	0.3149	515	0.5683	774	0.8169	1033	0.9959
257	0.3151	516	0.5698	775	0.8168	1034	0.9971
258	0.3150	517	0.5700	776	0.8174	1035	0.9973
259	0.3155	518	0.5701	777	0.8189	1036	0.9979
260	0.3160	519	0.5706	778	0.8202	1037	0.9992
261	0.3158	520	0.5697	779	0.8222	1038	0.9996

Pixel	Efficiency	Pixel	Efficiency	Pixel	Efficiency	Pixel	Efficiency
262	0.3161	521	0.5694	780	0.8252	1039	0.9999

Table D.2: Efficiency as a function of pixel number for a grating position of 940 nm

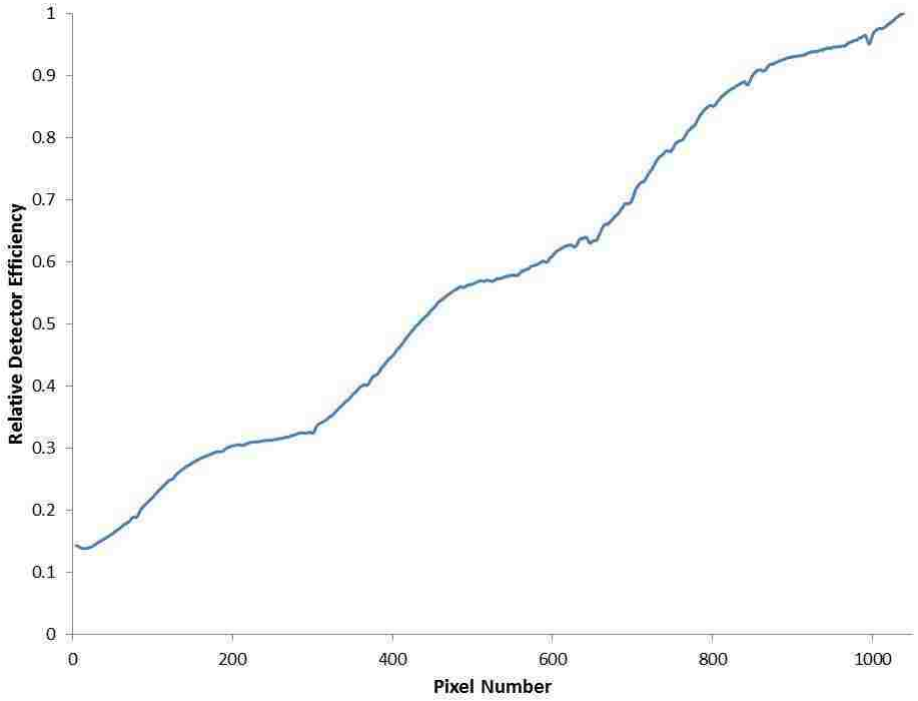

Figure D.2: Efficiency as a function of pixel number for a grating position of 940 nm.

Pixel	Efficiency	Pixel	Efficiency	Pixel	Efficiency	Pixel	Efficiency
4	0.4282	263	0.6292	522	0.7994	781	0.9514
5	0.4268	264	0.6312	523	0.7986	782	0.9530
6	0.4247	265	0.6317	524	0.7998	783	0.9551
7	0.4229	266	0.6319	525	0.7995	784	0.9572
8	0.4212	267	0.6333	526	0.8021	785	0.9570
9	0.4184	268	0.6324	527	0.8039	786	0.9566
10	0.4169	269	0.6335	528	0.8047	787	0.9586
11	0.4156	270	0.6331	529	0.8079	788	0.9587
12	0.4140	271	0.6340	530	0.8082	789	0.9592
13	0.4134	272	0.6358	531	0.8100	790	0.9592
14	0.4125	273	0.6353	532	0.8105	791	0.9598
15	0.4112	274	0.6373	533	0.8124	792	0.9602
16	0.4109	275	0.6378	534	0.8122	793	0.9600
17	0.4102	276	0.6381	535	0.8133	794	0.9598
18	0.4106	277	0.6387	536	0.8147	795	0.9598
19	0.4099	278	0.6390	537	0.8162	796	0.9608
20	0.4109	279	0.6399	538	0.8187	797	0.9592
21	0.4102	280	0.6401	539	0.8197	798	0.9587
22	0.4108	281	0.6424	540	0.8211	799	0.9573
23	0.4110	282	0.6410	541	0.8213	800	0.9559
24	0.4115	283	0.6433	542	0.8237	801	0.9547
25	0.4125	284	0.6419	543	0.8236	802	0.9546
26	0.4125	285	0.6417	544	0.8253	803	0.9545
27	0.4128	286	0.6415	545	0.8263	804	0.9548
28	0.4136	287	0.6393	546	0.8276	805	0.9570
29	0.4156	288	0.6390	547	0.8282	806	0.9569
30	0.4160	289	0.6367	548	0.8301	807	0.9579
31	0.4166	290	0.6372	549	0.8314	808	0.9592
32	0.4169	291	0.6358	550	0.8317	809	0.9599
33	0.4190	292	0.6342	551	0.8315	810	0.9610
34	0.4197	293	0.6343	552	0.8320	811	0.9618
35	0.4197	294	0.6333	553	0.8326	812	0.9626
36	0.4204	295	0.6320	554	0.8323	813	0.9617
37	0.4210	296	0.6325	555	0.8324	814	0.9613
38	0.4226	297	0.6308	556	0.8341	815	0.9629
39	0.4228	298	0.6281	557	0.8352	816	0.9636

Pixel	Efficiency	Pixel	Efficiency	Pixel	Efficiency	Pixel	Efficiency
40	0.4239	299	0.6260	558	0.8382	817	0.9626
41	0.4241	300	0.6258	559	0.8396	818	0.9638
42	0.4244	301	0.6278	560	0.8424	819	0.9636
43	0.4250	302	0.6306	561	0.8456	820	0.9640
44	0.4264	303	0.6345	562	0.8466	821	0.9646
45	0.4253	304	0.6385	563	0.8465	822	0.9634
46	0.4265	305	0.6426	564	0.8495	823	0.9641
47	0.4260	306	0.6466	565	0.8488	824	0.9641
48	0.4276	307	0.6491	566	0.8528	825	0.9646
49	0.4281	308	0.6496	567	0.8524	826	0.9640
50	0.4287	309	0.6511	568	0.8521	827	0.9641
51	0.4303	310	0.6508	569	0.8543	828	0.9642
52	0.4304	311	0.6504	570	0.8555	829	0.9640
53	0.4320	312	0.6511	571	0.8563	830	0.9649
54	0.4327	313	0.6507	572	0.8584	831	0.9650
55	0.4335	314	0.6507	573	0.8601	832	0.9645
56	0.4334	315	0.6502	574	0.8614	833	0.9658
57	0.4342	316	0.6505	575	0.8619	834	0.9651
58	0.4347	317	0.6505	576	0.8620	835	0.9657
59	0.4357	318	0.6507	577	0.8627	836	0.9654
60	0.4370	319	0.6517	578	0.8630	837	0.9658
61	0.4374	320	0.6518	579	0.8657	838	0.9661
62	0.4383	321	0.6527	580	0.8665	839	0.9654
63	0.4391	322	0.6520	581	0.8659	840	0.9645
64	0.4408	323	0.6525	582	0.8676	841	0.9640
65	0.4414	324	0.6525	583	0.8687	842	0.9630
66	0.4425	325	0.6521	584	0.8687	843	0.9601
67	0.4410	326	0.6530	585	0.8714	844	0.9607
68	0.4416	327	0.6543	586	0.8722	845	0.9610
69	0.4407	328	0.6540	587	0.8719	846	0.9623
70	0.4406	329	0.6554	588	0.8733	847	0.9648
71	0.4426	330	0.6560	589	0.8719	848	0.9654
72	0.4455	331	0.6551	590	0.8694	849	0.9672
73	0.4471	332	0.6574	591	0.8689	850	0.9689
74	0.4486	333	0.6575	592	0.8702	851	0.9700
75	0.4500	334	0.6589	593	0.8706	852	0.9709
76	0.4481	335	0.6575	594	0.8725	853	0.9734

Pixel	Efficiency	Pixel	Efficiency	Pixel	Efficiency	Pixel	Efficiency
77	0.4464	336	0.6587	595	0.8738	854	0.9732
78	0.4447	337	0.6587	596	0.8770	855	0.9748
79	0.4434	338	0.6578	597	0.8784	856	0.9734
80	0.4448	339	0.6591	598	0.8788	857	0.9745
81	0.4447	340	0.6598	599	0.8811	858	0.9731
82	0.4490	341	0.6605	600	0.8819	859	0.9734
83	0.4518	342	0.6599	601	0.8838	860	0.9728
84	0.4545	343	0.6587	602	0.8855	861	0.9730
85	0.4576	344	0.6592	603	0.8855	862	0.9720
86	0.4600	345	0.6592	604	0.8889	863	0.9716
87	0.4609	346	0.6605	605	0.8892	864	0.9703
88	0.4634	347	0.6600	606	0.8907	865	0.9721
89	0.4639	348	0.6607	607	0.8925	866	0.9714
90	0.4648	349	0.6619	608	0.8922	867	0.9727
91	0.4638	350	0.6618	609	0.8925	868	0.9745
92	0.4663	351	0.6639	610	0.8946	869	0.9744
93	0.4664	352	0.6638	611	0.8952	870	0.9766
94	0.4681	353	0.6643	612	0.8951	871	0.9772
95	0.4690	354	0.6652	613	0.8969	872	0.9793
96	0.4685	355	0.6643	614	0.8963	873	0.9782
97	0.4698	356	0.6667	615	0.8978	874	0.9795
98	0.4723	357	0.6670	616	0.8985	875	0.9794
99	0.4726	358	0.6680	617	0.8982	876	0.9784
100	0.4727	359	0.6674	618	0.8996	877	0.9801
101	0.4758	360	0.6688	619	0.8995	878	0.9808
102	0.4765	361	0.6665	620	0.8998	879	0.9804
103	0.4778	362	0.6670	621	0.9001	880	0.9814
104	0.4789	363	0.6658	622	0.9003	881	0.9820
105	0.4800	364	0.6653	623	0.8995	882	0.9810
106	0.4809	365	0.6630	624	0.8980	883	0.9820
107	0.4840	366	0.6601	625	0.8954	884	0.9819
108	0.4837	367	0.6570	626	0.8937	885	0.9832
109	0.4854	368	0.6556	627	0.8934	886	0.9835
110	0.4847	369	0.6553	628	0.8939	887	0.9837
111	0.4870	370	0.6564	629	0.8945	888	0.9834
112	0.4875	371	0.6576	630	0.8974	889	0.9847
113	0.4903	372	0.6606	631	0.9002	890	0.9838

Pixel	Efficiency	Pixel	Efficiency	Pixel	Efficiency	Pixel	Efficiency
114	0.4900	373	0.6630	632	0.9005	891	0.9856
115	0.4909	374	0.6660	633	0.9048	892	0.9855
116	0.4926	375	0.6675	634	0.9066	893	0.9860
117	0.4939	376	0.6666	635	0.9082	894	0.9858
118	0.4949	377	0.6671	636	0.9088	895	0.9859
119	0.4956	378	0.6668	637	0.9085	896	0.9861
120	0.4973	379	0.6649	638	0.9083	897	0.9866
121	0.4966	380	0.6645	639	0.9098	898	0.9870
122	0.4980	381	0.6657	640	0.9104	899	0.9876
123	0.4960	382	0.6668	641	0.9080	900	0.9874
124	0.4965	383	0.6688	642	0.9078	901	0.9875
125	0.4977	384	0.6698	643	0.9044	902	0.9870
126	0.4978	385	0.6728	644	0.8996	903	0.9882
127	0.4995	386	0.6743	645	0.8975	904	0.9885
128	0.5025	387	0.6763	646	0.8937	905	0.9891
129	0.5055	388	0.6764	647	0.8912	906	0.9892
130	0.5064	389	0.6787	648	0.8912	907	0.9891
131	0.5096	390	0.6789	649	0.8914	908	0.9893
132	0.5107	391	0.6800	650	0.8919	909	0.9901
133	0.5115	392	0.6810	651	0.8917	910	0.9903
134	0.5132	393	0.6826	652	0.8913	911	0.9916
135	0.5146	394	0.6844	653	0.8907	912	0.9910
136	0.5156	395	0.6841	654	0.8913	913	0.9913
137	0.5167	396	0.6855	655	0.8925	914	0.9917
138	0.5181	397	0.6850	656	0.8955	915	0.9928
139	0.5198	398	0.6856	657	0.8958	916	0.9918
140	0.5204	399	0.6864	658	0.9002	917	0.9930
141	0.5234	400	0.6864	659	0.9031	918	0.9937
142	0.5243	401	0.6865	660	0.9060	919	0.9945
143	0.5245	402	0.6866	661	0.9113	920	0.9956
144	0.5263	403	0.6894	662	0.9142	921	0.9956
145	0.5276	404	0.6921	663	0.9168	922	0.9953
146	0.5282	405	0.6925	664	0.9198	923	0.9959
147	0.5293	406	0.6927	665	0.9230	924	0.9961
148	0.5297	407	0.6931	666	0.9210	925	0.9965
149	0.5321	408	0.6941	667	0.9212	926	0.9965
150	0.5333	409	0.6954	668	0.9199	927	0.9977

Pixel	Efficiency	Pixel	Efficiency	Pixel	Efficiency	Pixel	Efficiency
151	0.5345	410	0.6948	669	0.9216	928	0.9971
152	0.5354	411	0.6964	670	0.9202	929	0.9973
153	0.5366	412	0.6977	671	0.9213	930	0.9974
154	0.5378	413	0.6992	672	0.9219	931	0.9978
155	0.5388	414	0.6996	673	0.9226	932	0.9971
156	0.5401	415	0.7014	674	0.9229	933	0.9978
157	0.5413	416	0.7028	675	0.9241	934	0.9984
158	0.5417	417	0.7035	676	0.9227	935	0.9983
159	0.5441	418	0.7034	677	0.9241	936	0.9990
160	0.5447	419	0.7053	678	0.9261	937	0.9988
161	0.5438	420	0.7066	679	0.9252	938	0.9978
162	0.5456	421	0.7091	680	0.9264	939	0.9990
163	0.5464	422	0.7093	681	0.9250	940	0.9993
164	0.5486	423	0.7088	682	0.9250	941	1.0004
165	0.5498	424	0.7104	683	0.9259	942	0.9994
166	0.5502	425	0.7108	684	0.9266	943	0.9999
167	0.5512	426	0.7123	685	0.9287	944	0.9994
168	0.5505	427	0.7117	686	0.9297	945	1.0001
169	0.5529	428	0.7138	687	0.9294	946	0.9997
170	0.5535	429	0.7141	688	0.9291	947	0.9991
171	0.5555	430	0.7143	689	0.9318	948	0.9993
172	0.5563	431	0.7146	690	0.9328	949	0.9993
173	0.5571	432	0.7155	691	0.9313	950	0.9997
174	0.5571	433	0.7153	692	0.9294	951	0.9995
175	0.5587	434	0.7163	693	0.9277	952	0.9995
176	0.5591	435	0.7159	694	0.9249	953	0.9996
177	0.5601	436	0.7168	695	0.9245	954	0.9989
178	0.5607	437	0.7181	696	0.9230	955	0.9988
179	0.5625	438	0.7178	697	0.9213	956	0.9991
180	0.5633	439	0.7202	698	0.9228	957	0.9997
181	0.5626	440	0.7202	699	0.9258	958	0.9993
182	0.5636	441	0.7198	700	0.9271	959	0.9982
183	0.5634	442	0.7212	701	0.9302	960	0.9985
184	0.5654	443	0.7203	702	0.9325	961	0.9983
185	0.5641	444	0.7212	703	0.9357	962	0.9984
186	0.5653	445	0.7223	704	0.9384	963	0.9984
187	0.5659	446	0.7236	705	0.9404	964	0.9985

Pixel	Efficiency	Pixel	Efficiency	Pixel	Efficiency	Pixel	Efficiency
188	0.5693	447	0.7255	706	0.9421	965	0.9977
189	0.5688	448	0.7252	707	0.9426	966	0.9985
190	0.5720	449	0.7263	708	0.9434	967	0.9984
191	0.5734	450	0.7279	709	0.9433	968	0.9996
192	0.5742	451	0.7272	710	0.9434	969	0.9991
193	0.5759	452	0.7287	711	0.9429	970	0.9994
194	0.5777	453	0.7300	712	0.9423	971	1.0003
195	0.5790	454	0.7306	713	0.9417	972	1.0005
196	0.5779	455	0.7324	714	0.9408	973	1.0001
197	0.5791	456	0.7348	715	0.9418	974	1.0000
198	0.5800	457	0.7352	716	0.9419	975	1.0002
199	0.5821	458	0.7361	717	0.9425	976	1.0000
200	0.5826	459	0.7372	718	0.9424	977	1.0005
201	0.5824	460	0.7375	719	0.9444	978	1.0001
202	0.5837	461	0.7387	720	0.9438	979	0.9997
203	0.5849	462	0.7399	721	0.9433	980	0.9996
204	0.5846	463	0.7402	722	0.9437	981	1.0002
205	0.5859	464	0.7404	723	0.9447	982	1.0003
206	0.5872	465	0.7415	724	0.9439	983	1.0003
207	0.5876	466	0.7421	725	0.9473	984	1.0005
208	0.5882	467	0.7428	726	0.9483	985	1.0008
209	0.5866	468	0.7435	727	0.9491	986	1.0006
210	0.5860	469	0.7451	728	0.9489	987	1.0011
211	0.5853	470	0.7460	729	0.9510	988	1.0009
212	0.5852	471	0.7473	730	0.9514	989	1.0008
213	0.5852	472	0.7469	731	0.9530	990	1.0008
214	0.5858	473	0.7499	732	0.9527	991	1.0004
215	0.5882	474	0.7497	733	0.9527	992	0.9993
216	0.5886	475	0.7512	734	0.9529	993	0.9970
217	0.5914	476	0.7537	735	0.9525	994	0.9950
218	0.5929	477	0.7531	736	0.9516	995	0.9927
219	0.5950	478	0.7550	737	0.9515	996	0.9918
220	0.5969	479	0.7551	738	0.9521	997	0.9931
221	0.5973	480	0.7553	739	0.9510	998	0.9933
222	0.5980	481	0.7580	740	0.9499	999	0.9957
223	0.5992	482	0.7595	741	0.9507	1000	0.9973
224	0.5997	483	0.7612	742	0.9498	1001	0.9988

Pixel	Efficiency	Pixel	Efficiency	Pixel	Efficiency	Pixel	Efficiency
225	0.6023	484	0.7608	743	0.9478	1002	1.0004
226	0.6027	485	0.7610	744	0.9469	1003	1.0013
227	0.6026	486	0.7608	745	0.9462	1004	1.0015
228	0.6035	487	0.7619	746	0.9432	1005	1.0021
229	0.6030	488	0.7625	747	0.9430	1006	1.0021
230	0.6032	489	0.7629	748	0.9415	1007	1.0023
231	0.6041	490	0.7628	749	0.9427	1008	1.0022
232	0.6058	491	0.7646	750	0.9431	1009	1.0014
233	0.6065	492	0.7662	751	0.9447	1010	1.0021
234	0.6071	493	0.7683	752	0.9458	1011	1.0012
235	0.6077	494	0.7679	753	0.9454	1012	1.0007
236	0.6092	495	0.7699	754	0.9481	1013	1.0010
237	0.6104	496	0.7701	755	0.9472	1014	1.0006
238	0.6101	497	0.7710	756	0.9467	1015	1.0008
239	0.6130	498	0.7703	757	0.9465	1016	1.0011
240	0.6127	499	0.7716	758	0.9457	1017	1.0012
241	0.6138	500	0.7717	759	0.9445	1018	1.0020
242	0.6154	501	0.7728	760	0.9448	1019	1.0014
243	0.6164	502	0.7751	761	0.9438	1020	1.0014
244	0.6149	503	0.7765	762	0.9431	1021	1.0007
245	0.6164	504	0.7797	763	0.9422	1022	1.0015
246	0.6177	505	0.7799	764	0.9430	1023	1.0016
247	0.6184	506	0.7828	765	0.9441	1024	1.0011
248	0.6177	507	0.7831	766	0.9456	1025	1.0013
249	0.6195	508	0.7849	767	0.9453	1026	1.0009
250	0.6193	509	0.7868	768	0.9478	1027	1.0005
251	0.6206	510	0.7880	769	0.9488	1028	1.0000
252	0.6223	511	0.7869	770	0.9488	1029	0.9996
253	0.6225	512	0.7878	771	0.9485	1030	0.9991
254	0.6243	513	0.7897	772	0.9480	1031	0.9987
255	0.6243	514	0.7912	773	0.9483	1032	0.9983
256	0.6263	515	0.7905	774	0.9493	1033	0.9978
257	0.6256	516	0.7924	775	0.9479	1034	0.9974
258	0.6266	517	0.7944	776	0.9479	1035	0.9970
259	0.6276	518	0.7944	777	0.9477	1036	0.9965
260	0.6279	519	0.7954	778	0.9479	1037	0.9961
261	0.6276	520	0.7969	779	0.9482	1038	0.9957

Pixel	Efficiency	Pixel	Efficiency	Pixel	Efficiency	Pixel	Efficiency
262	0.6281	521	0.7970	780	0.9513	1039	0.9952

Table D.3: Efficiency as a function of pixel number for a grating position of 1020 nm

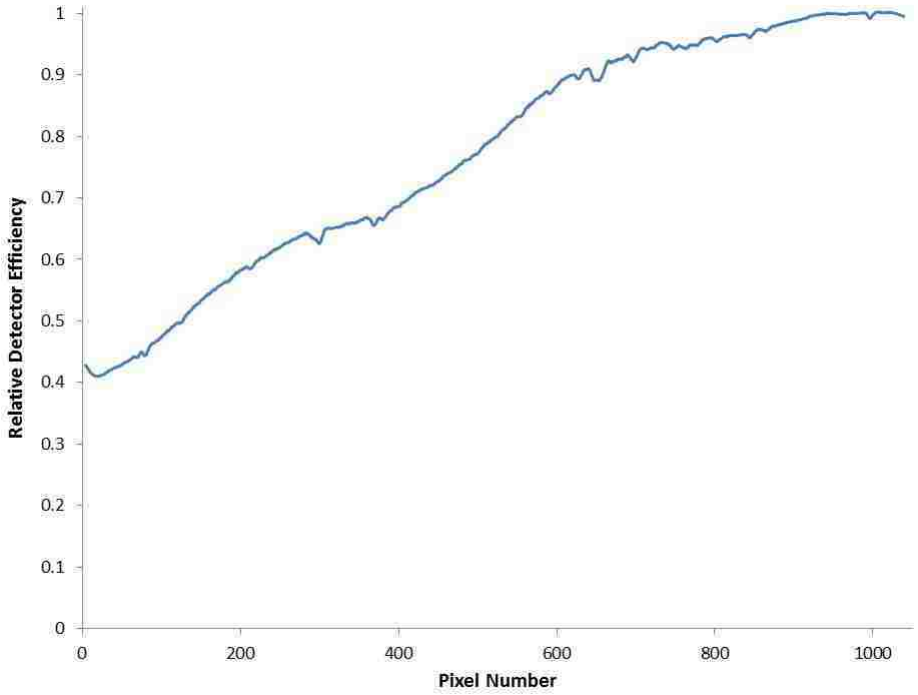

Figure D.3: Efficiency as a function of pixel number for a grating position of 1020 nm.

Bibliography

[1] R. J. Le Roy, "RKR1 2.0: A Computer Program Implementing the First-Order RKR Method for Determining Diatomic Molecule Potential Energy Curves", University of Waterloo Physics Research Report CP-657R, R. J. Le Roy (2004), see http://leroy.uwaterloo.ca/programs/.

[2] A. Pashov, W. Jastrzebski, and P. Kowalczyk, "Construction of potential curves for diatomic molecular states by the IPA method", Comp. Phys. Comm. **128**, 622–634 (2000).

[3] S. Ashman, B. McGeehan, C. M. Wolfe, C. Faust, K. Richter, J. Jones, A. P. Hickman, and J. Huennekens, "Experimental Studies of the NaCs $5^3\Pi_0$ and $1(a)^3\Sigma^+$ Electronic States", J. Chem. Phys. **136**, 114313 (2012).

[4] A. Grochola, A. Pashov, J. Deiglmayr, M. Repp, E. Tiemann, R. Wester, and M. Weidemller, "Photoassociation spectroscopy of the $B^1\Pi$ state of LiCs", J. Chem. Phys. **131**, 054304 (2009).

[5] C. Gabbanini and O. Dulieu, "Formation of ultracold metastable RbCs molecules by short-range photoassociation", Phys. Chem. Chem. Phys. **13**, 18905 (2011).

[6] J. Danzl, M. Mark, E. Haller, M. Gustavsson, R. Hart, J. Aldegunde, J. Hutson, and H.-C. Ngerl, "An ultracold high-density sample of rovibronic ground-state molecules in an optical lattice", Nature Physics **6**, 265 (2010).

[7] P. Zabawa, A. Wakim, A. Neukirch, C. Haimberger, N. Bigelow, A. Stolyarov, E. Pazyuk, M. Tamanis, and R. Ferber, "Near-dissociation photoassociative production of deeply bound NaCs molecules", Phys. Rev. A **82**, 040501 (2010).

[8] D. DeMille, "Quantum Computation with Trapped Polar Molecules", Phys. Rev. Lett. **88**, 067901 (2002).

[9] M. Aymar and O. Dulieu, "Calculation of accurate permanent dipole moments of the lowest $^{1,3}\Sigma^+$ states of heteronuclear alkali dimers using extended basis sets", J. Chem. Phy. **122**, 204302 (2005).

[10] Handbook of Basic Atomic Spectroscopic Data, National Institute of Standards and Technology.

[11] G. Herzberg, *Spectra of Diatomic Molecules* (Van Nostrand Reinhold, New York, 1950).

[12] M. Korek, S. Bleik, and A. R. Allouche, "Theoretical calculation of the low laying electronic states of the molecule NaCs with spin-orbit effect", J. Chem. Phys. **126**, 124313 (2007).

[13] S. Magnier, M. Aubert-Frecon, and P. Millie, "Potential energies, permanent and transition dipole moments for numerous electronic excited states of NaK", J. Mol. Spectrosc. **200**, 96 (2000).

[14] R. Malenda, Ph.D. thesis, Lehigh University, 2012.

[15] O. Docenko, M. Tamanis, R. Ferber, A. Pashov, H. Knöckel, and E. Tiemann, "Spectroscopic studies of NaCs for the ground state asymptote of Na + Cs pairs", Eur. Phys. J. D **31**, 205–211 (2004).

[16] J. Zaharova, O. Docenko, M. Tamanis, R. Ferber, A. Pashov, H. Knöckel, and E. Tiemann, "The $B^1\Pi$ state of NaCs: High resolution laser induced fluorescence spectroscopy and potential construction", J. Chem. Phys. **127**, 224302 (2007).

[17] M. Aymar and O. Dulieu, "Calculations of transition and permanent dipole moments of heteronuclear alkali dimers NaK, NaRb and NaCs", Molecular Physics **105**, 1733 (2007).

[18] B. McGeehan, S. Ashman, C. Wolfe, R. Steinhardt, M. Monaco, J. Huennekens, and A. Hickman, "NaK boundfree and boundbound $4^3\Sigma^+ \rightarrow a^3\Sigma^+$ emission", J. of Mol. Spectrosc. **265**, 75 (2011).

[19] H. Lefebvre-Brion and R. W. Field, *The Spectra and Dynamics of Diatomic Molecules* (Elsevier, Amsterdam, 2004).

[20] J. L. Dunham, "The Energy Levels of a Rotating Vibrator", Phys. Rev. **41**, 721–731 (1932).

[21] R. J. Le Roy, "DParFit 3.3: A Computer Program for Fitting Multi-Isotopologue Diatomic Molecule Spectra", University of Waterloo Physics Research Report CP-663, (2007), see http://leroy.uwaterloo.ca/programs/.

[22] C. Beckel and R. Engelke, "Power-Series Expansions of Vibrational Potentials. IV. Radii of Convergence", J. Chem. Phys. **49**, 5199 (1968).

[23] E. U. Condon, "Nuclear Motions Associated with Electron Transitions in Diatomic Molecules", Phys. Rev. **32**, 858–872 (1928).

[24] R. J. Le Roy, "BCONT 2.2: Computer Program for Calculating Absorption Coefficients, Emission Intensities or (Golden Rule) Predissociation Rates", University of Waterloo Physics Research Report CP-650R, R. J. Le Roy (2004), see http://leroy.uwaterloo.ca/programs/.

[25] R. J. Le Roy, "LEVEL 8.0: A Computer Program for Solving the Radial Schrodinger Equation for Bound and Quasibound Levels", University of Waterloo Physics Research Report CP-663, (2007), see http://leroy.uwaterloo.ca/programs/.

[26] B. H. Bransden and C. J. Joachain, *Physics of Atoms and Molecules* (Addison Wesley Longman Limited, Essex, 1983).

[27] C. R. Vidal and J. Cooper, "Heat Pipe Oven: A New, Well-Defined Metal Vapor Device for Spectroscopic Measurements", J. of Appl. Phys. **40**, 3370–3374 (1969).

[28] S. Ashman, Ph.D. thesis, Lehigh University, 2010.

[29] *Coherent 899-21 Titanium:Sapphire Ring Laser: Operators Manual*, Coherent, Inc., Palo Alto, CA, 1990.

[30] B. Palmer, R. Keller, and J. R. Engleman, "An Atlas of Uranium Emission Intensities in a Hollow Cathode Discharge", Rough Draft of LASL Rep. LA-8251-MS J. R. Engleman (1980).

[31] S. Gerstenkorn and P. Luc, *Atlas du Spectre D'Absorption de la Molecule D'Iode* (Centre National de la Recherche Scientifique, Paris, 1978).

[32] E. Hecht, *Optics* (Pearson Education, New Jersey, 2012).

[33] R. Stair, W. E. Schneider, and J. K. Jackson, "A New Standard of Spectral Irradiance", Appl. Opt. **2**, 1151–1154 (1963).

[34] H. Wang, L. Li, A. M. Lyyra, and W. C. Stwalley, "CW optical-optical double-resonance excitations of $^{39}K_2$ Rydberg states", J. Mol. Spectrosc. **137**, 304 (1989).

[35] Z. J. Jabbour and J. Huennekens, "A study of the predissociation of NaK molecules in the $6^1\Sigma^+$ state by optical–optical double resonance spectroscopy", J. Chem. Phys. **107**, 1094–1105 (1997).

[36] E. Laub, I. Mazsa, S. Webb, J. L. Civita, I. Prodan, Z. Jabbour, R. Namiotka, and J. Huennekens, "Experimental Study of the NaK $3^1\Pi$ State", J. of Mol. Spectrosc. **193**, 376–388 (1999).

[37] J. Zaharova, M. Tamanis, R. Ferber, A. N. Drozdova, E. A. Pazyuk, and A. V. Stolyarov, "Solution of the fully-mixed-state problem: Direct deperturbation analysis of the $A^1\Sigma^+ - b^3\Pi$ complex in a NaCs dimer", Phys. Rev. A **79**, 012508 (2009).

[38] P. Burns, L. Sibbach-Morgus, A. D. Wilkins, F. Halpern, L. Clarke, R. D. Miles, Li Li, A. P. Hickman, and J. Huennekens, "The $4^3\Sigma^+$ state of NaK: Potential energy curve and hyperfine structure", J. Chem. Phys. **119**, 4743–4754 (2003).

[39] A. D. Wilkins, L. Morgus, J. Hernandez-Guzman, J. Huennekens, and A. P. Hickman, "The NaK $1^{1,3}\Delta$ states: Theoretical and experimental studies of fine and hyperfine structure of rovibrational levels near the dissociation limit", J. Chem. Phys. **123**, 124306 (2005).

[40] L. Morgus, P. Burns, R. D. Miles, A. D. Wilkins, U. Ogba, A. P. Hickman, and J. Huennekens, "Experimental study of the NaK $3^3\Pi$ double minimum state", J. Chem. Phys. **122**, 144313 (2005).

[41] H. Salami, T. Bergeman, B. Beser, J. Bai, E. H. Ahmed, S. Kotochigova, A. M. Lyyra, J. Huennekens, C. Lisdat, A. V. Stolyarov, O. Dulieu, P. Crozet, and A. J. Ross, "Spectroscopic observations, spin-orbit functions, and coupled-channel deperturbation analysis of data on the $A^1\Sigma_u^+$ and $b^3\Pi_u$ states of Rb_2", Phys. Rev. A **80**, 022515 (2009).

[42] C. Wolfe, S. Ashman, J. Bai, B. Beser, E. H. Ahmed, A. M. Lyyra, and J. Huennekens, "Collisional Transfer of Population and Orientation in NaK", J. Chem. Phys. **134**, 174301 (2011).

[43] R. Rydberg, Z. Physik **73**, 376 (1931).

[44] R. Rydberg, Z. Physik **80**, 514 (1933).

[45] O. Klein, Z. Physik **76**, 226 (1932).

[46] A. Rees, Proc. Phys. Soc. (London) **59**, 998 (1947).

[47] C. R. Vidal and H. Scheingraber, "Determination of diatomic molecular constants using an inverted perturbation approach : Application to the system of Mg_2", J. of Mol. Spectrosc. **65**, 46–64 (1977).

[48] L. Veseth, Theor. Chim. Acta **18**, 368 (1970).

[49] M. Korek, A. Allouche, K. Fakhreddine, and A. Chaalan, "Theoretical study of the electronic structure of LiCs, NaCs, and KCs molecules", Can. J. Phys. **78**, 977–988 (2000).

[50] R. D. Miles, L. Morgus, D. O. Kashinski, J. Huennekens, and A. P. Hickman, "Nonadiabatic coupling in the $3^3\Pi$ and $4^3\Pi$ states of NaK", J. Chem. Phys. **125**, 154304 (2006).

[51] P. Burns, A. D. Wilkins, A. P. Hickman, and J. Huennekens, "The NaK $1(b)^3\Pi_{\Omega=0}$ state hyperfine structure and the $1(b)^3\Pi_{\Omega=0} \sim 2(A)^1\Sigma^+$ spin-orbit interaction", J. Chem. Phys. **122**, 074306 (2005).

[52] H. Sun and J. Huennekens, "Spin-orbit perturbations between the $A(2)^1\Sigma^+$ and $b(1)^3\Pi_0$ states of NaK", J. Chem. Phys. **97**, 4714–4722 (1992).

Vita

Carl Faust attended Marian High School and graduated in 2004. Carl went on to college at Kutztown University where he graduated Summa Cum Laude with a Bachelors of Science degree in physics in 2009. While at Kutztown, Carl worked as a physics tutor and lab assistant, acted as president of Kutztown's chapter of the Society of Physics Students, and was inducted into Sigma Pi Sigma. After recieving his Bachelors degree, Carl enrolled in graduate school at Lehigh University to study physics. At Lehigh, Carl was awarded the GAANN fellowship (2009-2011) and pursued research in Lehigh's experiemental AMO group. He received a masters degree in physics from Lehigh in January 2011, and his Ph.D. in physics in July 2014. Carl will join the physics department at the Susquehanna University in the Fall of 2014.